UNIVERSITY OF CALIFORNIA

Santa Barbara

From Transition Metals to Actinides: A Homogenous Approach for Clean Alternative Energy and Storage Applications

A dissertation submitted in partial satisfaction

of the requirements for the degree Doctor of Philosophy

in Chemistry

by

Megan Renee Keener

Committee in charge:

Professor Gabriel Ménard, Chair

Professor Trevor Hayton

Professor Susannah Scott

Professor Mahdi Abu–Omar

September 2020

The dissertation of Megan Renee Keener is approved.

_____
Trevor Hayton

_____
Mahdi Abu–Omar

_____
Susannah Scott

_____
Gabriel Ménard, Chair

August 2020

Acknowledgements

First, I would like to acknowledge my supervisor, Prof. Gabriel Ménard. Gab, thank you for the countless conversations, endless guidance, and helping me become the chemist that I am today. Thank you for always having your door open and answering all the questions I've had over the years (there were a lot!). Thank you for always pushing me and allowing me to explore my chemistry in the lab. I am genuinely grateful for all the opportunities you have given me and cannot thank you enough. Additionally, I want to thank Trevor Hayton. Trevor, thank you for allowing me to encroach in your lab space and allowing me to use all the uranium, space, and supplies I needed. Even though I was never an "official" member of your lab, I want to thank you for always being so welcoming and inviting me to various meetings and lab outings – you always made me feel a part of the actinide team, and I am grateful.

I would also like to thank the Gab Lab and Hayton Lab for the countless discussions and interesting conversations. Specifically, I want to thank Maddy Peterson in Gab Lab who was not only one of the best lab/office mates, but someone who has become one of my greatest friends, I am really going to miss our walks and in-n-out trips. Hayton Lab, thank you all for welcoming me into your group. You all have shown nothing but kindness toward me over the past few years. Even though I was never officially in the lab, you always made me feel a part of the team, thank you.

I want to thank my mom and dad, as well as my family. I love you all. Mom and Dad, I could not be here today without all the support and opportunities you have given me. Lastly, I couldn't have done all this without my partner in crime and husband, Travis. Thank you for being my support and helping me succeed in my PhD. You always knew I could do this, and I can never thank you enough. I love you (Luna too).

Vita of Megan Renee Keener

August 2020

EDUCATION

Bachelor of Science in Chemistry, California State University, Chico, May 2015
Doctor of Philosophy in Chemistry, University of California, Santa Barbara, Aug. 2020 (expected)

PROFESSIONAL EMPLOYMENT

Summer 2019 NSF-IRES Fellow, RWTH Aachen University, Aachen, Germany.
2015-2020 Teaching Assistant, Department of Chemistry, UCSB, CA, USA.
Summer 2015 Visiting Scholar, University of California, Santa Barbara, CA, USA.

SELECT PUBLICATIONS

Keener, M., Zheng, S-L., Wu, G., Hayton, T. W., Dobrovetsky, R., Ménard, G. *Manuscript in progress*.

Keener, M., Hunt, C., Carroll, T. G., Kampel, V., Dobrovetsky, R., Hayton, T. W., Ménard, G. *Nature,* 2020, 577, 652–655.

Keener, M., Peterson, M., Hernández-Sanchez, R., Oswald, V. F., Wu, G., Ménard, G. *Chem. Eur. J.* 2017, 23, 11479–11484.

AWARDS

2020 Graduate Division Dissertation Fellowship, University of California, Santa Barbara
2019 NSF-IRES Fellowship, UCSB; in collaboration with RWTH Aachen University
2019 DeWolfe Distinguished Teaching Fellow Award, UCSB
2017-2019 Graduate Student Research Funding, University of California, Santa Barbara
2018 Mellichamp Academic Initiative in Sustainability Fellow
2018 Outstanding Service to the UCSB Chemistry Department Award, UCSB

FIELDS OF STUDY

Major Field: Inorganic and Coordination Chemistry

Abstract

Transition Metals to Actinides: A Homogenous Approach for Clean Alternative Energy and Storage Applications

by

Megan Renee Keener

Over the past two centuries, fossil fuels have been our main global energy currency of choice by exploiting the energy stored in C–H chemical bonds. Fossil fuels comprise roughly 86% of our primary global energy and their combustion contributes to irreversible climate change. The development of alternative energy storage platforms is considered necessary in the shift to decarbonize energy through use of clean alternative energy sources. However, due to the intermittent energy production of these, the development of new energy storage technologies is needed in order to meet an increasing global energy demand. The use of chemical energy vectors, such as H_2, has been considered one of the most complementary platforms to reaching large-scale energy storage. Although H_2 has many attractive qualities, there are many factors impeding us from utilizing it as our main energy currency. H_2 has the highest gravimetric energy density of any clean fuel, but it has the lowest volumetric energy density, making the storage and transportation difficult. Therefore, H_2 storage carriers – like NH_3 – have been proposed to overcome this. Our focus in this work has been to utilize a homogenous approach with readily available transition metal frameworks, specifically a

(salen)M≡N complex, to probe the requirements necessary to undergo NH_3 oxidation to N_2, to release the H_2 equivalents stored within. A nitride homo–coupling reaction to N_2 – a major step in catalytic NH_3 oxidation – will be detailed with our results in isolating and characterizing a rare, mixed–valent Mn^{III}–N≡M^{V} species. Subsequent development of a genuine synthetic cycle for NH_3 oxidation based on this chemistry will be described, in an effort toward generating a truly catalytic system.

Nuclear energy is considered one of the most important components in decarbonizing energy, but the inadvertent release of radioactive materials from storage repositories into the environment poses a potential threat to human health. Uranium (most commonly found as the uranyl ion; UO_2^{2+}) is the key element in nuclear fuel and comprises > 96 % of spent nuclear waste, which can be reprocessed and reused for fuel, while reducing the long–term radiotoxicity and quantity of waste stored in geological repositories. Therefore, developing methods for the separation and recovery of UO_2^{2+} from lanthanides and trans-uranics is of upmost importance for the long–term viability and safety of the nuclear energy sector. Herein, we highlight our results in harnessing the redox-switchable chelating and donating properties of *ortho*-substituted *closo*-carboranes, leading to the controlled chemical or electrochemical sequestration and recovery of UO_2^{2+} in monophasic (organic) or biphasic (organic/aqueous) schemes. Building on these results, we also describe the development of a biphasic extraction system for selective UO_2^{2+} separation and recovery in aqueous mixtures of actinides(IV), lanthanides(III), and alkali(I) metals, commonly found in nuclear waste.

Table of Contents

List of Figures

List of Schemes

List of Tables

List of Symbols and Abbreviations

CV	cyclic voltammetry
Fc and Fc^+	ferrocene and ferrocenium
BDFE	bond dissociation free energy
HAA	hydrogen atom abstraction
NBS	*N*–bromosuccinimide
GC–MS	gas chromatography–mass spectrometry
GC–TCD	gas chromatography–thermal conductivity detector
HB	Haber–Bosch
RE	renewable energy
RFB	redox–flow batteries
GBE	galvanostatic bulk electrolysis
GHG	greenhouse gas
MOX	mixed-oxide
HHLW	hot high–level waste
PUREX	Plutonium URanium EXtraction
UREX	URanium EXtraction
°C	degrees Celcius
μ	bridging
Å	angstrom, 10^{-10} m
δ	chemical shift
η	eta (bonding mode)
λ	wavelength

π	pi bond
σ	sigma bond
υ	frequency
atm	atmosphere
H_2	dihydrogen
N_2	dinitrogen
NH_3	ammonia
CO_2	carbon dioxide
UO_2^{2+}	uranyl
Ln/An	lanthanide/actinide
^{t}Bu	tert–butyl
Et	ethyl
Me	methyl
Ph	phenyl
MeCN-d_3	deuterated acetonitrile
$CDCl_3$	deuterated chloroform
DCM-d_2	deuterated dichloromethane
FB	fluorobenzene
NMR	nuclear magnetic resonance
ppb	parts per billion, 10^{-9}
ppm	parts per million, 10^{-6}
mmol	millimole

Chapter 1 – Introduction

1.1 Overview of energy storage technologies and shift to clean energy sources

Over the past two centuries, fossil fuels (coal, oil, and natural gas) have been our main global energy currency of choice by exploiting the energy stored in C–H chemical bonds. Fossil fuels comprise 86% of our primary global energy[1] and the rapid increase in the global population, energy–intensive modern lifestyles, and industrialization are all contributing to issues concerning energy – directly relating to the increase of CO_2 into the environment, contributing to irreversible climate change.[2] The Paris Agreement on climate change was adopted in 2015 in hopes to strengthen global response to the threat of climate change by "holding the increase in the global average temperature to well below 2 ºC above pre–industrial levels and pursuing efforts to limit the temperature increase to 1.5 ºC above pre–industrial levels".[3] This goal requires an extensive reduction in CO_2 and greenhouse gas (GHG) emissions, requiring a shift to clean, alternative energy sources. Renewable and non–renewable energy (RE and non–RE) sectors are rapidly growing, which include but are not limited to wind, solar, hydroelectric, geothermal, and tidal technologies as RE sources. Non–RE sources include, but are not limited to, nuclear power generation from ^{235}U. Nuclear is generally considered non–RE because U is a finite source but, is overall considered a clean energy source and critical in combatting CO_2 emissions. Due to this intermittent nature of RE sources, the development of new energy storage technologies is needed.[4]

To meet global demands for both grid–level energy storage and transportation–based energy vectors, a combination of multiple energy storage platforms will be needed to meet demands. Energy storage systems come in various forms and their cost and scalability are widely dependent on the form of stored energy (kinetic, thermal, potential, electromagnetic,

chemical). Some storage forms are better suited for small–scale applications versus large–scale applications and vice versa.[5] To complement the current main grid-scale energy storage platforms, such as pumped hydropower, flywheels, etc., electrochemical and chemical storage technologies are considered critical to stabilize and balance fluctuating intermittent renewable energy sources. Electrochemical energy storage technologies mainly include batteries (e.g. Li–ion, redox-flow batteries, etc.),[6] where chemical energy vectors are NH_3, MeOH, or H_2.[7-9] Chemical storage vectors tend to have greater energy density than current battery technologies and have large discharge rates since they can be stored for any period of time. There have been multiple promising chemical energy storage systems proposed, but for the scope of this thesis, use of H_2 (section 1.2) and NH_3 (sections 1.3 and 1.3.1) as potential chemical energy vectors, and NH_3 as a H_2 storage carrier we will described in further detail.

1.1.1 Chemical bond energy storage – hydrogen (H_2) economy

The concept of a hydrogen (H_2) economy has gained considerable attention in recent years.[10-14] H_2 as an energy carrier is not only desirable but argued to be an important key in combatting further climate change.[15-16] H_2 has the highest gravimetric energy density (143 MJ/kg) of any clean fuel, a lower heating value of 33.3 kWh/kg, and a combustion emissions profile free from CO_2 – as H_2O is the only byproduct when used in a H_2 fuel cell or in a H_2 combustion chamber.[17-18] However, even though industry produces and consumes more than 60 million tons of H_2 every year, there are multiple overwhelming factors impeding us from utilizing H_2 as our main form of stored energy.[19] In order to satisfy the world's energy demand, more than $3x10^{12}$ kg of H_2 would need to be produced per year, which is roughly 100 times more than current H_2 production.[20] This would dramatically increase the global CO_2 emission

profiles because currently, 1 ton of H_2 produced from coal, oil, and gas by steam reforming or the water gas shift reaction (WGSR) liberates more than 10 tons of CO_2.[21-22]

In order for H_2 to be a clean energy vector: (1) the H_2 must be produced from renewable sources, for example H_2O electrolysis from solar energy or a method without CO_2 generation (e.g. methane decomposition to carbon and H_2).[23-24] Although progress has been made in developing systems for H_2O electrolysis to H_2, it is currently not a thermodynamically favorable process as it requires voltages up to 1.23V, which translates to 180 MJ of energy just to generate 1 kg of H_2.[25] This makes H_2O electrolysis currently not a financially large–scale viable option as it is more expensive than current H_2 production from natural gas – as 96% of world H_2 production comes from fossil fuels.[22, 26] Yet, progress is being made toward building plants capable of performing this electrocatalysis large scale from renewables such as solar in order to reduce costs.[7] (2) Although H_2 has the highest gravimetric density, it unfortunately has a low volumetric energy density of only 0.01 MJ/L or 3 Wh/L, making the storage and transportation at ambient temperatures and pressures difficult (where the density is 0.0898 g/L at 0 ºC and 1 bar).[27] In order to circumvent this, alternative storage methods need to be realized for mobile applications in order to efficiently store and transport H_2.[9]

1.1.2 H_2 storage carriers – NH_3 as a H_2 source and energy vector

In 2017, the Department of Energy (DOE) set targets for H_2 storage at 5.5 wt.% and 40 g/L for gravimetric and volumetric energy capacities, respectively. Additional targets include ease of regeneration of material, system cost, and operating temperature and stability.[28] There have been many systems developed for the uptake (storage) and release of H_2 and can be described in two main categories. The first is by physisorption materials where H_2 is absorbed into porous materials such as zeolites, MOFs, clathrate hydrates, and various carbon materials

and polymers, which generally have low uptake, but excellent reversibility.[29-36] The second is by means of chemical storage where a H_2 rich material undergoes a chemical process to release the stored H_2 or H^+/e^- equivalents. Ideally, these processes are reversible with ease of uptake and release. Examples of solid–state systems can include, but are not limited to, metal (alkali and TM) and non–metal hydrides, amines, and amides.[37-41] Additionally, liquid carriers such a derivatized carbazoles, alcohols, and formic acid have also been investigated as good candidates.[42-45] Although most of these systems meet some of the DOE requirements – for example ammonia borane (BH_3NH_3) contains 19.5 wt.% H_2, far exceeding target values of 5.5 wt%, or the dehydrogenation of MeOH (12.6 wt.%) to H_2 and CO_2 (in the form of carbonate), which can be coupled with the reverse for regeneration of material for the hydrogenation of CO_2 to MeOH.[46-47] – most of the technologies are still in their infancy and scalability and practicality proves to be a limiting factor.

An alternative storage method involves using ammonia (NH_3) produced through the industrial Haber–Bosch (HB) process – first realized in 1909 by Fritz Haber and later transformed into an industrial process by Carl Bosch in 1913 for BASF.[48] NH_3 has been proposed as a platform for H_2 storage[49-51] because it contains 17.6 wt.% H_2, it is easy to store (–33°C b.p.),[50] it has a volumetric density which is 1.7 times that of liquid H_2, and is low in cost (\$1.4–1.7/kg H_2).[51-52] Additionally, the production (175 Mt/year) and distribution of NH_3 are already established through the HB process, circumventing the need for developing new systems and infrastructure.[9, 50, 52-55] NH_3 is the second most manufactured commodity chemical in the world, where 75–90% of production is used for fertilizer, and accounts for ~ 2% of the total global primary energy use and 1% of all CO_2 emissions.[56-57] Many have argued that N_2 reduction through the HB process is problematic due to its high operating temperatures and

pressures (400–500°C and 100–300 atm),[4] posing an energy intensive process in which new catalysts and systems need to be realized to improve the current industrial practice.[7-8, 58] This has placed a lot of effort in trying to better understand N_2 reduction chemistry, which has harnessed research attention for the past 60 years. Performing this chemistry at ambient temperatures and pressures would be ideal, but current HB is a very efficient process, with almost 100% conversion of H_2/N_2 to NH_3 when reactants are passed through the catalyst bed multiple times, outcompeting current alternative systems.[57] Overall, in order to promote a renewable, carbon–free H_2 economy will require: (1) production of H_2 or H^+/e^- equivalents from H_2O electrolysis and coupling this process with; (2) concurrent H_2 storage which could be accomplished in reacting N_2 with H_2 to produce NH_3 through the HB process (**Scheme 1.1**).

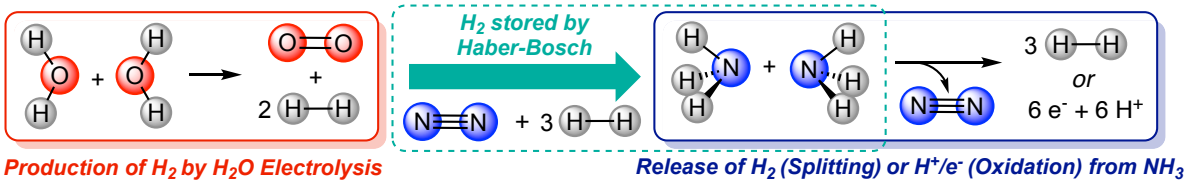

Scheme 1.1. Pathway from renewable H_2 production, storage, and usage.

The key to utilizing NH_3 as an H_2 storage vector, whether for H_2 release or direct use in fuel cells, is developing systems which can efficiently promote the difficult $6e^-$ oxidation chemistry of NH_3 to N_2 (**Equation 1.1**).

(1) $2\ NH_3 \longrightarrow N_2 + 6\ H^+ + 6\ e^-$

(2) $6\ H^+ + 6\ e^- \longrightarrow 3\ H_2$

(3) $2\ NH_3 \longrightarrow N_2 + 3\ H_2$

Equation 1.1.

NH_3 as a storage medium for H_2 has shown promise primarily through: (1) heterogenous systems,[59-63] where catalysts are capable of splitting (cracking) NH_3 to N_2 and

H_2, typically using precious metals (e.g. Ru), operate at high temperatures (400–600 ºC), and have low TON most likely due to the poor understanding of what is occurring at the heterogeneous active sites.[52, 61-65] (2) Electrochemical systems[53, 66-69] have also been realized for conversion of H_2 to electricity by polymer electrolyte membrane fuel cells (PEMFC) – commonly used and industrially relevant in the transportation sector in H_2 fuel cell cars – or solid oxide fuel cells (SOFC), which are typically employed for stationary power generation.[70-71] Additionally, direct use of NH_3 in alkaline membrane fuel cells (AMFC) are being explored but are still in their infancy for use and development due to the higher oxidation potential of NH_3 compared to H_2, causing lower power generation compared to H_2 fuel cells.[72-75] Typically, precious metal electrodes such as Pt, Rh, and Ir are used in these systems, and tend to have large overpotentials due to poisoning at the electrode surface because of irreversible nitride formation, leading to detrimental effects on the fuel cell catalysts.[10, 53, 65, 68-69, 76-77] Lastly, NH_3 combustion has been proposed, but will be an unlikely solution because if its low flammability compared to hydrocarbons and H_2.[8]Additionally, the by–products can be a mixture of NOx compounds, contributing to photochemical smog production and GHG emissions (N_2O), ultimately circumventing its use as a renewable energy vector.[4, 78] Due to the promising role of AMFCs for utilizing the energy stored in NH_3 chemical bonds, probing the $6e^-$ conversion of NH_3 to N_2 with coordination complexes may provide mechanistic insights into what is required for the multi–electron oxidation, leading to innovations in catalyst design.

1.1.2.1 Brief history of N_2 reduction chemistry

N_2 reduction, has been extensively studied for the past century due to the vast importance in understanding key intermediates for the catalytic HB process as well as biological N_2 fixation through the nitrogenase enzyme.[79-81] Fixation of N_2 is a challenging task

due to the inertness and extremely strong N≡N triple bond (BDE = 944 kJ/mol), zero dipole moment, and large HOMO–LUMO gap.[82-83] Since the first discovery of the first N_2 complex by Allen and Senoff in 1965,[84-85] there has been extensive work in designing complexes that bind and activate N_2. Even though N_2 is a poor σ–donor and weak π–acceptor ligand, N_2 complexes for almost every transition metal have been synthesized. Some of the early work in designing systems was aimed at modeling what was believed to be the primary active site of nitrogenase (FeMo–cofactor, although there are others that have been discovered).[86-88] Other systems have been designed to develop new catalytic processes for alternative functionalization and fixation of N_2 in relation to HB. The bonding of N_2 to a metal is generally described as the degree in which the N≡N bond is activated, either strongly or weakly.[89]

Coordination of N_2 can vary by mono– or bimetallic systems with end–on or side–on binding modes (**Figure 1.1**). The degree in which N_2 binds and is activated is largely dependent on the metal, oxidation state, and ligand framework surrounding the metal.

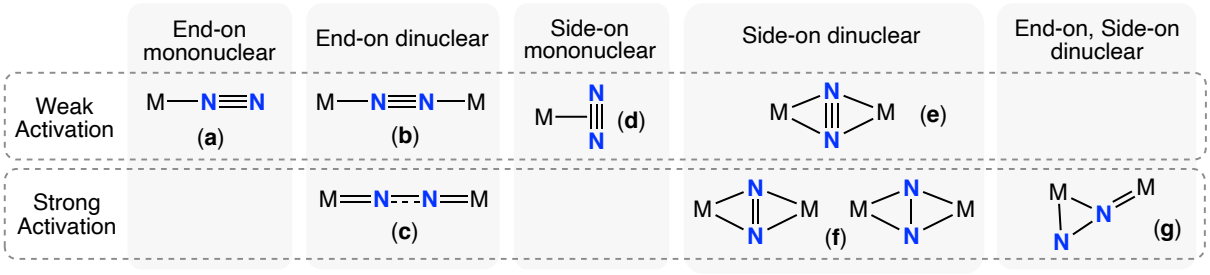

Figure 1.1. Representative binding modes for various N_2 complexes.

For example, strongly activated N_2 generally requires a strongly reducing metal and is commonly observed with mid to early transition metals, generally dinuclear in an end–on (**c**)[90-92] or side–on (**f**)[83, 93-96] binding mode. Alternatively, most N_2 complexes contain N_2 that is weakly coordinated where the N_2 bond is not significantly elongated compared to free N_2. The most common binding modes include mononuclear end–on (**a**), with examples dinuclear of

end–on (**b**),[97-98] side–on dinuclear (**e**),[99-100] and side–on mononuclear (**d, Figure 1.1**).[101] Intuitively, one would think the more activated the N_2, the greater likelihood it will react. Yet, it has been shown that strong activation is not necessarily a requisite for increased reactivity. It is also highly dependent on the ligand environment, sterics, and electronics of the complex. For example, in 2018, Liddle *et. al*. reported the first example of catalytic NH_3 conversion at a Ti^{III} center with a formal weakly activated N_2 molecule, showing strong activation is not a requirement for reactivity.[102]

The vast number of examples of N_2 complexes and types of functionalization exceeds the scope of this thesis, but it is important to note the historical examples pertaining to N_2 reduction chemistry, and how this has contributed in developing systems for the reverse, NH_3 oxidation. Stoichiometric activation and functionalization of N_2 can occur by various pathways; hydrogenation by metal–N_2 or metal–nitride complexes – where nitride activation is considered an intermediate step in conversion to NH_3 – and protonation and reduction chemistry with addition of H^+/e^- sources. Additionally, the catalytic conversion of N_2 to NH_3 has been realized. Stoichiometric or catalytic N_2 reduction chemistry has been demonstrated with various transition metal complexes, such as Co and Os, but most systems include mid to late transition metals such as Mo, Ru, and Fe.[103-109] Due to Mo being considered the active site for biological NH_3 generation in the FeMo–cofactor of nitrogenase, Mo is amongst one the most studied metals for stoichiometric[110-115] and catalytic[104, 109, 116] N_2 reduction chemistry. More recently, catalytic N_2 reduction chemistry has been shown with Fe[103, 117] – due to the importance in the FeMo–cofactor and industrial HB, which proceeds via a Fe heterogenous catalyst. Some early transition metals complexes such as Zr, W, Cr, and V[83, 118-120] have also been shown to facilitate N_2 activation, with a recent example including the first catalytic

conversion of N_2 to NH_3 using an early transition metal at Ti.[102] Catalytic N_2 reduction to $N(Me_3Si)_3$ with Ti – an alternative desired N_2 fixation product – has also been shown by Okuda *et. al*.[121] N_2 reduction chemistry is not limited to transition metals, as actinide complexes of U have been shown by Mazzanti *et. al*. to undergo N_2 fixation chemistry to NH_3.[122] Interestingly, before a Fe–based catalyst was adopted for the HB process, a U–based heterogenous catalyst was reported to be one of the most effective heterogenous catalysts used for NH_3 production.[123-124] Before their report in 2017, U–N_2 complexes were rare[99, 125-129] and conversion to NH_3 with a homogenous U complex was unprecedented. Although N_2 reduction will not be covered any further and is out of the scope of this thesis, noting the systems that are capable of performing this chemistry can give a broader insight for what may be required for the reverse, NH_3 oxidation. For example, Peters *et. al*. has reported catalytic N_2 reduction to NH_3 for various systems using Fe. They adopted a similar ligand framework in order to perform the electrocatalytic NH_3 oxidation to N_2. The primary development was designing a ligand that was robust in oxidative conditions, versus their N_2 reduction catalysts which were reductively robust.[103, 117, 130] Nishibayashi *et. al*. has also shown similar rational in catalyst design to develop their Ru catalysts. Both demonstrate that understanding the systems that promote N_2 reduction, although not directly transferrable in all systems, can help guide new development for systems capable of performing efficient NH_3 oxidation.

1.1.2.2 Brief history of NH_3 activation

Molecular N–H activation of NH_3 under mild conditions is of great interest in current catalysis science.[50, 52] Due to the high BDFE for NH_3 ($BDFE_{N–H}$: 104 kcal/mol)[56] and low acidity ($pKa^{dmso} = \sim 41$)[131], activation under mild conditions is challenging, but can occur upon binding or interacting with a transition metal center. The formation of a N–N bond is

considered the requisite step in the oxidation of NH_3 to N_2 (where formation of the N≡N triple bond is 226 kcal/mol)[132] and understanding the mechanism is crucial for designing systems capable of performing this transformation. In 1967, Taube reported the first example of NH_3 oxidation using $[Co(NH_3)_6]^{3+}$ and $[Co(NH_3)_5(H_2O)]^{3+}$ forming N_2, NH_4^+, and Co^{II}.[133] After almost a decade, in 1979, Taube and Buhr reported both chemical and electrochemical oxidation of NH_3 in aqueous solutions by $[Os(NH_3)_5(CO)]^{2+}$, forming N_2 in the bridging μ–N_2 product $[(Os(NH_3)_4(CO))_2N_2]^{4+}$.[134] This study pioneered research into NH_3 oxidation chemistry using molecular complexes and the field started gaining traction. In 1992, Collman *et. al*. studied chemical and electrochemical NH_3 oxidation with Ru porphyrins via alternative pathways such as hydrazine and diazene intermediates.[135] Since these early examples, there have since been various homogenous approaches developed in order to overcome the high bond strength to stoichiometrically cleave N–H bonds including: deprotonation (**a**), N–H oxidative addition (**b**), (reversible) metal–ligand cooperativity (1,2 addition) (**c**), 1,2 addition across a metal–metal bond (**d**), and HAA (**e**) (**Scheme 1.2**). [136-149] [139, 141, 150-155]

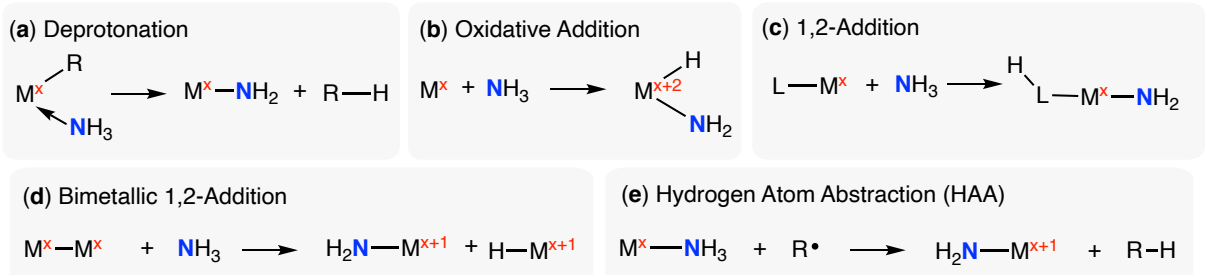

Scheme 1.2. Various NH_3 activation pathways.

Most of these systems include mid to late transition metals in mid to low oxidation states in order to promote a formal oxidation of the metal (**b**, **d**, **e**). In addition to these systems, a synthetic cycle for NH_3 oxidation was elusive until we reported our progress toward catalytic NH_3 oxidation using a simple Mn^V≡N complex which is further detailed in Chapter 2.

Additionally, until very recently, catalytic NH_3 oxidation was unprecedented, and only within the past year has been realized utilizing HAA,[156-157] homogenous electrocatalysis,[130, 158] and oxidation/deprotonation chemistry.[159] Currently, there are only five reports of active catalysts containing Ru centers, with one example of Fe. Building off our previous results for a synthetic cycle for NH_3 oxidation, before these systems for catalysis were realized, we also attempted to develop a catalytic cycle and these results will be described further in Chapter 3.

1.2 Nuclear for alternative energy

In addition to developing energy storage systems (detailed in section 1.1), understanding the various types of RE and non–RE sources is crucial in the global battle against climate change and reduction of GHG emissions. Wind, solar, geothermal, hydroelectric, etc. are considered abundant RE sources, but due to their intermittent nature and need for developing alternative energy storage technologies, outlined above, our main energy currency cannot solely rely on renewables. Alternative non–RE sources are considered key to shifting to cleaner energy sources. Natural gas (CH_4) has been widely considered a bridge in the shift from fossil fuels to clean sources but is not a long–term solution because it is not a carbon free source and produces roughly half the amount of CO_2 emissions compared to burning of coal.[58] Alternatively, nuclear power is considered one of the most important components in decarbonizing energy. Nuclear fission was first discovered soon after the breakout of WWII in hopes of exploiting nuclear for destructive capabilities. In 1942, the world's first reactor in Chicago, Pile–1, proved that a large–scale nuclear chain–reaction could be sustained. Soon after, this type of reactor was adopted by the Manhattan project in order to produce materials for the first nuclear weapons.[160] Since, reactors have undergone various iterations for safer and more efficient reactor systems in terms of energy development –

generating heat to convert to consumable energy. To date, there are four reactor types with most utilizing Generation II (1960s design) and III (1990s design), with various types of heat conversion to power systems.[160]

While nuclear power is generally considered clean, due to its carbon–free emissions profiles through the uranium–235 (^{235}U) fission process, U mining is energy-intensive and uranium itself is a finite resource – unlike wind, solar, and water. Nuclear power plants release GHGs only from ancillary pathways – use of fossil fuels during construction, fuel processing, maintenance, mining, and decommissioning – which is roughly 4–5% as much as a natural gas power plant. Today, roughly 32% of the energy produced in the US is generated from nuclear power, with 13% produced globally.[161-162] France on the other hand has been a global leader in nuclear energy production, providing a large quantity of energy safely to consumers, accounting for 87% of the country's energy source.[163] The International Atomic Energy Agency (IAEA) has predicted nuclear power generation may increase worldwide by up to 56% over the next 10 years.[164] Global conversion and proliferation resistance of nuclear stems from safety for concerns in waste remediation and disposal, accidents and failures of nuclear power plants, and national security for safely producing and using enriched U for reactors.[165-166] Despite these concerns and the potential quantity of energy nuclear can provide, there is no doubt that the handling of radioactive materials, before and after use, as well as consideration of extraction for U is still of upmost importance in nuclear science today.[167]

1.2.1 Uranium extraction for use as fuel

Uranium (U) is a key element for nuclear fuel, and the mining and recovery of U from spent nuclear fuel rods is of upmost importance for continued energy security globally.[168] Currently, U extraction proceeds through terrestrial mining by various extraction techniques.[169]

At our current consumption rate and increasing demand of nuclear energy, it is expected that conventional U reserves could be depleted in roughly a century.[167, 170] The recovery of U from seawater has received considerable attention within recent years due to the size of this untapped source, containing 4.5 billion tons of U, which is over a thousand times more than the known terrestrial supply.[171-172] Development of technology that can efficiently recover U from seawater could make the oceans a limitless source of fuel for nuclear reactors. Concentrations of U (most commonly found as the uranyl ion; UO_2^{2+}) in the ocean are low (~3.3 μg/L) making it difficult to extract. Additionally, seawater contains trace amounts of almost every naturally occurring element, making selectivity toward U necessary for efficient extraction (**Table 1.1**).[168, 172-174]

Table 1.1. Abundance of selected ions in seawater.[173]

Metal	Concentration		Notes
Na	1.08% (w/w)	0.456 M	at 3.5% salinity
K	392 ppm	9.7 mM	
Ca	411 ppm	40 mM	
Li	0.17 ppm	24 uM	
Fe	3.4 ppb	59 nm	
Cu	0.9 ppb	14 nM	
U	3.3 ppb	13 nM	as $Ca(UO_2)(CO_3)_3$
V	1.9 ppb	36 nM	80–90% V^V, 10–20% V^{IV}
Au	11 ppt	50 pm	

U extraction from seawater was first proposed in the 1960s, based on phosphates and other UO_2^{2+} extractants that have been used in the PUREX (Plutonium URanium EXtraction) process for processing spent nuclear fuel.[175-176] In the past 50 years, several technologies have been investigated for extraction and commonly relies on extremely strong chelating/binding affinities to UO_2^{2+} including synthetic organic polymers,[172-174, 177-182] protein–based sorbents,[183] ionic liquids,[184] organic and inorganic frameworks,[185-194] carbon–based

sorbents,[195-198] alternating current electrochemical systems,[199-200] and homogenous systems.[201-202] Out of these systems, amidoxime–based sorbents historically have been the most heavily studied and utilized for U extraction from seawater.[172, 184, 203-210] However, cost analyses have revealed that none of the currently reported extraction systems are competitive against terrestrial mining. Today, seawater extraction has been estimated to cost between $450–1500/kg of U_3O_8 using known sorbents, widely stemming from synthesis costs, reusability, and lifetime of the materials.[172, 177, 211-212] For example, a pilot plant in Japan (through Japan Atomic Energy Agency; JAEA) tested a stack of sheets or braid–type adsorbents, resulting in 1 kg of uranium yellow cake after a 240–day campaign.[213] Their adsorbent was able to capture 1.5 mg of U/g of adsorbent in 30 days with contact with seawater.[214] After additional cost analysis performed by US researchers for this technique, U extraction was estimated to be $1,230/kg of U (in 2011 US dollars). Alternatively, the Pacific Northwest National Laboratory (PNNL) in 2014 performed similar field tests and cost analyses utilizing a lab–proven adsorbent developed by Oak Ridge National Lab (ORNL) in the US They found that using in–line filters or in–flow columns could yield 3.3 mg of U/g of adsorbent after 8 weeks of contact in seawater. The U adsorption was roughly three times compared to the JAEA study with a drop in cost to $610/kg of U.[177] Although significant progress has been made in extraction technology, terrestrial mining is still more economically feasible at $45–160/kg of U_3O_8.[215]

The chemistry of seawater also plays an important role in U extraction in terms of chemical speciation of metals, salinity, pH, and biological activity.[168] Primarily due to the pH, the chemical form of U in seawater consists of uranyl calcium carbonate complexes.[216-217] These complexes are generally difficult to extract because the calcium and carbonate ions need to be displaced, and the concentrations of these are high in seawater. Selectivity of U over

other trace metal ions proves to be one of the most challenging tasks in extraction science today. For example, one of the most developed systems for extraction shows selectivity toward V (14.9%) >> Fe (1.6%) > UO_2^{2+} (1.0%), with V occupying roughly 15 times as many sites as UO_2^{2+} even though the concentrations are comparable in solution (**Table 1.1**).[168] The added complexity to investigating selectivity is the aqueous chemistry surrounding V. Similar to U, V can exist as polynuclear species at given pH values, and undergo redox chemistry between V^V and V^{IV}, where V^{IV} only comprises of 10–20% of V in seawater.[218-220] This is primarily due to the biochemistry that occurs in seawater. Marine organisms that take up these different trace elements can alter chemical compositions and vary based on season, oceanic depth, temperature, and location, further complicating the optimization for extraction and selectivity chemistry.[218, 221] In addition to uptake of U, the controlled release of UO_2^{2+} and regeneration of captured material is much less established and can generally be difficult, expensive, and destructive to the initial material.[173, 212] For example, the stripping of V^V from amidoxime sorbents for reuse is incredibly harsh compared to the eluents used for U and other cations, ultimately destroying the sorbent.[209-210] Understanding the selective coordination chemistry of UO_2^{2+}, with the controlled, non–destructive release is crucial in developing novel U extraction material with high selectivity, capacity, and regeneration of all materials that is economically and environmentally viable.[222]

1.2.2 Nuclear waste remediation and reprocessing

Nuclear waste is generated through irradiation of nuclear fuel where the isotopic and elemental composition changes. In commercial reactors, the fissile material decreases and fission products accumulate, particularly neutron–absorbing products such as lanthanides, causing a decrease in efficiency. This requires the nuclear fuel to be replaced periodically in

the core of the reactor, generating spent fuel rods which are then treated as nuclear waste. In a reactor that utilizes U as the fuel, most of the spent fuel is potentially useful, where fissile products contain 1% Pu, 3–4% other fission products, 95% ^{238}U and 1% of ^{235}U. Thus, the primarily fertile ^{238}U and Pu can be separated from the other fission products and reused potentially for fuel,[223] which is coined as a "closed fuel cycle". Alternatively, an "open fuel cycle" determines the nuclear waste is deemed as having no further value and spent fuel is stored in deep geological repositories to decrease the radiotoxcity of the long–lived actinides. In 1970, the US decided to adopt an "open fuel cycle" based on arguments for national security (securing the generation of Pu used for nuclear weapons in repositories) and for halting global proliferation of nuclear technologies under the Non–Nuclear Proliferation Treaty.[165] Handling waste in terms of an "open fuel cycle" presents environmental and potential threats to living organisms due to the presence of long–lived, heat–generating, radiotoxic actinides stored in geological repository facilities. Primarily the actinides– ^{237}Np with a half–life of about 2 million years, ^{241}Am, and ^{244}Cu; (which undergoes spontaneous fission) present the most concern, with alkali metals, for example, ^{137}Cs one of the many isotopes of Cs) also contributing to the long-lived radiotoxicity.[224-225] Storing this hot high–level waste (HHLW) requires storage for 100–150 years isolated underground before it can be disposed of in a geological repository, requiring fuel to be widely spaced out to safely decay. This means repository "footprints" tend to be quite large and require massive amounts of land for storage. To mitigate the quantity of waste and decrease repository footprints, reducing the radioactivity of the HHLW that needs to be stored in "closed fuel cycles" presents many alternative advantages in managing waste. Since > 90% of the spent fuel is reusable, reprocessing allows

the extraction and reuse of valuable fissile products, ultimately reducing the long–term radioactivity of the waste and potentially decreasing toxicity risks at disposal facilities.

1.2.2.1 The PUREX Process

The standard industrial process for reprocessing spent fuel is through the PUREX (Plutonium URanium EXtraction) process which was developed in the US in the 1950s.[226-227] Both the UK and France have adopted this system to reprocess their nuclear fuel on large–scale, with some Japanese plants beginning to incorporate this system for waste remediation. This technology has been successfully carried out for over 50 years and is based on solvent extraction between an aqueous nitric acid and organic kerosene phase – where the extractant, tributyl phosphate (TBP) is dissolved. In this process, U (reused in new fuel) and plutonium (Pu; use as fuel in mixed oxide (MOX) systems) are selectivity separated while keeping most of the minor actinides (Np, Am, Cm) and fission products dissolved in the aqueous nitric acid layer (**Figure 1.2**).[226, 228] Additionally, the PUREX process can be modified to incorporate the coextraction of neptunium (Np) by alternating nitric acid concentrations and use of a coextractant – which is desirable for conversion to ^{238}Pu for spacecraft thermo–electric generators.[229]

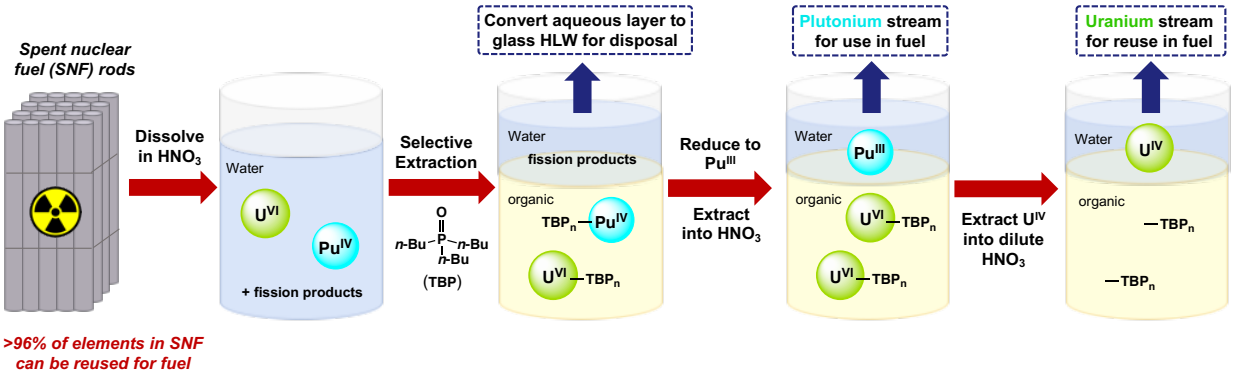

Figure 1.2. Schematic of the PUREX extraction process.

Like most extraction schemes, there are many factors that contribute to selective extraction of various ions in raffinate including the oxidation state of the metal ions, coordination capacity (ionic radius), the solvent/extractant combination utilized for separation, and solubility properties/hydrolysis effects of the metal ions in the aqueous acidic raffinate – which is widely pH dependent. In terms of selective UO_2^{2+}/Pu^{IV} separation, the mechanism behind the PUREX process has been extensively studied and is well–established, known for its exceptional extraction ability of metal ions in tetravalent and hexavalent states, specifically UO_2^{2+} (U^{VI}) and Pu^{IV}.[230-231] The selectivity in extracting UO_2^{2+} and Pu^{VI} into the TBP organic layer is based on the similarity of U^{VI} and Pu^{IV} complexation with TBP and extractability into the organic phase of the nitrate complexes formed from the acidic aqueous raffinate. Trivalent An^{III} and Ln^{III} nitrate complexes formed in the acidic media tend to be less soluble in the TBP organic phase and are not extracted. Formation of Pu^{III} during reprocessing is an excellent example to describe how valency sways extraction. Pu^{IV} is highly stabilized by concentrated nitric acid solutions due to the oxidizing nature of the solvent. During reprocessing, if the acid concentration becomes too dilute, Pu^{IV} will favorably disproportionate into Pu^{III}, Pu^{IV}, and Pu^{VI}, ultimately generating nuclear raffinate containing mixtures of Pu oxidation states. This disproportionation cannot be reversed and to reestablish Pu^{IV}, reduction to Pu^{III} occurs with subsequent oxidation by chemical pretreatment. This pretreatment step is crucial in Pu extraction because unlike Pu^{IV}, the extraction of Pu^{III} (and partially Pu^{VI}) does not readily occur because of the insolubility in the TBP organic layer. Additionally, to separate the UO_2^{2+} and Pu^{IV} further down the line in the process, the insolubility of Pu^{III} is exploited by reductively back–extracting Pu into the aqueous layer. Not only does this show how control of the oxidation state of Pu is key for Pu–U extraction in the PUREX process, but how the extraction

steps are largely dependent on the valency of the ion (i.e. how selective it is toward tetra– and hexavalent ions versus trivalent species, independent of the element).

1.2.2.2 Further developments of the PUREX process

Despite decades of research into U separation technologies, and industrial utilization of the decades–old PUREX process, there is still considerable attention given to the selective extraction of UO_2^{2+} from aqueous solutions containing transuranics (all elements with a higher atomic number than uranium), lanthanides, or transition metals.[232-236] Many have argued developing alternative extraction schemes to the PUREX process are crucial for the following. For instance, while the PUREX process is a widely understood, it does have weaknesses. PUREX was originally designed for spent fuels with low fissile product content. Current fuels generate roughly 10 times more fissile products than what the PUREX process was designed to handle. Also, the radiation fields are so great, degradation products can form and have potential to interfere with the solvent extraction process. Like most solvent extraction systems, many steps are involved in order to purify the products, ultimately creating large volumes of secondary radioactive waste. Even though this process makes use of fissile materials and widely contributes in remediation efforts, it has been argued to be complicated and expensive.[160, 237] Furthermore, proliferation concerns for national security for the separation and isolation of elementally pure Pu through the PUREX process have created societal and political resistance. For these reasons, alternative systems generating pure U streams (eliminating separation of Pu independently) have seen considerable attention recently, specifically in the US with some research in France.[238]

Some of these alternative methods include UREX+ processes, which were being developed in the US under the International Framework for Nuclear Energy Cooperation

(IFNEC). In these processes, the central feature is to keep Pu with either U or the other transuranic elements and the remainder of the waste is then handled by disposal or transmutation in fast reactors to ease proliferation resistance by not isolating pure Pu streams. There have been various iterations of UREX+ which vary predominantly on how the Pu is coextracted with the other fission products. Ultimately, there were major issues in separation of Pu and other TRU elements from the undesirable fission products in the aqueous phase and UREX variations have since been abandoned.

Currently, there have been various other systems developed, with a few examples including NUEX (similar to UREX+1a; separates U, then TRUs, without carrying fission products through), COEX (separates U and Pu; can be modified for Np together from minor An's and fission products) and GANEX (separates U and Pu as in COEX, then An's and Ln's from fission products). All these systems have shown promise, but unlike the PUREX process, none are industrially viable, suffering due to complexity and lack of understanding.[160, 238-240] In this thesis, our work in developing alternative methods of reprocessing and remediation of nuclear waste will be highlighted in Chapter 5.

1.3 Scope of thesis

As will be described in this thesis, the main objective of this graduate research was to develop readily available ligands and synthetically useful frameworks capable of carrying out the desired metal–based, inorganic reactions. Although the topics – NH_3 oxidation with transition metal complexes to uranyl extraction, separation, and recovery – may seem disjointed, the common theme in this thesis work was to develop and understand how ligand environments play a role in complex stability and reactivity, while understanding the

requirements needed in synthesizing metal complexes capable of performing the desired transformations.

Half of the work described in this thesis focuses on understanding stoichiometric and catalytic NH_3 oxidation utilizing simple Mn–salen complexes. The first portion (Chapter 2) describes our initial success in understanding a crucial step, the homocoupling N–N bond formation, for performing and understanding NH_3 oxidation.[241] The second portion of this work (Chapter 3) describes our progress toward completing a catalytic cycle for NH_3 Ultimately, this led us toward investigating the mechanism required to oxidize NH_3 as will be described. The remainder of this thesis (Chapters 4–5) presents a change in direction from transition metal complexes to actinide and lanthanide chemistry. Chapter 4 is our recent work for electrochemical uranyl capture and release using derivatized *o*–carboranes.[242] Our most current work will be detailed in utilizing *o*–carboranes for other systems such as transition metal complexes and the selective separation and recovery of uranyl in the presence of metal ions in terms of nuclear waste remediation (a publication has been prepared for this work), and seawater extraction chemistry (Chapter 5).

1.4 References

1. Gautam, P.; Kumar, S.; Lokhandwala, S., Chapter 11 - Energy-Aware Intelligence in Megacities. In *Current Developments in Biotechnology and Bioengineering*, Kumar, S.; Kumar, R.; Pandey, A., Eds. Elsevier: 2019; pp 211-238.

2. IEA *World Energy Outlook 2019*; Paris, 2019.

3. Nations, U., The Paris Agreement. 2015.

4. Kobayashi, H.; Hayakawa, A.; Somarathne, K. D. Kunkuma A.; Okafor, Ekenechukwu C., Science and technology of ammonia combustion. *Proceedings of the Combustion Institute* **2019,** *37* (1), 109-133.

5. Revankar, S. T., Chapter Six - Chemical Energy Storage. In *Storage and Hybridization of Nuclear Energy*, Bindra, H.; Revankar, S., Eds. Academic Press: 2019; pp 177-227.

6. Yang, Z.; Zhang, J.; Kintner-Meyer, M. C. W.; Lu, X.; Choi, D.; Lemmon, J. P.; Liu, J., Electrochemical Energy Storage for Green Grid. *Chemical Reviews* **2011,** *111* (5), 3577-3613.

7. Service, R. F., Liquid sunshine. *Science* **2018,** *361* (6398), 120.

8. Giddey, S.; Badwal, S. P. S.; Munnings, C.; Dolan, M., Ammonia as a Renewable Energy Transportation Media. *ACS Sustainable Chemistry & Engineering* **2017,** *5* (11), 10231-10239.

9. Dalebrook, A. F.; Gan, W.; Grasemann, M.; Moret, S.; Laurenczy, G., Hydrogen storage: beyond conventional methods. *Chemical Communications* **2013,** *49* (78), 8735-8751.

10. Muradov, N. Z.; Veziroğlu, T. N., "Green" path from fossil-based to hydrogen economy: An overview of carbon-neutral technologies. *Int. J. Hydrogen Energy* **2008,** *33* (23), 6804-6839.

11. Turner, J. A., Sustainable Hydrogen Production. *Science* **2004,** *305* (5686), 972.

12. Armaroli, N.; Balzani, V., The Hydrogen Issue. *ChemSusChem* **2011,** *4* (1), 21-36.

13. Lewis, N. S.; Nocera, D. G., Powering the planet: Chemical challenges in solar energy utilization. *Proc. Natl. Acad. Sci. U.S.A.* **2006,** *103* (43), 15729-15735.

14. Whitesides, G. M.; Crabtree, G. W., Don't Forget Long-Term Fundamental Research in Energy. *Science* **2007,** *315* (5813), 796.

15. Jones, L. In *Perspectives on the evolution into a hydrogen economy*, Miami Univ. First World Hydrogen Energy Conf. Proc, 1976.

16. Abe, J. O.; Popoola, A. P. I.; Ajenifuja, E.; Popoola, O. M., Hydrogen energy, economy and storage: Review and recommendation. *International Journal of Hydrogen Energy* **2019,** *44* (29), 15072-15086.

17. Bockris, J. O. M., The hydrogen economy: Its history. *International Journal of Hydrogen Energy* **2013,** *38* (6), 2579-2588.

18. Singh, S.; Jain, S.; Ps, V.; Tiwari, A. K.; Nouni, M. R.; Pandey, J. K.; Goel, S., Hydrogen: A sustainable fuel for future of the transport sector. *Renewable and Sustainable Energy Reviews* **2015,** *51*, 623-633.

19. Holladay, J. D.; Hu, J.; King, D. L.; Wang, Y., An overview of hydrogen production technologies. *Catalysis Today* **2009,** *139* (4), 244-260.

20. Züttel, A., Hydrogen storage methods. *Naturwissenschaften* **2004,** *91* (4), 157-172.

21. Jess, A. W., Peter Industrial Hydrogen Production from Hydrocarbon Fuels and Biomass. In *Hydrogen Science and Engineering : Materials, Processes, Systems and Technology*, 2016; pp 237-252.

22. Dufour, J.; Serrano, D. P.; Gálvez, J. L.; Moreno, J.; García, C., Life cycle assessment of processes for hydrogen production. Environmental feasibility and reduction of greenhouse gases emissions. *International Journal of Hydrogen Energy* **2009,** *34* (3), 1370-1376.

23. Wang, M.; Wang, Z.; Gong, X.; Guo, Z., The intensification technologies to water electrolysis for hydrogen production – A review. *Renewable and Sustainable Energy Reviews* **2014,** *29*, 573-588.

24. Villacampa, J. I.; Royo, C.; Romeo, E.; Montoya, J. A.; Del Angel, P.; Monzón, A., Catalytic decomposition of methane over Ni-Al2O3 coprecipitated catalysts: Reaction and regeneration studies. *Applied Catalysis A: General* **2003,** *252* (2), 363-383.

25. Kim, S.; Koratkar, N.; Karabacak, T.; Lu, T.-M., Water electrolysis activated by Ru nanorod array electrodes. *Applied Physics Letters* **2006,** *88* (26), 263106.

26. Tremel, A.; Wasserscheid, P.; Baldauf, M.; Hammer, T., Techno-economic analysis for the synthesis of liquid and gaseous fuels based on hydrogen production via electrolysis. *International Journal of Hydrogen Energy* **2015,** *40* (35), 11457-11464.

27. Veziroğlu, T. N.; Şahi˙n, S., 21st Century's energy: Hydrogen energy system. *Energy Conversion and Management* **2008,** *49* (7), 1820-1831.

28. Energy, O. o. E. E. a. R. E. U. S. D. o. *Executive Summaries for the Hydrogen Storage Materials Center of Excellence - Chemical Hydrogen Storage CoE, Hydrogen Sorption CoE, and Metal Hydride CoE*; 2017.

29. Li, Y.; Yang, R. T., Hydrogen Storage in Low Silica Type X Zeolites. *The Journal of Physical Chemistry B* **2006,** *110* (34), 17175-17181.

30. Stoeck, U.; Krause, S.; Bon, V.; Senkovska, I.; Kaskel, S., A highly porous metal–organic framework, constructed from a cuboctahedral super-molecular building block, with exceptionally high methane uptake. *Chemical Communications* **2012,** *48* (88), 10841-10843.

31. Farha, O. K.; Özgür Yazaydın, A.; Eryazici, I.; Malliakas, C. D.; Hauser, B. G.; Kanatzidis, M. G.; Nguyen, S. T.; Snurr, R. Q.; Hupp, J. T., De novo synthesis of a metal–organic framework material featuring ultrahigh surface area and gas storage capacities. *Nature Chemistry* **2010,** *2* (11), 944-948.

32. Lee, H.; Lee, J.-w.; Kim, D. Y.; Park, J.; Seo, Y.-T.; Zeng, H.; Moudrakovski, I. L.; Ratcliffe, C. I.; Ripmeester, J. A., Tuning clathrate hydrates for hydrogen storage. *Nature* **2005,** *434* (7034), 743-746.

33. Bae, S. H.; Lee, Y. M.; Fukuzumi, S.; Nam, W., Fine Control of the Redox Reactivity of a Nonheme Iron(III)-Peroxo Complex by Binding Redox-Inactive Metal Ions. *Angew Chem Int Ed Engl* **2016**.

34. Felderhoff, M.; Weidenthaler, C.; von Helmolt, R.; Eberle, U., Hydrogen storage: the remaining scientific and technological challenges. *Physical Chemistry Chemical Physics* **2007,** *9* (21), 2643-2653.

35. Aboutalebi, S. H.; Aminorroaya-Yamini, S.; Nevirkovets, I.; Konstantinov, K.; Liu, H. K., Enhanced Hydrogen Storage in Graphene Oxide-MWCNTs Composite at Room Temperature. *Advanced Energy Materials* **2012,** *2* (12), 1439-1446.

36. Budd, P. M.; Butler, A.; Selbie, J.; Mahmood, K.; McKeown, N. B.; Ghanem, B.; Msayib, K.; Book, D.; Walton, A., The potential of organic polymer-based hydrogen storage materials. *Physical Chemistry Chemical Physics* **2007,** *9* (15), 1802-1808.

37. Guo, Z. X.; Shang, C.; Aguey-Zinsou, K. F., Materials challenges for hydrogen storage. *Journal of the European Ceramic Society* **2008,** *28* (7), 1467-1473.

38. Urgnani, J.; Torres, F. J.; Palumbo, M.; Baricco, M., Hydrogen release from solid state NaBH4. *International Journal of Hydrogen Energy* **2008,** *33* (12), 3111-3115.

39. Hu, J.; Fichtner, M.; Chen, P., Investigation on the Properties of the Mixture Consisting of Mg(NH2)2, LiH, and LiBH4 as a Hydrogen Storage Material. *Chemistry of Materials* **2008,** *20* (22), 7089-7094.

40. Xiong, Z.; Wu, G.; Hu, J.; Chen, P., Ca–Na–N–H system for reversible hydrogen storage. *Journal of Alloys and Compounds* **2007,** *441* (1), 152-156.

41. Bowden, M.; Autrey, T.; Brown, I.; Ryan, M., The thermal decomposition of ammonia borane: A potential hydrogen storage material. *Current Applied Physics* **2008,** *8* (3), 498-500.

42. Teichmann, D.; Arlt, W.; Wasserscheid, P., Liquid Organic Hydrogen Carriers as an efficient vector for the transport and storage of renewable energy. *International Journal of Hydrogen Energy* **2012,** *37* (23), 18118-18132.

43. Bshish, A.; Yaakob, Z.; Narayanan, B.; Ramakrishnan, R.; Ebshish, A., Steam-reforming of ethanol for hydrogen production. *Chemical Papers* **2011,** *65* (3), 251-266.

44. Kusche, M.; Enzenberger, F.; Bajus, S.; Niedermeyer, H.; Bösmann, A.; Kaftan, A.; Laurin, M.; Libuda, J.; Wasserscheid, P., Enhanced Activity and Selectivity in Catalytic Methanol Steam Reforming by Basic Alkali Metal Salt Coatings. *Angewandte Chemie International Edition* **2013,** *52* (19), 5028-5032.

45. Benson, E. E.; Kubiak, C. P.; Sathrum, A. J.; Smieja, J. M., Electrocatalytic and homogeneous approaches to conversion of CO2 to liquid fuels. *Chemical Society Reviews* **2009,** *38* (1), 89-99.

46. Nielsen, M.; Alberico, E.; Baumann, W.; Drexler, H.-J.; Junge, H.; Gladiali, S.; Beller, M., Low-temperature aqueous-phase methanol dehydrogenation to hydrogen and carbon dioxide. *Nature* **2013,** *495* (7439), 85-89.

47. Balaraman, E.; Gunanathan, C.; Zhang, J.; Shimon, L. J. W.; Milstein, D., Efficient hydrogenation of organic carbonates, carbamates and formates indicates alternative routes to methanol based on CO2 and CO. *Nature Chemistry* **2011,** *3* (8), 609-614.

48. Ertl, G., Reactions at Surfaces: From Atoms to Complexity (Nobel Lecture). *Angewandte Chemie International Edition* **2008,** *47* (19), 3524-3535.

49. Kandemir, T.; Schuster, M. E.; Senyshyn, A.; Behrens, M.; Schlögl, R., The Haber–Bosch Process Revisited: On the Real Structure and Stability of "Ammonia Iron" under Working Conditions. *Angew. Chem. Int. Ed.* **2013,** *52* (48), 12723-12726.

50. Klerke, A.; Christensen, C. H.; Norskov, J. K.; Vegge, T., Ammonia for hydrogen storage: challenges and opportunities. *J. Mater. Chem.* **2008,** *18* (20), 2304-2310.

51. Christensen, C. H.; Johannessen, T.; Sørensen, R. Z.; Nørskov, J. K., Towards an ammonia-mediated hydrogen economy? *Catalysis Today* **2006,** *111* (1), 140-144.

52. Lan, R.; Irvine, J. T. S.; Tao, S., Ammonia and related chemicals as potential indirect hydrogen storage materials. *International Journal of Hydrogen Energy* **2012,** *37* (2), 1482-1494.

53. Little, D. J.; Smith, I. I. I. M. R.; Hamann, T. W., Electrolysis of liquid ammonia for hydrogen generation. *Energy Environ. Sci.* **2015,** *8* (9), 2775-2781.

54. Schuth, F.; Palkovits, R.; Schlogl, R.; Su, D. S., Ammonia as a possible element in an energy infrastructure: catalysts for ammonia decomposition. *Energy & Environmental Science* **2012,** *5* (4), 6278-6289.

55. Rees, N. V.; Compton, R. G., Carbon-free energy: a review of ammonia- and hydrazine-based electrochemical fuel cells. *Energy Environ. Sci.* **2011,** *4* (4), 1255-1260.

56. Warren, J. J.; Tronic, T. A.; Mayer, J. M., Thermochemistry of Proton-Coupled Electron Transfer Reagents and its Implications. *Chemical Reviews* **2010,** *110* (12), 6961-7001.

57. Krietsch Boerner, L., Industrial ammonia production emits more CO2 than any other chemical-making reaction. Chemists want to change that. *Chemical & Engineering News Archive* **2019,** *97* (24).

58. Ahlgren, W. L., The Dual-Fuel Strategy: An Energy Transition Plan. *Proceedings of the IEEE* **2012,** *100* (11), 3001-3052.

59. David, W. I. F.; Makepeace, J. W.; Callear, S. K.; Hunter, H. M. A.; Taylor, J. D.; Wood, T. J.; Jones, M. O., Hydrogen Production from Ammonia Using Sodium Amide. *Journal of the American Chemical Society* **2014,** *136* (38), 13082-13085.

60. Li, L.; Wang, Y.; Xu, Z. P.; Zhu, Z., Catalytic ammonia decomposition for CO-free hydrogen generation over Ru/Cr2O3 catalysts. *Applied Catalysis A: General* **2013,** *467*, 246-252.

61. Lorenzut, B.; Montini, T.; Pavel, C. C.; Comotti, M.; Vizza, F.; Bianchini, C.; Fornasiero, P., Embedded Ru@ZrO2 Catalysts for H2 Production by Ammonia Decomposition. *ChemCatChem* **2010,** *2* (9), 1096-1106.

62. Varisli, D.; Elverisli, E. E., Synthesizing hydrogen from ammonia over Ru incorporated SiO2 type nanocomposite catalysts. *International Journal of Hydrogen Energy* **2014,** *39* (20), 10399-10408.

63. Raróg-Pilecka, W.; Szmigiel, D.; Kowalczyk, Z.; Jodzis, S.; Zielinski, J., Ammonia decomposition over the carbon-based ruthenium catalyst promoted with barium or cesium. *Journal of Catalysis* **2003,** *218* (2), 465-469.

64. Taylor, G. B., Oxidation of Ammonia. *Industrial & Engineering Chemistry* **1927,** *19* (11), 1250-1252.

65. Cheddie, D., Ammonia as a Hydrogen Source for Fuel Cells: A Review. In *Hydrogen Energy - Challenges and Perspectives*, Minic, D., Ed. InTech: Rijeka, 2012; p Ch. 13.

66. Little, D. J.; Edwards, D. O.; Smith, M. R.; Hamann, T. W., As Precious as Platinum: Iron Nitride for Electrocatalytic Oxidation of Liquid Ammonia. *ACS Applied Materials & Interfaces* **2017,** *9* (19), 16228-16235.

67. Adli, N. M.; Zhang, H.; Mukherjee, S.; Wu, G., Review—Ammonia Oxidation Electrocatalysis for Hydrogen Generation and Fuel Cells. *Journal of The Electrochemical Society* **2018,** *165* (15), J3130-J3147.

68. Gwak, J.; Choun, M.; Lee, J., Alkaline Ammonia Electrolysis on Electrodeposited Platinum for Controllable Hydrogen Production. *ChemSusChem* **2016,** *9* (4), 403-408.

69. Dong, B.-X.; Tian, H.; Wu, Y.-C.; Bu, F.-Y.; Liu, W.-L.; Teng, Y.-L.; Diao, G.-W., Improved electrolysis of liquid ammonia for hydrogen generation via ammonium salt electrolyte and Pt/Rh/Ir electrocatalysts. *International Journal of Hydrogen Energy* **2016,** *41* (33), 14507-14518.

70. Ma, Q.; Ma, J.; Zhou, S.; Yan, R.; Gao, J.; Meng, G., A high-performance ammonia-fueled SOFC based on a YSZ thin-film electrolyte. *Journal of Power Sources* **2007,** *164* (1), 86-89.

71. Meng, G.; Jiang, C.; Ma, J.; Ma, Q.; Liu, X., Comparative study on the performance of a SDC-based SOFC fueled by ammonia and hydrogen. *Journal of Power Sources* **2007,** *173* (1), 189-193.

72. Zhao, Y.; Setzler, B. P.; Wang, J.; Nash, J.; Wang, T.; Xu, B.; Yan, Y., An Efficient Direct Ammonia Fuel Cell for Affordable Carbon-Neutral Transportation. *Joule* **2019,** *3* (10), 2472-2484.

73. Joseph, M.; Leigh, T.; Swain, L., Synthesis of and Novel Reactions with Bis[imidazol-2-yl]nitromethane. *Imperial Chemical Industries Lmited* **1977**.

74. Sjödin, M.; Styring, S.; Åkermark, B.; Sun, L.; Hammarström, L., Proton-Coupled Electron Transfer from Tyrosine in a Tyrosine−Ruthenium−tris-Bipyridine Complex: Comparison with TyrosineZ Oxidation in Photosystem II. *Journal of the American Chemical Society* **2000,** *122* (16), 3932-3936.

75. Irebo, T.; Reece, S. Y.; Sjödin, M.; Nocera, D. G.; Hammarström, L., Proton-Coupled Electron Transfer of Tyrosine Oxidation: Buffer Dependence and Parallel Mechanisms. *Journal of the American Chemical Society* **2007,** *129* (50), 15462-15464.

76. Litwinienko, G.; Ingold, K. U., Abnormal Solvent Effects on Hydrogen Atom Abstraction. 2. Resolution of the Curcumin Antioxidant Controversy. The Role of Sequential Proton Loss Electron Transfer. *The Journal of Organic Chemistry* **2004,** *69* (18), 5888-5896.

77. Adão, P.; Barroso, S.; Avecilla, F.; Oliveira, M. C.; Pessoa, J. C., CuII–salan compounds: Synthesis, characterization and evaluation of their potential as oxidation catalysts. *Journal of Organometallic Chemistry* **2014,** *760*, 212-223.

78. Otomo, J.; Koshi, M.; Mitsumori, T.; Iwasaki, H.; Yamada, K., Chemical kinetic modeling of ammonia oxidation with improved reaction mechanism for ammonia/air and ammonia/hydrogen/air combustion. *International Journal of Hydrogen Energy* **2018,** *43* (5), 3004-3014.

79. Burgess, B. K.; Lowe, D. J., Mechanism of Molybdenum Nitrogenase. *Chemical Reviews* **1996,** *96* (7), 2983-3012.

80. Hoffman, B. M.; Dean, D. R.; Seefeldt, L. C., Climbing Nitrogenase: Toward a Mechanism of Enzymatic Nitrogen Fixation. *Accounts of Chemical Research* **2009,** *42* (5), 609-619.

81. Einsle, O.; Tezcan, F. A.; Andrade, S. L. A.; Schmid, B.; Yoshida, M.; Howard, J. B.; Rees, D. C., Nitrogenase MoFe-Protein at 1.16 Å Resolution: A Central Ligand in the FeMo-Cofactor. *Science* **2002,** *297* (5587), 1696.

82. Fryzuk, M. D.; Johnson, S. A., The continuing story of dinitrogen activation. *Coordination Chemistry Reviews* **2000,** *200-202*, 379-409.

83. Fryzuk, M. D.; Love, J. B.; Rettig, S. J.; Young, V. G., Transformation of coordinated dinitrogen by reaction with dihydrogen and primary silanes. *Science* **1997,** *275* (5305), 1445-1447.

84. Allen, A. D.; Senoff, C. V., Nitrogenopentammineruthenium(II) complexes. *Chemical Communications (London)* **1965,** (24), 621-622.

85. Allen, A. D.; Bottomley, F.; Harris, R. O.; Reinsalu, V. P.; Senoff, C. V., Ruthenium complexes containing molecular nitrogen. *Journal of the American Chemical Society* **1967,** *89* (22), 5595-5599.

86. Sippel, D.; Einsle, O., The structure of vanadium nitrogenase reveals an unusual bridging ligand. *Nature Chemical Biology* **2017,** *13* (9), 956-960.

87. Rees, J. A.; Bjornsson, R.; Schlesier, J.; Sippel, D.; Einsle, O.; DeBeer, S., The Fe–V Cofactor of Vanadium Nitrogenase Contains an Interstitial Carbon Atom. *Angewandte Chemie International Edition* **2015,** *54* (45), 13249-13252.

88. Lancaster, K. M.; Roemelt, M.; Ettenhuber, P.; Hu, Y.; Ribbe, M. W.; Neese, F.; Bergmann, U.; DeBeer, S., X-ray Emission Spectroscopy Evidences a Central Carbon in the Nitrogenase Iron-Molybdenum Cofactor. *Science* **2011,** *334* (6058), 974.

89. Tuczek, F.; Lehnert, N., New Developments in Nitrogen Fixation. *Angewandte Chemie International Edition* **1998,** *37* (19), 2636-2638.

90. Nikiforov, G. B.; Vidyaratne, I.; Gambarotta, S.; Korobkov, I., Titanium-Promoted Dinitrogen Cleavage, Partial Hydrogenation, and Silylation. *Angewandte Chemie International Edition* **2009,** *48* (40), 7415-7419.

91. Hao, S.; Berno, P.; Minhas, R. K.; Gambarotta, S., The role of ligand steric hindrance in determining the stability of very short V□V contacts. Preparation and characterization of a series of V (II) and V (III) amidinates. *Inorganica Chimica Acta* **1996,** *244* (1), 37-49.

92. Berno, P.; Gambarotta, S., Formation of a Metalaaziridine Ring and Dinitrogen Fixation Promoted by a Niobium Amide Complex. *Organometallics* **1995,** *14* (5), 2159-2161.

93. MacLachlan, E. A.; Fryzuk, M. D., Synthesis and Reactivity of Side-On-Bound Dinitrogen Metal Complexes. *Organometallics* **2006,** *25* (7), 1530-1543.

94. Chirik, P. J., Dinitrogen functionalization with bis(cyclopentadienyl) complexes of zirconium and hafnium. *Dalton Transactions* **2007,** (1), 16-25.

95. Cohen, J. D.; Fryzuk, M. D.; Loehr, T. M.; Mylvaganam, M.; Rettig, S. J., Synthesis and Structure of a Zirconium Dinitrogen Complex with a Side-On Bridging N2 Unit. *Inorganic Chemistry* **1998,** *37* (1), 112-119.

96. Fryzuk, M. D.; Haddad, T. S.; Rettig, S. J., Reduction of dinitrogen by a zirconium phosphine complex to form a side-on-bridging N2 ligand. Crystal structure of {[Pri2PCH2SiMe2)2N]ZrCl}2(.mu.-.eta.2:.eta.2-N2). *Journal of the American Chemical Society* **1990,** *112* (22), 8185-8186.

97. de Wolf, J. M.; Blaauw, R.; Meetsma, A.; Teuben, J. H.; Gyepes, R.; Varga, V.; Mach, K.; Veldman, N.; Spek, A. L., Bis(tetramethylcyclopentadienyl)titanium Chemistry. Molecular Structures of [(C5HMe4)(μ-η1:η5-C5Me4)Ti]2 and [(C5HMe4)2Ti]2N2. *Organometallics* **1996,** *15* (23), 4977-4983.

98. Lee, D. W.; Kaska, W. C.; Jensen, C. M., Mechanistic Features of Iridium Pincer Complex Catalyzed Hydrocarbon Dehydrogenation Reactions: Inhibition upon Formation of a μ-Dinitrogen Complex. *Organometallics* **1998,** *17* (1), 1-3.

99. Roussel, P.; Scott, P., Complex of Dinitrogen with Trivalent Uranium. *Journal of the American Chemical Society* **1998,** *120* (5), 1070-1071.

100. Evans, W. J.; Ulibarri, T. A.; Ziller, J. W., Isolation and x-ray crystal structure of the first dinitrogen complex of an f-element metal, [(C5Me5)2Sm]2N2. *Journal of the American Chemical Society* **1988,** *110* (20), 6877-6879.

101. Jeffrey, J.; Lappert, M. F.; Riley, P. I., Organozirconium dinitrogen complexes [Zr(η-C5H4R')2(η2-N2)R] and [{Zr(η-C5H5)2R}2N2][R=(Me3Si)2CH,R'= H OR Me]. *Journal of Organometallic Chemistry* **1979,** *181* (1), 25-36.

102. Doyle, L. R.; Wooles, A. J.; Jenkins, L. C.; Tuna, F.; McInnes, E. J. L.; Liddle, S. T., Catalytic Dinitrogen Reduction to Ammonia at a Triamidoamine–Titanium Complex. *Angewandte Chemie International Edition* **2018,** *57* (21), 6314-6318.

103. Anderson, J. S.; Rittle, J.; Peters, J. C., Catalytic conversion of nitrogen to ammonia by an iron model complex. *Nature* **2013,** *501* (7465), 84-87.

104. Arashiba, K.; Kinoshita, E.; Kuriyama, S.; Eizawa, A.; Nakajima, K.; Tanaka, H.; Yoshizawa, K.; Nishibayashi, Y., Catalytic Reduction of Dinitrogen to Ammonia by Use of Molybdenum–Nitride Complexes Bearing a Tridentate Triphosphine as Catalysts. *Journal of the American Chemical Society* **2015,** *137* (17), 5666-5669.

105. Fajardo, J.; Peters, J. C., Catalytic Nitrogen-to-Ammonia Conversion by Osmium and Ruthenium Complexes. *Journal of the American Chemical Society* **2017,** *139* (45), 16105-16108.

106. Eizawa, A.; Arashiba, K.; Tanaka, H.; Kuriyama, S.; Matsuo, Y.; Nakajima, K.; Yoshizawa, K.; Nishibayashi, Y., Remarkable catalytic activity of dinitrogen-bridged dimolybdenum complexes bearing NHC-based PCP-pincer ligands toward nitrogen fixation. *Nature Communications* **2017,** *8* (1), 14874.

107. Kuriyama, S.; Arashiba, K.; Nakajima, K.; Matsuo, Y.; Tanaka, H.; Ishii, K.; Yoshizawa, K.; Nishibayashi, Y., Catalytic transformation of dinitrogen into ammonia and hydrazine by iron-dinitrogen complexes bearing pincer ligand. *Nature Communications* **2016,** *7* (1), 12181.

108. Kuriyama, S.; Arashiba, K.; Tanaka, H.; Matsuo, Y.; Nakajima, K.; Yoshizawa, K.; Nishibayashi, Y., Direct Transformation of Molecular Dinitrogen into Ammonia Catalyzed by Cobalt Dinitrogen Complexes Bearing Anionic PNP Pincer Ligands. *Angewandte Chemie International Edition* **2016,** *55* (46), 14291-14295.

109. Schrock, R. R., Catalytic Reduction of Dinitrogen to Ammonia by Molybdenum: Theory versus Experiment. *Angewandte Chemie International Edition* **2008,** *47* (30), 5512-5522.

110. Chatt, J.; Pearman, A. J.; Richards, R. L., The reduction of mono-coordinated molecular nitrogen to ammonia in a protic environment. *Nature* **1975,** *253* (5486), 39-40.

111. Pickett, C. J.; Talarmin, J., Electrosynthesis of ammonia. *Nature* **1985,** *317* (6038), 652-653.

112. George, T. A.; Tisdale, R. C., Reactions of coordinated dinitrogen. 21. Synthesis of mono(dinitrogen) complexes of molybdenum. Formation of ammonia and hydrazine. *Inorganic Chemistry* **1988,** *27* (17), 2909-2912.

113. George, T. A.; Koczon, L. M.; Tisdale, R. C.; Gebreyes, K.; Ma, L.; Shaikh, S. N.; Zubieta, J., Reactions of coordinated dinitrogen—XXII. Synthesis, characterization and reactions of hydrazido(2-) complexes of molybdenum. Crystal structures of two hydrazido(2-) complexes. *Polyhedron* **1990,** *9* (4), 545-551.

114. Stephan, G. C.; Peters, G.; Lehnert, N.; Habeck, C. M.; Näther, C.; Tuczek, F., Bonding, activation, and protonation of dinitrogen on a molybdenum pentaphosphine complex — Comparison

to trans-bis(dinitrogen) and -nitrile – dinitrogen complexes with tetraphosphine coordination. *Canadian Journal of Chemistry* **2005,** *83* (4), 385-402.

115. Hinrichsen, S.; Kindjajev, A.; Adomeit, S.; Krahmer, J.; Näther, C.; Tuczek, F., Molybdenum(0) Dinitrogen Complexes Supported by Pentadentate Tetrapodal Phosphine Ligands: Structure, Synthesis, and Reactivity toward Acids. *Inorganic Chemistry* **2016,** *55* (17), 8712-8722.

116. Yandulov, D. V.; Schrock, R. R., Catalytic Reduction of Dinitrogen to Ammonia at a Single Molybdenum Center. *Science* **2003,** *301* (5629), 76-78.

117. Chalkley, M. J.; Del Castillo, T. J.; Matson, B. D.; Roddy, J. P.; Peters, J. C., Catalytic N2-to-NH3 Conversion by Fe at Lower Driving Force: A Proposed Role for Metallocene-Mediated PCET. *ACS Central Science* **2017,** *3* (3), 217-223.

118. Smythe, N. C.; Schrock, R. R.; Müller, P.; Weare, W. W., Synthesis of [(HIPTNCH2CH2)3N]V Compounds (HIPT = 3,5-(2,4,6-i-Pr3C6H2)2C6H3) and an Evaluation of Vanadium for the Reduction of Dinitrogen to Ammonia. *Inorganic Chemistry* **2006,** *45* (23), 9197-9205.

119. Smythe, N. C.; Schrock, R. R.; Müller, P.; Weare, W. W., Synthesis of [(HIPTNCH2CH2)3N]Cr Compounds (HIPT = 3,5-(2,4,6-i-Pr3C6H2)2C6H3) and an Evaluation of Chromium for the Reduction of Dinitrogen to Ammonia. *Inorganic Chemistry* **2006,** *45* (18), 7111-7118.

120. Pool, J. A.; Lobkovsky, E.; Chirik, P. J., Hydrogenation and cleavage of dinitrogen to ammonia with a zirconium complex. *Nature* **2004,** *427* (6974), 527-530.

121. Ghana, P.; van Krüchten, F. D.; Spaniol, T. P.; van Leusen, J.; Kögerler, P.; Okuda, J., Conversion of dinitrogen to tris(trimethylsilyl)amine catalyzed by titanium triamido-amine complexes. *Chemical Communications* **2019,** *55* (22), 3231-3234.

122. Falcone, M.; Chatelain, L.; Scopelliti, R.; Živković, I.; Mazzanti, M., Nitrogen reduction and functionalization by a multimetallic uranium nitride complex. *Nature* **2017,** *547* (7663), 332-335.

123. Haber, F., Über die Darstellung des Ammoniaks aus Stickstoff und Wasserstoff. *Naturwissenschaften* **1922,** *10* (49), 1041-1049.

124. Haber, F., Bemerkung zu vorstehender Notiz. *Naturwissenschaften* **1923,** *11* (18), 339-340.

125. Cloke, F. G. N.; Hitchcock, P. B., Reversible Binding and Reduction of Dinitrogen by a Uranium(III) Pentalene Complex. *Journal of the American Chemical Society* **2002,** *124* (32), 9352-9353.

126. Lu, E.; Atkinson, B. E.; Wooles, A. J.; Boronski, J. T.; Doyle, L. R.; Tuna, F.; Cryer, J. D.; Cobb, P. J.; Vitorica-Yrezabal, I. J.; Whitehead, G. F. S.; Kaltsoyannis, N.; Liddle, S. T., Back-bonding between an electron-poor, high-oxidation-state metal and poor π-acceptor ligand in a uranium(v)–dinitrogen complex. *Nature Chemistry* **2019,** *11* (9), 806-811.

127. Mansell, S. M.; Kaltsoyannis, N.; Arnold, P. L., Small Molecule Activation by Uranium Tris(aryloxides): Experimental and Computational Studies of Binding of N2, Coupling of CO, and Deoxygenation Insertion of CO2 under Ambient Conditions. *Journal of the American Chemical Society* **2011,** *133* (23), 9036-9051.

128. Evans, W. J.; Kozimor, S. A.; Ziller, J. W., A Monometallic f Element Complex of Dinitrogen: (C5Me5)3U(η-N2). *Journal of the American Chemical Society* **2003,** *125* (47), 14264-14265.

129. Odom, A. L.; Arnold, P. L.; Cummins, C. C., Heterodinuclear Uranium/Molybdenum Dinitrogen Complexes. *Journal of the American Chemical Society* **1998,** *120* (23), 5836-5837.

130. Zott, M. D.; Garrido-Barros, P.; Peters, J. C., Electrocatalytic Ammonia Oxidation Mediated by a Polypyridyl Iron Catalyst. *ACS Catalysis* **2019,** *9* (11), 10101-10108.

131. Bordwell, F. G.; Drucker, G. E.; Fried, H. E., Acidities of carbon and nitrogen acids: the aromaticity of the cyclopentadienyl anion. *The Journal of Organic Chemistry* **1981,** *46* (3), 632-635.

132. Costentin, C.; Evans, D. H.; Robert, M.; Savéant, J.-M.; Singh, P. S., Electrochemical Approach to Concerted Proton and Electron Transfers. Reduction of the Water−Superoxide Ion Complex. *Journal of the American Chemical Society* **2005,** *127* (36), 12490-12491.

133. Thusius, D. D.; Taube, H., Oxidation of aquopentaammine and of hexaamminecobalt(III) ions. *The Journal of Physical Chemistry* **1967,** *71* (12), 3845-3857.

134. Buhr, J. D.; Taube, H., Oxidation of pentaamminecarbonylosmium(2+) to .mu.-dinitrogen-bis(cis-tetraamminecarbonylosmium)(4+). *Inorganic Chemistry* **1979,** *18* (8), 2208-2212.

135. Collman, J. P.; Hutchison, J. E.; Ennis, M. S.; Lopez, M. A.; Guilard, R., Reduced nitrogen hydride complexes of a cofacial metallodiporphyrin and their oxidative interconversion. An analysis of ammonia oxidation and prospects for a dinitrogen electroreduction catalyst based on cofacial metallodiporphyrins. *Journal of the American Chemical Society* **1992,** *114* (21), 8074-8080.

136. Holl, M. M. B.; Kersting, M.; Pendley, B. D.; Wolczanski, P. T., Ammonolysis of tantalum alkyls: formation of cubic tantalum nitride and a trimeric nitride, [Cp*MeTaN]3 tris[(.eta.5-pentamethylcyclopentadienyl)(methyl)nitridotantalum]. *Inorganic Chemistry* **1990,** *29* (8), 1518-1526.

137. Roesky, H. W.; Bai, Y.; Noltemeyer, M., Synthesis and Structure of [{(η5-C5Me5)Ti(NH)}3N], a Titanium Imide Nitride. *Angewandte Chemie International Edition in English* **1989,** *28* (6), 754-755.

138. Shima, T.; Hou, Z., Selective ammonolysis of half-sandwich rare-earth metal dialkyl and polyhydride complexes: synthesis of polyamido rare-earth complexes having novel structures. *Dalton Transactions* **2010,** *39* (29), 6858-6863.

139. Zhao, J.; Goldman, A. S.; Hartwig, J. F., Oxidative Addition of Ammonia to Form a Stable Monomeric Amido Hydride Complex. *Science* **2005,** *307* (5712), 1080.

140. Braun, T., Oxidative Addition of NH3 to a Transition-Metal Complex: A Key Step for the Metal-Mediated Derivatization of Ammonia? *Angewandte Chemie International Edition* **2005,** *44* (32), 5012-5014.

141. Casalnuovo, A. L.; Calabrese, J. C.; Milstein, D., Nitrogen-hydrogen activation. 1. Oxidative addition of ammonia to iridium(I). Isolation, structural characterization and reactivity of amidoiridium hydrides. *Inorganic Chemistry* **1987,** *26* (7), 971-973.

142. Hillhouse, G. L.; Bercaw, J. E., Reactions of water and ammonia with bis(pentamethylcyclopentadienyl) complexes of zirconium and hafnium. *Journal of the American Chemical Society* **1984,** *106* (19), 5472-5478.

143. Nakajima, Y.; Kameo, H.; Suzuki, H., Cleavage of Nitrogen–Hydrogen Bonds of Ammonia Induced by Triruthenium Polyhydrido Clusters. *Angewandte Chemie International Edition* **2006,** *45* (6), 950-952.

144. Peng, Y.; Ellis, B. D.; Wang, X.; Power, P. P., Diarylstannylene Activation of Hydrogen or Ammonia with Arene Elimination. *Journal of the American Chemical Society* **2008,** *130* (37), 12268-12269.

145. Ni, C.; Lei, H.; Power, P. P., Reaction of M(II) Diaryls (M = Mn or Fe) with Ammonia to Afford Parent Amido Complexes. *Organometallics* **2010,** *29* (8), 1988-1991.

146. Bezdek, M. J.; Chirik, P. J., Interconversion of Molybdenum Imido and Amido Complexes by Proton-Coupled Electron Transfer. *Angewandte Chemie International Edition* **2018,** *57* (8), 2224-2228.

147. Bezdek, M. J.; Guo, S.; Chirik, P. J., Coordination-induced weakening of ammonia, water, and hydrazine X–H bonds in a molybdenum complex. *Science* **2016,** *354* (6313), 730.

148. Scheibel, M. G.; Abbenseth, J.; Kinauer, M.; Heinemann, F. W.; Würtele, C.; de Bruin, B.; Schneider, S., Homolytic N–H Activation of Ammonia: Hydrogen Transfer of Parent Iridium Ammine, Amide, Imide, and Nitride Species. *Inorganic Chemistry* **2015,** *54* (19), 9290-9302.

149. Bhattacharya, P.; Heiden, Z. M.; Wiedner, E. S.; Raugei, S.; Piro, N. A.; Kassel, W. S.; Bullock, R. M.; Mock, M. T., Ammonia Oxidation by Abstraction of Three Hydrogen Atoms from a Mo–NH3 Complex. *Journal of the American Chemical Society* **2017**.

150. Margulieux, G. W.; Turner, Z. R.; Chirik, P. J., Synthesis and Ligand Modification Chemistry of a Molybdenum Dinitrogen Complex: Redox and Chemical Activity of a Bis(imino)pyridine Ligand. *Angewandte Chemie International Edition* **2014,** *53* (51), 14211-14215.

151. Margulieux, G. W.; Bezdek, M. J.; Turner, Z. R.; Chirik, P. J., Ammonia Activation, H2 Evolution and Nitride Formation from a Molybdenum Complex with a Chemically and Redox Noninnocent Ligand. *Journal of the American Chemical Society* **2017,** *139* (17), 6110-6113.

152. Khaskin, E.; Iron, M. A.; Shimon, L. J. W.; Zhang, J.; Milstein, D., N−H Activation of Amines and Ammonia by Ru via Metal−Ligand Cooperation. *Journal of the American Chemical Society* **2010,** *132* (25), 8542-8543.

153. Gutsulyak, D. V.; Piers, W. E.; Borau-Garcia, J.; Parvez, M., Activation of Water, Ammonia, and Other Small Molecules by PCcarbeneP Nickel Pincer Complexes. *Journal of the American Chemical Society* **2013,** *135* (32), 11776-11779.

154. Chang, Y.-H.; Nakajima, Y.; Tanaka, H.; Yoshizawa, K.; Ozawa, F., Facile N–H Bond Cleavage of Ammonia by an Iridium Complex Bearing a Noninnocent PNP-Pincer Type Phosphaalkene Ligand. *Journal of the American Chemical Society* **2013,** *135* (32), 11791-11794.

155. Fafard, C. M.; Adhikari, D.; Foxman, B. M.; Mindiola, D. J.; Ozerov, O. V., Addition of Ammonia, Water, and Dihydrogen Across a Single Pd−Pd Bond. *Journal of the American Chemical Society* **2007,** *129* (34), 10318-10319.

156. Bhattacharya, P.; Heiden, Z. M.; Chambers, G. M.; Johnson, S. I.; Bullock, R. M.; Mock, M. T., Catalytic Ammonia Oxidation to Dinitrogen by Hydrogen Atom Abstraction. *Angewandte Chemie International Edition* **2019,** *58* (34), 11618-11624.

157. Dunn, P. L.; Johnson, S. I.; Kaminsky, W.; Bullock, R. M., Diversion of Catalytic C–N Bond Formation to Catalytic Oxidation of NH3 through Modification of the Hydrogen Atom Abstractor. *Journal of the American Chemical Society* **2020,** *142* (7), 3361-3365.

158. Habibzadeh, F.; Miller, S. L.; Hamann, T. W.; Smith, M. R., Homogeneous electrocatalytic oxidation of ammonia to N₂ under mild conditions. *Proceedings of the National Academy of Sciences* **2019,** *116* (8), 2849.

159. Nakajima, K.; Toda, H.; Sakata, K.; Nishibayashi, Y., Ruthenium-catalysed oxidative conversion of ammonia into dinitrogen. *Nature Chemistry* **2019,** *11* (8), 702-709.

160. Gill, M.; Livens, F.; Peakman, A., Chapter 9 - Nuclear Fission. In *Future Energy (Second Edition)*, Letcher, T. M., Ed. Elsevier: Boston, 2014; pp 181-198.

161. Bone, S. E.; Dynes, J. J.; Cliff, J.; Bargar, J. R., Uranium(IV) adsorption by natural organic matter in anoxic sediments. *Proceedings of the National Academy of Sciences* **2017,** *114* (4), 711.

162. Abney, C. W.; Mayes, R. T.; Piechowicz, M.; Lin, Z.; Bryantsev, V. S.; Veith, G. M.; Dai, S.; Lin, W., XAFS investigation of polyamidoxime-bound uranyl contests the paradigm from small molecule studies. *Energy & Environmental Science* **2016,** *9* (2), 448-453.

163. Cany, C.; Mansilla, C.; Mathonnière, G.; da Costa, P., Nuclear power supply: Going against the misconceptions. Evidence of nuclear flexibility from the French experience. *Energy* **2018,** *151*, 289-296.

164. IAEA., *Energy, Electricity and Nuclear Power Estimates for the Period Up to 2050*. IAEA: 2017.

165. Campbell, J. L., *Collapse of an Industry*. Cornell University Press: 2019.

166. Poinssot, C.; Boullis, B.; Bourg, S., 2 - Role of recycling in advanced nuclear fuel cycles. In *Reprocessing and Recycling of Spent Nuclear Fuel*, Taylor, R., Ed. Woodhead Publishing: Oxford, 2015; pp 27-48.

167. Srivastava, R. R.; Pathak, P.; Perween, M., Environmental and Health Impact Due to Uranium Mining. In *Uranium in Plants and the Environment*, Gupta, D. K.; Walther, C., Eds. Springer International Publishing: Cham, 2020; pp 69-89.

168. Gill, G. A.; Kuo, L.-J.; Janke, C. J.; Park, J.; Jeters, R. T.; Bonheyo, G. T.; Pan, H.-B.; Wai, C.; Khangaonkar, T.; Bianucci, L.; Wood, J. R.; Warner, M. G.; Peterson, S.; Abrecht, D. G.; Mayes, R. T.; Tsouris, C.; Oyola, Y.; Strivens, J. E.; Schlafer, N. J.; Addleman, R. S.; Chouyyok, W.; Das, S.; Kim, J.; Buesseler, K.; Breier, C.; D'Alessandro, E., The Uranium from Seawater Program at the Pacific Northwest National Laboratory: Overview of Marine Testing, Adsorbent Characterization, Adsorbent Durability, Adsorbent Toxicity, and Deployment Studies. *Industrial & Engineering Chemistry Research* **2016,** *55* (15), 4264-4277.

169. Association, W. N. Uranium Mining Overview. https://www.world-nuclear.org/information-library/nuclear-fuel-cycle/mining-of-uranium/uranium-mining-overview.aspx.

170. Steiner, G.; Geissler, B.; Haneklaus, N., Making Uranium Recovery from Phosphates Great Again? *Environmental Science & Technology* **2020,** *54* (3), 1287-1289.

171. Sholl, D. S.; Lively, R. P., Seven chemical separations to change the world. *Nature* **2016,** *532* (7600), 435-7.

172. Kim, J.; Tsouris, C.; Mayes, R. T.; Oyola, Y.; Saito, T.; Janke, C. J.; Dai, S.; Schneider, E.; Sachde, D., Recovery of Uranium from Seawater: A Review of Current Status and Future Research Needs. *Separation Science and Technology* **2013,** *48* (3), 367-387.

173. Parker, B. F.; Zhang, Z.; Rao, L.; Arnold, J., An overview and recent progress in the chemistry of uranium extraction from seawater. *Dalton Transactions* **2018,** *47* (3), 639-644.

174. Ladshaw, A. P.; Das, S.; Liao, W. P.; Yiacoumi, S.; Janke, C. J.; Mayes, R. T.; Dai, S.; Tsouris, C., Experiments and Modeling of Uranium Uptake by Amidoxime-Based Adsorbent in the Presence of Other Ions in Simulated Seawater. *Industrial & Engineering Chemistry Research* **2016,** *55* (15), 4241-4248.

175. Davies, R. V.; Kennedy, J.; McIlroy, R. W.; Spence, R.; Hill, K. M., Extraction of Uranium from Sea Water. *Nature* **1964,** *203* (4950), 1110-1115.

176. Anderson, H. H.; Asprey, L. B. SOLVENT EXTRACTION PROCESS FOR PLUTONIUM. 1960-02-01, 1960.

177. Kim, J.; Tsouris, C.; Oyola, Y.; Janke, C. J.; Mayes, R. T.; Dai, S.; Gill, G.; Kuo, L.-J.; Wood, J.; Choe, K.-Y.; Schneider, E.; Lindner, H., Uptake of Uranium from Seawater by Amidoxime-Based Polymeric Adsorbent: Field Experiments, Modeling, and Updated Economic Assessment. *Industrial & Engineering Chemistry Research* **2014,** *53* (14), 6076-6083.

178. Yue, Y.; Mayes, R. T.; Kim, J.; Fulvio, P. F.; Sun, X.-G.; Tsouris, C.; Chen, J.; Brown, S.; Dai, S., Seawater Uranium Sorbents: Preparation from a Mesoporous Copolymer Initiator by Atom-Transfer Radical Polymerization. *Angewandte Chemie International Edition* **2013,** *52* (50), 13458-13462.

179. Wu, F.; Pu, N.; Ye, G.; Sun, T.; Wang, Z.; Song, Y.; Wang, W.; Huo, X.; Lu, Y.; Chen, J., Performance and Mechanism of Uranium Adsorption from Seawater to Poly(dopamine)-Inspired Sorbents. *Environmental Science & Technology* **2017,** *51* (8), 4606-4614.

180. Das, S.; Brown, S.; Mayes, R. T.; Janke, C. J.; Tsouris, C.; Kuo, L. J.; Gill, G.; Dai, S., Novel poly(imide dioxime) sorbents: Development and testing for enhanced extraction of uranium from natural seawater. *Chemical Engineering Journal* **2016,** *298*, 125-135.

181. Alexandratos, S. D.; Zhu, X.; Florent, M.; Sellin, R., Polymer-Supported Bifunctional Amidoximes for the Sorption of Uranium from Seawater. *Industrial & Engineering Chemistry Research* **2016,** *55* (15), 4208-4216.

182. Zhang, A.; Asakura, T.; Uchiyama, G., The adsorption mechanism of uranium(VI) from seawater on a macroporous fibrous polymeric adsorbent containing amidoxime chelating functional group. *Reactive and Functional Polymers* **2003,** *57* (1), 67-76.

183. Zhou, L.; Bosscher, M.; Zhang, C.; Özçubukçu, S.; Zhang, L.; Zhang, W.; Li, C. J.; Liu, J.; Jensen, M. P.; Lai, L.; He, C., A protein engineered to bind uranyl selectively and with femtomolar affinity. *Nature Chemistry* **2014,** *6* (3), 236-241.

184. Barber, P. S.; Kelley, S. P.; Griggs, C. S.; Wallace, S.; Rogers, R. D., Surface modification of ionic liquid-spun chitin fibers for the extraction of uranium from seawater: seeking the strength of chitin and the chemical functionality of chitosan. *Green Chemistry* **2014,** *16* (4), 1828-1836.

185. Feng, M.-L.; Sarma, D.; Qi, X.-H.; Du, K.-Z.; Huang, X.-Y.; Kanatzidis, M. G., Efficient Removal and Recovery of Uranium by a Layered Organic–Inorganic Hybrid Thiostannate. *Journal of the American Chemical Society* **2016,** *138* (38), 12578-12585.

186. Yuan, Y.; Yang, Y.; Ma, X.; Meng, Q.; Wang, L.; Zhao, S.; Zhu, G., Molecularly Imprinted Porous Aromatic Frameworks and Their Composite Components for Selective Extraction of Uranium Ions. *Advanced Materials* **2018,** *30* (12), 1706507.

187. Liu, W.; Dai, X.; Bai, Z.; Wang, Y.; Yang, Z.; Zhang, L.; Xu, L.; Chen, L.; Li, Y.; Gui, D.; Diwu, J.; Wang, J.; Zhou, R.; Chai, Z.; Wang, S., Highly Sensitive and Selective Uranium Detection in

Natural Water Systems Using a Luminescent Mesoporous Metal–Organic Framework Equipped with Abundant Lewis Basic Sites: A Combined Batch, X-ray Absorption Spectroscopy, and First Principles Simulation Investigation. *Environmental Science & Technology* **2017,** *51* (7), 3911-3921.

188. Li, B.; Sun, Q.; Zhang, Y.; Abney, C. W.; Aguila, B.; Lin, W.; Ma, S., Functionalized Porous Aromatic Framework for Efficient Uranium Adsorption from Aqueous Solutions. *ACS Applied Materials & Interfaces* **2017,** *9* (14), 12511-12517.

189. Manos, M. J.; Kanatzidis, M. G., Layered Metal Sulfides Capture Uranium from Seawater. *Journal of the American Chemical Society* **2012,** *134* (39), 16441-16446.

190. Carboni, M.; Abney, C. W.; Liu, S.; Lin, W., Highly porous and stable metal–organic frameworks for uranium extraction. *Chemical Science* **2013,** *4* (6), 2396-2402.

191. Xiong, L.-p.; Lv, K.; Gu, M.; Yang, C.-t.; Wu, F.-c.; Han, J.; Hu, S., Efficient capture of actinides from strong acidic solution by hafnium phosphonate frameworks with excellent acid resistance and radiolytic stability. *Chemical Engineering Journal* **2019,** *355*, 159-169.

192. Sun, Q.; Aguila, B.; Perman, J.; Ivanov, A. S.; Bryantsev, V. S.; Earl, L. D.; Abney, C. W.; Wojtas, L.; Ma, S., Bio-inspired nano-traps for uranium extraction from seawater and recovery from nuclear waste. *Nature Communications* **2018,** *9* (1), 1644.

193. Bai, H.; Liu, Z.; Sun, D. D., Hierarchical ZnO/Cu "Corn-Like" materials with high photodegradation and antibacterial capability under visible light. *Phys Chem Chem Phys* **2011,** *13*.

194. Jang, J.-H.; Dempsey, B. A.; Burgos, W. D., A Model-Based Evaluation of Sorptive Reactivities of Hydrous Ferric Oxide and Hematite for U(VI). *Environmental Science & Technology* **2007,** *41* (12), 4305-4310.

195. Shao, D.; Li, J.; Wang, X., Poly(amidoxime)-reduced graphene oxide composites as adsorbents for the enrichment of uranium from seawater. *Science China Chemistry* **2014,** *57* (11), 1449-1458.

196. Yue, Y.; Sun, X.; Mayes, R. T.; Kim, J.; Fulvio, P. F.; Qiao, Z.; Brown, S.; Tsouris, C.; Oyola, Y.; Dai, S., Polymer-coated nanoporous carbons for trace seawater uranium adsorption. *Science China Chemistry* **2013,** *56* (11), 1510-1515.

197. Mellah, A.; Chegrouche, S.; Barkat, M., The removal of uranium(VI) from aqueous solutions onto activated carbon: Kinetic and thermodynamic investigations. *Journal of Colloid and Interface Science* **2006,** *296* (2), 434-441.

198. Kim, J. H.; Lee, H. I.; Yeon, J.-W.; Jung, Y.; Kim, J. M., Removal of uranium(VI) from aqueous solutions by nanoporous carbon and its chelating polymer composite. *Journal of Radioanalytical and Nuclear Chemistry* **2010,** *286* (1), 129-133.

199. Chi, F.; Zhang, S.; Wen, J.; Xiong, J.; Hu, S., Highly Efficient Recovery of Uranium from Seawater Using an Electrochemical Approach. *Industrial & Engineering Chemistry Research* **2018,** *57* (23), 8078-8084.

200. Tsouris, C., Uranium extraction: Fuel from seawater. *Nature Energy* **2017,** *2* (4), 17022.

201. Mehio, N.; Ivanov, A. S.; Williams, N. J.; Mayes, R. T.; Bryantsev, V. S.; Hancock, R. D.; Dai, S., Quantifying the binding strength of salicylaldoxime–uranyl complexes relative to competing salicylaldoxime–transition metal ion complexes in aqueous solution: a combined experimental and computational study. *Dalton Transactions* **2016,** *45* (22), 9051-9064.

202. Hadjithoma, S.; Papanikolaou, M. G.; Leontidis, E.; Kabanos, T. A.; Keramidas, A. D., Bis(hydroxylamino)triazines: High Selectivity and Hydrolytic Stability of Hydroxylamine-Based Ligands for Uranyl Compared to Vanadium(V) and Iron(III). *Inorganic Chemistry* **2018,** *57* (13), 7631-7643.

203. Kanno, M., Present Status of Study on Extraction of Uranium from Sea Water. *Journal of Nuclear Science and Technology* **1984,** *21* (1), 1-9.

204. Saito, K.; Uezu, K.; Hori, T.; Furusaki, S.; Sugo, T.; Okamoto, J., Recovery of uranium from seawater using amidoxime hollow fibers. *AIChE Journal* **1988,** *34* (3), 411-416.

205. Schenk, H. J.; Astheimer, L.; Witte, E. G.; Schwochau, K., Development of Sorbers for the Recovery of Uranium from Seawater. 1. Assessment of Key Parameters and Screening Studies of Sorber Materials. *Separation Science and Technology* **1982,** *17* (11), 1293-1308.

206. Li, W. P.; Han, X. Y.; Wang, X. Y.; Wang, Y. Q.; Wang, W. X.; Xu, H.; Tan, T. S.; Wu, W. S.; Zhang, H. X., Recovery of uranyl from aqueous solutions using amidoximated polyacrylonitrile/exfoliated Na-montmorillonite composite. *Chemical Engineering Journal* **2015,** *279*, 735-746.

207. Chouyyok, W.; Pittman, J. W.; Warner, M. G.; Nell, K. M.; Clubb, D. C.; Gill, G. A.; Addleman, R. S., Surface functionalized nanostructured ceramic sorbents for the effective collection and recovery of uranium from seawater. *Dalton Transactions* **2016,** *45* (28), 11312-11325.

208. Yue, Y.; Zhang, C.; Tang, Q.; Mayes, R. T.; Liao, W.-P.; Liao, C.; Tsouris, C.; Stankovich, J. J.; Chen, J.; Hensley, D. K.; Abney, C. W.; Jiang, D.-e.; Brown, S.; Dai, S., A Poly(acrylonitrile)-Functionalized Porous Aromatic Framework Synthesized by Atom-Transfer Radical Polymerization for the Extraction of Uranium from Seawater. *Industrial & Engineering Chemistry Research* **2016,** *55* (15), 4125-4129.

209. Kang, S. O.; Vukovic, S.; Custelcean, R.; Hay, B. P., Cyclic Imide Dioximes: Formation and Hydrolytic Stability. *Industrial & Engineering Chemistry Research* **2012,** *51* (19), 6619-6624.

210. Pan, H.-B.; Liao, W.; Wai, C. M.; Oyola, Y.; Janke, C. J.; Tian, G.; Rao, L., Carbonate–H2O2 leaching for sequestering uranium from seawater. *Dalton Transactions* **2014,** *43* (28), 10713-10718.

211. Lindner, H.; Schneider, E., Review of cost estimates for uranium recovery from seawater. *Energy Economics* **2015,** *49*, 9-22.

212. Kuo, L.-J.; Pan, H.-B.; Wai, C. M.; Byers, M. F.; Schneider, E.; Strivens, J. E.; Janke, C. J.; Das, S.; Mayes, R. T.; Wood, J. R.; Schlafer, N.; Gill, G. A., Investigations into the Reusability of Amidoxime-Based Polymeric Adsorbents for Seawater Uranium Extraction. *Industrial & Engineering Chemistry Research* **2017,** *56* (40), 11603-11611.

213. Seko, N.; Katakai, A.; Hasegawa, S.; Tamada, M.; Kasai, N.; Takeda, H.; Sugo, T.; Saito, K., Aquaculture of Uranium in Seawater by a Fabric-Adsorbent Submerged System. *Nuclear Technology* **2003,** *144* (2), 274-278.

214. Tamada, M., CURRENT STATUS OF TECHNOLOGY FOR COLLECTION OF URANIUM FROM SEAWATER. In *International Seminar on Nuclear War and Planetary Emergencies ? 42nd Session*, WORLD SCIENTIFIC: 2010; pp 243-252.

215. Drysdale, J. A.; Buesseler, K. O., Uranium adsorption behaviour of amidoximated fibers under coastal ocean conditions. *Progress in Nuclear Energy* **2020,** *119*, 103170.

216. Endrizzi, F.; Rao, L., Chemical Speciation of Uranium(VI) in Marine Environments: Complexation of Calcium and Magnesium Ions with [(UO2)(CO3)3]4− and the Effect on the Extraction of Uranium from Seawater. *Chemistry – A European Journal* **2014,** *20* (44), 14499-14506.

217. Endrizzi, F.; Leggett, C. J.; Rao, L., Scientific Basis for Efficient Extraction of Uranium from Seawater. I: Understanding the Chemical Speciation of Uranium under Seawater Conditions. *Industrial & Engineering Chemistry Research* **2016,** *55* (15), 4249-4256.

218. Wang, D.; Sañudo Wilhelmy, S. A., Vanadium speciation and cycling in coastal waters. *Marine Chemistry* **2009,** *117* (1), 52-58.

219. Emerson, S. R.; Huested, S. S., Ocean anoxia and the concentrations of molybdenum and vanadium in seawater. *Marine Chemistry* **1991,** *34* (3), 177-196.

220. Heath, E.; Howarth, O. W., Vanadium-51 and oxygen-17 nuclear magnetic resonance study of vanadate(V) equilibria and kinetics. *Journal of the Chemical Society, Dalton Transactions* **1981,** (5), 1105-1110.

221. Vraspir, J. M.; Butler, A., Chemistry of Marine Ligands and Siderophores. *Annual Review of Marine Science* **2009,** *1* (1), 43-63.

222. Pan, H.-B.; Kuo, L.-J.; Wai, C. M.; Miyamoto, N.; Joshi, R.; Wood, J. R.; Strivens, J. E.; Janke, C. J.; Oyola, Y.; Das, S.; Mayes, R. T.; Gill, G. A., Elution of Uranium and Transition Metals from Amidoxime-Based Polymer Adsorbents for Sequestering Uranium from Seawater. *Industrial & Engineering Chemistry Research* **2016,** *55* (15), 4313-4320.

223. Marshalkin, V. E., The Second-Generation Fissile Materials in the Nuclear Power Industry. *Physics of Atomic Nuclei* **2018,** *81* (8), 1211-1226.

224. De Roo, G.; Parsons, J. E., A methodology for calculating the levelized cost of electricity in nuclear power systems with fuel recycling. *Energy Economics* **2011,** *33* (5), 826-839.

225. Law, J. D.; Herbst, R. S.; Peterman, D. R.; Tillotson, R. D.; Todd, T. A., Development of a Cobalt Dicarbollide/Polyethylene Glycol Solvent Extraction Process for Separation of Cesium and Strontium to Support Advanced Aqueous Reprocessing. *Nuclear Technology* **2004,** *147* (2), 284-290.

226. Herbst, R. S.; Baron, P.; Nilsson, M., 6 - Standard and advanced separation: PUREX processes for nuclear fuel reprocessing. In *Advanced Separation Techniques for Nuclear Fuel Reprocessing and Radioactive Waste Treatment*, Nash, K. L.; Lumetta, G. J., Eds. Woodhead Publishing: 2011; pp 141-175.

227. Na, C.; Yamagishi, I.; Choi, Y.-J.; Glatz, J.-P.; Hyland, B.; Uhlir, J.; Baron, P.; Warin, D.; De Angelis, G.; Luce, A. *Spent Nuclear Fuel Reprocessing Flowsheet. A Report by the WPFC Expert Group on Chemical Partitioning of the NEA Nuclear Science Committee*; Organisation for Economic Co-Operation and Development: 2012.

228. Silvennoinen, P., Chapter 1 - Nuclear Fuel Cycle. In *Nuclear Fuel Cycle Optimization*, Silvennoinen, P., Ed. Pergamon: 1982; pp 1-13.

229. Kumari, N.; Pathak, P. N.; Prabhu, D. R.; Manchanda, V. K., Comparison of Extraction Behavior of Neptunium from Nitric Acid Medium Employing Tri-n-Butyl Phosphate and N,N-dihexyl Octanamide as Extractants. *Separation Science and Technology* **2012,** *47* (10), 1492-1497.

230. Nilsson, M.; Ekberg, C.; Foreman, M.; Hudson, M.; Liljenzin, J. O.; Modolo, G.; Skarnemark, G., Separation of Actinides(III) from Lanthanides(III) in Simulated Nuclear Waste Streams using 6,6′-Bis-(5,6-dipentyl-[1,2,4]triazin-3-yl)-[2,2′]bipyridinyl (C5-BTBP) in Cyclohexanone. *Solvent Extraction and Ion Exchange* **2006,** *24* (6), 823-843.

231. Modolo, G.; Geist, A.; Miguirditchian, M., 10 - Minor actinide separations in the reprocessing of spent nuclear fuels: recent advances in Europe. In *Reprocessing and Recycling of Spent Nuclear Fuel*, Taylor, R., Ed. Woodhead Publishing: Oxford, 2015; pp 245-287.

232. Riisiö, A.; Väisänen, A.; Sillanpää, R., Uranyl Complexes of Alkyl-Bridged Ditopic Diaminotetraphenol Ligands and Their Use as Uranyl Ion Extractors. *Inorganic Chemistry* **2013,** *52* (15), 8591-8600.

233. Kiegiel, K.; Steczek, L.; Zakrzewska-Trznadel, G., Application of Calixarenes as Macrocyclic Ligands for Uranium(VI): A Review. *Journal of Chemistry* **2013,** *2013*, 762819.

234. Hu, P.; Qian, L.; Zhou, X.; Pan, D.; Wu, W., Solvent extraction of uranyl by N,N,N′,N′-tetraoctylsuccinylamide from nitric acid solution. *Journal of Radioanalytical and Nuclear Chemistry* **2013,** *295* (2), 1209-1213.

235. Takao, K.; Bell, T. J.; Ikeda, Y., Actinide Chemistry in Ionic Liquids. *Inorganic Chemistry* **2013,** *52* (7), 3459-3472.

236. Benay, G.; Wipff, G., Liquid–Liquid Extraction of Uranyl by an Amide Ligand: Interfacial Features Studied by MD and PMF Simulations. *The Journal of Physical Chemistry B* **2013,** *117* (24), 7399-7415.

237. Borges Silverio, L.; Lamas, W. d. Q., An analysis of development and research on spent nuclear fuel reprocessing. *Energy Policy* **2011,** *39* (1), 281-289.

238. Association, W. N., Outline history of nuclear energy. *World Nuclear Association* **2010**.

239. Association, N. E., Actinide and Fission Product Partitioning and Transmutation. In *Seventh Information Exchange Meeting*, European Commision and the International Atomic Energy Agency: Jeju, Republic of Korea, 2002.

240. Mathur, J. N.; Murali, M. S.; Nash, K. L., ACTINIDE PARTITIONING—A REVIEW. *Solvent Extraction and Ion Exchange* **2001,** *19* (3), 357-390.

241. Keener, M.; Peterson, M.; Hernández Sánchez, R.; Oswald, V. F.; Wu, G.; Ménard, G., Towards Catalytic Ammonia Oxidation to Dinitrogen: A Synthetic Cycle by Using a Simple Manganese Complex. *Chemistry - A European Journal* **2017,** *23* (48), 11479-11484.

242. Keener, M.; Hunt, C.; Carroll, T. G.; Kampel, V.; Dobrovetsky, R.; Hayton, T. W.; Ménard, G., Redox-switchable carboranes for uranium capture and release. *Nature* **2020**.

Chapter 2 – Synthetic NH_3 Oxidation Chemistry using a Simple Manganese–Salen Complex

2.1 Introduction

In order to meet sustainable targets for worldwide energy supply and demand, carbon–free fuels are an attractive medium to combat rapid increase of CO_2 emissions to the atmosphere, resulting in global climate change.[1] NH_3, massively produced through the HB process, offers appealing attributes compared to carbon–based fuels due to its high gravimetric energy density, ease of transport as a liquid due to the well–established infrastructure, potential use of direct NH_3 fuel cells where the by–product of oxidation is N_2, and use as a H_2 storage medium. However, the study of molecular systems for NH_3 oxidation has lagged compared to the microscopic reverse N_2 reduction, making it essential to develop systems in order to better understand the mechanism required for the $6e^-$ oxidation chemistry. In the oxidation of NH_3 to N_2, formation of a N–N bond is a requisite step, so understanding the mechanism for this transformation is crucial to the design of systems capable of oxidizing NH_3.

Metal complexes of Mn,[2-5] Co,[6] Mo,[7] Ru,[8] Os,[9-11] and Ir[12-13] have been shown to chemically or electrochemically oxidize NH_3 to metal–nitride ($M–N^{3-}$, **A→B**), bimetallic μ–N_2 complexes (**A→C**), or elimination of N_2 (**A→D**; **Scheme 2.1**).

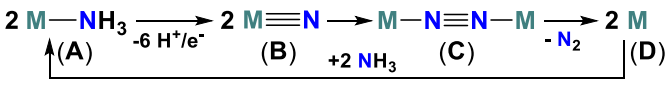

Scheme 2.1. Proposed pathways from NH_3 oxidation to N_2 formation.

For the latter N–N bond formation pathways, intermediate metal–nitride coupling is proposed to be the main pathway to μ–N_2 or N_2 formation through bimolecular nitridyl ($M{\equiv}N\cdot$)[5, 14-16] or nucleophilic ($M{\equiv}N^{\delta-}$) + electrophilic couplings ($M{\equiv}N^{\delta+}$).[17] For example, Neese *et. al.* reported

the N–N coupling of cryogenically trapped Fe^{V}–nitrides which was proposed to occur through a radical coupling process (**a**, **Figure 2.1**). Alternatively, Seymore and Brown reported heterobimetallic N–N coupling with electronically dissimilar Mo– and Os–nitride complexes., where a nucleophilic Mo^{VI}–nitride reacts with the electrophilic Os^{VI}–nitride (b, **Figure 2.1**).

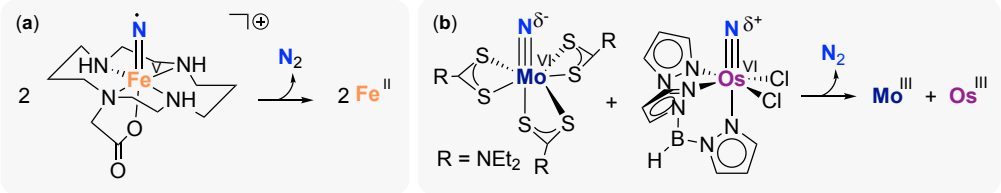

Figure 2.1. Examples of N–N coupling through (**a**) nitridyl and (**b**) nucleophilic/electrophilic pathways.

Other nitrides, generated through N–atom transfer chemistry (N_3^- photolysis), have also shown similar coupling behavior.[14-15, 17-21] Although significant progress had been made in the following examples, at the time of our first publication in *Chem. Eur. J.*,[22] a cycle for "synthetic" NH_3 oxidation had not been realized. Since the time of publication, there have been alternative systems developed for stoichiometric NH_3 oxidation (detailed in section 1.1.2.1), and more recently, catalytic systems – which will be described in more detail in Chapter 3. Our goal in this initial work was to complete a synthetic cycle, investigate the mechanism for the coupling pathway to N_2 formation, and move toward a system for catalytic NH_3 oxidation using readily available, inexpensive metal complexes.

2.2 Results and Discussion

2.2.1 Oxidations with a nucleophilic M≡N salen complex: N_2 formation

The known nucleophilic Mn^{V}-nitride, (salen)Mn≡N (**2.1**), generated through NH_3 oxidation with NaOCl,[2] represents the first step of a potential synthetic cycle (**A→B**, **Scheme 1.1**; a, **Figure 2.2**).[22] We were curious in determining if chemical oxidation could render the

nucleophilic M≡N (**2.1**) to become a nitrogen–centered radical (nitridyls; **2.1**$^{\bullet}$) or render it electrophilic in character (**2.1**$^{+}$) and susceptible to nucleophilic attack by an equivalent of **2.1** (**Scheme 2.2**). Electrochemical analysis of **2.1** in dichloromethane (DCM) by cyclic voltammetry (CV) revealed a quasi–reversible oxidation at 0.53 V relative to the Fc/Fc^{+} couple (b, **Figure 2.2**).

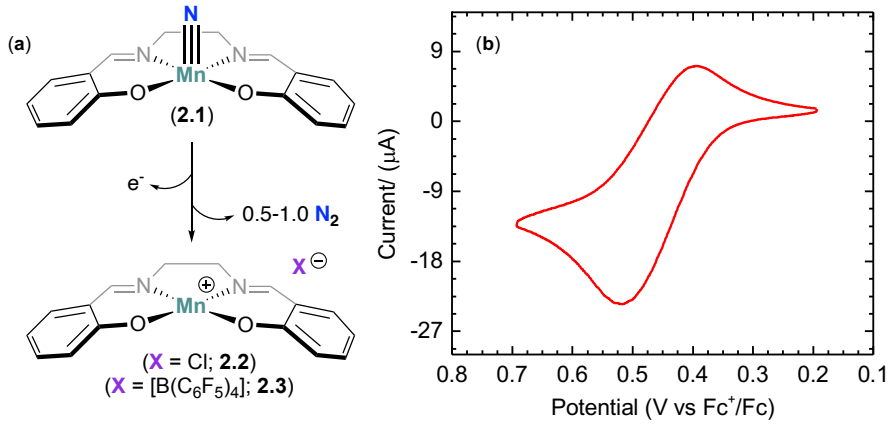

Figure 2.2. (**a**) Oxidation of **2.1** with [Ar$_3$N][X] to yield **2.2** (X = Cl) or **2.3** (X = [B(C$_6$F$_5$)$_4$]). (**b**) Cyclic voltammogram of **2.1** with [Bu$_4$N][PF$_6$] electrolyte in DCM (glassy C working electrode, scan rate 100 mV/s, referenced to Fc/Fc^{+}).

We probed this oxidation using the commercially available oxidant, [Ar$_3$N][SbCl$_6$] (Ar = *p*–bromophenyl; E^0 = 0.70 V vs. Fc/Fc^{+})[23], where exposure of this to 1 equivalent of **2.1** in fluorobenzene resulted in loss of the diamagnetic signals of **2.1** and formation of diamagnetic signals for NAr$_3$, as observed by ^{1}H NMR spectroscopy.

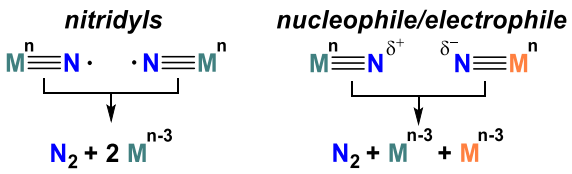

Scheme 2.2. Proposed nucleophilic/electrophilic and nitridyl pathways for N–N coupling.

Isolated from the reaction was a major paramagnetic product that was recrystallized by vapor diffusion of MeCN/Et_2O to give suitable X–Ray quality crystals that were determined to be the known Mn^{III} dimer $[(salen)MnCl]_2$ (**2.2**) in an 82 % yield. The solid–state structure revealed loss of the nitride with subsequent capture of a chloride from the $[SbCl_6]^-$ counter ion. Similarly, treatment with an oxidant containing a non–coordinating anion, $[Ar_3N][B(C_6F_5)_4]$, in fluorobenzene again resulted in replacement of the diamagnetic peaks of **2.1** with a set of three paramagnetically shifted resonances at –8.7, –28.2, –3.2 ppm in the ^1H NMR spectrum. Separation of the NAr_3 from the reaction mixture resulted in recrystallization of the product by vapor diffusion with FB/Et_2O yielding a Mn^{III} Et_2O–ligated paramagnetic product, $[(salen)Mn(OEt_2)]_2][B(C_6F_5)_4]_2$ (**2.3**) in an 80 % yield (**Figure 2.3**). Pertinent bond lengths for **2.3** were Mn1–O5 (2.252(9) Å) and Mn1–$O2_{trans}$ (2.337 Å).[24-25] Evans' method measurements of the spin state of **2.3** in MeCN–d_3 revealed a S = 2 spin state assuming a monomer in solution.[26-27]

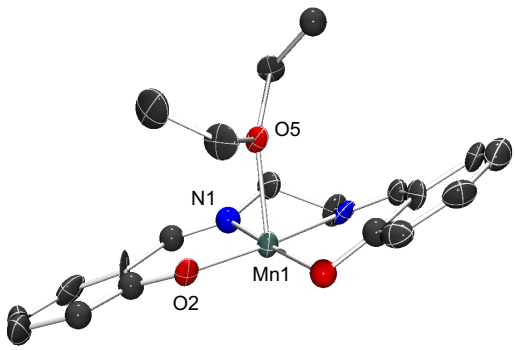

Figure 2.3. Solid–state molecular structure of $[(salen)Mn(Et_2O)]_2[B(C_6F_5)_4]_2$ (**2.3**) obtained from a red–block crystal and the structure is symmetry–generated. H atoms, $[B(C_6F_5)_4]^-$ anions, and the dimeric structure are omitted for clarity.

The oxidation of **2.1**→**2.2** or **2.1**→**2.3,** through an intermediate **2.1**$^+$, resulted in loss

of nitride and subsequent 3e$^-$ metal reduction to Mn^{III} (**2.2** or **2.3**; a, **Figure 2.2**). As observed in other systems, such metal–nitride oxidation is typically accompanied by N_2 generation.[5, 15, 21, 28-29] In order to unambiguously confirm this here, we isotopically enriched the nitride in **2.1** to **2.1**–^{15}**N** using $^{15}NH_3$ in the initial synthesis.[2, 30] The Mn≡N stretching frequency shifted from 1046 cm^{-1} to 1018 cm^{-1} in the IR spectrum for the ^{14}N and ^{15}N isotopomers, respectively. The headspace gas of an oxidation reaction (**2.1**→**2.3**) performed under Ar was sampled and analyzed by GC–MS using a gastight syringe.[31] The presence of 27.5 % $^{15}N_2$ relative to background $^{14}N_2$, marked a significant deviation from natural abundance (0.13 % $^{15}N_2$ vs. $^{14}N_2$) (**Figure 2.4**). Similar to other systems,[5, 28] we were unable to completely eliminate $^{14}N_2$ from the background. Treatment of a 1:1 mixture of **2.1**: **2.1**–^{15}**N** to an equivalent of oxidant also resulted in the appearance of the mixed isotopomer $^{14}N{\equiv}^{15}N$, in addition to $^{15}N_2$, in an approximate 2:1 ratio (19 % and 9.1 %, respectively), confirming the expected bimolecular coupling sequence (**Figure 2.4**). Similar results were obtained for the **2.1**→**2.2** oxidation (**Figure 2.4**).

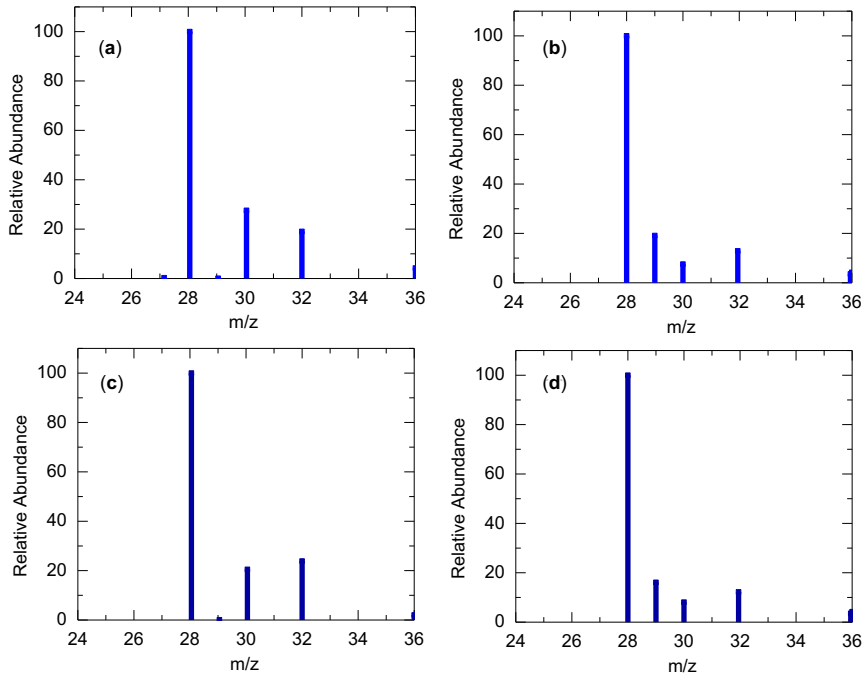

Figure 2.4. (**a**) Mass spectrum from reaction of **2.1**–^{15}**N** with [(*p*–$C_6H_4Br)_3N$][$B(C_6F_5)_4$] after 30 mins. (**b**) Mass spectrum for from a 50:50 mixture of **2.1**–^{15}**N** and **2.1**. (**c**) Mass spectrum from the reaction of **2.1**–^{15}**N** with [(*p*–$C_6H_4Br)_3N$][$SbCl_6$] after 30 mins. (**d**) Mass spectrum from a 50:50 mixture of **2.1**–^{15}**N** and **2.1**.

2.2.2 Nitridyl versus nucleophilic/electrophilic coupling pathways to N_2 formation

We were interested in probing the coupling pathway at play – nitridyl vs. nucleophilic/electrophilic (**Scheme 2.2**). With the pseudo–square pyramidal geometry and π orbital overlap between Mn and the nitride in **2.1**, oxidation of **2.1** should remove an electron from the non–bonding d_{xy} orbital (**Figure 2.5**) as seen in similar complexes.[5, 32]

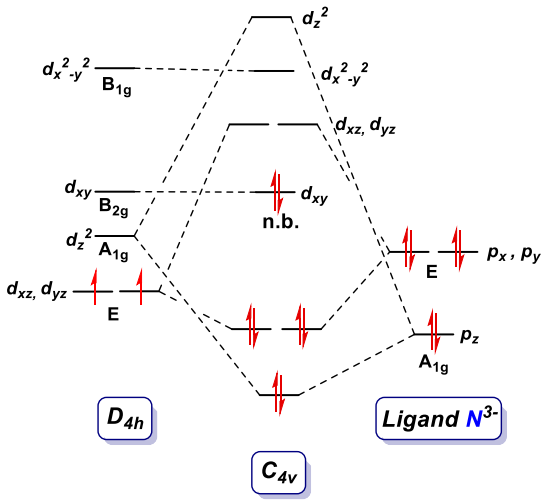

Figure 2.5. Representative molecular orbital diagram for **2.1** in a pseudo–square pyramidal geometry.

Given the locus of orbital oxidation (d_{xy}) bears no π or π* contributions, we wanted to probe if the nitride in **2.1**$^+$ would have electrophilic or radical character. If a nucleophilic/electrophilic mechanism were at play, only half an equivalent of oxidant – oxidizing 0.5 eq. of **2.1** to **2.1**$^+$ for subsequent reaction with 0.5 eq. of nucleophilic **2.1** – would be required for full conversion to all nitrides to N_2 (**Scheme 2.2**). To test this, we treated **2.1** to 0.5 eq. of $[Ar_3N][B(C_6F_5)_4]$ in fluorobenzene Separation of NAr_3 from the reaction mixture resulted in the isolation of a red, acetonitrile–soluble, ^{1}H NMR–silent fraction. The complex was crystallized by vapor diffusion of a FB/DCM mixture in 70 % yield and identified by XRD studies as the bridged species, $[(salen)Mn^V(\mu\text{–}N)Mn^{III}(salen)][B(C_6F_5)_4]$ (**2.4**) (a, **Figure 2.6**). The mixed–valency was assigned based on crystallographic, magnetometric, and spectroscopic analyses.

The solid–state structure of **2.4** reveals a Mn1–N5 bond length of 1.550(3) Å with a Mn center puckered out of the plane of the salen ligand by 0.440(3) Å consistent with a slightly elongated Mn≡N triple bond (Mn≡N = 1.512 Å and 0.451(1) Å out of plane Mn in **2.1**).[2] In

contrast, the Mn2 center sits mostly in the plane of the salen ligand (out of plane by 0.071(2) Å) flanked at the apical site by N5 to form an elongated Mn2–N5 bond of 2.419(3) Å. In addition to these bonds, the cations of **2.4** form an infinite 1D chain,[33-35] wherein Mn2 also connects at the other axial site to O2 (2.276(3) Å) from the neighboring Mn^{V}–nitride bound salen (b, **Figure 2.6**). The long Mn2–O2 and Mn2–N5 linkages are consistent with a localized Jahn–Teller distorted Mn^{III} center in a pseudo–octahedral field.[33-35]

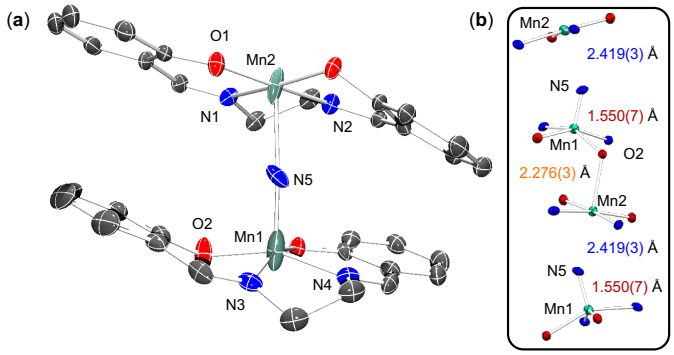

Figure 2.6. (**a**) Solid–state structure of **2.4** with $[B(C_6F_5)_4]^-$ and H atoms omitted for clarity. (**b**) The truncated 1–D chain of **2.4**.

To gain further insight into the electronic structure of **2.4** we collected variable temperature magnetic susceptibility ($\chi_M T$) and low temperature magnetization data (**Figure 2.7**). First, we collected magnetization data for **2.4** at 100 K from 0–5 T (a, **Figure 2.7**), where (**b**) is zoomed in plot of (**a**), to check for ferromagnetic impurities in the sample – the linear trend indicates the sample was pure. The $\chi_M T$ data collected at 0.5 T remains almost constant going from 3.16 to 3.31 cm^3K/mol when scanned from 30 to 300 K, respectively. This is in agreement with the spin–only value of an ideal S = 2 (3.0 cm^3K/mol) system. Similarly, magnetization data at low temperature indicates the effect of zero–field splitting since data at 2 K and 5 T saturates at 3.12 μ_B, which is lower than the ideal value of M = gS of 4 μ_B for an S = 2 (c, inset, **Figure 2.7**). Both $\chi_M T$ and reduced magnetization data were fit well to an S =

2 (red and black continuous lines in c, **Figure 2.7**), as described in the experimental section. The $\chi_M T$ fit parameters that best describe the data are: $g = 2.04$ and TIP = 5.1 x 10^{-4} cm^3/mol; while for the reduced magnetization data we obtained: $g = 2.42$ and $D = -8.5$ cm^{-1}, where D corresponds to the axial zero–field splitting parameter.

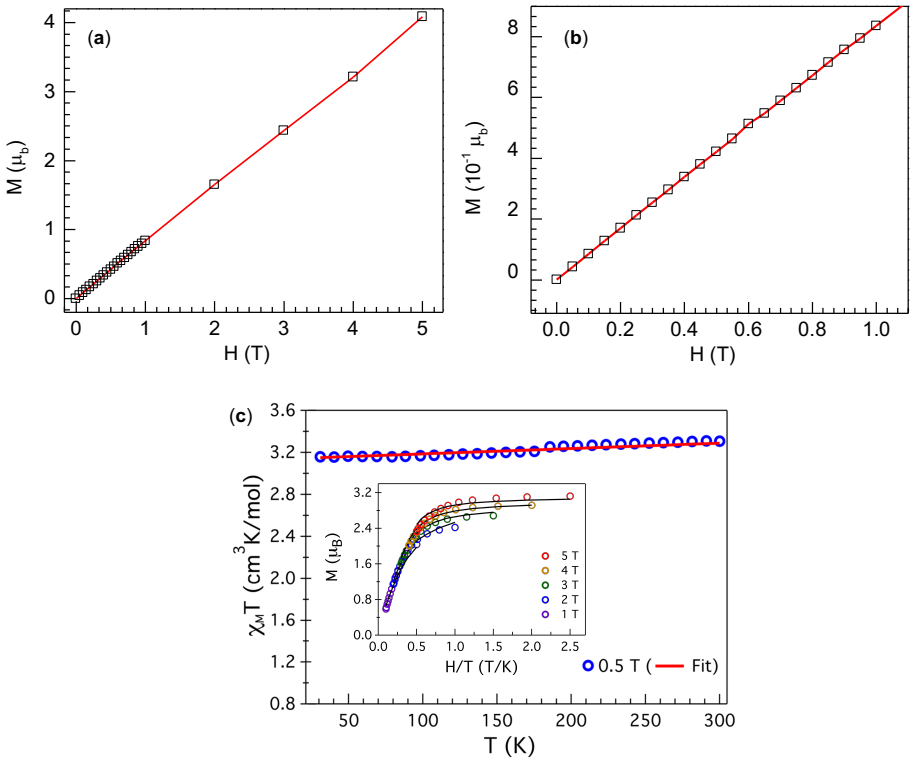

Figure 2.7. (**a**) Magnetization data for (**2.4**) at 100 K from 0 to 5 T. (**b**) Zoomed in plot of (**a**) from 0 to 1 T. This plot was used to check for ferromagnetic impurities. (**c**) Variable–temperature magnetic susceptibility measurements of **2.4** collected at 0.5 T (blue circles). Inset: variable–temperature, variable–field magnetization data collected from 2–10 K with fields from 1–5 T.

The $S = 2$ assignment for **2.4** is further supported by X–band EPR measurements. We analyzed **2.4** by perpendicular– and parallel–mode EPR spectroscopy in acetonitrile at 6 K (a and b, **Figure 2.8**). The perpendicular–mode spectrum was featureless as expected for an

integer spin system, whereas the parallel–mode spectrum displayed a characteristic signal at g = 7.84, indicative of a high–spin (S = 2) Mn^{III} center.[36-37] Lastly, the extent of redox localization was probed by UV–Vis–NIR (NIR = near–IR) spectroscopy (e, **Figure 2.8**).

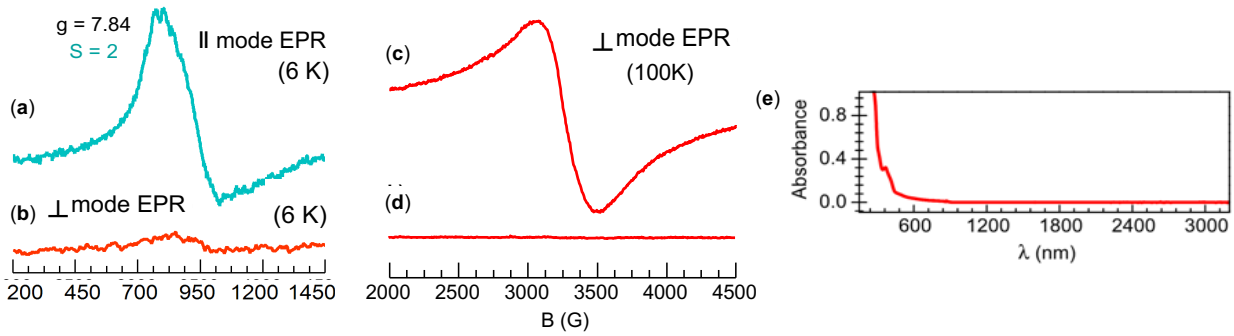

Figure 2.8. (**a**) X–Band EPR spectra of **2.4** taken at 6 K in parallel–mode (teal) in MeCN. (**b**) X–Band EPR spectra of **2.4** taken at 6 K in perpendicular–mode (orange) in MeCN. (**c**) X–Band perpendicular–mode EPR spectra for (salen)Mn^{II}. (**d**) reaction mixture of **2.1** and 0.5 eq. of $[Ar_3N][B(C_6F_5)_4]$ after 60 mins. Both (**c**) and (**d**) were taken at 100 K in acetonitrile. (**e**) UV–Vis–NIR of **2.4** in MeCN.

Intervalence charge transfer (IVCT) bands in the NIR appear due to inner–sphere electron charge transfer (thermally or photoinduced) between mixed–valent species. Three categories are used to describe the degree of communication: Class I equates to localized redox states with no interaction between redox–sites; Class II corresponds to a partially delocalized mixed–valent state, and; Class III describes a fully delocalized redox state.[38] The lack of an IVCT band in the NIR spectrum of **2.4** between 800−3300 nm (e, **Figure 2.8**) is consistent with a Class 1 assignment, with a localized (S = 2) Mn^{III} center and a diamagnetic (S = 0) Mn^{V} center (similar to the diamagnetism observed in **2.1**[2]). Collectively, these data support our mixed–valent oxidation state assignment with a localized high–spin Mn^{III} center bridged to a diamagnetic Mn^{V} nitride center.

The conversion of **2.1** to **2.4** with 0.5 eq. of oxidant suggests that a nucleophilic/electrophilic coupling pathway is not at play here. Such a coupling would not be expected to produce **2.6** and instead would involve $\mathbf{2.1}^{+}$ reacting with **2.1**, resulting in complete nitride conversion to N_2, as well as generation of (salen)Mn^{II} and **2.3** (left, **Figure 2.8**). Low valent Mn^{II} production was observed in Lau's report of Mn^{V}–imido coupling to generate N_2 (*vide supra*).[39] To further probe this, a reaction mixture of **2.1** and 0.5 eq. of $[Ar_3N][B(C_6F_5)_4]$ in MeCN was analyzed by perpendicular–mode EPR spectroscopy (d, **Figure 2.8**) and compared to an authentic sample of the known (salen)Mn^{II} starting material (c, **Figure 2.8**). Whereas the latter displayed a broad isotropic feature at g = 2.1 consistent with literature reports,[40] the former was featureless precluding the formation of any Mn^{II} by–products. These experimental results support Storr's DFT calculations suggesting that significant nitridyl character in $\mathbf{2.1}^{+}$ (and similar species) may be expected and are likely operational in this coupling.[5] With this, we believe that production of **2.4** is the result of a bimolecular coupling of two nitridyls ($\mathbf{2.1}^{+}$) to generate **2.3** (right, **Scheme 2.2**) which rapidly reacts with the remaining **2.1** in solution to generate **2.4**.

We next investigated whether **2.4** could be further oxidized to generate 2 equivalents of **2.3** (b, **Figure 2.9**. The CV of **2.4** displays a cathodically shifted oxidation event (relative to **2.1**) at +0.43 V (a, **Figure 2.9**), which is again accessible using the $[Ar_3N][B(C_6F_5)_4]$ oxidant. Addition of 1.0 eq. of oxidant to a solution of **2.4** in MeCN–d_3 results in the immediate formation of the paramagnetically shifted resonances of **2.3** in the ^{1}H–NMR spectrum, confirming that **2.4** is but an accessible side product in the oxidation of **2.1**→**2.3**.

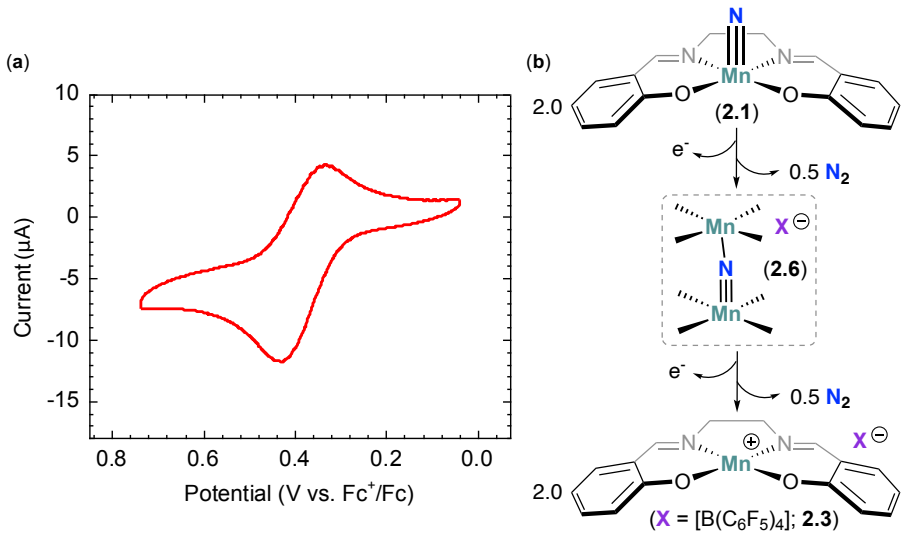

Figure 2.9. (**a**) Cyclic voltammogram (CV) for **2.4** in CH_2Cl_2 (0.5 mM). The quasi–reversible redox event exhibits a single electron oxidation feature at 0.43 V versus Fc^+/Fc couple ($E_{1/2}$ = 0.35 V). Scan rate: 100 mV/s. (**b**) Stepwise oxidations with 0.5–1.0 equivalents of oxidant to form intermediate **2.4** and products **2.2** and **2.3**.

2.2.3 First reported synthetic cycle for NH_3 oxidation

As part of our goal to generate a catalytic system for NH_3 oxidation to N_2, we turned to our initial results for the oxidation of **2.1**→**2.2** (**Scheme 2.3**). At time of publication, we believed the oxidants, $[Ar_3N][X]$ (X = $SbCl_6$, $B(C_6F_5)_4$), were incompatible with NH_3, but it has been since reported that a Ru catalyst coupled with $[Ar_3N][SbCl_6]$ can be used with strong base and NH_3 in a catalytic cycle to generate N_2.[41] **2.2** may be re–oxidized to **2.1** using NH_3 and NaOCl following literature procedures,[42] effectively closing the synthetic cycle, **D**→**B** (**Scheme 2.1**). We performed several larger scale oxidations of **2.1** using $[Ar_3N][SbCl_6]$, quantified the gas evolved via a gas burette, and – assuming ideal gas behavior – found the reactions to produce between 70–84% N_2 within 10 minutes of mixing (**Table 2.1**). Furthermore, removal of the solvent, followed by treatment with NH_3/NaOCl in a

DCM:MeOH solvent mixture, followed by purification as reported,[42] resulted in the isolation of pure **2.1** in varying yields from 50–63 % (**Scheme 2.3**, **Table 2.1**). This represents a closed synthetic cycle for NH_3 oxidation and was to our knowledge the first example using an abundant metal, such as Mn.

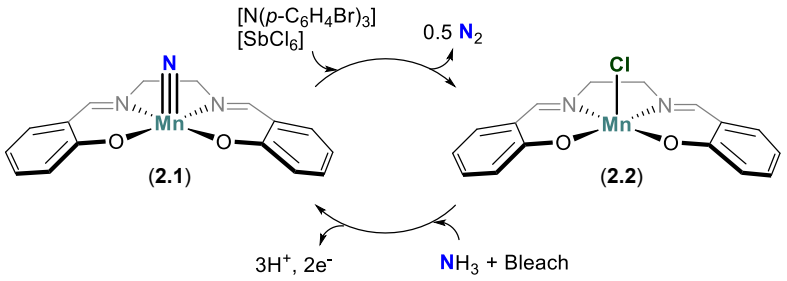

Scheme 2.3. First reported synthetic cycle for NH_3 oxidation.

Table 2.1. Values of gas quantification experiments using a gas burette.

Trial	V gas produced (mL)	Yield N_2 (%)	M≡N (2.1) Yield
1	4.0 ± 0.1	84 ± 2	50 %
2	3.3 ± 0.1	70 ± 2	58 %
3	3.8 ± 0.1	81 ± 2	63 %

2.3 Conclusions

In summary, this chapter has described the oxidation–initiated $6e^-$ reductive nitride coupling reaction to N_2 at a simple Mn–salen complex, including the experimental elucidation of the likely nitridyl coupling pathway, in support of previous theoretical work.[5] Isolation of a rare mixed valent Mn^{III}/Mn^{V} intermediate, including full characterization of the mixed redox state, was also described. The reduced Mn species can be further oxidized with NH_3 and oxidant, closing the synthetic cycle for NH_3 oxidation, was the first of its kind at the time of our first publication.

2.4 Experimental Section

2.4.1 General considerations

All manipulations were performed under an atmosphere of dry, oxygen–free N_2 or Ar by means of standard Schlenk or glovebox techniques (MBraun glovebox equipped with a –38 °C freezer). Hexanes, toluene, dichloromethane (DCM), and benzene were dried on an MBraun solvent purification system. Acetonitrile (–H_3 and –D_3) was purchased from Aldrich and dried over CaH_2 for several days prior to distillation. All solvents were degassed by freeze–pump–thaw and stored on activated 4 Å molecular sieves prior to use. Tris(4–bromophenyl)amine was purchased from TCI, $LiB(C_6F_5)_4$•Et_2O from Boulder Scientific, and [(*p*–$C_6H_4Br)_3N$][$SbCl_6$] from Aldrich. All were used without further purification. [(*p*–$C_6H_4Br)_3N$][$B(C_6F_5)_4$] was prepared from $AgB(C_6F_5)_4$•$(C_6H_5)_3$[43] and Tris(4–bromophenyl)amine by a modified literature procedure.[44] (salen)Mn≡N (**2.1**) was prepared according to literature procedure.[2]

NMR spectra were obtained on a Varian Unity Inova 500 MHz or Agilent Technologies 400 MHz spectrometer, and referenced to residual solvent of MeCN–d_3 (1.94 ppm) or externally (^{15}N: 80% CH_3NO_2, ^{11}B: 85% $(Et_2O)BF_3$, ^{19}F: $CFCl_3$). Chemical shifts (δ) are recorded in ppm and the coupling constants are in Hz.

UV–Vis/NIR spectroscopy was performed using a Perkin Elmer Spectrum 100, FT–IR spectrometer, with an attached Universal ATR sampling accessory. Measurements were done with IR Silica cuvettes equipped with an air–tight J–Young adaptor.

Elemental analyses (C, N, H) were recorded at the University of California, Berkeley using a Perkin Elmer 2400 Series II combustion analyzer.

Cyclic Voltammetry was performed on a CH Instruments Electrochemical Analysis potentiometer, equipped with a glassy carbon working electrode, an Ag wire pseudo–reference electrode, and a Pt counter electrode with [^{n}Bu4N][PF_6] (0.1 M) solution in CH_2Cl_2. Ferrocene was used as an internal standard.

EPR spectroscopy: Perpendicular– and parallel–mode X–band EPR spectra were collected on a Bruker EMX EPR Spectrometer equipped with an Oxford ESR 900 liquid helium cryostat. A modulation frequency of 100 kHz was used for all EPR spectra and the data was plotted using SpinCount.[45]

Mass spectrometry was performed on a Shimadzu model QP2010 GC–MS equipped with a secondary electron multiplier TIC detector. The constituent gases were separated by passing through an Agilent DB–1 column using helium as the carrier gas.

X–ray crystallography data was collected on a Bruker KAPPA APEX II diffractometer equipped with an APEX II CCD detector using a TRIUMPH monochromator with a Mo Kα X–ray source (α = 0.71073 Å). The crystals were mounted on a cryoloop under Paratone–N oil, and all data were collected at 100(2) K using an Oxford nitrogen gas cryostream system. A hemisphere of data was collected using ω scans with 0.5° frame widths. Data collection and cell parameter determination were conducted using the SMART program. Integration of the data frames and final cell parameter refinement were performed using SAINT software. Absorption correction of the data was carried out using SADABS. Structure determination was done using direct or Patterson methods and difference Fourier techniques. All hydrogen atom positions were idealized and rode on the atom of attachment. Structure solution, refinement, graphics, and creation of publication materials were performed using SHELXTL.

Evan's Method measurements were carried out in a NMR tube that was charged with known weights of both the magnetic sample and deuterated solvent of choice, along with a few drops of fluorobenzene. A small capillary tube was filled with a 1:1 mixture of deuterated solvent: fluorobenzene, sealed, and placed into the NMR tube. A ^{19}F–NMR was obtained showing two distinct signals. The $S = 2$ state was calculated considering the χdia contribution on Pacal's data.[46]

2.4.2 Synthesis of compounds

Isolation of [(salen)MnCl]$_2$ (2.2): The reported[47] compound **2.2** was isolated from the reaction mixture of **2.1** with [(*p*–$C_6H_4Br)_3N$][$SbCl_6$] as follows: A 10 ml round bottom flask equipped with a magnetic stirbar was charged with **2.1** (12.3 mg, 0.037 mmol) and 2 ml of fluorobenzene. This layer was frozen using a liquid N_2–cooled cold well in the glovebox. In a separate vial, [(*p*–$C_6H_4Br)_3N$][$SbCl_6$] (30.2 mg, 0.037 mmol) was dissolved in 2 ml of fluorobenzene and added to the frozen solution of **2.1**. The frozen sample was removed from the cold well, placed on a stirplate, and allowed to thaw and stir at r.t. for 3 hours. The solvent was removed yielding a brown–yellow solid which was washed on celite with benzene followed by fluorobenzene which was collected in a separate vial. Recrystallization of the fluorobenzene fraction with Et_2O yielded single crystals of **2.2** suitable for X–ray diffraction (10.7 mg, 0.03 mmol, 82%).

Synthesis of [(salen)Mn(Et_2O)]$_2$[$B(C_6F_5)_4$]$_2$ (2.3): A 20 ml vial equipped with a magnetic stirbar was charged with **2.1** (12.7 mg, 0.037 mmol) and 5 mL fluorobenzene (FB). In a separate 20 ml vial, [(*p*–$C_6H_4Br)_3N$][$B(C_6F_5)_4$] (0.0441 g, 0.037 mmol) was dissolved in 5 mL of fluorobenzene and added dropwise to the **2.1** solution. The solution stirred for 6 hours after which the solvent was removed. The brown–red oil was washed with and run through a plug

of celite. A layer of brown solid was left on the celite and was removed with fluorobenzene. The fluorobenzene layer was collected and the solvent was removed yielding a dark red oil. The product was isolated by recrystallization from fluorobenzene/Et_2O yielding the pure product as single crystals (32.6 mg, 0.03 mmol, 80%).

Anal. Calcd. for $C_{44}H_{24}BF_{20}MnN_2O_3$: C, 49.19; H, 2.25; N, 2.61. Found: C, 48.81; H, 1.99; N, 2.53. **^{1}H NMR** (400 MHz, CD_3CN): δ –8.7, –28.2, –32.2. **^{11}B{^{1}H} NMR** (400 MHz, CD_3CN): –16.6 (s). **^{19}F{^{1}H} NMR** (400 MHz, CD_3CN): δ –133.86 (d, $^{3}J_{F–F}$ = 12.0 Hz, *o*–C_6F_5), –163.94 (t, $^{3}J_{F–F}$ = 20.0 Hz, *p*–C_6F_5), δ –168.40 (m, *m*–C_6F_5). **Evan's method:** *S = 2* (**Table 2.2**).

Synthesis of [(salen)Mn^{V}(μ–N)Mn^{III}(salen)][B(C_6F_5)$_4$] (2.4): A 20 ml vial equipped with a magnetic stirbar was charged with [(*p*–$C_6H_4Br)_3N$][B(C_6F_5)$_4$] (29.0 mg, 0.025 mmol) and fluorobenzene (5 ml). A separate vial was charged with (salen)MnN (**2.1**) (16.7 mg, 0.05 mmol) and 5 ml of fluorobenzene. The [(*p*–$C_6H_4Br)_3N$][B(C_6F_5)$_4$] solution was added dropwise to the solution of **2.1**. The solution was stirred at room temperature and turned dark brown. The reaction mixture stirred for 6 hours and the solvent was removed yielding a brown oil. The oil was washed with benzene and filtered on celite. The filter was further washed with fluorobenzene, followed by MeCN. The MeCN extract was brought to dryness to yield a brown–red oil. This oil was recrystallized from vapor diffusion of fluorobenzene/DCM yielding the product **2.4** as single crystals suitable for X–ray diffraction (13.3 mg, 0.010 mmol, 70% based on a 2:1 ratio of **2.1**:**2.2**). Bulk purity was determined by 100K magnetization data (a and b, **Figure 2.7**) to check for ferromagnetic impurities and elemental analysis. *Anal. Calcd*. for $C_{56}H_{28}BF_{20}Mn_2N_5O_4$•$CH_2Cl_2$: C, 48.20; H, 2.13; N, 4.93. Found: C, 48.10; H, 2.09; N, 4.97. **^{1}H NMR** (400 MHz, CD_3CN): silent. **^{11}B{^{1}H} NMR** (400 MHz, CD_3CN): –16.6 (s).

$^{19}F\{^{1}H\}$ NMR (400 MHz, CD_3CN): –133.86 (d, $^{3}J_{F–F}$ = 12.0 Hz, *o*–C_6F_5), –163.94 (t, $^{3}J_{F–F}$ = 20.0 Hz, *p*–C_6F_5), δ –168.40 (m, *m*–C_6F_5).

Literature modification [(*p*–$C_6H_4Br)_3N][B(C_6F_5)_4$][43]: In the dark, a 100 mL roundbottom flask was charged with (139.7 mg, 0.29 mmol) of Tris(4–bromophenyl)amine in 5 mL DCM and (295.9 mg, 0.29 mmol) of $AgB(C_6F_5)_4•(C_6H_5)_3$ in 5 mL of DCM. Iodine (40.6 mg, 0.16 mmol) in 5 mL DCM was added dropwise to the flask and the solution was stirred for 3 hours, turning dark blue in color. The solution was concentrated to 8 mL *via vacuo*. Pentane (25 mL) was added and the solution was stored in the freezer overnight forming a purple filtrate and dark blue crystals that were filtered and dried *via vacuo* at ambient temperature for 16 hours (278 mg, 0.24 mmol, 83%).

2.4.4 Qualitative N_2 determination: Gas chromatography (GC–MS) experiments

2.4.4.1 Oxidations with [(*p*–$C_6H_4Br)_3N][B(C_6F_5)_4$]

Oxidation of 2.1–^{15}N: A 5 ml schlenk flask equipped with a magnetic stirbar was charged with **2.1–^{15}N** (12.0 mg, 0.036 mmol) and fluorobenzene (1 ml) and was frozen in a dry ice/acetone–cooled bath using schlenk technique. Cooling only the solvent, the flask was back–filled with Ar for 30 mins and then capped with a septum. A gas–tight syringe containing a solution of [(*p*–$C_6H_4Br)_3N][B(C_6F_5)_4$] (41.7 mg, 0.036 mmol) in fluorobenzene (1 ml) was layered on top of the frozen solution of **2.1–^{15}N**. Both layers were frozen completely and back–filled with Ar for an additional 10 minutes. The Ar source was removed and the solution was brought to room temperature with stirring. Within 30 minutes, the headspace was sampled (60 μL) using a gastight syringe and directly injected into the GC–MS. The peaks in the GC trace show $^{15}N_2$ (with contamination from atmospheric $^{14}N_2$ and O_2) and Ar combined at retention time 1.5 and fluorobenzene at retention time 2.6. The mass spectrum at retention time 1.5 (a, **Figure 2.4**) is

shown (with Ar excluded) and displays the relative abundance of $^{15}N_2$ at 27.5 % compared to atmospheric $^{14}N^{14}N$ which is set to relative abundance of 100.

Oxidation of (50:50 mixture) 2.1–^{15}N:2.1: A 5 ml schlenk flask equipped with a magnetic stirbar was charged with **2.1–^{15}N** (6.0 mg, 0.018 mmol) and **2.1** (6.0 mg, 0.018 mmol) in fluorobenzene (1 ml) and was frozen in a dry ice/acetone–cooled bath using schlenk technique. Cooling only the solvent, the flask was back–filled with Ar for 30 mins and then capped with a septum. A gas–tight syringe containing a solution of [(*p*–$C_6H_4Br)_3N$][$B(C_6F_5)_4$] (41.7 mg, 0.036 mmol) in fluorobenzene (1 ml) was layered on top of the frozen solution of **2.1–^{15}N** and **2.1**. Both layers were frozen completely and back–filled with Ar for an additional 10 minutes. The Ar source was removed and the solution was brought to room temperature with stirring. Within 30 minutes, the headspace was sampled (60 μL) using a gastight syringe and directly injected into the GC–MS. The peaks in the GC trace show $^{15}N_2$ and $^{14}N^{15}N$ (with contamination from atmospheric $^{14}N_2$ and O_2) and Ar combined at retention time 1.5 and fluorobenzene at retention time 2.6. The mass spectrum at retention time 1.5 (b, **Figure 2.4**) is shown (with Ar excluded) and displays the relative abundance of $^{15}N_2$ at 9.1 %, whereas the 50:50 mixture, $^{14}N^{15}N$ is 19 %. Both are compared to $^{14}N^{14}N$, which is set to a relative abundance of 100.

2.4.4.2 Oxidations with [(*p*–$C_6H_4Br)_3N$][$SbCl_6$]

Oxidation of 2.1–^{15}N: A 5 ml schlenk flask equipped with a magnetic stirbar was charged with **2.1–^{15}N** (12.0 mg, 0.036 mmol) and fluorobenzene (1 ml) and was frozen in a dry ice/acetone–cooled bath using schlenk technique. Cooling only the solvent, the flask was back–filled with Ar for 30 mins and then capped with a septum. A gas–tight syringe containing a solution of [(*p*–$C_6H_4Br)_3N$] [$SbCl_6$] (29.3 mg, 0.036 mmol) in fluorobenzene (1 ml) was layered on top of the frozen solution of **2.1–^{15}N**. Both layers were frozen completely and back–filled with Ar for

an additional 10 minutes. The Ar source was removed and the solution was brought to room temperature with stirring. Within 30 minutes, the headspace was sampled (60 μL) using a gastight syringe and directly injected into the GC–MS. The peaks in the GC trace show $^{15}N_2$ (with contamination from atmospheric $^{14}N_2$ and O_2) and Ar combined at retention time 1.5 and fluorobenzene at retention time 2.6. The mass spectrum at retention time 1.5 (c, **Figure 2.4**) is shown (with Ar excluded) and displays the relative abundance of $^{15}N_2$ at 20.5 % compared to atmospheric $^{14}N^{14}N$ which is set to relative abundance of 100.

Oxidation of (50:50 mixture) 2.1–^{15}N:2.1: A 5 ml schlenk flask equipped with a magnetic stirbar was charged with **2.1–^{15}N** (6.0 mg, 0.018 mmol) and **2.1** (6.0 mg, 0.018 mmol) in fluorobenzene (1 ml) and was frozen in a dry ice/acetone–cooled bath using schlenk technique. Cooling only the solvent, the flask was back–filled with Ar for 30 mins and then capped with a septum. A gas–tight syringe containing a solution of [(*p*–$C_6H_4Br)_3N$][$SbCl_6$] (29.3 mg, 0.036 mmol) in fluorobenzene (1 ml) was layered on top of the frozen solution of **2.1–^{15}N** and **2.1**. Both layers were frozen completely and back–filled with Ar for an additional 10 minutes. The Ar source was removed and the solution was brought to room temperature with stirring. Within 30 minutes, the headspace was sampled (60 μL) using a gastight syringe and directly injected into the GC–MS. The peaks in the GC trace show $^{15}N_2$ and $^{14}N^{15}N$ (with contamination from atmospheric $^{14}N_2$ and O_2) and Ar combined at retention time 1.5 and fluorobenzene at retention time 2.6. The mass spectrum at retention time 1.5 (d, **Figure 2.4)** is shown (with Ar excluded) and displays the relative abundance of $^{15}N_2$ at 8.1 %, whereas the 50:50 mixture, $^{14}N^{15}N$ is 16.1 %. Both are compared to $^{14}N^{14}N$, which is set to relative abundance of 100.

2.4.5 Magnetization Data

2.4.5.1 Magnetic data: Evans' method

The χ_{dia} and μ_{eff} values were estimated using Pascal's constants[46] and the μ_{eff} calculated assuming spin–only contributions as below. An *S = 2* system for complex **2.3** (in coordination g MeCN) was determined by using the data in **Table 2.2**.

$$\mu_{eff} = 2\sqrt{S\ (S+1)}$$

Table 2.2. List of Evans' Method Experimental and Calculated Values

Trial	Weight (mg)	$C_6H_5CF_3$ peak 1 (ppm)	$C_6H_5CF_3$ peak 2 (ppm)	μ_{eff} (μ_b)	Calculated S Value
1	1.5	–114.72	–114.60	4.965	2.03
2	1.2	–114.72	–114.62	5.069	2.08
3	1.4	–114.70	–114.59	4.919	2.01

2.4.5.2 Magnetization data

Magnetic data for **2.4** was collected using a Quantum Design MPMS SQUID Magnetometer in the RSO mode. The general sample preparation consisted on placing 16.1 mg of a polycrystalline powder of **2.4** into a gelatin capsule size #4. The gelatin capsule was inserted into a plastic straw. Prior to full data collection the purity of the sample was determined by collecting magnetization data from 0 to 5 T at 100 K (a and b, **Figure 2.7**).

2.4.5.3 Variable–temperature magnetic susceptibility measurements

Magnetic susceptibility measurements for **2.4** were collected in the temperature range from 30 to 300 K under an applied field of 0.5 and 1 T. Low temperature magnetization data was acquired on heating from 2 to 10 K at increasing magnetic fields of 1 – 5 T in increments of 1 T. Magnetic susceptibility data was corrected for diamagnetism of the sample, estimated using Pascal's constants, in addition to contributions from the sample holder (straw and gelatin capsule). $\chi_M T$ data was modeled according to the spin Hamiltonian: $\widehat{H} = g_{\text{iso}}\mu_B \mathbf{S}\cdot\mathbf{H}$; similarly, the reduced magnetization data was modeled according to: $\widehat{H} = D\hat{S}_Z^2 + g_{\text{iso}}\mu_B \mathbf{S}\cdot\mathbf{H}$, where an $S = 2$ was considered for data sets and D stands for the axial zero–field splitting parameter. *PHI* was used to model all the magnetic data (c, **Figure 2.7**).[48]

2.4.6 N_2 Quantification via Gas Burette

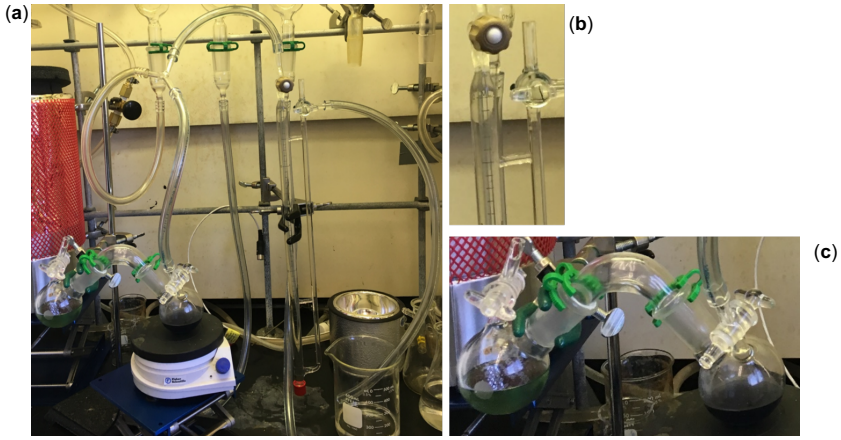

Figure 2.10. (**a**) Experimental setup. (**b**) Gas measuring burette. (**c**) Flask containing **2.1** (left) and the oxidant (right) connected by a glass bridge allowing for transfer of one solution to the other.

Gas quantification was performed using a standard gas burette and measuring the evolved gas through solvent displacement in the burette (regulated to 1 atm). We used an inert solvent (hexanes) in the burette so as to avoid exposing our air–sensitive oxidation reaction to any reactive solvent vapors. The experimental setup was performed under a 1 atm N_2 environment on the Schlenk line as follows: Two 100 mL Schlenk flasks were prepared by charging one with **2.1** (130.0 mg, 0.4 mmol) and 30 mL of fluorobenzene, as well as a magnetic stirbar. The other was filled with $[(p\text{–}C_6H_4Br)_3N][SbCl_6]$ (320.0 mg, 0.4 mmol) in 20 mL fluorobenzene. Both stopcocks were closed, the flasks were connected together using a small glass bridge, and were brought out on the Schlenk line. One of the stopcock arms was attached to the Schlenk line through a 3–way glass connector which also joined the closed burette (**Figure 2.10**). The line was purged by cycling vacuum and N_2 several times. The N_2 atmosphere was then opened to the reaction mixture as well as the burette. The N_2 feed to the Schlenk line was then closed

and the burette solvent level was allowed to stabilize. The flask containing the oxidant was turned over so as to allow the oxidant solution to transfer to the stirring solution of **2.1**. The combined solution was stirred rapidly as gas evolution occurred and was measured in the burette. The evolved gas was measured after 10 minutes. Three separate trials were run by measuring the displacement of hexanes in the burette, thus quantifying the produced N_2 (**Table 2.1**).

2.5 References

1. Marangoni, G.; Tavoni, M.; Bosetti, V.; Borgonovo, E.; Capros, P.; Fricko, O.; Gernaat, D. E. H. J.; Guivarch, C.; Havlik, P.; Huppmann, D.; Johnson, N.; Karkatsoulis, P.; Keppo, I.; Krey, V.; O Broin, E.; Price, J.; van Vuuren, D. P., Sensitivity of projected long-term CO2 emissions across the Shared Socioeconomic Pathways. *Nature Clim. Change* **2017,** *7* (2), 113-117.

2. Du Bois, J.; Hong, J.; Carreira, E. M.; Day, M. W., Nitrogen Transfer from a Nitridomanganese(V) Complex: Amination of Silyl Enol Ethers. *J. Am. Chem. Soc.* **1996,** *118* (4), 915-916.

3. Du Bois, J.; Tomooka, C. S.; Hong, J.; Carreira, E. M., Nitridomanganese(V) Complexes: Design, Preparation, and Use as Nitrogen Atom-Transfer Reagents. *Accounts of Chemical Research* **1997,** *30* (9), 364-372.

4. Würminghausen, T.; Sellmann, D., Cyclovoltammetrische und präparative untersuchungen zum redoxverhalten der N2-, N2H2-, N2H4- und NH3-komplexe [C5H5Mn(CO)2]xL MIT x = 1 für L = N2, N2H4, NH3 und x = 2 für L = N2H2. *Journal of Organometallic Chemistry* **1980,** *199* (1), 77-85.

5. Clarke, R. M.; Storr, T., Tuning Electronic Structure To Control Manganese Nitride Activation. *J. Am. Chem. Soc.* **2016,** *138* (47), 15299-15302.

6. Thusius, D. D.; Taube, H., Oxidation of aquopentaammine and of hexaamminecobalt(III) ions. *The Journal of Physical Chemistry* **1967,** *71* (12), 3845-3857.

7. Bhattacharya, P.; Heiden, Z. M.; Wiedner, E. S.; Raugei, S.; Piro, N. A.; Kassel, W. S.; Bullock, R. M.; Mock, M. T., Ammonia Oxidation by Abstraction of Three Hydrogen Atoms from a Mo–NH3 Complex. *Journal of the American Chemical Society* **2017**.

8. Guilardt, J. P. C. J. E. H. M. S. E. M. A. L. R., Reduced Nitrogen Hydride Complexes of a Cofacial Metallodiporphyrin and Their Oxidative Interconversion. An Analysis of Ammonia Oxidation and Prospects for a Dinitrogen Electroreduction Catalyst Based on Cofacial Metallodiporphyrins . **1992**.

9. Buhr, J. D.; Taube, H., Oxidation of pentaamminecarbonylosmium(2+) to .mu.-dinitrogen-bis(cis-tetraamminecarbonylosmium)(4+). *Inorganic Chemistry* **1979,** *18* (8), 2208-2212.

10. Coia, G. M.; Demadis, K. D.; Meyer, T. J., Oxidation of Ammonia in Osmium Polypyridyl Complexes. *Inorganic Chemistry* **2000,** *39* (10), 2212-2223.

11. Pipes, D. W.; Bakir, M.; Vitols, S. E.; Hodgson, D. J.; Meyer, T. J., Reversible interconversion between a nitrido complex of osmium(VI) and an ammine complex of osmium(II). *Journal of the American Chemical Society* **1990,** *112* (14), 5507-5514.

12. Scheibel, M. G.; Abbenseth, J.; Kinauer, M.; Heinemann, F. W.; Würtele, C.; de Bruin, B.; Schneider, S., Homolytic N–H Activation of Ammonia: Hydrogen Transfer of Parent Iridium Ammine, Amide, Imide, and Nitride Species. *Inorganic Chemistry* **2015,** *54* (19), 9290-9302.

13. Abbenseth, J.; Finger, M.; Wurtele, C.; Kasanmascheff, M.; Schneider, S., Coupling of terminal iridium nitrido complexes. *Inorganic Chemistry Frontiers* **2016,** *3* (4), 469-477.

14. Krahe, O.; Bill, E.; Neese, F., Decay of Iron(V) Nitride Complexes By a N□N Bond-Coupling Reaction in Solution: A Combined Spectroscopic and Theoretical Analysis. *Angewandte Chemie International Edition* **2014,** *53* (33), 8727-8731.

15. Scheibel, M. G.; Wu, Y.; Stückl, A. C.; Krause, L.; Carl, E.; Stalke, D.; de Bruin, B.; Schneider, S., Synthesis and Reactivity of a Transient, Terminal Nitrido Complex of Rhodium. *Journal of the American Chemical Society* **2013,** *135* (47), 17719-17722.

16. Bendix, J.; Anthon, C.; Schau-Magnussen, M.; Brock-Nannestad, T.; Vibenholt, J.; Rehman, M.; Sauer, S. P., Heterobimetallic nitride complexes from terminal chromium(V) nitride complexes: hyperfine coupling increases with distance. *Angew Chem Int Ed Engl* **2011,** *50* (19), 4480-3.

17. Seymore, S. B.; Brown, S. N., Polar Effects in Nitride Coupling Reactions. *Inorganic Chemistry* **2002,** *41* (3), 462-469.

18. Betley, T. A.; Peters, J. C., A Tetrahedrally Coordinated L3Fe−Nx Platform that Accommodates Terminal Nitride (FeIV⋮N) and Dinitrogen (FeI−N2−FeI) Ligands. *Journal of the American Chemical Society* **2004,** *126* (20), 6252-6254.

19. Man, W.-L.; Tang, T.-M.; Wong, T.-W.; Lau, T.-C.; Peng, S.-M.; Wong, W.-T., Highly Electrophilic (Salen)ruthenium(VI) Nitrido Complexes. *Journal of the American Chemical Society* **2004,** *126* (2), 478-479.

20. Scheibel, M. G.; Askevold, B.; Heinemann, F. W.; Reijerse, E. J.; de Bruin, B.; Schneider, S., Closed-shell and open-shell square-planar iridium nitrido complexes. *Nat Chem* **2012,** *4* (7), 552-558.

21. Ware, D. C.; Taube, H., Substitution-induced nitrogen-nitrogen coupling for nitride coordinated to osmium(VI). *Inorganic Chemistry* **1991,** *30* (24), 4605-4610.

22. Keener, M.; Peterson, M.; Hernández Sánchez, R.; Oswald, V. F.; Wu, G.; Ménard, G., Towards Catalytic Ammonia Oxidation to Dinitrogen: A Synthetic Cycle by Using a Simple Manganese Complex. *Chemistry - A European Journal* **2017,** *23* (48), 11479-11484.

23. Connelly, N. G., William, Chemical Redox Agents for Organometallic Chemistry. **1996**.

24. Meng, X.; Wang, H.-N.; Wang, X.-L.; Yang, G.-S.; Wang, S.; Shao, K.-Z.; Su, Z.-M., Construction and property investigation of inorganic–organic hybrid materials based on metal–salens and Keggin polyoxometalates. *Inorganica Chimica Acta* **2012,** *390*, 135-142.

25. Šilha, T.; Nemec, I.; Herchel, R.; Trávníček, Z., Structural and magnetic characterizations of the first manganese(iii) Schiff base complexes involving hexathiocyanidoplatinate(iv) bridges. *CrystEngComm* **2013,** *15* (26), 5351-5358.

26. Miyasaka, H.; Clérac, R.; Ishii, T.; Chang, H.-C.; Kitagawa, S.; Yamashita, M., Out-of-plane dimers of Mn(iii) quadridentate Schiff-base complexes with saltmen2− and naphtmen2− ligands: structure analysis and ferromagnetic exchange. *Journal of the Chemical Society, Dalton Transactions* **2002,** (7), 1528-1534.

27. Miyasaka, H.; Matsumoto, N.; Ōkawa, H.; Re, N.; Gallo, E.; Floriani, C., Complexes Derived from the Reaction of Manganese(III) Schiff Base Complexes and Hexacyanoferrate(III): Syntheses, Multidimensional Network Structures, and Magnetic Properties. *Journal of the American Chemical Society* **1996,** *118* (5), 981-994.

28. Krahe, O.; Bill, E.; Neese, F., Decay of Iron(V) Nitride Complexes By a N□N Bond-Coupling Reaction in Solution: A Combined Spectroscopic and Theoretical Analysis. *Angew. Chem. Int. Ed.* **2014,** *53* (33), 8727-8731; *Angew. Chem.* **2014**, *0126*, 8872-8876.

29. Chantarojsiri, T.; Reath, A. H.; Yang, J. Y., Cationic Charges Leading to an Inverse Free-Energy Relationship for N−N Bond Formation by MnVI Nitrides. *Angewandte Chemie International Edition* **2018,** *57* (43), 14037-14042.

30. Golubkov, G.; Gross, Z., Chromium(V) and Chromium(VI) Nitrido Complexes of Tris(pentafluorophenyl)corrole. *Angew. Chem. Int. Ed.* **2003,** *42* (37), 4507-4510; *Angew. Chem.* **2003**, *0115*, 4645-4648.

31. See Supporting Information for experimental setup.

32. Meyer, K.; Bendix, J.; Metzler-Nolte, N.; Weyhermüller, T.; Wieghardt, K., Nitridomanganese(V) and -(VI) Complexes Containing Macrocyclic Amine Ligands. *J. Am. Chem. Soc.* **1998,** *120* (29), 7260-7270.

33. Yuan, M.; Zhao, F.; Zhang, W.; Pan, F.; Wang, Z.-M.; Gao, S., Hydrogencyanamide-Bridged One-Dimensional Polymers Built on MnIII–Schiff Base Fragments: Synthesis, Structure, and Magnetism. *Chem. Eur. J.* **2007,** *13* (10), 2937-2952.

34. Zhou, H.-B.; Wang, H.-S.; Chen, Y.; Xu, Y.-L.; Song, X.-J.; Song, Y.; Zhang, Y.-Q.; You, X.-Z., Synthesis, structure, magnetic properties and DFT calculations of two hydroxo-bridged complexes based on MnIII(Schiff-Bases). *Dalton Trans.* **2011,** *40* (22), 5999-6006.

35. Song, J. H.; Lim, K. S.; Ryu, D. W.; Yoon, S. W.; Suh, B. J.; Hong, C. S., Synthesis, Structures, and Magnetic Properties of End-to-End Azide-Bridged Manganese(III) Chains: Elucidation of Direct Magnetostructural Correlation. *Inorg. Chem.* **2014,** *53* (15), 7936-7940.

36. Gupta, R.; Taguchi, T.; Borovik, A. S.; Hendrich, M. P., Characterization of Monomeric MnII/III/IV–Hydroxo Complexes from X- and Q-Band Dual Mode Electron Paramagnetic Resonance (EPR) Spectroscopy. *Inorg. Chem.* **2013,** *52* (21), 12568-12575.

37. Gupta, R.; Taguchi, T.; Lassalle-Kaiser, B.; Bominaar, E. L.; Yano, J.; Hendrich, M. P.; Borovik, A. S., High-spin Mn–oxo complexes and their relevance to the oxygen-evolving complex within photosystem II. *Proc. Natl. Acad. Sci. U.S.A.* **2015,** *112* (17), 5319-5324.

38. Day, P.; Hush, N. S.; Clark, R. J. H., Mixed valence: origins and developments. *Phil. Trans. R. Soc. A* **2008,** *366* (1862), 5-14.

39. Yiu, S.-M.; Lam, W. W. Y.; Ho, C.-M.; Lau, T.-C., Facile N···N Coupling of Manganese(V) Imido Species. *J. Am. Chem. Soc.* **2007,** *129* (4), 803-809.

40. Bryliakov, K. P.; Babushkin, D. E.; Talsi, E. P., Detection of EPR spectra in S = 2 states of MnIII(salen) complexes. *Mendeleev Commun.* **1999,** *9* (1), 29-31.

41. Nakajima, K.; Toda, H.; Sakata, K.; Nishibayashi, Y., Ruthenium-catalysed oxidative conversion of ammonia into dinitrogen. *Nature Chemistry* **2019,** *11* (8), 702-709.

42. Chang, C. J.; Connick, W. B.; Low, D. W.; Day, M. W.; Gray, H. B., Electronic Structures of Nitridomanganese(V) Complexes. *Inorg. Chem.* **1998,** *37* (12), 3107-3110.

43. Ogawa, K.; Kitagawa, T.; Ishida, S.; Komatsu, K., Synthesis and Structure of a New Tetrakis(pentafluorophenyl)borate Salt of the Silver(I) Cation with Novel Trigonal Planar Tris(benzene) Coordination. *Organometallics* **2005,** *24* (20), 4842-4844.

44. O'Connor, A. R.; Nataro, C.; Golen, J. A.; Rheingold, A. L., Synthesis and reactivity of [N(C6H4Br)3][B(C6F5)4]: the X-ray crystal structure of [Fe(C5H5)2][B(C6F5)4]. *J. Organomet. Chem.* **2004,** *689* (14), 2411-2414.

45. Golombek, A. P.; Hendrich, M. P., Quantitative analysis of dinuclear manganese(II) EPR spectra. *J. Magn. Reson.* **2003,** *165* (1), 33-48.

46. Bain, G. A.; Berry, J. F., Diamagnetic Corrections and Pascal's Constants. *J. Chem. Educ.* **2008,** *85* (4), 532.

47. Vincent L. Pecoraro, W. M. B., Structure ofN, N'-Ethylenebis(salieylideneiminato)manganese(III) Chloride Aeetonitrile Solvate. **1985**.

48. Chilton, N. F.; Anderson, R. P.; Turner, L. D.; Soncini, A.; Murray, K. S., PHI: A powerful new program for the analysis of anisotropic monomeric and exchange-coupled polynuclear d- and f-block complexes. *J. Comput. Chem.* **2013,** *34* (13), 1164-1175.

Chapter 3 – Progress Towards Catalytic NH_3 Oxidation Chemistry using Simple Manganese–Salen Complexes

3.1 Introduction

The inherent stability of N–H bonds of NH_3 presents on of the greatest challenges in developing molecular NH_3 oxidation catalysts. As thoroughly outlined in Chapter 1, due to the high BDFE for NH_3 ($BDFE_{N–H}$: 104 kcal/mol)[1] and low acidity (pKa^{dmso} = ~41)[2], activation under mild conditions is challenging, but has been previously achieved by multiple homogenous and electrochemical molecular systems for stoichiometric NH_3 activation. As outlined in Chapter 2, we were able to contribute to these previous works by developing the first synthetic cycle for NH_3 oxidation to N_2 by employing a Mn(salen)≡N complex.[3]

Although significant progress has been made, the removal of six electrons and six protons from two NH_3 molecules to form N_2 is still a challenging task, and because of this, molecular catalysts for NH_3 oxidation are exceedingly rare. Only within the past two years (2019–2020), have molecular catalysts for the oxidation of NH_3 to N_2 been realized. Currently, there are five known molecular systems capable of performing this transformation, all being Ru catalysts with one Fe example (**Scheme 3.1**).[4-8] These examples include work by Bullock and Mock,[4] developing a system built on a previous system developed by Mock *et. al.* for stoichiometric N–H activation by HAA abstraction chemistry with $^tBu_3ArO•$.[9] They found the cleavage of N–H bonds could be performed with HAA equivalents leading to formation of N_2 with their highest catalytic TON = 10. Additionally, Bullock *et. al.* devised a similar HAA catalysis as their previous system and were able to improve catalytic TON to 125 utilizing a tetramesitylporphryin complex.[8] Lastly, Nishibayshi *et. al*. recently developed a system capable of performing NH_3 (as NH_4OTf) oxidation with a strong oxidant and base, [N(*p*–

$C_6H_4Br)_3][SbCl_6]$ and 2,4,6–collidine respectively[5]. At the time of our work in moving towards developing a NH_3 oxidation catalyst – which was investigated before these current systems were developed – we were hoping to build off our previous results for a synthetic cycle and develop a molecular catalyst capable of performing this transformation.

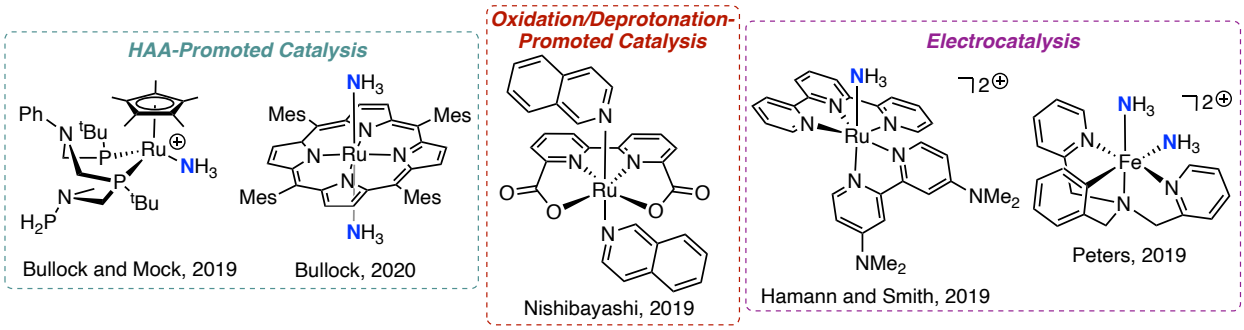

Scheme 3.1. Molecular NH_3 oxidation catalysts.

Additionally, we were interested in probing the mechanism to try and understand this 6e– chemistry. In this Chapter, our work toward developing and understanding a catalytic cycle for NH_3 oxidation will be described.

3.2 Results and Discussion

3.2.1 Probing catalytic NH_3 oxidation using *N*–bromosuccinimide (NBS)

Building on our previous results, for the oxidation of (salen)Mn≡N[10] (**2.1**), which initiates a reductive nitridyl–radical homocoupling to produce N_2, the reduced Mn^{III} product could be further oxidized in the presence of NH_3 and oxidant, closing a synthetic cycle for NH_3 oxidation (**Scheme 2.3**).[3, 11] In an effort to generate a truly catalytic system we sought the use of milder oxidants. At the time of this work, we found previous studies have shown that $1e^-$ oxidants, NBS and Cl_2 can chemically oxidize Schiff base–derived $Mn^{III}X$ (X = Cl, OAc) in the presence of NH_3 to yield five coordinate Mn^{V}≡N.[10, 12-14] The theoretical estimated oxidation potential, derived from experimental values, for NBS was found to be >1.43 V vs. Fc/Fc^+,[15]

far surpassing the potential of **2.1** (b, **Figure 2.2**; b, **Figure 3.2**), in which we could theoretically induce the reductive nitride coupling to N_2.[3, 16] Addition of NBS to a solution of **2.1** in acetonitrile (MeCN) under UV–light or heat did not result in chemical oxidation. The ^{1}H NMR spectrum showed shifted diamagnetic signals, as well as formation of succinimide. The mass spectral analysis for the headspace of **2.1–^{15}N** and NBS revealed no $^{15}N_2$ formation, indicating nitride coupling was not the active pathway. Isolation of a brown–red product in a 72% yield of crystals suitable for XRD studies revealed a partially aromatic–halogenated product, [(salen–(3,5–Br)(3–Br))Mn≡N] (**3.1**) (a, **Figure 3.1**) Similar systems have shown that phenyl rings are susceptible to halogenation by NBS.[17-19]

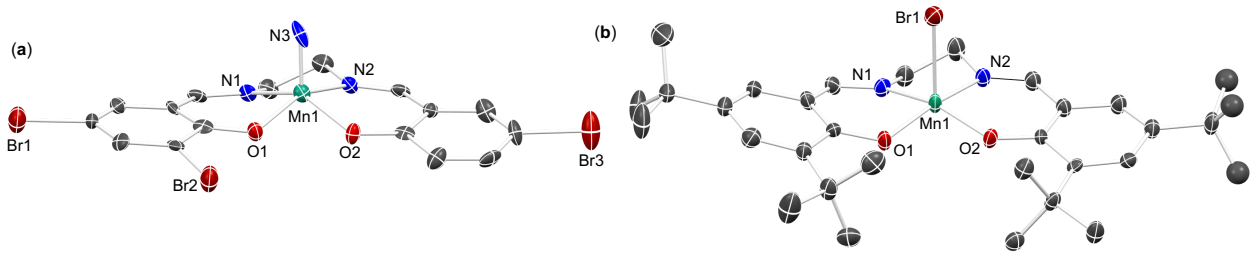

Figure 3.1. (**a**) Solid state molecular structure of [(salen–(3,5–Br)(3–Br))Mn≡N] (**3.1**) and (**b**) [(salen–(3,5–^{t}Bu)$_2$)MnBr] (**3.**3). Hydrogen atoms omitted for clarity.

In order to induce chemical oxidation and prevent aromatic halogenation, we turned to altering the substituents on the phenyl groups of the ligand. Storr and coworkers have shown that addition of electron withdrawing or donating substituents can shift the resulting oxidation potential as well as the locus of chemical oxidation of the complex.[16] Additionally, adding substituents to the 3,5–positions of the aromatic ring can prevent halogenation from occurring. They found that increasing the electron–donating ability of the substituents shifts the oxidation potential cathodically versus **2.1**. Conversely, a significant increase in electron–donation can shift the locus of chemical oxidation from metal to ligand based.[16] To maintain oxidation at

the metal and lower the resulting oxidation potential versus **2.1**, while incorporating substituents on the periphery to prevent further halogenation, we turned our attention toward the previously reported [(salen–(3,5–^{t}Bu)$_2$)Mn≡N][20-21] (**3.2**; a, **Figure 3.2**). **3.2** in dichloromethane (DCM) exhibits a quasi–reversible oxidation at 0.33 V (vs. Fc/Fc$^+$) compared to **2.1** (0.56 V vs. Fc/Fc$^+$) (b, **Figure 3.2**).

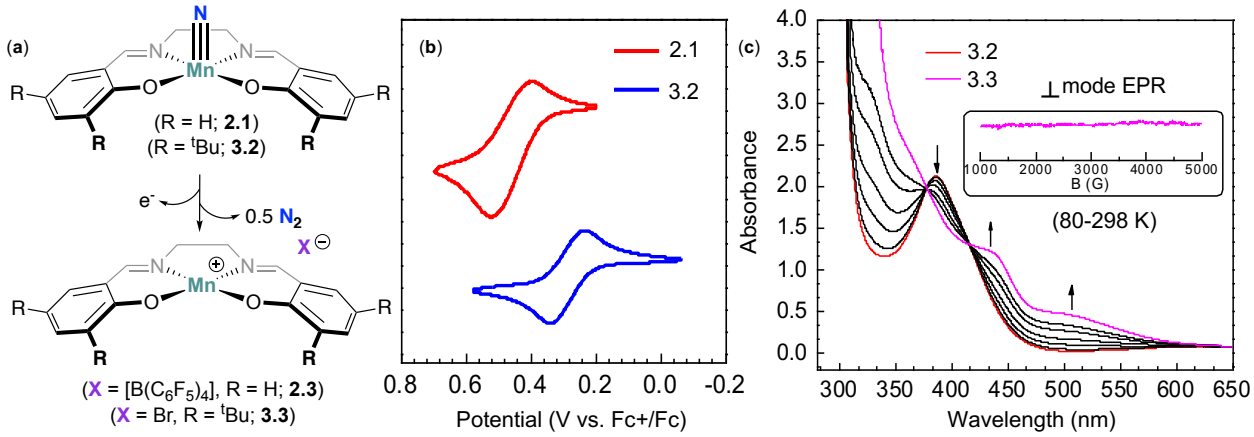

Figure 3.2. (**a**) Oxidation of **2.1** with [Ar$_3$N][X] to yield **2.3** (X = [B(C$_6$F$_5$)$_4$]) and oxidation of **3.2** with NBS to yield **3.3**. (**b**) Overlay of cyclic voltammograms for **2.1** (1.0 mM) and **3.2** (1.0 mM) with 0.1mM [Bu$_4$N][PF$_6$] electrolyte in DCM (glassy carbon working electrode, scan rate = 100 mV/s). The following oxidation potentials are 0.56 V (**2.1**) and 0.33 V (**3.2**) vs. Fc/Fc$^+$ couple respectively. (**c**) Oxidation absorption spectra of **3.2** with NBS, yielding the corresponding formally reduced Mn^{III} species **3.3**. Inset: X–band EPR of **3.3** taken at 80–298 K (MeCN) in perpendicular mode.

Oxidation of **3.2** with NBS in acetonitrile (MeCN) under ambient light resulted in loss of diamagnetic peaks in the ^{1}H NMR spectrum with the formation of a paramagnetic product in a 78% yield. The structure was identified by single crystal XRD studies as [(salen–(3,5–^{t}Bu)$_2$)MnBr] (**3.3**; b, **Figure 3.1**). The solid-state molecular structure revealed a Mn1–Br1 bond

length of 2.588(3) Å, consistent with previously reported manganese bromide pseudo-C_{4V} complexes.[22-23] The absorption spectra for the oxidation of **3.2** with NBS revealed the formation of two prominent bands at 448 nm and 500 nm, consistent with previously reported $Mn^{III}Br$(salen) complexes in DCM (c, **Figure 3.2**).[23] The spin state of **3.3** was determined by the Evans' method in MeCN–d_3, revealing a high spin $S = 2$ complex (**Table 3.2**) consistent with previously reported Mn^{III} complexes.[3] This assignment was further supported by perpendicular mode EPR. The perpendicular mode spectrum of **3.3** in MeCN within a temperature range of 80–298 K was completely featureless, consistent with an integer spin system ($S = 2$) (c, inset, **Figure 3.2**).[24]

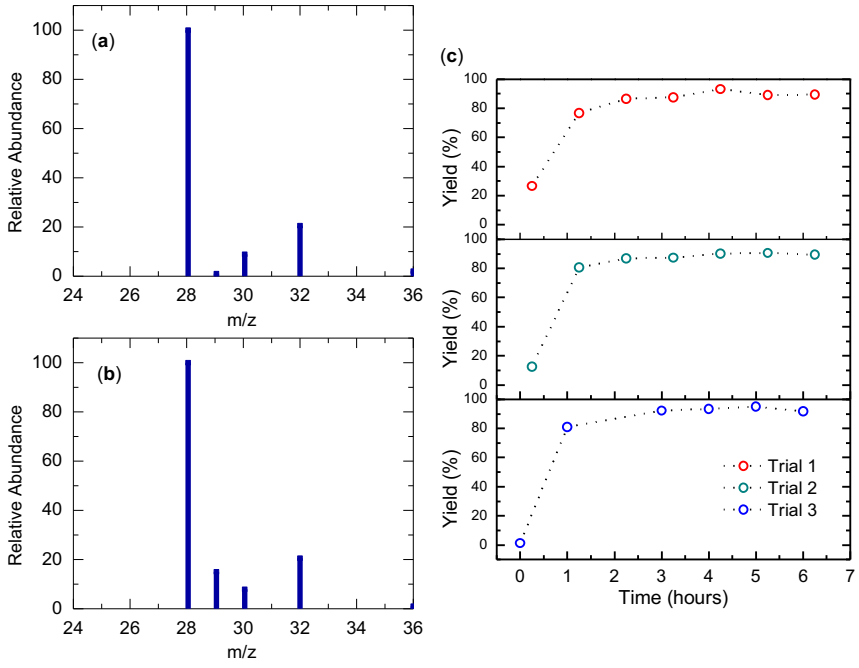

Figure 3.3. (**a**) Mass spectrum from reaction of **3.2–^{15}N** with NBS after 3 hours. (**b**) Mass spectrum from a 50:50 mixture of **3.2**:**3.2–^{15}N**. (**c**) Oxidation reaction of **3.2** with NBS in MeCN over the course of 6.5 hours monitored by GC–TCD.

The solid-state structure revealed loss of nitride with subsequent bromide capture, indicating a 3e⁻ reductive nitride coupling pathway, as seen in our previous example as well as other reports.[3, 16] Loss of the nitride, shown in these previous examples, typically indicates N_2 generation (a, **Figure 3.2**).[16, 25] N_2 formation was monitored by isotopically enriching **3.2** to **3.2–^{15}N** using $^{15}NH_3$ in the initial synthesis. The reaction (**3.2–^{15}N→3.3**) was monitored by sampling the gas in the headspace by GC–MS using a gas–tight syringe. The presence of 10% $^{15}N_2$ relative to atmospheric $^{14}N_2$ indicated a significant enough increase compared to natural abundance of $^{15}N_2$ (0.13% $^{15}N_2$ to $^{14}N_2$; a, **Figure 3.3**).[16, 25] Addition of NBS to a 1:1 mixture of **3.2**:**3.2–^{15}N** resulted in the formation of $^{15}N{\equiv}^{14}N$ and $^{15}N{\equiv}^{15}N$ in a 2:1 mixture (8.1 and 16 %) as expected for an intermolecular coupling reaction between two molecules of 50 % labeled **3.2–^{15}N** (b, **Figure 3.3**).

In addition to the qualitative isotopic labeling GC–MS experiments of **3.2**, we performed several larger scale oxidations of **3.2** using NBS, quantifying the resulting gas evolved via GC–TCD. The headspace of the reaction vessel was back filled with an inert gas, krypton (Kr), and was analyzed to quantify the N_2 produced from the nitride–coupling reaction. Three oxidation trials produced between 80–94% N_2 over the course of 6.5 hours (c, **Figure 3.3**). Due to the sampling method used in both GC–MS and GC–TCD analyses, we were unsuccessful in fully eliminating atmospheric N_2 from the background, similar to our previous report.[3, 16, 26] Atmospheric N_2 contamination is reflected in the GC–MS data shown above and was calibrated in the GC–TCD data. Reductive nitride coupling **3.2→3.3** with NBS represents the forward reaction in a potential catalytic cycle for NH_3 oxidation (top, **Scheme 3.2**). The reverse reaction, utilizing the same oxidant/base, required oxidizing **3.3** with NBS in the presence of NH_3 (**3.3→3.2**), which has been previously realized using Schiff base–derived

$Mn^{III}X$ (X = Cl, OAc) complexes.[10, 12] This was probed by treating **3.3** with NH_3 and NBS in CD_2Cl_2 and monitoring the reaction by ^1H NMR spectroscopy. Over the course of 5 minutes, the featureless spectrum displayed diamagnetic signals consistent with **3.2**. Oxidation of **3.3**→**3.2** in the presence of NH_3 represents the reverse reaction, generating a synthetic cycle (top, **Scheme 3.2**).

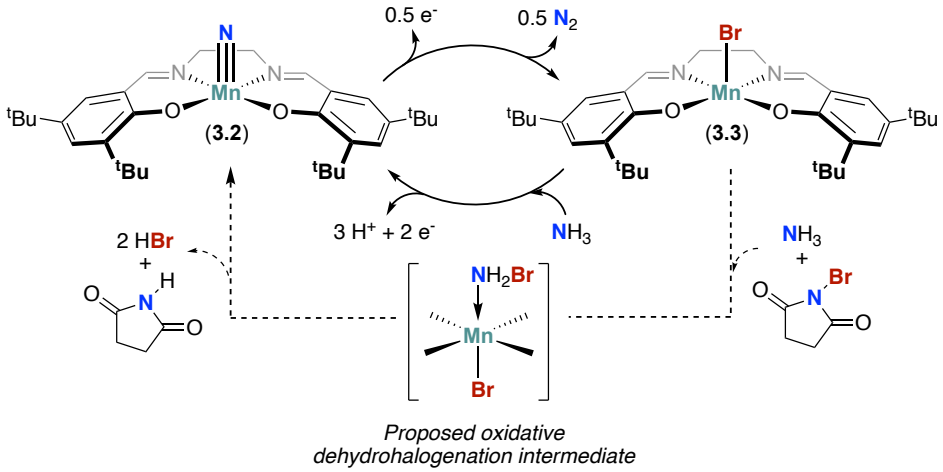

Scheme 3.2. Second synthetic cycle for NH_3 oxidation. NH_3 oxidation with NBS occurs through proposed oxidative dehydrohalogenation pathway with Mn^{III} (detailed with dashed arrows).

As the forward and reverse reactions have been realized, preliminary catalytic activity was tested by reacting a catalytic amount of **3.2** in the presence of 25.0 eq. $^{15}NH_3$ gas and 100.0 eq. of NBS in CCl_4, while monitoring $^{15}N_2$ formation by mass spectral analysis. NH_3 gas and NBS are suggested to form a proposed bromoamine (NH_2Br) intermediate[27-30] which may undergo an oxidative dehydrogenation pathway when reacted with $Mn^{III}X$ (X = Cl, OAc) to yield $Mn^{V}{\equiv}N$ (bottom, **Scheme 3.2**).[10, 12] Controlling the amount of NH_3 and NBS used was crucial because an excess of NH_3 promotes formation of NH_2Br while depleting the oxidant needed for the forward reaction. Additionally, excess NH_3 can promote decomposition of

NH_2Br to N_2 and NH_4Br – which has been demonstrated by reacting NH_3 and Br_2.[27] Consequently, NBS was used in a four–fold excess to circumvent unwanted side reactivity. Addition of an aqueous $^{15}NH_4OH$ solution (preliminary reactions were carried out with $^{15}NH_4OH$ as $^{15}NH_3$ gas was not readily available) to a frozen (–78°C; dry ice/acetone) solution of **3.2** (catalyst loading of 4%) and NBS in CCl_4 resulted in a red solution that was stirred under UV–light. After 10 minutes of stirring, a white solid began to form in the reaction vessel. After an hour, qualitative analysis of the headspace with a gas–tight syringe revealed significant formation of $^{15}N^{15}N$ (78.1% compared to atmospheric $^{14}N^{14}N$; where $^{14}N^{14}N$ was set to relative abundance of 100). Additionally, there was small formation of $^{14}N^{15}N$ (relative abundance of 4.5% compared to $^{14}N^{14}N$) (a, **Figure 3.4**). This was then compared to a control reaction that contained the same reaction conditions listed above, except in the absence of **3.2**. This revealed no formation of $^{15}N^{15}N$, but with the presence of the proposed bromamine intermediate ($^{15}NH_2Br$, m/z = 97.9; m/z is not shown in the following plot) (b, **Figure 3.4**). ^1H NMR spectroscopy analysis of the solid generated in the reaction revealed succinimide formed as a by–product.

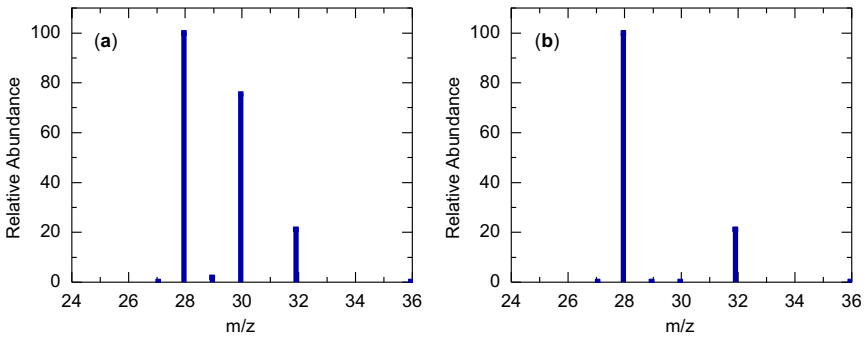

Figure 3.4. Preliminary catalytic NH_3 oxidation screenings using GC–MS. (**a**) Mass spectrum from the reaction of **3.2**, $^{15}NH_4OH$, and NBS in DCM after 1 hour. (**b**) Mass spectrum from the reaction of $^{15}NH_4OH$ and NBS in DCM after 1 hour.

Based on the significant amount of $^{15}N^{15}N$ and a small quantity of $^{14}N^{15}N$ and the control showing no formation of $^{15}N^{15}N$, this suggested catalytic NH_3 oxidation to N_2 might be at play. Next, GC–TCD was used to quantify the N_2 produced in the headspace of the reaction vessel (see experimental for details). After months of developing the GC–TCD experimental parameters, equipping the instrument with the correct column and methods, as well as appropriate data analysis for N_2 quantification, we were able to collect the necessary calibration curves, control tests, and preliminary catalytic data. For N_2, or any type of gas assuming ideal gas behavior, in order to accurately calculate the amount of gas within the headspace of the reaction vessel, it is important to mimic atmospheric pressure as to not skew the calculations (PV = nRT). We found the most consistent results led to utilizing a large headspace with smaller quantities of N_2 being produced.

First, we equipped the GC–TCD with the appropriate column (Carboxen–1010 PLOT). At the time, this column was suggested by multiple sources, to separate N_2 and O_2, which can be difficult for most columns because the retention time is very similar. In running these experiments, contamination from air was inevitable due to puncturing of the septa with a needle. Theoretically, we could have equipped the GC–TCD with a sample loop and 6–port valve to eliminate air, and would have been the best option, but at the time of this chemistry, it was not advised by those we were sharing the instrument with. Once we devised an accurate sampling method and experimental setup – where Kr was used as the inert gas (see experimental) – we generated a calibration curve for known amounts of N_2 sampled between 5–25 μL determining the amount (in mmol) of N_2 in each sample (**Figure 3.9**, section 3.4.5.1). Additionally, it is important to note that all solvents used in the following reactions were

degassed with Kr before use due to the solvent containing N_2, which was shown to widely skew initial results.

We turned back to our overall goal in developing a catalytic system for NH_3 oxidation. Using a reaction flask with an increased headspace (68 mL), we replaced back filling the flask with Kr gas to NH_3 gas because this was the most direct way to incorporate NH_3 gas into the reaction vessel without drastically changing the pressure. We first ran control experiments with NH_3 gas and NBS. As detailed above, qualitative GC–MS experiments were initially carried out with $^{15}NH_4OH$ and NBS to determine if there was reactivity. In the experiment with $^{15}NH_4OH$ (4:1 ratio of NBS:NH_3) and excess of NBS, we found there was no formation of $^{15}N_2$, but there was formation of the proposed $^{15}NH_2Br$ intermediate (**Figure 3.4**).

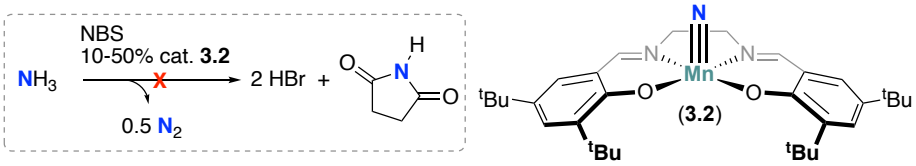

Scheme 3.3. Catalytic reaction conditions with **3.2**.

As for the control experiments, much later developed for the GC–TCD, with NH_3 gas and NBS (1:3 ratio of NBS:NH_3), we found there was a large amount of N_2 produced in these control experiments with formation of a white solid in solution, which we found by ^1H NMR spectroscopy to be succinimide. Each trial had an excess of NH_3 gas within the reaction vessel, and based on 0.8 mmol of NBS added, 0.26–0.29 mmol of N_2 were produced (200% yield of N_2 assuming a 6:2 ratio of NBS:NH_3 to generate 1.0 equivalent of N_2). This was a drastic difference between our initial GC–MS experiments and later GC–TCD results. Additionally, we ran the same control experiments but instead with 0.4 mmol of NBS. We found that half the amount of N_2 was being produced (0.12–0.15 mmol) in the headspace, showing a general

trend in N_2 formation (**Table 3.1**). We rationalized tracking N_2 formation during control reactions, we could further compare the values to the catalytic system and determine if our proposed system was catalytic.

Table 3.1. Results for controls and catalytic reactions for GC–TCD.

Control: NBS + NH_3		**Control: NBS + NH_3**		**Catalysis: 10–50% of 2.1**	
NBS	Calc. N_2 (area)	NBS	Calc. N_2 (area)	NBS	Calc. N_2 (area)
0.8 mmol	0.26–0.27 mmol	0.4 mmol	0.13–0.14 mmol	0.8 mmol	0.27–0.30 mmol
0.8 mmol	0.25–0.27 mmol	0.4 mmol	0.12–0.14 mmol	0.8 mmol	0.29–0.29 mmol
0.8 mmol	0.27–0.29 mmol	0.4 mmol	0.14–0.15 mmol	0.8 mmol	0.25–0.29 mmol

Unfortunately, we found after many trials that reaction of **3.2** (10–50% loading) with NBS and 1 atm of NH_3 in 68 mL headspace, generated the same amount of N_2 in all trials, and was the same quantities observed in the control reactions without **3.2**, indicating there was most likely no catalytic system at play (**Scheme 3.3**; **Table 3.1**). At the time of these experiments, this was the most logical route, but upon a current analysis of this data, there were fundamental issues at the time that were not realized and need to be currently addressed.

In the preliminary qualitative GC–MS experiments, NH_4OH solution was used while anhydrous NH_3 gas was used in the GC–TCD experiments. It has been reported that Br_2 in the presence of excess NH_3 gas can undergo decomposition to N_2 and NH_4Br in organic solvent through a proposed NH_2Br intermediate (bottom, **Scheme 3.2**; **Equation 3.1**).[27-30]

(**1**) $Br_2 + 2\,NH_3 \longrightarrow NH_2Br + NH_4Br$ *NH_3 & Br_2 Reactivity*

(**2**) $NH_2Br + 2\,NH_3 \longrightarrow 3\,NH_4Br + N_2$ *NH_2Br Decomposition with NH_3*

Equation 3.1.

In the initial GC–MS experiments, care was taken to not utilize excess NBS in the presence of NH_3, which is the most likely the reason for lack of decomposition to N_2. At the time of this chemistry, this was known and understood, but based on the experimental setup we had developed by back filling the reaction vessel, we were using a large excess of NH_3 gas in the headspace. Alternatively, we should have utilized a known solution of NH_3 in MeCN (which could be titrated to determine the concentrations for more accurate additions) or added NH_4Br as our NH_3 source – similar to our preliminary results with $^{15}NH_4OH$. We knew from these NBS reactions with NH_3 gas led to N_2, succinimide, and the proposed NH_2Br intermediate, seen by GC–MS (where succinimide was isolated as a white solid). We were curious if Br_2 would give similar results as NBS. We found addition of 0.4 mmol of Br_2 to a flask back filled with 1 atm of NH_3 gas led to formation of a white solid, which was confirmed to be NH_4Br by ^1H NMR spectroscopy. The headspace was sampled and showed formation of N_2 (0.22 mmol), similar to the NBS reactions. We suggest once NH_4Br was formed, this was an end point in the decomposition to N_2.

We tested this by taking a solution of NH_4Br and reacting it with Br_2. The GC–TCD showed there was no additional N_2 formed. In addition to the suggestions listed above, one potential way to further test catalysis is utilizing an NH_4^+ salt or solution, similar to what we had observed in the preliminary catalytic GC–MS experiments (with NH_4OH). This is a common technique used in catalytic NH_3 oxidation, and would be easier to deploy than utilizing NH_3 gas.[5] Additionally, in our preliminary catalytic work, we added an excess of NBS (4:1 ratio). For further studies, it would be beneficial to return to this stoichiometry to keep the oxidant concentration greater than NH_3.

3.2.2 Probing NH_3 oxidation – oxidative dehydrohalogenation and H–atom abstraction

At the time of this work, while we were trying to develop an ideal system for catalytic NH_3 oxidation, we shifted our attention in order to better understand the mechanism for this chemistry. We have previously shown that nitride coupling to N_2 is a potential step for catalytic NH_3 oxidation. This step is heavily dependent on nitride formation, which is most commonly synthesized by reactions with NaOCl or NBS.[10, 31] Although these procedures are widely used, there are no well–established mechanisms for either of these reactions. Gaining a mechanistic understanding of this oxidation, including whether $1e^-$ or $2e^-$ pathways dominate, may reveal the energetically demanding steps to these conversions, thus providing a pathway for optimization and long–term catalytic NH_3 oxidation. Our primary focus was oxidation with various halogen–based oxidants such as NBS, Br_2, NCS (*N*–chlorosuccinimide), and Cl_2. It has been proposed that nitride synthesis with NBS proceeds by an oxidative dehydrogenation mechanism through a coordinated Mn^{III}–NH_2X intermediate.[10, 27] Although plausible, there has been no further support for this type of reactivity. Alternatively, NBS could be a source of halogen radical (Br•), acting as a H–atom abstraction reagent (HAA) with NH_3. We investigated both of these pathways by synthesizing a series of (un)substituted (salen)$Mn^{III/II}$ complexes by modified literature preps; [(salen–(3,5–^{t}Bu)$_2$)Mn^{II}][32] (**3.4**), [(salen–(3,5–^{t}Bu)$_2$)Mn^{III}(THF)$_2$][PF_6] (**3.5**), and [(salen–(3–^{t}Bu,5–OMe)$_2$)Mn^{III}(THF)$_2$][PF_6] (**3.6**) (this was achieved by synthesizing the corresponding salicylaldehyde), and [(salen)Mn^{III}(THF)$_2$][PF_6] (**3.7**).[33] Probing both pathways can help in establishing a mechanism and provide greater insight into the requirements needed for efficient catalysis.

3.2.2.1 Probing oxidative dehydrohalogenation pathways

While bromamine exists in a pH–controlled equilibrium mixture of NH_3 and HNX_2 (X = halogen), the related chloro derivatives decompose violently if not cooled.[28] In contrast, *N*–bromo–alkylamines are known and can be readily prepared – particularly with large alkyl groups – by treating primary amines with Br_2 under basic conditions to capture the formed HBr. Complexes **3.3**–**3.6** were utilized to probe the oxidative dehydrohalogenation pathway (**Scheme 3.4**) by investigating the coordination behavior of *N*–bromo–tert–butylamine (^{t}BuNHBr)[34-35] and *N*–bromo–bromotritylamine ((Ph_3C)NHBr)[36], in hopes of isolating (salen)Mn=N–R intermediates (**Scheme 3.4**). Due to the brominating ability of ^{t}BuNHBr, we avoided using unsubstituted (salen)Mn complexes – trying to avoid similar reactivity as seen in section 3.2.1 where bromination occurs on the periphery of the aromatic rings. Reactivity of complexes **3.3** and **3.4** with independently synthesized and isolated, ^{t}BuNHBr and (Ph_3C)NHBr, led to formation (**3.4→3.3**) or regeneration of the starting material. There was no generation of diamagnetic signals corresponding to a Mn^V product in the ^{1}H NMR spectrum (for a $2e^-$ oxidation of Mn^{III} to Mn^V). These reactions were also tracked by UV–Vis spectroscopy, where there were negligible changes in all spectra. We also attempted to heat these reactions between 80–90 ºC, but were unsuccessful in isolating any products other than **3.3** and unidentifiable signals in the ^{1}H NMR spectrum which were most likely decomposition of the bromamines.

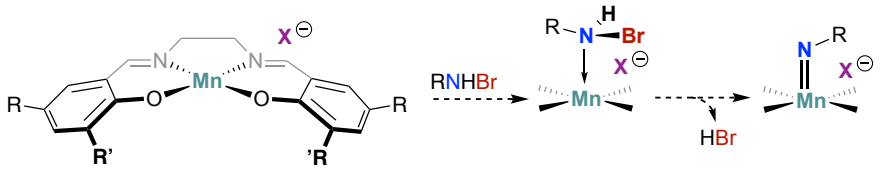

(**3.3**; **X**=Br), (**3.4**; Mn^{II}), (**3.5**; **X**=PF_6); R/R'=^{t}Bu)
(**3.6**; **X**=PF_6; R=^{t}Bu, R'=OMe)

Scheme 3.4. Probing proposed oxidative dehydrohalogenation pathways with RNHBr (where R = ^{t}Bu and (Ph_3C)). The Mn–center is shown without ligands for clarity.

Lastly, we attempted *in situ* recrystallizations by dissolving known amounts of **3.3** and adding the following bromamines with the desired recrystallization solvents (FB/pentane and DCM/pentane; coordinating solvents were avoided because we previously found Et_2O and THF strongly coordinate to the Mn^{III}–center). The *in situ* recrystallizations led to a large quantity of white solid submerged in a red–brown supernatant. White solid was isolated from the ^{t}BuNHBr reactions and was determined to be a pronated salt form, ^{t}BuNH$_3$Br. Reactivity with independently synthesized substituted bromamine compounds were proving to be unsuccessful. Next, we sought to react the following Mn^{II}/Mn^{III} complexes with in–situ generated bromamines by NBS and substituted amines (**Scheme 3.4**). We found reacting **3.3** with ^{t}BuNH$_2$ and (Ph_3C)NH$_2$ and excess NBS (5 equiv.) led to isolation of red–brown and white crystals in both reactions. The red–brown crystals were confirmed to be unreacted **3.3**, and the white crystals were ^{t}BuNH$_3$Br and (Ph_3C)NH$_3$Br respectively – similarly to what we found in the above *in situ* recrystallizations. Based on the formation of these products in high yield, we were unable to determine how protonation occurred to form the following salts and why there was no interaction at the Mn^{III}–center. Trying to generate the following bromamines *in situ* was also not yielding results that could be rationalized. Due to isolation of **3.3** after various attempts of reactivity, we rationalized an outer–sphere counterion such as $[PF_6]^-$ (**3.5** and **3.6**) may provide an open coordination site to promote reactivity with (un)substituted amine or bromamine species. Utilizing similar reaction conditions as listed above with independently synthesized bromamines, generating bromamines *in situ* by reacting amines with NBS, and *in situ* recrystallizations with bromamines, we found there was no

distinguishable reactivity or isolation of desired products by ^{1}H NMR spectroscopy, UV–Vis, or XRD analysis. Based on these reactions yielding no tangible results, we proceeded further by probing the alternative HAA pathway.

3.2.2.2 Probing HAA pathways

We next attempted to probe HAA reactivity required reacting Mn^{III} with alkyl or arylamines (RNH_2; where R = (Ph_3C), ^{i}Pr, or ^{t}Bu; **Scheme 3.5**), and a HAA reagent (X•, where X = $^{t}Bu_3ArO$[4, 9]), in hopes of isolating the following amide or imide intermediates.

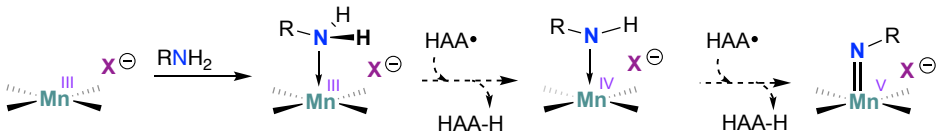

Scheme 3.5. Proposed HAA abstraction pathways with Mn^{III}. The ligand has been omitted for clarity.

We turned to our previously synthesized substituted salen complexes, **3.5** and **3.6**, and unsubstituted **3.7** (rational for use of this complex will be detailed below). First, we attempted generating the following alkyl and arylamines by *in situ* vapor diffusion recrystallizations. Known amounts of **3.5** were taken and setup as vapor diffusion recrystallizations with FB/pentane or DCM/pentane with the following amines; $(Ph_3C)NH_2$, $^{i}PrNH_2$, and $^{t}BuNH_2$. Amine–ligated structures were isolated from $^{i}PrNH_2$ as [(salen–(3,5–$^{t}Bu)_2$)Mn^{III}($^{i}PrNH_2$)$_2$][PF_6] (**3.8**) (a, **Figure 3.5**) and $^{t}BuNH_2$ as [(salen–(3,5–$^{t}Bu)_2$)$_2$$Mn^{III}$($^{t}BuNH_2$)$_2$][$PF_6$] (**3.9**) (b, **Figure 3.5**). **3.9** contained a lot of disorder and was difficult to refine all non–H atoms anisotropically. Refinement was performed to the extent

required for this thesis. Alternatively, a bridging fluoride structure was obtained from $(Ph_3C)NH_2$ as $[(salen–(3,5–^tBu)Mn^{III})_2(\mu–F)][PF_6]$ (**3.10**) (c, **Figure 3.5**).

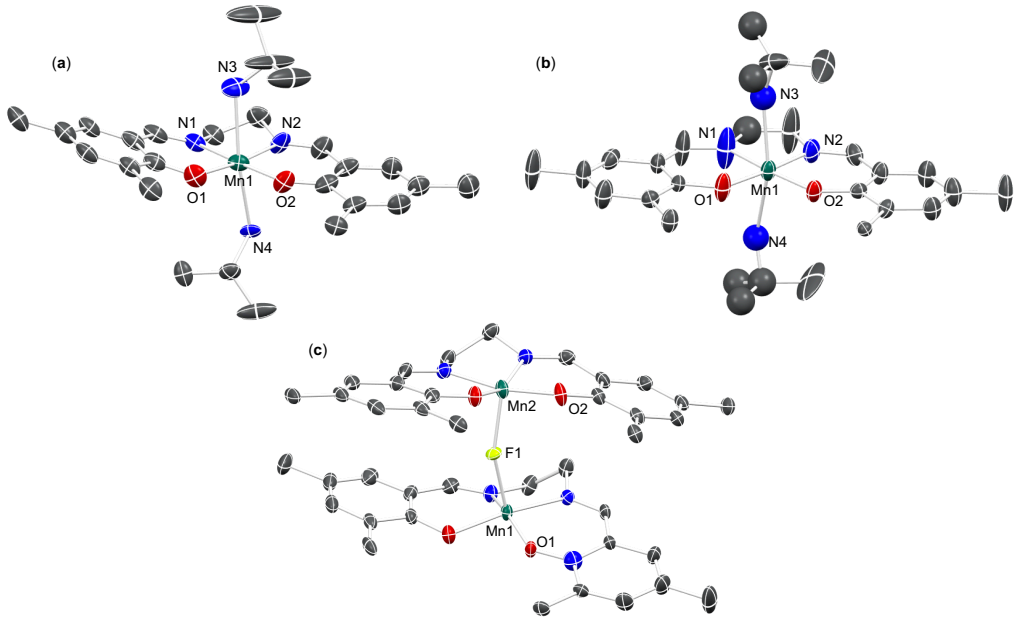

Figure 3.5. Solid–state molecular structures of (**a**) $[(salen–(3,5–^tBu)_2)Mn^{III}(^iPrNH_2)_2][PF_6]$ (**3.8**), (**b**) $[(salen–(3,5–^tBu)_2)_2Mn^{III}(^tBuNH_2)_2][PF_6]$ (**3.9**), and (**c**) $[(salen–(3,5–^tBu)Mn^{III})_2(\mu–F)][PF_6]$ (**3.10**). PF_6^- counter ions, ^{t}Bu substituents, and hydrogen atoms were omitted for clarity.

Complexes **3.8** and **3.9** were isolated and used for further HAA reactions. 5.0 equivalents of $^tBu_3ArO•$ (BDFE of $^tBu_3ArOH$ = 76.7 kcal/mol in benzene)[1] was added to independent solutions of **3.8** and **3.9** in FB, resulting in a color changes from red–brown to green in color (top, **Scheme 3.6**). Initially, these were promising in that formation of a Mn^V complex would be indicated by a green color. Yet, analysis of the ^{1}H NMR spectra during and after the reactions indicated no formation of diamagnetic signals for a Mn^V species or $^tBu_3ArOH$, and no free $^iPrNH_2$. We proposed the drastic color change could be occurring by $^tBu_3ArO•$ interacting with the Mn^{III}–center. We tested this by reacting a solution of **3.5** with $^tBu_3ArO•$ in

FB, as predicted, a color change to green was observed. Isolation of red–brown crystals in high yield, analyzed by XRD indicated formation of the bridging fluoride species **3.10**. We had been able to isolate the bridging Mn^{III}–F–Mn^{III} species in various reactions while using FB as the solvent. Unfortunately, we have been unable to determine the mechanism in forming this product and did not further investigate as we deemed it an undesirable by–product of these reactions. It is important to note that although structures of these complexes (**3.8** and **3.9**) were obtained, the yields for were relatively low and isolation of large amounts of material for reactivity studies provided to be demanding. Due to this, we turned to utilizing salen ligands that could yield higher crops of material.

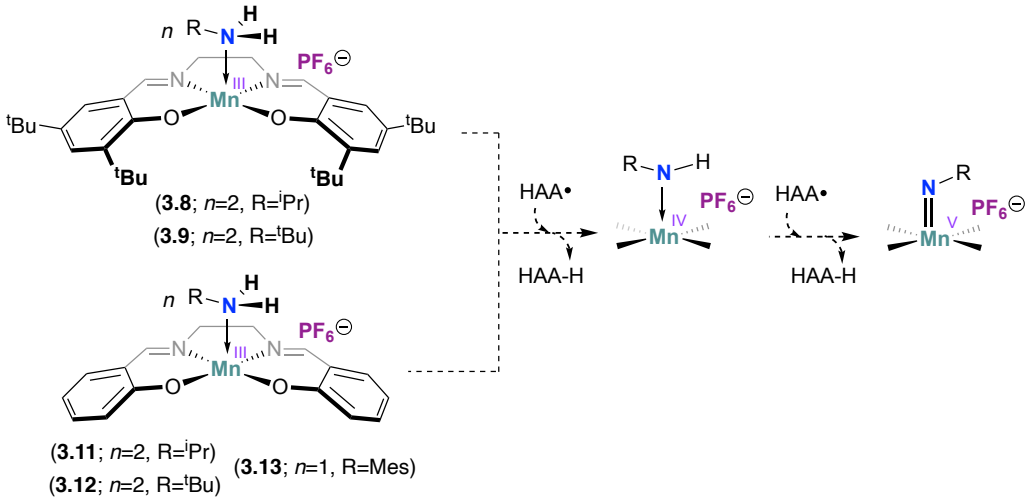

Scheme 3.6. Proposed HAA pathways (where HAA• = $^{t}Bu_3ArO$•). The following proposed Mn^{IV}– and Mn^{V}–centers are shown without the ligand for clarity.

3.6 was originally synthesized to improve the solubility and recrystallization ability by addition of –OMe groups on the periphery, but we found synthesis of the amine–ligated complexes did not yield the desired structures. Instead, we turned our attention to our original unsubstituted salen ligand ($salenH_2$) in order to improve the recrystallization of the products by eliminating the –tBu groups (which had been further complicating isolation of material).

We were able to synthesis [(salen)$Mn^{III}(THF)_2$][PF_6] (**3.7**) by salt metathesis and react it with the following amines; $^{i}PrNH_2$, $^{t}BuNH_2$, and $MesNH_2$ ($(Ph_3C)NH_2$ was avoided due to the observed formation of **3.10** in FB), by bulk *in situ* recrystallizations from DCM solutions, yielding products [(salen)$Mn^{III}(^{i}PrNH_2)_2$][PF_6] (**3.11**), [(salen)$Mn^{III}(^{t}BuNH_2)_2$][PF_6] (**3.12**), and [(salen)$Mn^{III}(MesNH_2)$][PF_6] (**3.13**) (**Figure 3.6**).

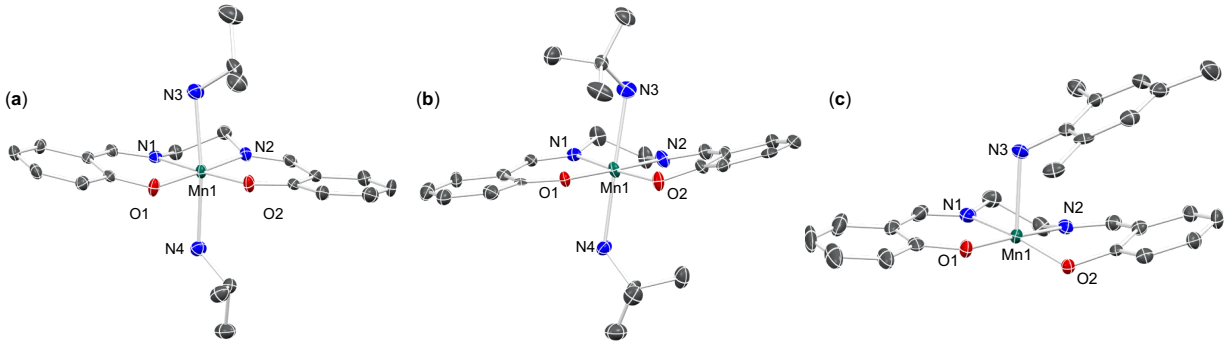

Figure 3.6. Solid–state molecular structures for amine–ligated complexes; (**a**) [(salen)$Mn^{III}(^{i}PrNH_2)_2$][PF_6] (**3.11**), (**b**) [(salen)$Mn^{III}(^{t}BuNH_2)_2$][PF_6] (**3.12**), and (**c**) [(salen)$Mn^{III}(MesNH_2)$][PF_6] (**3.13**). PF_6^- counter ions, solvent molecules, and hydrogen atoms were omitted for clarity.

Although the following were more attainable by recrystallization, all complexes proved to be insoluble in most solvents that were compatible in performing the proposed HAA reactions with $^{t}Bu_3ArO\bullet$ (bottom, **Scheme 3.6**). The solvents were used to increase solubility and probe reactivity were MeCN and THF, but displacement by the coordinating solvent of the amines occurs and is seen by ^1H NMR spectroscopy. Reactions of **3.11** and **3.12** with $^{t}Bu_3ArO\bullet$ dissolved in THF resulted in negligible changes as seen by ^1H NMR spectroscopy. Alternatively, the reaction of **3.13** in THF with $^{t}Bu_3ArO\bullet$ exhibited a color change to a brown–green solution. Analysis by ^1H NMR spectrum indicates formation of $^{t}Bu_3ArOH$ with no additional diamagnetic signals from an expected Mn^{V} species. Unfortunately, analysis of a

mixture of $MesNH_2$ and $^tBu_3ArO\bullet$ in THF results in a similar color change with concurrent formation of $^tBu_3ArOH$ indicated by ^1H NMR spectroscopy, indicating there is most likely no reactivity at the Mn^{III}–center. Lastly, we also tried to coordinate NH_3 gas to the following complexes by performing in situ vapor diffusion recrystallizations in Schlenk flasks back filled with NH_3 gas. Unfortunately, none of these reactions led to complexes with coordinated NH_3, instead we were only successful in isolating fluoride or chloride bridged species, similar to our results seen for **3.10**.

3.3 Scope of chapter and further directions

In an attempt to garner further mechanistic information, we explored Mn^{III} complexes with more–stable ligand frameworks (phthalocyanine (Pc) or corrole) (**Scheme 3.7**).

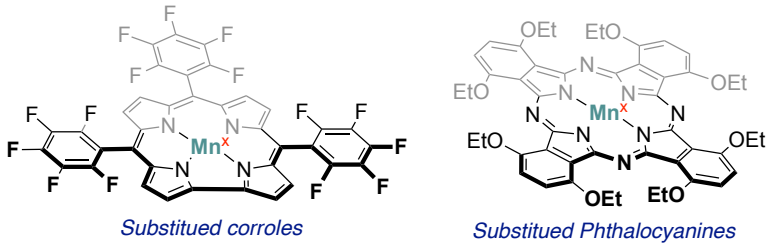

Scheme 3.7. Corroles and phthalocyanines for investigating further mechanistic chemistry.

The reasoning behind these included: (1) Pc ligands offer added stability to higher oxidation states due to enhanced redox participation of the ligand, whereas salen ligands result in primarily metal–based redox events and higher activity, and; (2) corroles have been extensively used in synthesizing terminal Mn^V=N–R complexes by azide photolysis of N_3–R (R = $MesNH_2$) due to the increased stability of the macrocycle.[37-39] We thought in continuing to investigate these mechanistic reactions, the most logical step was too increase the stability of the ligand because the salen ligands may have been too reactive, as it has been previously shown that (salen)Mn=N–R complexes tend to be reactive intermediates and have only been

proposed and not isolated.[20] Building off this proposed stability with Pc's or corroles, another direction to study the mechanistic chemistry could have included probing reactive oxo–species and the potential role in NH_3 oxidation. Some of the earliest terminal metal nitride complexes were derived using porphyrin and similar tetrapyrrole ligands.[40-42] It was discovered that porphyrin nitrides could be synthesized by replacing alkanes in alkane hydroxylation reactions with NH_3.[43-44] In these reactions, an O–atom donor (OAD) iodosobenzene (PhIO) was used and the proposed hydroxylating agent is an porphyrin–Mn–oxo intermediate which can also be generated with NaOCl,[45] similar to how Mn≡N complexes are synthesized.[10] Terminal porphyrin–Mn–oxo complexes are typically short–lived and only observed spectroscopically; however, there has been one example showing stabilization in basic conditions by introducing EWGs to the porphyrin system.[46]

PcMn complexes have been shown to react with O_2 where only bridging PcMn–O–MnPc complexes have been obtained with no terminal PcMn=O species identified.[47-48] Terminal oxo complexes could play an important role in the oxidation of NH_3 and using PcMn or (corrole)Mn complexes is the most logical route in investigating these. We had begun synthesis and isolation of these Mn^{III} complexes to start probing reactivity, but after much discussion and where the direction of the *o*–carborane project was heading (described in Chapters 4–5), we decided it was wise to take time away from this project. For the remainder of my PhD, I did not come back to this work due to the wide success with *o*-carboranes. But this project still possesses interesting questions and ultimately provides a synthetically challenging project.

3.4 Conclusions

In conclusion, after multiple attempts to ascertain the conditions required for catalysis as well as probing the mechanism for NH_3 oxidation, in this chapter, we have shown this was widely unsuccessful. This chemistry is most likely much more complicated than predicted and at the time and we made a decision to step away from this project and switched my focus to *o*–carboranes.

3.4 Experimental Section

3.4.1 General considerations

All manipulations were performed under an atmosphere of dry, oxygen–free N_2 or Ar by means of standard Schlenk or glovebox techniques (MBraun glovebox equipped with a –38 °C freezer). Kr gas (99.999% purity) was used for all GC–TCD experiments and was purchased through Praxair in a 300 L gas cylinder (size D4). Kr was used in its own Schlenk line equipped with minimal tubing to limit the amount of gas used in all experiments due to the extraneous price ($397.50 USD). NH_3 gas (Sigma Aldrich) was supplied by use of a lecture bottle (independent regulator) for all reactions and was equipped with a separate line (minimal tubing and separate glass bubbler) attached to the same Schlenk line equipped with Kr as the primary gas (**Figure 3.10**). All solvents were dried on an MBraun solvent purification system. Acetonitrile ($–H_3$ and $–D_3$) was purchased from Aldrich and dried over CaH_2 for several days prior to distillation. All solvents were stored on activated 4 Å molecular sieves prior to use. $^{i}PrNH_2$, $^{t}BuNH_2$, and $MesNH_2$ were distilled before use and stored at –38 °C. $^{t}BuNHBr$,[35] $^{t}Bu_3ArO\bullet$,[49] [(salen–(3,5–$^{t}Bu)_2$)Mn^{II}][32] (**3.4**) were prepared by literature procedures. Salen–(3,5–$^{t}Bu)_2$[31] and Salen–(3–^{t}Bu,5–OMe)$_2$ was prepared by a modified literature procedure with the appropriate salicylaldehyde; where 3,5–tert–butylsalicylaldehyde was purchased from

Fischer and 3–tert–butyl–5–methoxysalicylaldehyde was synthesized by a literature procedure.[33] [(salen–(3,5–^{t}Bu)$_2$)Mn^{III}(THF)$_2$][PF$_6$] (**3.5**), [(salen–(3–^{t}Bu,5–OMe)$_2$)Mn^{III}(THF)$_2$][PF$_6$] (**3.6**), and [(salen)Mn^{III}(THF)$_2$][PF$_6$] (**3.7**) were synthesized by a modified literature prep by adding KPF_6 instead of NaCl during the salt metathesis and using Et_2OH/toluene as the solvent.[33]

UV–Vis spectroscopy was performed using a Perkin Elmer Spectrum 100, FT–IR spectrometer, with an attached Universal ATR sampling accessory. Measurements were done with IR Silica cuvettes equipped with an air–tight J–Young adaptor.

Elemental analyses (C, N, H) were recorded at the University of California, Berkeley using a Perkin Elmer 2400 Series II combustion analyzer.

Cyclic Voltammetry was performed on a CH Instruments Electrochemical Analysis potentiometer, equipped with a glassy carbon working electrode, an Ag wire pseudo–reference electrode, and a Pt counter electrode with [^{n}Bu4N][PF$_6$] (0.1 M) solution in CH_2Cl_2. Ferrocene was used as an internal standard.

EPR spectroscopy: Perpendicular–mode X–band EPR spectra were collected on a Bruker EMX EPR Spectrometer equipped with an Oxford ESR 900 liquid helium cryostat. A modulation frequency of 100 kHz was used for EPR spectra.

Mass spectrometry was performed on a Shimadzu model QP2010 GC–MS equipped with a secondary electron multiplier TIC detector. The constituent gases were separated by passing through an Agilent DB–1 column using helium as the carrier gas.

GC–TCD was performed on a An Agilent 6890N (G1530N) gas chromatograph equipped with a Supelco Carboxen–1010 PLOT column (30.0m x 530 μm) and a thermal conductivity detector. The inlet temperature was 200°C with a splitless injection and helium carrier gas at a

total flow rate of 148 mL/min and pressure of 1.691 bar. The column temperature was held at 32°C for 16 min and then ramped to 240 °C at 60 °C/min, where it was held for 6 min under a flow rate of 2.5 mL/min. Due to the sensitivity of N_2 quantification in all reactions, all solvents were freeze pumped thawed and degassed prior to use with Kr gas. Unless specified, all vessels were degassed and back filled with either Kr or NH_3 gas, removing all N_2 contamination. All chromatograms were analyzed and plotted in Origin software. Curve fitting was performed by a Bigaussian function for the two "over–lapping" peak areas of O_2/N_2 (**Figure 3.8**). Percentages based on the total area were obtained from the software and used to calculate the true areas of O_2/N_2 generated from the chromatogram. Once a known value for O_2 was obtained, N_2 from contamination of air could be calculated and subtracted from the total N_2 peak area, determining the N_2 from the sample.

X–ray crystallography data was collected on a Bruker KAPPA APEX II diffractometer equipped with an APEX II CCD detector using a TRIUMPH monochromator with a Mo Kα X–ray source (α = 0.71073 Å). The crystals were mounted on a cryoloop under Paratone–N oil, and all data were collected at 100(2) K using an Oxford nitrogen gas cryostream system. A hemisphere of data was collected using ω scans with 0.5° frame widths. Data collection and cell parameter determination were conducted using the SMART program. Integration of the data frames and final cell parameter refinement were performed using SAINT software. Absorption correction of the data was carried out using SADABS. Structure determination was done using direct or Patterson methods and difference Fourier techniques. All hydrogen atom positions were idealized and rode on the atom of attachment. Structure solution, refinement, graphics, and creation of publication materials were performed using SHELXTL.

Evan's Method measurements were carried out in a NMR tube that was charged with known weights of both the magnetic sample and deuterated solvent of choice, along with a few drops of fluorobenzene. A small capillary tube was filled with a 1:1 mixture of deuterated solvent: fluorobenzene, sealed, and placed into the NMR tube. A ^{19}F–NMR spectrum was obtained showing two distinct signals. The $S = 2$ state was calculated considering the χdia contribution based on Pascal's data.[50]

3.4.2 Synthesis of compounds

Synthesis of [(salen–(3,5–^{t}Bu)$_2$)Mn≡N] (3.2): This compound was synthesized following a modified procedure.[31] Salen–(3,5–^{t}Bu)$_2$ (49.27 mg, 1 mmol) was suspended in 13 mL of MeOH and the mixture was heated to 60 °C. To the yellow suspension was added Mn(OAc)$_2$•4H$_2$O (25.73 mg, 1.05 mmol, 1.05 eq.) in one portion. The resulting dark brown solution was refluxed for 1.5 hours. Heat was removed and the reaction mixture was brought to r.t. before adding concentrated NH$_4$OH (15 M, 15.0 eq., 15 mmol) dropwise over the course of a few minutes. To the stirring solution, Clorox bleach (0.7 M, 6 eq., 6 mmol, 8.5 mL) was added dropwise over a 5 minute period in which a white gas is observed. After the addition of bleach, 10 mL of DCM was cautiously added, resulting in a biphasic mixture. The solution was then transferred to a seperatory funnel where the organic layer was washed with H$_2$O (3 x 20 mL) and brine (2 x 10 mL). The brown–green organic layer was separated and dried via vacou yielding a crude dark brown–green solid. This solid was dissolved in a minimal amount of DCM and was purified via column chromatography using Brockmann activity IV basic Al$_2$O$_3$ and DCM as the eluent. A dark green band was collected, leaving a large dark brown band on the top of the column. The dark green solution was concentrated under reduced pressure and a bright green solid was collected. Multiple attempts were taken in growing an isolating crystals

suitable for XRD analysis, but were unsuccessful. *Anal. Calcd*. for $C_{32}H_{46}MnN_3O_2$: C, 68.67; H, 8.28; N, 7.51. Found: C, 68.43; H, 8.32; N, 7.77. **^{1}H NMR** (400 MHz, C_6D_6): δ 7.76 (d, 2H); 7.04 (s, 2H); 6.86 (d, 2H); 2.54 (s, 4H); 1.83 (s, 18H); 1.40 (s, 18H). **MS (ESI):** m/z 559.3 $[M]^+$.

Synthesis of [(salen–(3,5–^{t}Bu)$_2$)Mn≡^{15}N] (3.2–^{15}N): This compound was synthesized in an analogous fashion to **3**. Salen–(3,5–^{t}Bu)$_2$ (49.27 mg, 1 mmol) was suspended in 13 mL of MeOH and the mixture was heated to 60 °C. To the yellow suspension was added $Mn(OAc)_2$•$4H_2O$ (25.73 mg, 1.05 mmol, 1.05 eq.) in one portion. The resulting dark brown solution was refluxed for 1.5 hours. Heat was removed and the reaction mixture was brought to r.t. before adding $^{15}NH_4Cl$ (260.0 mg, 5.0 eq., 5 mmol) in one portion. Then, NaOH solution (15 M, 15.0 eq., 15.0 mmol) was added dropwise over the course of a few minutes. To the stirring solution, Clorox bleach (0.7 M, 6 eq., 6 mmol, 8.5 mL) was added dropwise over a 5 minute period in which a white gas is observed. After the addition of bleach, 10 mL of DCM was cautiously added, resulting in a biphasic mixture. The solution was then transferred to a seperatory funnel where the organic layer was washed with H_2O (3 x 20 mL) and brine (2 x 10 mL). The brown–green organic layer was separated and dried via vacou yielding a crude dark brown–green solid. This solid was dissolved in a minimal amount of DCM and was purified via column chromatography using Brockmann activity IV basic Al_2O_3 and DCM as the eluent. A dark green band was collected, leaving a large dark brown band on the top of the column. The dark green solution was concentrated under reduced pressure and a bright green solid was collected. **^{1}H NMR** (400 MHz, C_6D_6): δ 7.76 (d, 2H); 7.04 (s, 2H); 6.86 (d, 2H); 2.54 (s, 4H); 1.83 (s, 18H); 1.40 (s, 18H). **MS (ESI):** m/z 560.3 $[M]^+$.

Synthesis of [(salen–(3,5–^{t}Bu)$_2$)MnBr] (3.3): This compound was synthesized via a modified literature procedure.[33] A 100 mL, schlenk flask equipped with a stirbar and a reflux condenser, was charged with Mn(OAc)•4H$_2$O (490.2 mg, 2 mmol, 3.0 equiv.) and ethanol (6 mL). The stirred solution was heated to reflux (85 °C) and a solution of Salen–(3,5–^{t}Bu)$_2$ (330.1 mg, 0.67 mmol, 1.0 equiv) in toluene (10 mL) was added dropwise and the mixture was stirred at reflux for 2 hrs. The reflux condenser was replaced with a line of air, which was bubbled through the solution for 30 mins. Heating and air addition were discontinued and a solution of KBr (saturated) in water (5 mL) was added. The mixture was cooled to room temperature and extracted with toluene (30 mL). The brown organic layer was washed with water (3 x 10 mL) and brine (10 mL) and then dried over Na_2SO_4. Solvent removal in vacuo yielded a brown solid which was isolated as the desired product **3.3** (75% yield). Crystals suitable for XRD analysis were grown by vapor diffusion of THF/pentane. *Anal. Calcd*. for $C_{32}H_{46}BrMnN_2O_2$: C, 61.44; H, 7.41; N, 4.48. Found: C, 62.01; H, 7.56; N, 4.55. **MS (ESI):** m/z 545.3 $[M–Br]^+$, 586.3 $[M–Br+CH_3CN]^+$. **Evan's method:** *S = 2* (**Table 3.2**).

Synthesis of [(salen–(3,5–^{t}Bu)$_2$)Mn^{III}(THF)$_2$][PF$_6$] (3.5): This compound was synthesized via a modified literature procedure.[33] A 50 mL, schlenk flask equipped with a stirbar and a reflux condenser, was charged with Mn(OAc)•4H$_2$O (490.2 mg, 2 mmol, 3.0 equiv.) and ethanol (6 mL). The stirred solution was heated to reflux (85 °C) and a solution of Salen–(3,5–^{t}Bu)$_2$ (330.1 mg, 0.67 mmol, 1.0 equiv) in toluene (10 mL) was added dropwise and the mixture was stirred at reflux for 2 hrs. The reflux condenser was replaced with a line of air, which was bubbled through the solution for 30 mins. Heating and air addition were discontinued and KPF_6 (245.6 mg, 1.34 mmol, 2.0 equiv.) in water (5 mL) was added. The mixture was cooled to room temperature and extracted with toluene (30 mL). The brown organic layer was washed with

water (3 x 10 mL) and brine (10 mL) and then dried over Na_2SO_4. Solvent removal in vacuo yielded a brown solid which was recrystallized by vapor diffusion from THF/pentane to yield the desired product (82% yield). Complexes **3.6** and **3.7** were adapted by the same procedure but used different starting salicylaldehyde's (3–tert–butyl–5–methoxysalicylaldehyde and salicylaldehyde respectively).

General synthesis for complexes (3.8), (3.9), (3.10), (3.11), (3.12), and (3.13): All complexes were synthesized and isolated by *in situ* vapor diffusion recrystallizations. A small vial containing a known amount of **3.5** (**3.8**–**3.10**) or **3.7** (**3.11**–**3.13**) was dissolved in the desired solvent and an excess of the desired amine (10.0 equivalents) were added and dissolved in the solution. The following were setup as vapor diffusion recrystallizations (with pentane) and allowed to recrystallize over 1–3 days. The crystals were then tested and determined to be the following ligated–amines or bridging fluoride species (**3.10**). Batches to synthesize the complexes in bulk were done by scaling up the amount of Mn^{III} complex dissolved.

3.4.3 Magnetic data: Evans' method

The χ_{dia} were estimated using Pascal's constants[50] and the μ_{eff} calculated assuming spin–only contributions as below. An S = 2 system for complex **3.3** (in C_6D_6) was determined by using the data in **Table 3.2**.

$$\mu_{eff} = 2\sqrt{S\ (S+1)}$$

Table 3.2. List of Evans' Method Experimental and Calculated Values for **3.3**.

Trial	Weight (mg)	$C_6H_5CF_3$ peak 1 (ppm)	$C_6H_5CF_3$ peak 2 (ppm)	μ_{eff} (μ_b)	Calculated S Value
1	2.8	–112.87	–113.33	5.061	2.08
2	2.9	–112.91	–113.29	5.119	2.11
3	2.9	–112.89	–113.31	5.133	2.11

3.4.4 Qualitative N_2 determination: Gas chromatography (GC–MS) experiments

3.4.4.1 Oxidation with NBS

Oxidation of 3.2–^{15}N: A 5 mL Schlenk flask equipped with a magnetic stirbar was charged with **3.2–^{15}N** (5.6 mg, 0.03 mmol) and MeCN (1 mL) and was frozen in a dry ice/acetone–cooled bath. Cooling only the solvent, the flask was brought under vacuum and back filled with Ar, then capped with a septum. A gas–tight syringe containing a solution of NBS (8.9 mg, 0.15 mmol) in MeCN (1 mL) was layered on top of the frozen solution of **3.2–^{15}N**. Both layers were frozen completely. The Ar source was removed and the solution was brought to room temperature with stirring. Within 3 hours, the headspace was sampled (20 μL) using a gastight syringe and directly injected into the GC–MS. The peaks in the GC trace show $^{15}N_2$ (with contamination from atmospheric $^{14}N_2$ and O_2) and Ar combined at retention time 1.5 and MeCN at retention time 2.6. The mass spectrum at retention time 1.5 (a, **Figure 3.3**) is shown (with Ar excluded) and displays the relative abundance of $^{15}N_2$ at 10.0 % compared to atmospheric $^{14}N_2$ which is set at a relative abundance of 100.

Oxidation of (50:50 mixture) 3.2:3.2–^{15}N: This was performed in an analogous fashion, but instead a mixture of **3.2–^{15}N** (6.0 mg, 0.018 mmol) and **3.2** (6.0 mg, 0.018 mmol). The mass spectrum at retention time 1.5 (b, **Figure 3.3**) is shown (with Ar excluded) and displays the relative abundance of $^{15}N_2$ at 8.1 % and $^{14}N^{15}N$ at 16 % (relative to $^{14}N_2$ set to a relative abundance of 100).

3.4.4.2 Qualitative N_2 determination for catalytic reactions

Preliminary catalytic experiment with 3.2, NBS, and $^{15}NH_4OH$: A 5 mL Schlenk flask equipped with a magnetic stirbar was charged with **3.2** (5.6 mg, 0.01 mmol) DCM (1 mL) and was frozen in a dry ice/acetone–cooled bath. Cooling only the solvent, the flask was brought

under vacuum and back filled with Ar, then capped with a septum. A gas–tight syringe containing a solution of NBS (177.9 mg, 1.0 mmol) in DCM (1 mL) was layered on top of the frozen solution of **3.2**. Both layers were frozen completely. The Ar source was removed and the solution was brought to room temperature with stirring, where $^{15}NH_4OH$ (0.075 mL, 0.25 mmol, 3.3 N) was added via syringe. Within 1 hour, the headspace was sampled (60 µL) using a gastight syringe and directly injected into the GC–MS. The peaks in the GC trace show $^{15}N_2$ (with contamination from atmospheric $^{14}N_2$ and O_2) and Ar combined at retention time 1.5. The mass spectrum at retention time 1.5 (a, **Figure 3.4**) is shown (with everything outside O_2/N_2 excluded; $^{15}NH_2Br$, m/z = 97.9; m/z is not shown in the following plot) and displays the relative abundance of $^{15}N_2$ and $^{15}N^{14}N$ at 78.1% and 4.5%, respectively compared to atmospheric $^{14}N_2$ which is set at a relative abundance of 100.

Control experiment with NBS and $^{15}NH_4OH$: A 5 mL Schlenk flask equipped with a magnetic stirbar was charged with NBS (177.9 mg, 1.0 mmol) in DCM (2 mL), frozen and back filled with Ar. The Ar source was removed and the solution was brought to room temperature with stirring, where $^{15}NH_4OH$ (0.075 mL, 0.25 mmol, 3.3 N) was added via syringe. Within 1 hour, the headspace was sampled (60 µL) using a gastight syringe and directly injected into the GC–MS. The peaks in the GC trace do not show a trace of $^{15}N_2$ (with only signal as contamination from atmospheric $^{14}N_2$ and O_2; $^{15}NH_2Br$, m/z = 97.9; m/z is not shown in the following plot) and Ar combined at retention time 1.5 (b, **Figure 3.4**).

3.4.5 N_2 quantification: Gas chromatography – thermal conductivity (GC–TCD) experiments

3.4.5.1 Control experiments and system development for N_2 analysis

Inert gas control experiments for GC–TCD: Alternative to GC–MS experiments, where Ar was used as the inert gas, the retention times for gases cannot be the same because the TCD generates a signal for change in thermal conductivity of the gas and cannot distinguish between different gases with similar thermal conductivities. With this column, Ar has the same retention time as O_2, so we were unable to use Ar to fill the headspace (a, **Figure 3.7**). We also tried He and Kr. We found He was unfit for the experiments because the density was too low and leakage of air and contamination into the flask was too great. Kr was chosen because the retention time of N_2/O_2 compared to Kr is so different (b, **Figure 3.7**).

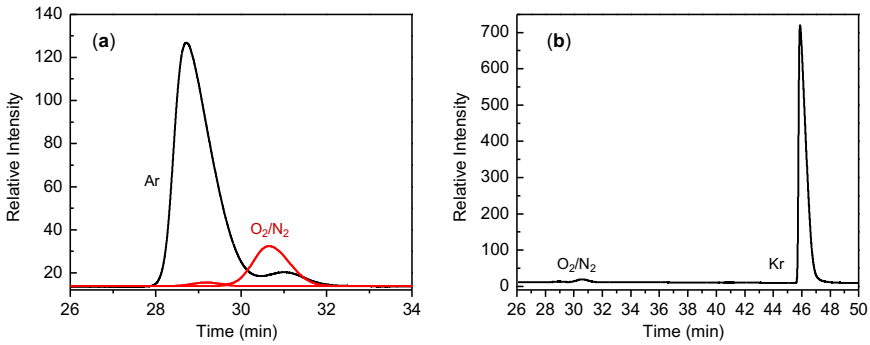

Figure 3.7. (**a**) GC–TCD chromatogram trace of Ar (black line) and O_2/N_2 from air (red line), at over–lapping retention times. (**b**) GC–TCD chromatogram trace of Kr with trace O_2/N_2 from air.

Air (O_2/N_2) injection control experiments for GC–TCD: To quantify N_2 from our experiments with inevitable contamination of N_2/O_2 from air, we devised multiple control experiments to determine how much N_2/O_2 leaked into the system by first puncturing the septa of the reaction flask and the injection port and determining the ratio of N_2/O_2 (a and c, **Figure**

3.8). Additionally, we injected various amounts of air into the instrument (10–30 μL injections) to determine relative ratios of N_2/O_2 (b and d, **Figure 3.8**). Once we determined the relative ratio of N_2/O_2 (N_2:$O_{2,avg}$ = 4.18:1.0) from the following controls, based on the area of O_2 from air, we were able to back–calculate how much N_2 was from our sample.

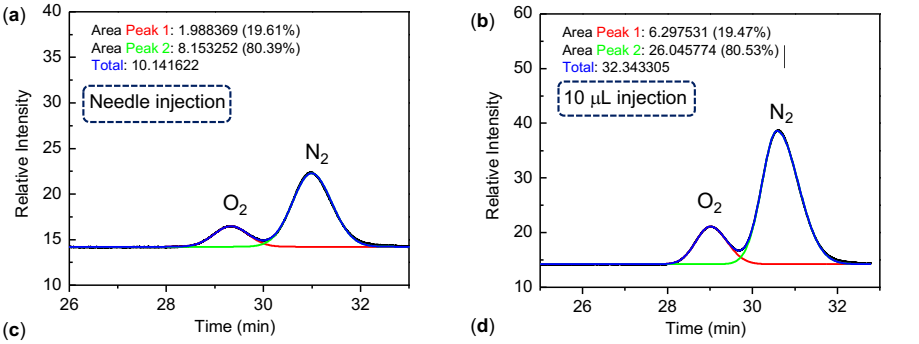

(c)

Sample	O_2 air (area)	N_2 air (area)	Ratio
1	113.20799	464.08926	1: 4.09
2	117.53867	486.46272	1: 4.14
3	110.41377	465.85851	1: 4.12

Triplicates were run for each injection

(d)

Sample	O_2 air (area)	N_2 air (area)	Ratio
10 µL	375.03423	1551.181648	1: 4.14
20 µL	604.85836	2519.41006	1: 4.17
30 µL	994.689132	4177.90125	1: 4.20

Triplicates were run for each injection

Figure 3.8. (**a**) GC–TCD chromatogram containing O_2/N_2 by puncturing the injection septa with a gas–tight syringe needle. (**b**) GC–TCD chromatogram containing O_2/N_2 by injection various amounts of air. (**c**) Ratios for O_2/N_2 calculated from the total area obtained by the chromatograms in (**a**). (**d**) Ratios for O_2/N_2 calculated from the total area obtained by the chromatograms in (**b**).

Calibration curve for N_2 for GC–TCD: A flask equipped with a gas–tight septum was charged with 1 atm of analytically pure N_2. Known amounts (5.0–25.0 μL) of N_2 were injected into the instrument for 3 trials each (**Figure 3.9**).

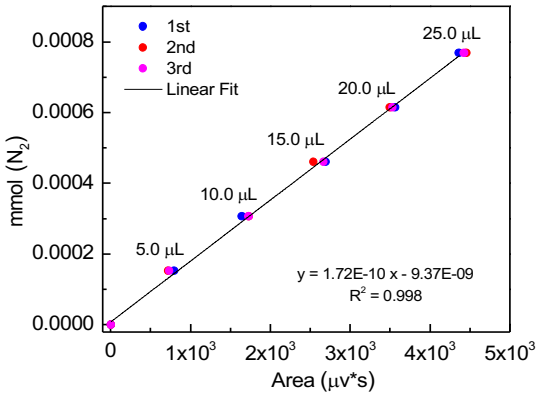

Figure 3.9. Calibration curve for known amounts of N_2 gas obtained from the GC–TCD.

Control experiments with NBS and NH_3: A conical Schlenk flask (68.4 mL headspace) equipped with a magnetic stirbar and the flask was evacuated and back filled with NH_3 and capped with a septum. A solution of NBS (142.4 mg, 0.8 mmol) in DCM (2 mL) – which had been freeze pumped thawed and back filled with Kr prior to use (**Figure 3.10**) – was cannula transferred to the flask containing NH_3 gas. Upon addition, a white solid crashed out of solution, and the headspace was sampled every 15 mins, using a gastight syringe and was directly injected into the GC–TCD. Over multiple trials, the N_2 produced was found to be 0.26–0.29 mmol (**Table 3.1**) and the white solid was confirmed to be succinimide by ^{1}H NMR spectroscopy.

3.4.5.2 Experimental setup: stoichiometric and catalytic N_2 analysis

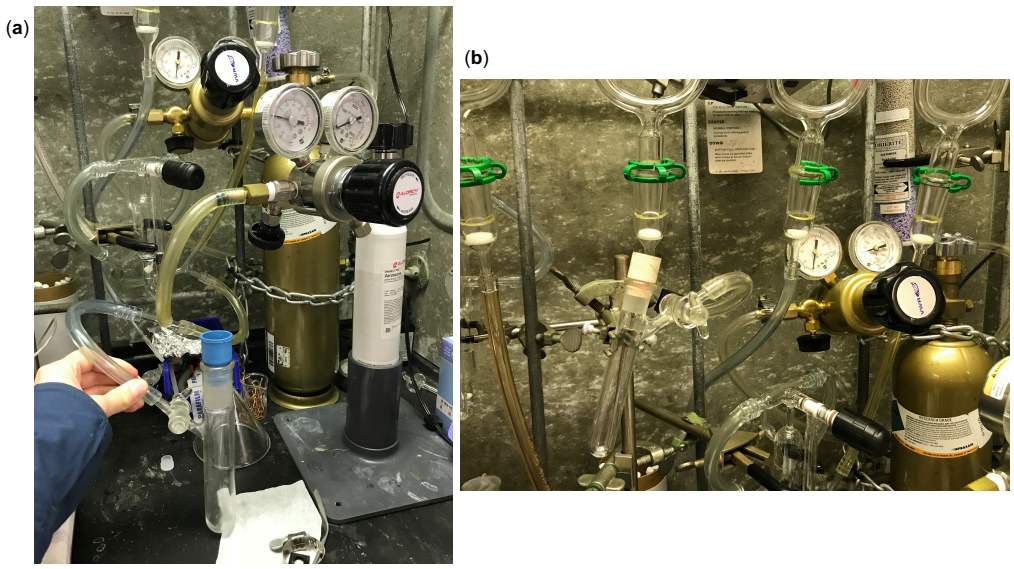

Figure 3.10. (**a**) and (**b**) Experimental/Schlenk line setup with Kr and NH_3 gas lines attached to the manifold.

Stoichiometric N_2 analysis: A 15 mL conical Schlenk flask equipped with a magnetic stirbar was charged with **3.2** (11.1 mg, 0.02 mmol). The flask was evacuated and back filled with Kr and capped with a septum. A solution of NBS (17.8 mg, 0.1 mmol) in MeCN (1 mL) – which had been freeze pumped thawed and back filled with Kr prior to use – was cannula transferred to the flask containing **3.2**. Upon addition the solution turned brown–red and the headspace was sampled (60 μL) over 6.5 hours, using a gastight syringe and was directly injected into the GC–TCD. Over three trials, the yield of N_2 was found to be 80–94% (c, **Figure 3.3**).

General procedure for catalytic N_2 analysis: A conical Schlenk flask (68.4 mL headspace) equipped with a magnetic stirbar was charged with varying amounts of **3.2** (10–50% cat. loading). The flask was evacuated and back filled with NH_3 and capped with a septum. A solution of NBS (142.4 mg, 0.8 mmol) in DCM (2 mL) – which had been freeze pumped

thawed and back filled with Kr prior to use (**Figure 3.10**) – was cannula transferred to the flask containing **3.2**. Upon addition, the solution turned brown–red with formation of a white solid, and the headspace was sampled every 15 mins, using a gastight syringe and was directly injected into the GC–TCD. Over varying trials, the N_2 produced was found to be 0.27–0.29 mmol (same yields as control experiments).

3.5 References

1. Warren, J. J.; Tronic, T. A.; Mayer, J. M., Thermochemistry of Proton-Coupled Electron Transfer Reagents and its Implications. *Chemical Reviews* **2010,** *110* (12), 6961-7001.

2. Bordwell, F. G.; Drucker, G. E.; Fried, H. E., Acidities of carbon and nitrogen acids: the aromaticity of the cyclopentadienyl anion. *The Journal of Organic Chemistry* **1981,** *46* (3), 632-635.

3. Keener, M.; Peterson, M.; Hernández Sánchez, R.; Oswald, V. F.; Wu, G.; Ménard, G., Towards Catalytic Ammonia Oxidation to Dinitrogen: A Synthetic Cycle by Using a Simple Manganese Complex. *Chemistry - A European Journal* **2017,** *23* (48), 11479-11484.

4. Bhattacharya, P.; Heiden, Z. M.; Chambers, G. M.; Johnson, S. I.; Bullock, R. M.; Mock, M. T., Catalytic Ammonia Oxidation to Dinitrogen by Hydrogen Atom Abstraction. *Angewandte Chemie International Edition* **2019,** *58* (34), 11618-11624.

5. Nakajima, K.; Toda, H.; Sakata, K.; Nishibayashi, Y., Ruthenium-catalysed oxidative conversion of ammonia into dinitrogen. *Nature Chemistry* **2019,** *11* (8), 702-709.

6. Habibzadeh, F.; Miller, S. L.; Hamann, T. W.; Smith, M. R., Homogeneous electrocatalytic oxidation of ammonia to N₂ under mild conditions. *Proceedings of the National Academy of Sciences* **2019,** *116* (8), 2849.

7. Zott, M. D.; Garrido-Barros, P.; Peters, J. C., Electrocatalytic Ammonia Oxidation Mediated by a Polypyridyl Iron Catalyst. *ACS Catalysis* **2019,** *9* (11), 10101-10108.

8. Dunn, P. L.; Johnson, S. I.; Kaminsky, W.; Bullock, R. M., Diversion of Catalytic C–N Bond Formation to Catalytic Oxidation of NH3 through Modification of the Hydrogen Atom Abstractor. *Journal of the American Chemical Society* **2020,** *142* (7), 3361-3365.

9. Bhattacharya, P.; Heiden, Z. M.; Wiedner, E. S.; Raugei, S.; Piro, N. A.; Kassel, W. S.; Bullock, R. M.; Mock, M. T., Ammonia Oxidation by Abstraction of Three Hydrogen Atoms from a Mo–NH3 Complex. *Journal of the American Chemical Society* **2017**.

10. Du Bois, J.; Tomooka, C. S.; Hong, J.; Carreira, E. M., Nitridomanganese(V) Complexes: Design, Preparation, and Use as Nitrogen Atom-Transfer Reagents. *Accounts of Chemical Research* **1997,** *30* (9), 364-372.

11. Chang, C. J.; Connick, W. B.; Low, D. W.; Day, M. W.; Gray, H. B., Electronic Structures of Nitridomanganese(V) Complexes. *Inorganic Chemistry* **1998,** *37* (12), 3107-3110.

12. Bois, J. D.; Tomooka, C. S.; Hong, J.; Carreira, E. M.; Day, M. W., Synthesis and Structure of Novel MnIII and Mnv Complexes: Development of a New, Mild Method for Forming Mn□N Bonds. *Angewandte Chemie International Edition in English* **1997,** *36* (15), 1645-1647.

13. Abu-Omar, R. A. E. M. M., Nitrido and imido transition metal complexes of Groups 6–8. *Coordination Chemistry Reviews* **2003,** *243* (1-2), 83-124.

14. Svenstrup, N.; Bogevig, A.; G. Hazell, R.; Anker Jorgensen, K., Enantioselective [small alpha]-amination of ketones mediated by chiral nitridomanganese(V) complexes using ammonia as the terminal nitrogen source. *Journal of the Chemical Society, Perkin Transactions 1* **1999,** (11), 1559-1566.

15. Jang, G.-G.; Roper, D. K., Balancing Redox Activity Allowing Spectrophotometric Detection of Au(I) Using Tetramethylbenzidine Dihydrochloride. *Analytical Chemistry* **2011,** *83* (5), 1836-1842.

16. Clarke, R. M.; Storr, T., Tuning Electronic Structure To Control Manganese Nitride Activation. *J. Am. Chem. Soc.* **2016,** *138* (47), 15299-15302.

17. Rajesh, K.; Somasundaram, M.; Saiganesh, R.; Balasubramanian, K. K., Bromination of Deactivated Aromatics: A Simple and Efficient Method. *The Journal of Organic Chemistry* **2007,** *72* (15), 5867-5869.

18. Lambert, F. L.; Ellis, W. D.; Parry, R. J., Halogenation of Aromatic Compounds by N-Bromo- and N-Chlorosuccinimide under Ionic Conditions. *The Journal of Organic Chemistry* **1965,** *30* (1), 304-306.

19. Pearson, D. E.; Wysong, R. D.; Breder, C. V., Ortho bromination of phenols. *The Journal of Organic Chemistry* **1967,** *32* (7), 2358-2360.

20. Yiu, S.-M.; Lam, W. W. Y.; Ho, C.-M.; Lau, T.-C., Facile N···N Coupling of Manganese(V) Imido Species. *Journal of the American Chemical Society* **2007,** *129* (4), 803-809.

21. Chidara, V. K.; Du, G., An Efficient Catalyst Based on Manganese Salen for Hydrosilylation of Carbonyl Compounds. *Organomet.* **2013,** *32* (18), 5034-5037.

22. Chang, W.-P.; Lin, W.-C.; Chen, J.-H.; Wang, S.-S.; Tung, J.-Y., A 13C and 1H NMR spectroscopic investigation of the structure of the iminium ion with a dipolar form in metal complexes of 2-N-substituted N-confused porphyrins. *Dalton Transactions* **2012,** *41* (43), 13454-13464.

23. Feth, M. P.; Bolm, C.; Hildebrand, J. P.; Köhler, M.; Beckmann, O.; Bauer, M.; Ramamonjisoa, R.; Bertagnolli, H., Structural Investigation of High-Valent Manganese–Salen Complexes by UV/Vis, Raman, XANES, and EXAFS Spectroscopy. *Chemistry - A European Journal* **2003,** *9* (6), 1348-1359.

24. Campbell, K. A.; Lashley, M. R.; Wyatt, J. K.; Nantz, M. H.; Britt, R. D., Dual-Mode EPR Study of Mn(III) Salen and the Mn(III) Salen-Catalyzed Epoxidation of cis-β-Methylstyrene. *J. Am. Chem. Soc.* **2001,** *123* (24), 5710-5719.

25. Keener, M.; Peterson, M.; Hernández Sánchez, R.; Oswald, V. F.; Wu, G.; Ménard, G., Towards Catalytic Ammonia Oxidation to Dinitrogen: A Synthetic Cycle by Using a Simple Manganese Complex. *Chemistry - A European Journal* **2017**.

26. Krahe, O.; Bill, E.; Neese, F., Decay of Iron(V) Nitride Complexes By a N□N Bond-Coupling Reaction in Solution: A Combined Spectroscopic and Theoretical Analysis. *Angewandte Chemie International Edition* **2014,** *53* (33), 8727-8731.

27. Clemens, D. F.; Woodford, W.; Dellinger, E.; Tyndall, Z., Gas-phase synthesis and some reactions of bromamine and dimethylbromamine. *Inorg. Chem.* **1969,** *8* (4), 998-1000.

28. Kovacic, P.; Lowery, M. K.; Field, K. W., Chemistry of N-bromamines and N-chloramines. *Chemical Reviews* **1970,** *70* (6), 639-665.

29. Moldenhauer, W.; Burger, M., Über Monobromamin. *Berichte der deutschen chemischen Gesellschaft (A and B Series)* **1929,** *62* (6), 1615-1618.

30. Bray, W. C.; Dowell, C. T., THE REACTIONS BETWEEN CHLORINE AND AMMONIA. *Journal of the American Chemical Society* **1917,** *39* (5), 905-913.

31. Du Bois, J.; Hong, J.; Carreira, E. M.; Day, M. W., Nitrogen Transfer from a Nitridomanganese(V) Complex: Amination of Silyl Enol Ethers. *J. Am. Chem. Soc.* **1996,** *118* (4), 915-916.

32. Petersen, N.; Raebiger, J. W.; Miller, J. S., [MnII(t-Bu)4salen]2 and Its Reaction with TCNE. *Journal of Solid State Chemistry* **2001,** *159* (2), 403-406.

33. Larrow, J. F.; Jacobsen, E. N.; Gao, Y.; Hong, Y.; Nie, X.; Zepp, C. M., A Practical Method for the Large-Scale Preparation of [N,N'-Bis(3,5-di-tertbutylsalicylidene)-1,2-cyclohexanediaminato(2-)]manganese(III) chloride, a Highly Enantioselective Epoxidation Catalyst. *J. Org. Chem.* **1994,** *59* (7), 1939-1942.

34. Boozer, C. E.; Moncrief, J. W., Allylic Bromination by N-Bromo-t-butylamine1. *The Journal of Organic Chemistry* **1962,** *27* (2), 623-624.

35. Zhang, J.; Chang, X.; Bowman, E. C.; Holt, C. J.; Lodewyk, M. W.; Miller, R. M.; Xia, G., Experimental and Theoretical Investigations of the Bromination of Phenols with β and γ Aliphatic Substituents, including Rings. *The Journal of Organic Chemistry* **2015,** *80* (18), 9292-9296.

36. Vosburgh, I., THE MOLECULAR REARRANGEMENT OF TRIPHENYL-METHYLHALOGENAMINES.1. *Journal of the American Chemical Society* **1916,** *38* (10), 2081-2095.

37. Hunt, C.; Peterson, M.; Anderson, C.; Chang, T.; Wu, G.; Scheiner, S.; Ménard, G., Switchable Aromaticity in an Isostructural Mn Phthalocyanine Series Isolated in Five Separate Redox States. *Journal of the American Chemical Society* **2019,** *141* (6), 2604-2613.

38. Eikey, R. A.; Abu-Omar, M. M., Nitrido and imido transition metal complexes of Groups 6–8. *Coordination Chemistry Reviews* **2003,** *243* (1), 83-124.

39. Eikey, R. A.; Khan, S. I.; Abu-Omar, M. M., The Elusive Terminal Imido of Manganese(V). *Angewandte Chemie International Edition* **2002,** *41* (19), 3591-3595.

40. Buchler, J. W.; Dreher, C.; Lay, K.-L.; Raap, A.; Gersonde, K., Metal complexes with tetrapyrrole ligands. 29. Synthesis and electron spin resonance spectra and electron nuclear double resonance investigations of nitridochromium(V) porphyrins. *Inorganic Chemistry* **1983,** *22* (6), 879-884.

41. Buchler, J. W.; Dreher, C.; Lay, K. L.; Lee, Y. J.; Scheidt, W. R., Metal complexes with tetrapyrrole ligands. 30. The manganese-nitrogen triple bond. Synthesis and molecular stereochemistry of (5,15-dimethyl-2,3,7,8,12,13,17,18-octaethyl-5H,15H-porphinato)nitridomanganese(V). *Inorganic Chemistry* **1983,** *22* (6), 888-891.

42. Hill, C. L.; Hollander, F. J., Structural characterization of a complex of Manganese(V) nitrido[tetrakis(p-methoxyphenyl)porphinato] manganese(V). *Journal of the American Chemical Society* **1982,** *104* (25), 7318-7319.

43. Hill, C. L.; Schardt, B. C., Alkane activation and functionalization under mild conditions by a homogeneous manganese(III)porphyrin-iodosylbenzene oxidizing system. *Journal of the American Chemical Society* **1980,** *102* (20), 6374-6375.

44. Groves, J. T.; Kruper, W. J.; Haushalter, R. C., Hydrocarbon oxidations with oxometalloporphinates. Isolation and reactions of a (porphinato)manganese(V) complex. *Journal of the American Chemical Society* **1980,** *102* (20), 6375-6377.

45. Groves, J. T.; Lee, J.; Marla, S. S., Detection and Characterization of an Oxomanganese(V) Porphyrin Complex by Rapid-Mixing Stopped-Flow Spectrophotometry. *Journal of the American Chemical Society* **1997,** *119* (27), 6269-6273.

46. Song, W. J.; Seo, M. S.; DeBeer George, S.; Ohta, T.; Song, R.; Kang, M.-J.; Tosha, T.; Kitagawa, T.; Solomon, E. I.; Nam, W., Synthesis, Characterization, and Reactivities of Manganese(V)−Oxo Porphyrin Complexes. *Journal of the American Chemical Society* **2007,** *129* (5), 1268-1277.

47. Lever, A. B. P.; Wilshire, J. P.; Quan, S. K., Oxidation of manganese(II) phthalocyanine by molecular oxygen. *Inorganic Chemistry* **1981,** *20* (3), 761-768.

48. Afanasiev, P.; Kudrik, E. V.; Albrieux, F.; Briois, V.; Koifman, O. I.; Sorokin, A. B., Generation and characterization of high-valent iron oxo phthalocyanines. *Chemical Communications* **2012,** *48* (49), 6088-6090.

49. Manner, V. W.; Markle, T. F.; Freudenthal, J. H.; Roth, J. P.; Mayer, J. M., The first crystal structure of a monomeric phenoxyl radical: 2,4,6-tri-tert-butylphenoxyl radical. *Chemical Communications* **2008,** (2), 256-258.

50. Bain, G. A.; Berry, J. F., Diamagnetic Corrections and Pascal's Constants. *J. Chem. Educ.* **2008,** *85* (4), 532.

Chapter 4 – Redox–Controlled *o*–carboranes for Capture and Release of Uranyl

4.1 Introduction

The efficient isolation of uranium is of great interest due to the growing nuclear energy sector and associated requirements of fissile fuel supply and spent fuel remediation. While nuclear energy is often considered a cleaner energy source than fossil fuels,[1] the inadvertent release of radioactive materials to the environment poses potential serious threats to human health.[2] Therefore, strategies for the selective capture and release of uranium, the largest component of nuclear waste, is critical for both the long–term viability and safety of the nuclear energy sector. The primary fuel source in reactors, uranium, is most commonly found as the uranyl ion (UO_2^{2+}; U^{VI} oxidation state) in either terrestrial or aquatic environments. While the concentration in seawater is low (~3.3 μg/L), the total estimated quantity in the oceans is 4.5 billion tons, over a thousand times more than the known terrestrial supply.[3] Uranyl capture from either seawater or nuclear waste has been well studied and commonly relies on extremely strong chelating/binding affinities to UO_2^{2+} using chelating polymers,[3-4] porous inorganic,[5-7] or carbon–based materials,[8-9] as well as homogeneous compounds.[10] In contrast, the controlled release of uranyl after capture is less established and can be difficult, expensive, and/or destructive to the initial material.[4, 11] Therefore, new strategies that can both capture and release UO_2^{2+} in a non–destructive manner could offer a cost–competitive new approach to UO_2^{2+} supply and waste remediation efforts.

Recent reports on the redox–switchable capture and release of environmental contaminants using polymeric or porous scaffolds highlight the advantages of using electrochemistry for the reagent–less release of captured products.[12-14] Related work has further shown how redox–switchable hemilabile ligands can alter their chelating properties and

subsequent metal coordination by oxidation–state control.[15-16] In our recent publication published in *Nature*,[17] we harness the redox–switchable properties of a class of *ortho*–substituted *closo*–carboranes ($(CX)_2B_{10}H_{10}$; X = alkyl, phenyl, or donating group) to tune their chelating abilities, in turn allowing for the controlled capture and release of UO_2^{2+} in solution.

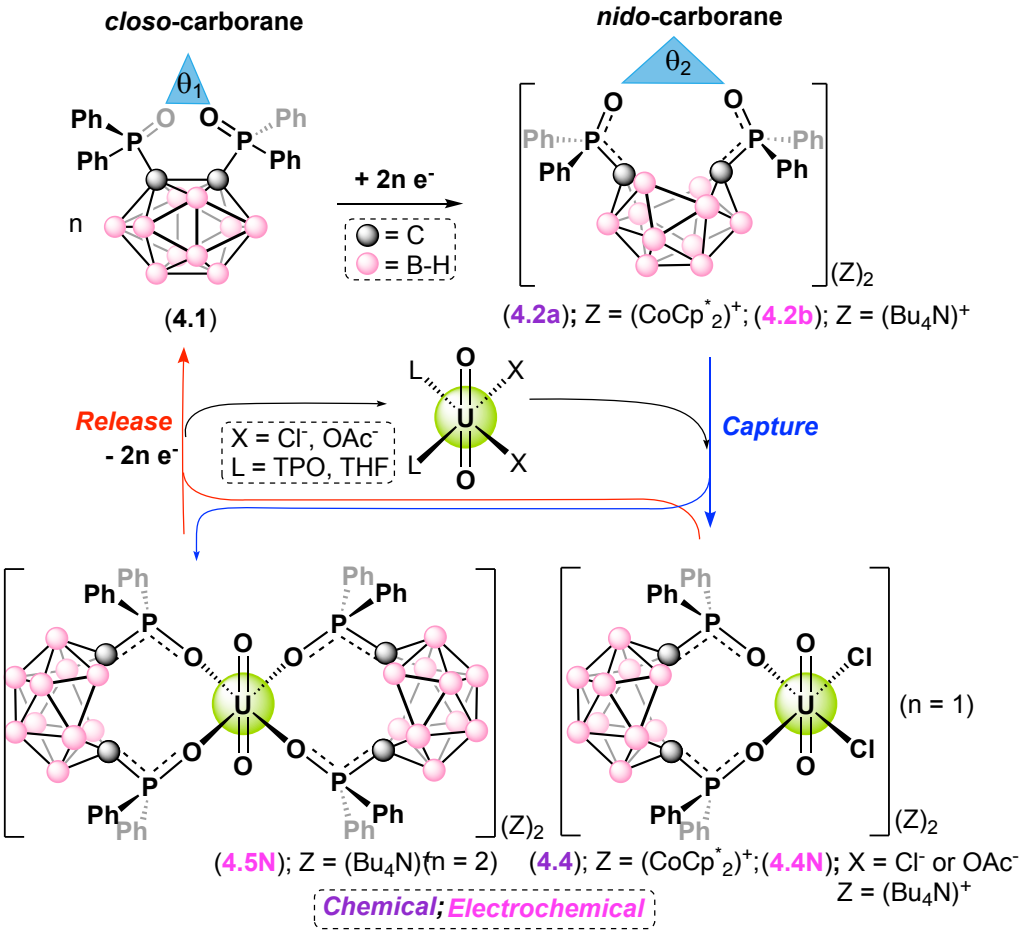

Figure 4.1. General electro/chemical mono– or bi–phasic capture of uranyl from $UO_2X_2L_2$ (X = Cl^-, OAc^-; L = THF, Ph_3PO) using the reduced cage "open" *nido*–carboranes (**4.2a**/**4.2b**) generated by reduction (ex. $CoCp^*_2$ or negative bias) of the cage "closed" *closo*–carborane (**4.1**). Corresponding relative bite angles (θ) are also shown. Oxidation (ex. $[FeCp_2][PF_6]$ or positive bias) of the captured products **4.4**/**4.5** or **4.4N**/**4.5N** leads to UO_2^{2+} release. Compounds labelled in purple have been chemically isolated whereas compounds in pink are proposed

electrochemical products. Blue and red pathways represent UO_2^{2+} capture and release, respectively.

Known for over 50 years, carboranes have been extensively studied in coordination chemistry (including with uranium), catalysis, luminescence, and energy storage applications.[18-25] But, most notably is their extraordinary robustness in terms of redox stability and chemical inertness, making them well sought out for various chemical transformations.[20, 26] Generally, *o–closo–*carboranes are considered redox–active ligand frameworks in that they can undergo $2e^-$ reduction, with stabilization and delocalization throughout the $[C_2B_{10}H_{10}]$ cluster. Studies have shown that reduction of substituted *closo–*carboranes to the *nido–*carboranes undergoes structural rearrangement and results in rupture of the C–C bond and cage opening with a simultaneous increase in ligand bite angle, θ (**Figure 4.1**; *closo* and *nido* refer to 2n + 2 and 2n + 4 framework bonding electrons, respectively).[20, 27-30] We rationalized that by incorporating donating X groups – specifically diphenylphosphine oxide ($X = Ph_2PO$) – we could tune the chelating properties of the cluster switching from opened to closed conformations by redox–control of the reduced and oxidized states, respectively. In this Chapter, we show how we harness this redox–switchable chelation and apply it to the chemical or electrochemical capture and release of UO_2^{2+} in mono– and bi–phasic solutions (**Figure 4.1**).

4.2 Results and Discussion

4.2.1 Synthesis of redox–active derivatized *o–*carboranes

The *closo–*carborane, $1,2–(Ph_2PO)_2–1,2–C_2B_{10}H_{10}$ (**4.1**), was synthesized and fully characterized, including by X–ray diffraction (XRD) studies (a, **Figure 4.2**)[31]. The ^1H NMR spectrum of **4.1** in d_3–MeCN exhibits three distinct diamagnetic aromatic signals for the aryl

C–H resonances at 7.54, 7.63, and 7.99 ppm. The H–B resonances in the cluster are not resolved and present a broad signal in the baseline at ~2.5 ppm, which is expected for proton coupling to a quadrapolar (S = 3/2) ^{11}B nucleus in a carborane cage.[32] The ^{11}B NMR spectrum shows two sharps resonances at 0.66 and –8.75 ppm, and the ^{31}P{^{1}H} NMR spectrum shows a diagnostic singlet at 22.8 ppm, which is expected for a symmetric product. X–Ray analysis reveals a cage C–C bond length (1.688(4) Å) and interatomic P···P distance (3.537 Å) are consistent with similar previous reports (**Table 4.1**)[31, 33]. The torsion angle for P1–C1–C2–P2 is 10.03(1)° which is characteristic for a carborane cluster bearing bulky substituents at the cluster carbons.[34] These metrics will be used throughout to correlate coordinated and uncoordinated carboranes, both in lieu of, yet proportional to the traditional bite angle, θ (**Figure 4.1**). The CV of **4.1** in tetrahydrofuran (THF) revealed two quasi–reversible cathodic waves at –0.93 V and –1.11 V relative to the ferrocene/ferrocenium (Fc/Fc^{+}) redox couple (**Figure 4.13**).

Reduction of **4.1** using 2.0 equivalents of decamethylcobaltocene ($CoCp^{*}_{2}$) afforded a yellow suspension from which the direduced nido–carborane, $[CoCp^{*}_{2}]_2[(nido–1,2–(Ph_2PO)_2–1,2–C_2B_{10}H_{10})]$ (**4.2a**) (b, **Figure 4.2**) could be isolated as a diamagnetic, gold crystalline solid in 95% yield. The ^{1}H NMR spectrum of **4.2a** in *d*$_3$–MeCN exhibited a sharp singlet at 1.62 ppm, corresponding to the $–CH_3$ resonances on the diamagnetic $[CoCp^{*}_{2}]^{+}$ counter ions and two aryl C–H resonances at 7.24 and 8.05 ppm, compared to the three distinct aromatic signals seen in **4.1**. The ^{11}B NMR spectrum showed four new resonances at 20.24, –0.62, –18.46, and –22.06 ppm, and the ^{31}P{^{1}H} NMR spectrum shows a slightly downfield–shifted singlet at 29.8 ppm corresponding to a single species. An analogous salt, $[Bu_4N]_2[(nido–1,2–(Ph_2PO)_2–1,2–C_2B_{10}H_{10})]$ (**4.2b**) to **4.2a** (**Figure 4.2**), was synthesized by reduction of **4.1** with KC_8, followed

by salt metathesis with [Bu_4N][Cl], which was relevant for the following electrochemical experiments described below.

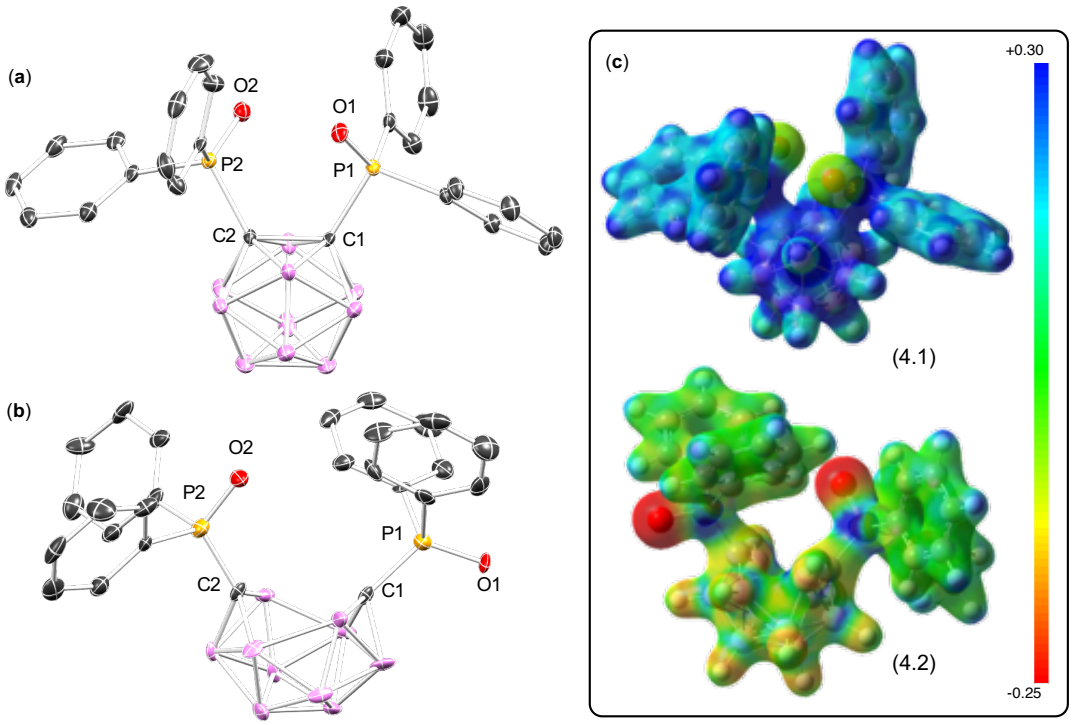

Figure 4.2. Solid–state molecular structures of complexes **4.1** (**a**) and **4.2a** (**b**). H atoms, $[CoCp^*_2]^+$ counter cations (**4.2a**), and all co–crystallized solvent molecules are omitted for clarity. (**c**) Electron density surfaces with colour–coded electrostatic potentials obtained from density functional theory (DFT) calculations using optimized structures of **4.1** and the anion of **4.2a** (labelled as **4.2**), (red, negative values are indicative of higher electron density).

It is worth noting isolation of a mono–reduced species was attempted and was unsuccessful. Monoanionic *o*–carborane species are especially rare,[34-42] and in our experiments, reduction with 1.0 equivalent of $CoCp^*_2$ led to formation of the (**4.2a**) with unreacted **4.1**, indicating under our conditions, the monoanion could not be readily isolated. The solid–state structure revealed the [$C_2B_{10}H_{10}$] cluster was preserved – which has been

shown previously with alkali metals[29, 43-46] – as an open–cage *nido*–carborane with a cleaved C–C bond (2.860 Å) and an elongated P···P distance (5.036 Å) relative to **4.1** (**Table 4.1**).

Table 4.1. Selected interatomic distances (Å), angles (°), and torsion angles (°) for **4.1** and **4.2a**.

	4.1	**4.2a**
P···P	3.537Å	5.036Å
C–C	1.688(4)Å	2.860Å
P1–O1	1.469(2)Å	1.487(3)Å
C1–P1	1.871(6)Å	1.745(2)Å
C1–P1–O1	109.98°	118.05°
C2–P2–O2	109.78°	114.79°
C2–C1–P1	119.57°	135.01°
C1–C2–P2	119.08°	122.38°
P1–C1–C2–P2	10.03°	–19.24°

It has been previously shown reversible *nido*–[$C_2B_{10}H_{10}$] cage opening/closing can be performed by acid/base reactions,[47] with few examples of redox–controlled reversibility.[27] Based on the electrochemical analysis of **4.1**, the oxidation potential of **4.2a** could be estimated to be ~ –1.0 V relative to the Fc/Fc^+ (Fc = ferrocene) couple.). Oxidation of **4.2a** could be chemically accessible through addition of 2.0 equivalent of ferrocenium hexafluorophosphate ([$FeCp_2$][PF_6]; E = 0.0 V in DCM).[48] Monitoring the oxidation of **4.2a** with 2.0 equivalent [$FeCp_2$][PF_6] in a J. Young tube with d_3–MeCN, resulted in consumption of **4.2a** with immediate formation of **4.1** as seen in the ^1H, ^{11}B, and $^{31}P\{^1H\}$ NMR spectra, as well as formation of ferrocene in the ^1H NMR spectrum. This demonstrates the C–C bond in **4.1** can be restored, controlling the reversibility of the cage opening/closing.

4.2.2 Coordination chemistry of redox–active derivatized *o*–carboranes

We next investigated the coordination chemistry of **4.1** and **4.2a**. Addition of four equivalents of **4.1** to dimeric $[UO_2Cl_2(THF)_2]_2$ in deuterated dichloromethane (d_2–DCM)

resulted in a light–yellow solution from which two new equivalent–intensity ^{31}P singlets appeared at 38.8 and 38.4 ppm in the NMR spectrum downfield shifted from **4.1** (22.8 ppm). Additionally, the ^{1}H NMR spectrum showed multiple new aromatic signals between 8.32 and 7.01 ppm, as well as unresolved H–B resonances in the cluster, present as a broad signal in the baseline at ~2.5 ppm. The inequivalent P environments and multiple aromatic signals in the ^{1}H NMR spectrum suggest either an octahedral geometry at U with two monodentate **4.1** ligands or a pentagonal bipyramidal geometry at U with two bidentate **4.1** and a chloride in the fifth equatorial site. While attempts to obtain single crystals for XRD studies failed, the NMR data suggests a 2:1 adduct is formed with a presumed formulation of UO_2Cl_2(**4.1**)$_2$ (Scheme).

It is important to note that the formation of UO_2Cl_2(**4.1**)$_2$ can be perturbed when the solvent is changed from MeCN or DCM to THF. Addition of 1.0 equivalent of dimeric $[UO_2Cl_2(THF)_2]_2$ to a solution of **4.1** in THF resulted in a yellow solid, which could be isolated in a 65% yield. The ^{1}H NMR spectrum of isolated material in d_3–MeCN showed formation of six new aryl C–H resonances between 7.9 and 7.2 ppm, with a broad singlet at –1.7 ppm, which was attributed to a B–H–B resonance.[49-51] The $^{11}B\{^{1}H\}$ NMR spectrum displayed resonances at 19.9, –9.7, –18.3, –31.6 and –34.4 ppm. The $^{31}P\{^{1}H\}$ NMR spectrum showed a significantly downfield–shifted singlet at 48.5 ppm. Single–crystals of complex **4.3** could be obtained by vapor diffusion in THF/hexanes, yielding light–yellow blocks suitable for XRD analysis, revealing decomposition of the $[C_2B_{10}H_{10}]$ cluster forming $[UO_2Cl(THF)_2]$[*nido*–7,8–$(Ph_2PO)_2$–7,8–$C_2B_9H_{10}$] (**4.3**) (**Figure 4.3**). The uranium center in **4.3** features a trigonal prismatic geometry with the *nido*–$[C_2B_9H_{10}]^{1-}$ cluster in an eclipsed conformation along the P–C atoms.[50] The solid–state structure revealed the *closo*–$C_2B_{10}H_{10}$ backbone was not preserved. In icosahedral carborane chemistry, it is well understood that partial degradation of

the *closo*–$C_2B_{10}H_{10}$ cluster to a *nido*–$[C_2B_9H_{10}]^{1-}$ system occurs by removal of B^+ vertex, incorporating a negative charge throughout the ligand.[51] The C–C bond length (1.622(1) Å) decreased in comparison to **4.1** (1.688(4)Å), which is expected for degradation to a *nido*–$[C_2B_9H_{10}]^{1-}$ cluster.[33, 49] Some early examples have described *nido*–$[C_2B_9H_{10}]^{1-}$ cluster formation by means of a reducing metal, such as Cu^+, Ag^+, and Au^+, where the carborane backbone undergoes a "pseudo–reduction" with subsequent nucleophilic attack, eliminating B^+ from the cluster.[49-50]

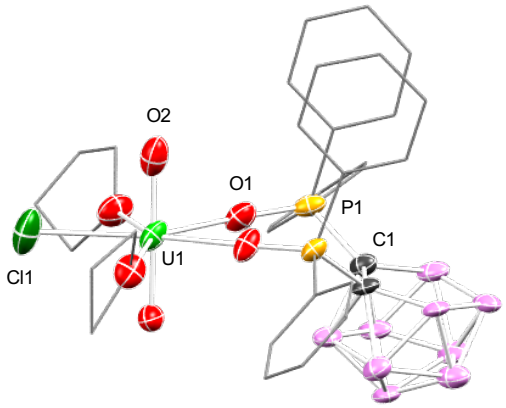

Figure 4.3. The solid–state molecular structure of $[UO_2Cl(THF)_2][$*nido*–7,8–$(Ph_2PO)_2$–7,8–$C_2B_9H_{10}]$ (**4.3**) with 50% probability elipsoids. All hydrogen atoms and C ellipsoids (not a part of the cluster) were omitted for clarity.

Alternatively, it has been shown *nido*–$[C_2B_9H_{10}]^{1-}$ can be formed without a reducing metal such as Rh^{3+} or Pd^{2+}.[50] Additionally, partial degradation of the cluster has been shown to occur by nucleophilic attack using nucleophiles such as alkoxides,[52-53] amines,[54] fluorides,[55-56] and phosphanes[57], indicating partial degradation can occur by multiple pathways and is not limited to the examples above. In our system, cluster degradation is proposed to occur primarily by solvent effects and nucleophilic attack of a chloride anion. 1.0 equivalent of chloride from $UO_2Cl_2(THF)_2$ can act as a nucleophile to remove B^+ from the cluster. Then, an additional

equivalent of $UO_2Cl_2(THF)_2$ is required in order to promote formation of **4.3**, most likely forming a reduced uranyl–containing by–product. This was determined by running simultaneous reactions where addition of 0.5 equivalent of $[UO_2Cl_2(THF)_2]_2$ to a d_8–THF solution of **4.1** shows formation of an intermediate product (34.7 ppm) in the $^{31}P\{^1H\}$ NMR spectrum as well as unreacted starting material (**4.1**). Attempts to isolate the intermediate product were unsuccessful. Alternatively, the $^{31}P\{^1H\}$ NMR spectrum with 1.0 equivalent of $[UO_2Cl_2(THF)_2]_2$ in the presence of **4.1** in d_8–THF, shows a new singlet at 47.5 ppm, which is shifted downfield compared to the intermediate product. Based on this, we propose *nido*–$[C_2B_9H_{10}]^{1-}$ cluster formation was promoted by an additional equivalent of $UO_2Cl_2(THF)_2$ and is highly dependent on THF as the solvent. To confirm, we found 1.0 equiv of $[UO_2Cl_2(THF)_2]_2$ with **4.1** in d_3–MeCN shows formation of UO_2Cl_2(**4.1**)$_2$, indicating degradation is solvent dependent. Although interesting, we determined the *nido*–$[C_2B_{19}H_{10}]^{1-}$ cluster is an undesirable product and THF was avoided as a solvent.

In contrast to **4.1**, treatment of two equivalents of **4.2a** to $[UO_2Cl_2(THF)_2]_2$ led to clean formation of a single new resonance at 51.1 ppm in the $^{31}P\{^1H\}$ NMR spectrum, consistent with a bidentate coordination mode. XRD studies confirmed the composition as the uranyl salt, $[CoCp^*_2]_2[UO_2Cl_2$(*nido*–1,2–$(Ph_2PO)_2$–1,2–$C_2B_{10}H_{10})]$ (**4.4**) (a, **Figure 4.4**).

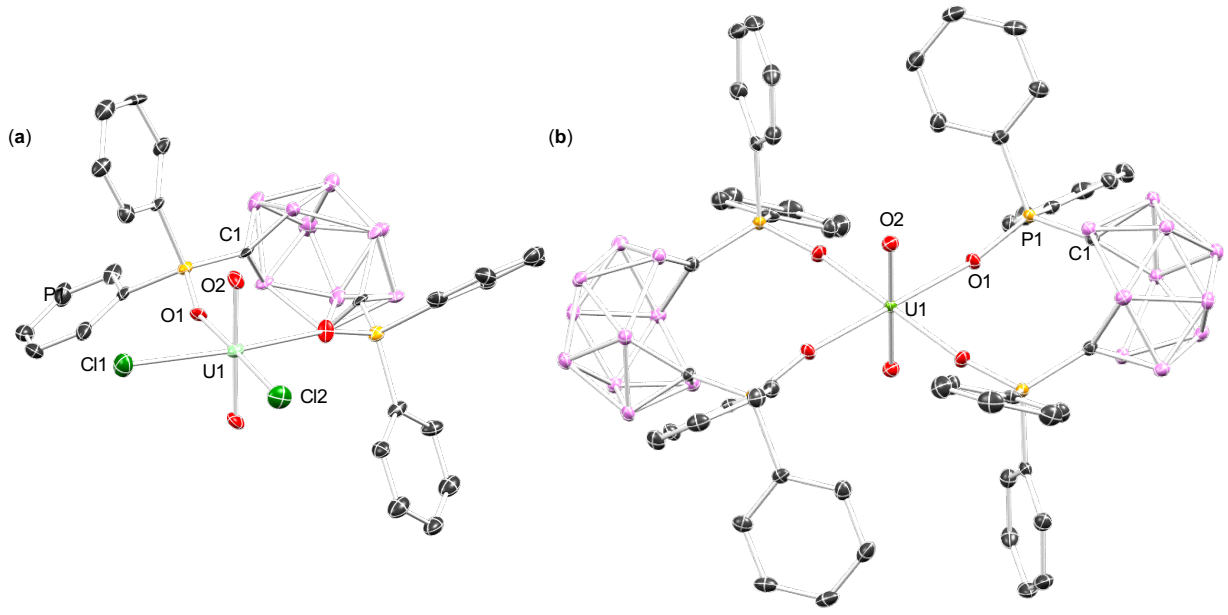

Figure 4.4. Solid–state molecular structures of **4.4** (**a**) and **4.5** (**b**) obtained from XRD studies. H atoms, $[CoCp^*_2]^+$ counter cations, and all co–crystallized solvent molecules are omitted for clarity.

A disubstituted uranyl salt was also obtained by addition of four equivalents of **4.2a** to $[UO_2Cl_2(THF)_2]_2$. Monitoring the reaction by $^{31}P\{^1H\}$ NMR spectroscopy revealed the clean conversion to a new product with a single peak at 52.0 ppm. The ^1H NMR spectrum showed formation of three new aryl C–H resonances at 7.24, 7.38, and 8.13 ppm. At 1.68 ppm, there is a slight shift in the $[CoCp^*_2]^+$ $–CH_3$ resonances. The $^{11}B\{^1H\}$ NMR spectrum, due to poor solubility in *d*$_3$–MeCN, becomes weak, yet shows two resonances at –17.15 and –22.66 ppm. XRD studies on single crystals confirmed the composition as the disubstituted complex, $[CoCp^*_2]_2[UO_2(nido–1,2–(Ph_2PO)_2–1,2–C_2B_{10}H_{10})_2]$ (**4.5**) (b, **Figure 4.4**). The bond metrics for **4.4** and **4.5** are similar. In **4.5**, the distorted icosahedral cluster was preserved from **4.2a**, and the C–C bond length was consistent 2.857 Å in comparison to 2.860 Å in **4.2a**. The U–O_{oxo} angle is 180.0°, which is completely linear, consistent with complexes incorporating the UO_2^{2+} moiety,[58-64] indicating the O–U–O bond is unchanged upon complexation.

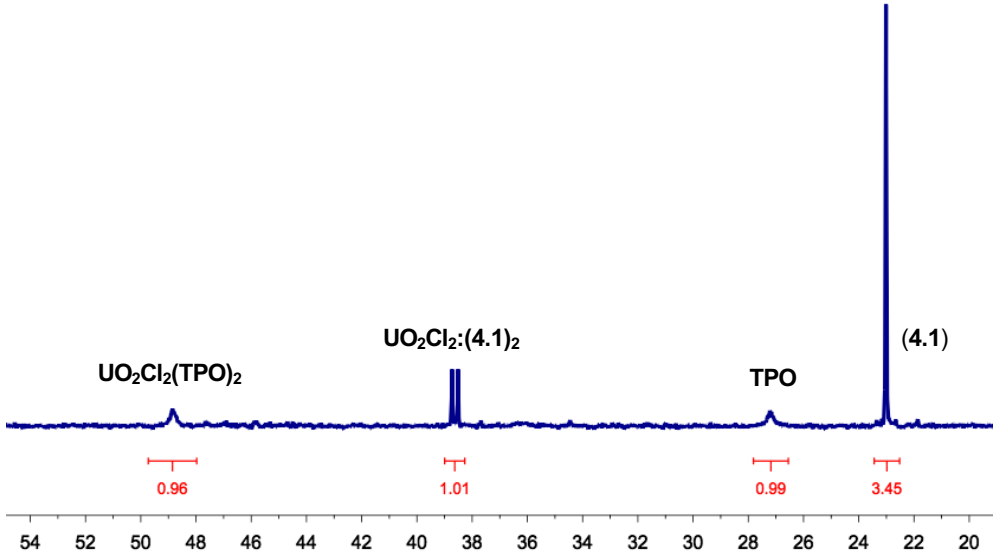

Figure 4.5. (**a**) $^{31}P\{^{1}H\}$ NMR spectrum of 2.0 equiv of **4.1** with 1.0 equiv of $UO_2Cl_2(TPO)_2$ in DCM–d_2. Relative integrations are shown in red.

While **4.1** and **4.2a** coordinate to UO_2^{2+}, we postulated that a third ligand with a competitive binding affinity to **4.1**, but weaker than **4.2a**, could enable a pathway to UO_2^{2+} release. Competition experiments using **4.1**, **4.2a**, and triphenylphosphine oxide (TPO), as part of $UO_2Cl_2(TPO)_2$[65], were performed and monitored by $^{31}P\{^{1}H\}$ NMR spectroscopy in DCM–d_2. Two equivalents of **4.1** were added to $UO_2Cl_2(TPO)_2$ for a 1:1 molar ratio of **4.1**:TPO. After an equilibration period, the $^{31}P\{^{1}H\}$ NMR spectrum revealed broadened resonances for $UO_2Cl_2(TPO)_2$ and free TPO, as well as a set of sharp resonances for UO_2Cl_2(**4.1**)$_2$ and free **4.1**. The ratio of UO_2Cl_2(**4.1**)$_2$: **4.1** was determined to be approximately 1:3 suggesting an equilibrium favouring the adduct, $UO_2Cl_2(TPO)_2$ (**Figure 4.5**).

The binding affinity of TPO was next compared to **4.2a** by addition of one equivalent of **4.2a** to $UO_2Cl_2(TPO)_2$. Rapid precipitation of products was observed. The $^{31}P\{^{1}H\}$ NMR spectrum of the DCM supernatant revealed complete conversion to the products **4.4** and **4.5**, along with a sharp singlet for TPO, and a minor unknown singlet at 47 ppm (b, **Figure 4.6**).

Analysis of the precipitate dissolved in propylene carbonate (PC) by $^{31}P\{^{1}H\}$ NMR spectroscopy revealed the presence of **4.5** (a, **Figure 4.6**). These data are consistent with full dissociation of TPO from $UO_2Cl_2(TPO)_2$ in the presence of **4.2a**. The binding affinity of TPO was next tested against PC, a coordinating solvent.[66] An initial $^{31}P\{^{1}H\}$ NMR spectrum of $UO_2Cl_2(TPO)_2$ dissolved in DCM–d_2 revealed two singlets in a 3:1 ratio at 48.09 and 47.97 ppm, respectively, likely arising from *trans*:*cis* isomerism.[67] While addition of two equivalents of PC led to negligible changes, addition of 20 and 40 equivalents led to increasing broadness of the aromatic peaks in the ^{1}H NMR spectra and broadening of the singlets in the $^{31}P\{^{1}H\}$ NMR spectra. Together, these data suggest a weak equilibrium with PC that it is heavily shifted towards $UO_2Cl_2(TPO)_2$. DFT calculations further supported these observations. Electron density surfaces with integrated electrostatic potentials for **4.1** and **4.2a** clearly indicate increased electron density at the P=O bonds of **4.2a** upon reduction, accounting for its experimentally observed increased Lewis basicity (**Figure 4.2**). This likely complements the increased bite angle (**Figure 4.1**) in rendering **4.2a** a stronger chelating agent than **4.1**. *In silico* isodesmic reactions of **4.2a**/TPO, TPO/**4.1**, or **4.1**/PC with proton as a model for the uranyl cation were also calculated (c,). Together with the experimental data, these data support a relative Lewis basicity trend of: **4.2a** >> TPO > **4.1** >> PC.

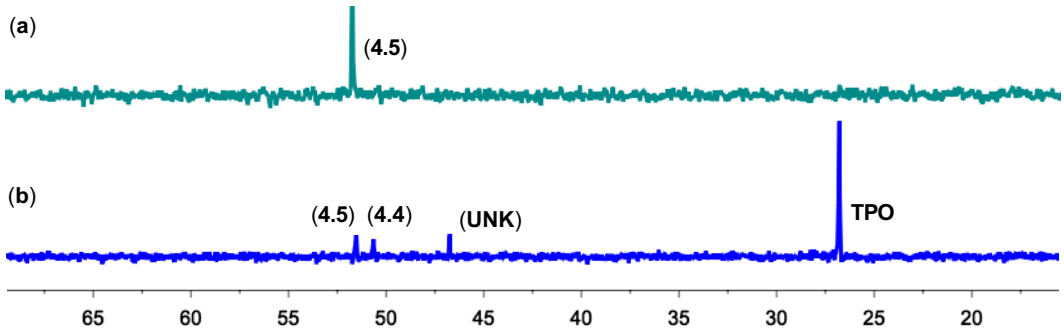

Figure 4.6. $^{31}P\{^{1}H\}$ NMR spectra of *in situ* reactions of 1.0 equivalent of **4.2a** with 1.0 equivalent of $UO_2Cl_2(TPO)_2$ in DCM–d_2. Rapid precipitation of a yellow solid was observed. (**a**) $^{31}P\{^{1}H\}$ NMR spectrum of the filtrate dissolved in PC with a DCM–d_2 capillary tube. (**b**) $^{31}P\{^{1}H\}$ NMR spectrum of the DCM–d_2 supernatant. An unknown by–product at 47 ppm is observed.

4.2.3 Monophasic chemical capture and release

We next investigated the *in situ* chemical capture and release of UO_2^{2+}. For optimal solubility, we utilized a 3:1 PC:benzene solvent mixture with a MeCN–d_3 capillary tube insert and Mes_3P as the analytical standard. A relaxation delay of 30 s was used in order to obtain accurate integrations of all species (see general considerations; **Table 4.2**). A 2:4 solution of **4.1**:TPO was analysed by $^{31}P\{^{1}H\}$ NMR spectroscopy which revealed two sharp resonances (a, **Figure 4.8**). Addition of half an equivalent of $[UO_2Cl_2(THF)_2]_2$ (one equivalent of U) resulted in no appreciable change to the resonance for **4.1**, but in significant broadening to the resonance for TPO (b, **Figure 4.8**). Only trace $UO_2Cl_2(TPO)_2$ is observed and is likely due to a combination of rapid exchange with excess TPO and the excess (~2000x) PC used relative to U. To initiate chemical capture of UO_2^{2+}, four equivalents of $CoCp^*_2$ were added (shown as "4 e^-") (**Figure 4.7**).

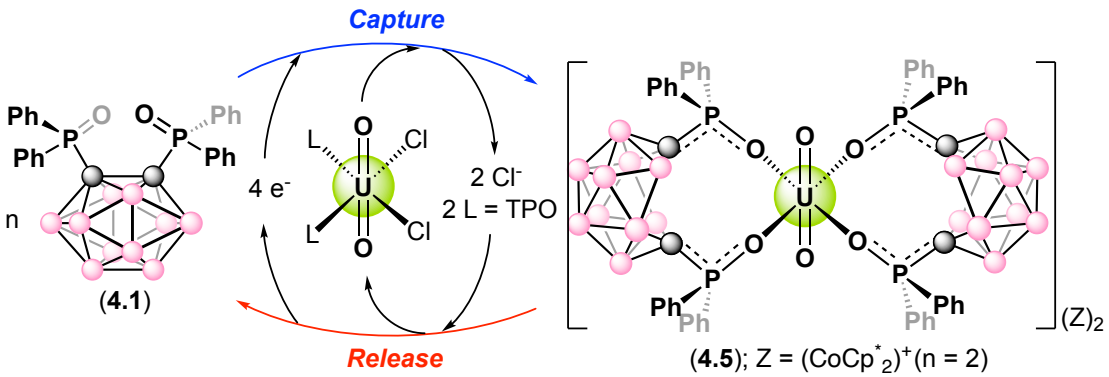

Figure 4.7. General chemical mono–phasic capture of uranyl from $UO_2Cl_2L_2$ (L = Ph_3PO) using the reduced cage "open" *nido*–carboranes (**4.2a**/**4.2b**) generated by reduction ($CoCp^*_2$, denoted as "4e⁻") of the cage "closed" *closo*–carborane (**4.1**). Oxidation with $[FeCp_2][PF_6]$ (denoted as "4e⁻") of the captured product **4.5** leads to UO_2^{2+} release. Blue and red pathways represent UO_2^{2+} capture and release, respectively.

Analysis by $^{31}P\{^1H\}$ NMR spectroscopy revealed the rapid and complete conversion of **4.1** to **4.5** with concomitant release of TPO (c, **Figure 4.8**; **Figure 4.7**). To initiate UO_2^{2+} release, we first determined the oxidation potential of **4.5** by CV which revealed a quasi–reversible anodic event at –0.42 V relative to Fc/Fc^+ (**Figure 4.14**, section 4.4.3). Thus, we exposed our *in situ* generated solution of **4.5** and TPO to four equivalents of $[Fc][PF_6]$ (**Figure 4.7**). Analysis by $^{31}P\{^1H\}$ NMR spectroscopy revealed the full conversion of **4.5** back to **4.1** along with the re–appearance of a broadened TPO resonance, similar to that of the pre–reduced solution (d, **Figure 4.8**). This capture and release could be performed in four cycles without degradation of products. Together, these results demonstrate the successful chemical capture and release of UO_2^{2+} in solution.

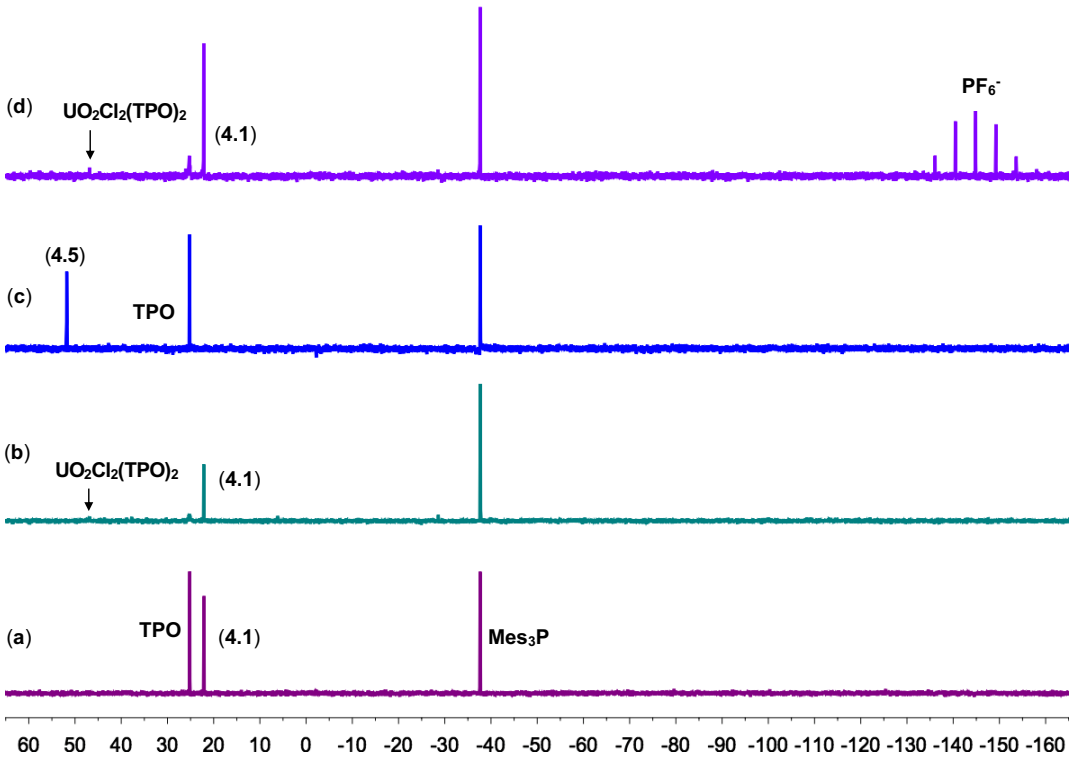

Figure 4.8. (**a**) $^{31}P\{^{1}H\}$ NMR spectrum of 4.0 equiv of TPO and 2.0 equiv of **4.1**. (**b**) $^{31}P\{^{1}H\}$ NMR spectrum of 4.0 equiv of TPO and 2.0 equiv of **4.1** in the presence of 0.5 equiv $[UO_2Cl_2(THF)_2]_2$. (**c**) $^{31}P\{^{1}H\}$ NMR spectrum of 4.0 equiv of $CoCp^*_2$ added to reaction (**b**). (**d**) $^{31}P\{^{1}H\}$ NMR spectrum after addition of 4.0 equiv of $[Fc][PF_6]$ to reaction (**c**).

4.2.4 Monophasic electrochemical capture and release

We next targeted the electrochemical capture and release of UO_2^{2+} by galvanostatic bulk electrolysis (GBE). This was conducted using a divided H–cell with coiled Pt electrodes, an anion exchange membrane (AEM), and an excess of the Fc/Fc^+ redox couple in the counter compartment (a**, Figure 4.9**). A 0.5:5:6 ratio of $[UO_2Cl_2(THF)_2]_2$:**4.1**:TPO was used in PC:benzene (3:1) with a MeCN–d_3 capillary tube insert with $[Ph_3PNPPh_3][PF_6]$ as the analytical standard. A relaxation delay of 40 s was used in order to obtain accurate integrations of all species (see general considerations; **Table 4.2**).

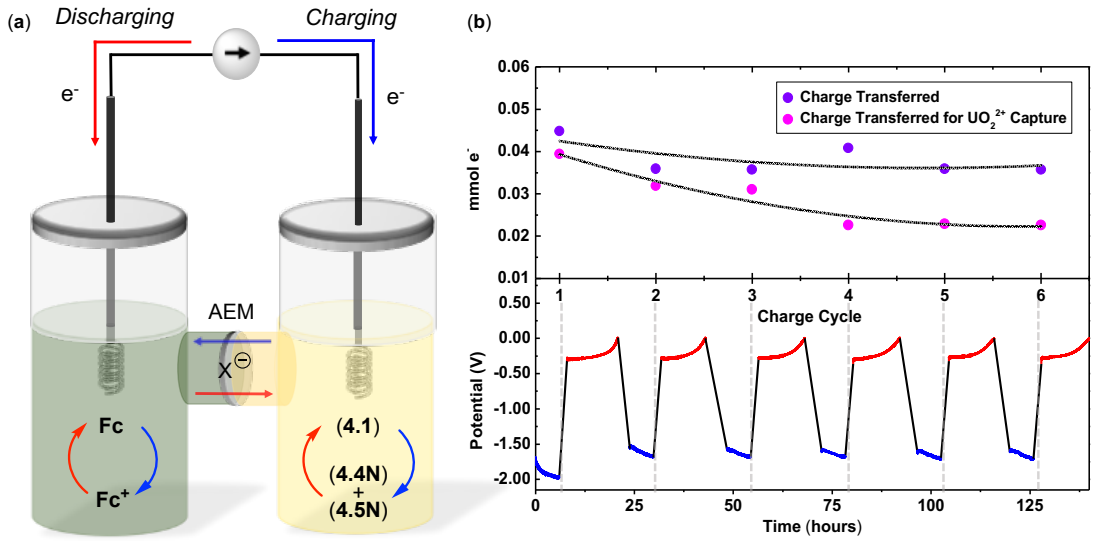

Figure 4.9. (**a**) Depiction of the H–cell used incorporating excess Fc/Fc^+ (left) and **4.1**, TPO, and $[UO_2Cl_2(THF)_2]_2$ (right) in a 3:1 PC:benzene solvent mixture. Charging the cell (blue) leads to the capture of UO_2^{2+} converting **4.1** to **4.5N** (major product) and **4.4N** (minor product). (**b**) Bottom: applied galvanostatic potentials for charge (blue) and discharge (red) cycles. Dashed lines represent wait periods necessary for $^{31}P\{^1H\}$ NMR data acquisition. Each cycle is 24 hours. Top: instrumental measure of delivered charge (purple) versus charge used for reduction of **4.1** measured by quantification of total reduced products, **4.4N** and **4.5N**, by $^{31}P\{^1H\}$ NMR spectroscopy (pink).

PC was used to solubilize **4.5** and benzene was used to solubilize the TPO and $CoCp_2^*$ in solution. While the use of excess TPO is well reasoned (*vide supra*), the use of excess **4.1** was found to be necessary for optimal electrochemical performance. An excess of **4.1** was used to keep the applied current (I_{app}) below the limiting current at any given time ($I_l(t)$) for the presumed EC mechanism involving reduction of **4.1** followed by uranyl ligation. This allowed the use of a galvanostatic charge/discharge procedure operating close to the mass–transfer–controlled plateau (similar to potentiostatic methods) but with the added benefit of not

requiring prior knowledge of the optimal applied voltage, which will be a function of both the onset of the reductive process and total cell impedance[68]. Attempts at GBE with stoichiometric equivalents of **4.1**, revealed an earlier than expected onset of $I_{app} > I_l(t)$, clearly indicating that additional and unwanted electrochemical processes were being accessed, perhaps indicating an initial degradation of **4.1** within the system. Therefore, an initial ratio of 0.5:6:8 for $[UO_2Cl_2(THF)_2]_2$:**4.1**:TPO reagents was utilized. An initial $^{31}P\{^1H\}$ NMR spectrum revealed a sharp signal for **4.1** and TPO (A, **Figure 4.10**). Upon addition of $[UO_2Cl_2(THF)_2]_2$, the signal for TPO becomes broadened, analogous to the chemical capture/release experiments (B, **Figure 4.10**). Electrochemical capture of UO_2^{2+} was initiated by galvanostatically charging the solution to a 75% theoretical state of charge (SOC) relative to the UO_2^{2+} concentration (b, **Figure 4.9**). Analysis of the reaction mixture by $^{31}P\{^1H\}$ NMR spectroscopy revealed the conversion of **4.1** to the captured products **4.4N** (X = Cl) and **4.5N** – the analogues of **4.4** and **4.5** but with $[Bu_4N]^+$ cations (**Figure 4.4**) – with release of all TPO, as determined by integration vs. the internal standard (**Figure 4.10**, cycle 1 (blue)). To initiate the electrochemical release of UO_2^{2+}, the cell was galvanostatically discharged to a final SOC of 15% (b, **Figure 4.9**, red; SOC extrema of 0 and 100% were not used in order to avoid unwanted secondary electrochemical processes).[68]

Analysis of the reaction mixture by $^{31}P\{^1H\}$ NMR spectroscopy revealed the full conversion of **4.4N** and **4.5N** back to **4.1**, along with the presence of a broadened TPO resonance (**Figure 4.10**, cycle 1 (red)). The capture and release by GBE was carried out over the course of another five full cycles (b, **Figure 4.9**), with analyses of the reaction mixtures by $^{31}P\{^1H\}$ NMR spectroscopy after each run (**Figure 4.10**). We observed that repeated cycling resulted in a loss of electrochemically generated **4.4N**, which we attributed to chloride

migration to the counter compartment over time. The gradual appearance of a minor unknown product with a $^{31}P\{^{1}H\}$ resonance at 45 ppm was also observed after each charge cycle (**Figure 4.10**). Analysis of the $^{31}P\{^{1}H\}$ NMR integrations revealed approximate average losses of: 0.3%/cycle for TPO, 3.4%/cycle for **4.5N**, and 7.2%/cycle for **4.1**, perhaps attributable to electrochemical side reactions[69-70]. Lastly, analysis of measured instrumental charge transferred relative to total charge transferred for UO_2^{2+} capture (determined by $^{31}P\{^{1}H\}$ NMR integrations) revealed a plateauing trend over increasing cycle number with differences in charge attributed to Faradaic losses (b, **Figure 4.9** top). Together, these results demonstrate the successful monophasic electrochemical capture and release of UO_2^{2+}.

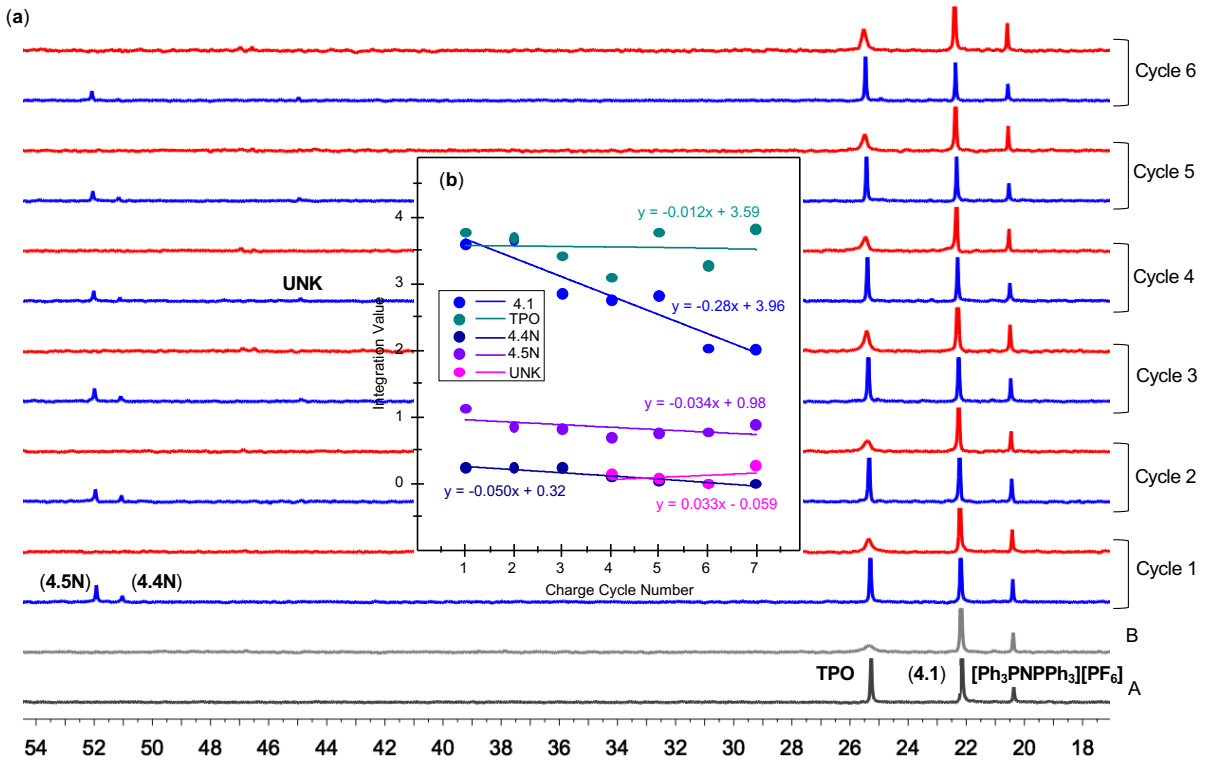

Figure 4.10. (**a**) A; $^{31}P\{^{1}H\}$ NMR spectrum of 6.0 equiv of TPO and 5.0 equiv of **4.**1 with 1.0 equiv of $[Ph_3PNPPh_3][PF_6]$ as the analytical standard. B; $^{31}P\{^{1}H\}$ NMR spectrum of 6.0 equiv of TPO and 5.0 equiv of **4.1** in the presence of 0.5 equiv $[UO_2Cl_2(THF)_2]_2$. Cycles 1–6; $^{31}P\{^{1}H\}$ NMR spectra of charged (blue) and discharged (red) solutions. An unknown species at 45 ppm

begins to appear after multiple cycles. (**b**) Plot of integrated values for all ^{31}P–containing species obtained from the charged spectra versus charge cycle number. The repeated cycling resulted in loss of electrochemically generated **4.4N** (average loss of 15.6 %/cycle) due to presumed chloride migration over the anion exchange membrane. There was little change in yield of TPO (average loss of 0.3 %/cycle) with larger losses in 1 (average loss of 7.2 %/cycle) and **4.5N** (average loss of 3.4 %/cycle). The %/cycle values were estimated from the calculated trendlines by taking the ratio of the slope vs. the y–intercept values.

4.2.5 Biphasic electrochemical capture and release

A biphasic extraction scheme involving dissolved UO_2^{2+} (from $UO_2(NO_3)_2(THF)_2$) in the aqueous phase and **4.1** in the organic phase was next explored as a model system (**Figure 4.11**)[71]. We switched solvents from PC to water–immiscible 1,2–dichloroethane (DCE) primarily because of the solubility of **4.4N**/**4.5N** in DCE. Additionally, we modified our H–cell design to include a physical glass frit separator coupled with a heterogeneous carbon additive acting as a capacitive buffer, analogous to a previous report[72], due to the incompatibility of DCE with the AEM. The capture and release of UO_2^{2+} was simultaneously monitored by $^{31}P\{^1H\}$ NMR and ultraviolet–visible absorption (UV/Vis) spectroscopies for the organic and aqueous layers, respectively. We note that the vibronic ligand–to–metal charge transfer (LMCT) absorption of UO_2^{2+} (425 nm) is pH–dependent, resulting in a variable extinction coefficient (ε)[73-74]; therefore, a buffered solution of UO_2^{2+} was used.

A DCE solution of **4.1** (1.0 equivalent) with $[Bu_4N][PF_6]$ as supporting electrolyte was galvanostatically charged to a ~ 75% theoretical SOC. Analysis of the solution by $^{31}P\{^1H\}$ NMR spectroscopy revealed the clean conversion of most of **4.1** to **4.2b** (a→b, **Figure 4.11**). A sodium acetate (NaOAc)–buffered (pH = 5.4) water solution containing 1.25 equivalents of

$UO_2(NO_3)_2(THF)_2$ was next added to the DCE layer with mixing. Approximately 0.9 equivalent of UO_2^{2+} was captured from the aqueous phase as evidenced by comparing the before and after UV/Vis spectra (b→d, **Figure 4.11**). Analysis of the DCE solution by $^{31}P\{^1H\}$ NMR spectroscopy revealed the clean formation of a single resonance at 51.5 ppm (d, **Figure 4.11**).

Given the similar chemical shifts of isolated complexes **4.4** (51.1 ppm) and **4.5** (52.0 ppm), as well as the quantity of UO_2^{2+} captured (0.9 equivalent), we reported that the uranyl is likely the mono–ligated **4.4N** (X = OAc^- due to the buffer); however, we have found in further experiments that upon isolation of the reaction mixture and recrystallization by vapor diffusion with DCE/Et_2O leads to large yellow block crystals suitable for XRD analysis, isolating complex **4.5N**. $^{31}P\{^1H\}$ analysis of the crystals in DCE shows a single resonance at a chemical shift (51.5 ppm) identical to the chemical shift in all biphasic experiments. We have yet been able to determine the reason for isolation of this product in high yield, as it is not the predicted stoichiometric product. Additionally, it is important to note that original experiments were conducted in a stoichiometry of 2:1 for **4.2b**:$UO_2(NO_3)_2(THF)_2$. It was predicted that excess of ligand would promote formation of complex **4.5N** in the biphasic capture scheme. We found that addition of excess ligand led to multiple unidentifiable side products that were we unable to isolate and characterize. We rationalized using an excess of UO_2^{2+} could decrease the formation of undesirable side products. We have since isolated and characterized the by–product formed in these reactions, indicating formation of a protonated *nido*–carborane (**5.5**) (detailed in 5.2.1, Chapter 5). In the biphasic scheme, the aqueous phase was next removed and the cell was galvanostatically discharged to achieve a theoretical final SOC of ~ 0 %. Mixing a fresh NaOAc–buffered solution (pH = 5.4) to this solution led to the release of

approximately 0.5 equivalent of UO_2^{2+} from the DCE layer as confirmed by UV/Vis spectroscopy (e→f, **Figure 4.11**).

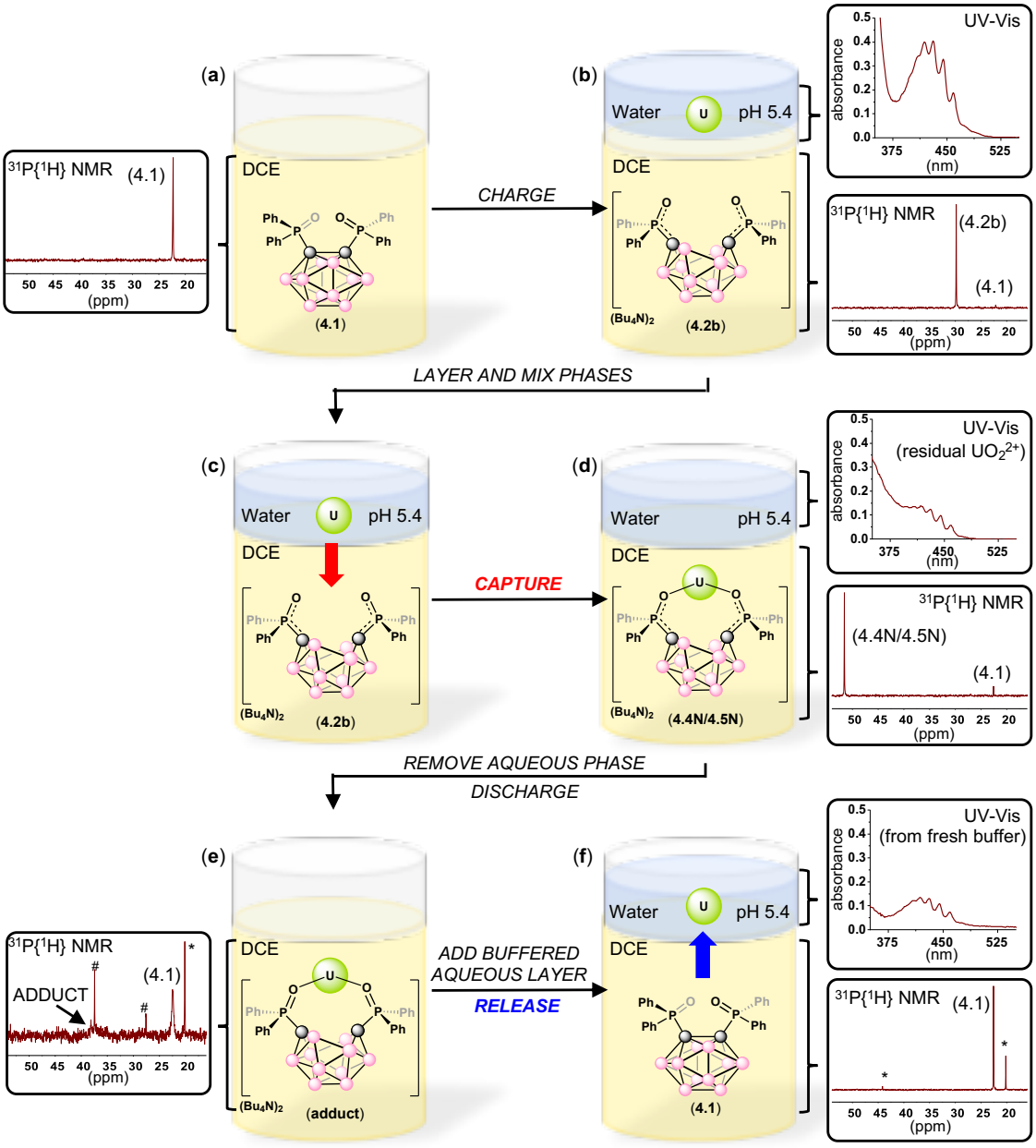

Figure 4.11. For simplicity, only half of the H–cell is displayed here. (**a**) $^{31}P\{^1H\}$ NMR spectrum of DCE layer containing only **4.1** and $[Bu_4N][PF_6]$ ($[PF_6]^-$ resonance not shown) prior to charging. (**b**) (top) UV–Vis spectrum of aqueous phase containing 1.25 equiv of UO_2^{2+} (from $UO_2(NO_3)_2(THF)_2$) prior to mixing with DCE phase. (bottom) $^{31}P\{^1H\}$ NMR spectrum

of DCE layer containing **4.2b** (major) and **4.1** (minor) after charging **4.1** (from (**a**)) galvanostatically. (**c**) Mixing of phases from (**b**) for 2 hours. **(d**) (top) UV–Vis spectrum of aqueous phase after mixing with DCE phase and revealing approximately 0.35 equiv of UO_2^{2+} remaining. (bottom) $^{31}P\{^1H\}$ NMR spectrum of DCE layer after mixing with aqueous phase and showing captured product **4.4N/4.5N** (major) and **4.1** (minor). (**e**) $^{31}P\{^1H\}$ NMR spectrum of DCE layer following phase separation and galvanostatic discharge. A broad peak is observed at 38 ppm which we attribute to an adduct of UO_2^{2+} with **4.1**. This, together with broadened **4.1**, accounts for ~ 75 % of products. Unknown by–products marked with # or * are also shown and account for the rest. (**f**) (top) UV–Vis spectrum of aqueous phase after addition of fresh buffer to the discharged DCE solution (**e**) and mixing for 12 hours. The spectrum reveals the release of approximately 0.50 equiv of UO_2^{2+}. (bottom) $^{31}P\{^1H\}$ NMR spectrum of DCE layer after mixing with fresh buffer and showing the free carborane **4.1** (major), as well as unknown by–products at 44 and 20 ppm, marked by * (~20 % total).

Analysis of the DCE layer by $^{31}P\{^1H\}$ NMR spectroscopy revealed the near quantitative conversion to **4.1**, as well as the formation of minor (~20 %) unknown byproducts (f, **Figure 4.11**). We propose that the acetate ions likely act as the biphasic analog of the monophasic TPO ligands by competitively binding with **4.1** to UO_2^{2+}. Control experiments revealed that negligible biphasic capture of UO_2^{2+} from the NaOAc buffered solution occurred in the presence or absence of **4.1**. Together, these biphasic GBE experiments demonstrate the potential applicability of this redox–switchable capture and release chemistry.

4.3 Conclusions

In summary, this chapter has outlined a new approach to uranyl management involving its capture and most importantly, its release by controlled redox–switchable chelation using a

derivatized *ortho*–carborane in monophasic or biphasic (organic/aqueous) environments. We anticipate this fundamentally new direction in cluster carborane chemistry may have a significant impact on nuclear fuel extraction and waste sequestration activities and may spawn new research directions in related metal capture and release activities.

4.4 Experimental Section

4.4.1 General considerations

All manipulations were performed under an atmosphere of dry, oxygen–free N_2 or Ar by means of standard Schlenk or glovebox techniques (MBraun (equipped with a –38 °C freezer) or VAC gloveboxes). Hexanes, pentane, dichloromethane (DCM), and benzene were dried on an MBraun solvent purification system. Acetonitrile ($–H_3$ and $–D_3$) was dried over CaH_2 for several days prior to distillation. THF was dried over sodium benzophenone and distilled. Propylene carbonate (PC) was degassed by freeze–pump–thaw and stored on activated 4 Å molecular sieves prior to use. 1,2–Dichloroethane (DCE) was initially distilled followed by drying over CaH_2 for several days prior to a second distillation and subsequent storage on activated 4 Å molecular sieves. $[FeCp_2][PF_6]$, $[Bu_4N][Cl]$, and triphenylphosphine oxide (TPO) were purchased from Fisher Scientific, trimesitylphosphine (Mes_3P) was purchased from VWR International, *n*BuLi (1.6 M in hexanes) was purchased from Aldrich, and all were used without further purification. *Ortho*–carborane was purchased from Boron Specialties and sublimed before use. Ph_2PCl was purchased from Aldrich and vacuum distilled prior to use. Decamethylcobaltocene ($CoCp^*_2$) was purchased from Aldrich and purified by filtration through Celite using pentane, followed by recrystallization from pentane at –38 °C over several days. $[Bu_4N][PF_6]$ was purchased from Oakwood Chemicals and purified by twice recrystallizing from hot ethanol. The recrystallized product was then washed with cold water,

cold ethanol, and pentane prior to drying at 100 °C under vacuum for 24 h. Sodium acetate (NaOAc) buffer was prepared from a stock solution purchased from Aldrich (pH 4.9) and adjusted to pH 5.4 using NaOH. The pH value was confirmed using a pH meter. Ketjenblack® EC–600JD (KB) was purchased from a private supplier. $UO_2Cl_2(TPO)_2$,[65] $[UO_2Cl_2(THF)_2]_2$,[59] $[UO_2(NO_3)_2(THF)_3]$,[75] KC_8,[76] and bis(triphenyl–phosphoranylidene)ammonium hexafluorophosphate ($[Ph_3PNPPh_3][PF_6]$)[77] were prepared by literature procedures.

NMR spectra were obtained on a Varian Unity Inova 500 MHz or Agilent Technologies 400 MHz spectrometer, and referenced to residual solvent resonances of acetonitrile (MeCN–d_3) or dichloromethane (DCM–d_2), or externally (^{11}B: 85% $(Et_2O)BF_3$, ^{31}P: 85% H_3PO_4,). Chemical shifts (δ) are recorded in ppm. All ^{11}B and ^{11}B{^{1}H} NMR spectra were processed using MestReNova software in order to reduce background signal with a linewidth of approximately 3000 Hz from the Pyrex NMR tubes. The NMR time–domain data were first left–shifted to discard the first ~0.1 ms. To correct the linear phase change, linear prediction (LP) is used to fill the initial discarded data before Fourier transform or an appropriate linear phase correction is applied to the frequency domain data after Fourier transform. T_1 relaxation values for ^{31}P nuclei were determined using the inversion–recovery method. The delay times after the 180–degree inversion pulse were varied up to the maximum of 5 times of the expected T_1 values. T_1's were calculated using the following equation.

Formula for calculating T_1 values from inversion recovery method.

$$\mathrm{I(t)} = \mathrm{A} * \exp\left(-\frac{\mathrm{t}}{T_1}\right) + \mathrm{B}$$

The signal recovery curve was fit with an exponential function to extract the T_1 values. Subsequent 1D spectra were acquired with 5 times the longest T_1 value measured for accurate integrations (**Figure 4.12**).

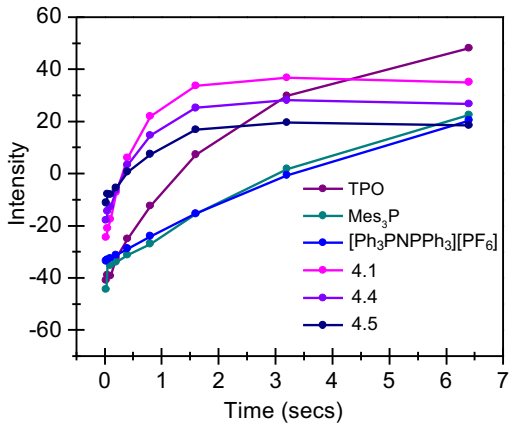

Figure 4.12. T_1 relaxation values for ^{31}P nuclei were determined using the inversion–recovery method. T_1 values (s) were determined for TPO: 2.3; Mes_3P: 5.1; $[Ph_3PNPPh_3][PF_6]$: 7.1; **4.1**: 0.51; **4.4**: 0.64; **4.5**: 0.57 (**Table 4.2**).

Table 4.2. Calculated T_1 values.

Compound	T_1 Value
TPO	2.3
Mes_3P	5.1
$[Ph_3PNPPh_3][PF_6]$	7.1
4.1	0.51
4.4	0.64
4.5	0.57

UV/Vis absorption spectra were collected on a Shimadzu UV–2401PC spectrophotometer. The UO_2^{2+} extinction coefficient (Ɛ) was experimentally determined to be 7.715 $L \bullet mol^{-1} \bullet cm^{-1}$ (460 nm) at pH 5.4.

Elemental analyses (C, N, H) were recorded at the University of California, Berkeley using a Perkin Elmer 2400 Series II combustion analyser.

Cyclic Voltammetry was performed on a CH Instruments Electrochemical Analysis potentiostat, equipped with a 3 mm diameter glassy carbon working electrode, a Ag wire pseudo–reference electrode, and a Pt wire counter electrode using a $[Bu_4N][PF_6]$ (0.1 M)

solution as supporting electrolyte. CVs were referenced to the ferrocene/ferrocenium (Fc/Fc^+) redox couple.

Galvanostatic Bulk Electrolysis cycling experiments were carried out using a Metrohm Autolab PGSTAT128N potentiostat/galvanostat and carried out inside an Ar glovebox. The full experimental setup for both the mono– and biphasic cycling experiments are described below.

X–ray crystallography data was collected on a Bruker KAPPA APEX II diffractometer equipped with an APEX II CCD detector using a TRIUMPH monochromator with a Mo Kα X–ray source (α = 0.71073 Å). The crystals were mounted on a cryoloop under Paratone–N oil, and all data were collected at 100(2) K using an Oxford nitrogen gas cryostream system. A hemisphere of data was collected using ω scans with 0.5° frame widths. Data collection and cell parameter determination were conducted using the SMART program. Integration of the data frames and final cell parameter refinement were performed using SAINT software. Absorption correction of the data was carried out using SADABS. Structure determination was done using direct or Patterson methods and difference Fourier techniques. All hydrogen atom positions were idealized and rode on the atom of attachment. Structure solution, refinement, graphics, and creation of publication materials were performed using SHELXTL or OLEX[2].

4.4.2 Synthesis of compounds

Synthesis of *closo*–(1,2–$(Ph_2PO)_2$–1,2–$C_2B_{10}H_{10}$) (4.1): The synthesis of compound **4.1** was accomplished in two steps by modifications to literature procedures.[31, 78]

Step 1: A solution of *n*BuLi in hexane (1.6 M, 28.2 mL, 45 mmol) was added at –78 °C dropwise to a solution of *ortho*–carborane (3.1 g, 21.5 mmol) in dry diethyl ether (250 mL), resulting in the formation of a fine colourless precipitate. The reaction was slowly warmed to

room temperature, and after stirring for 30 mins at room temperature, the mixture was cooled to 0 °C and Ph_2PCl (7.7 mL, 41.7 mmol) was added dropwise, resulting in a pale orange solution with a colourless precipitate. The mixture was stirred for 30 mins at 0 °C. The solution was brought to room temperature and stirred for 30 mins and was subsequently warmed to reflux and stirred for an additional 30 mins. The solution was cooled to 0 °C and water (30 mL) was slowly added to the mixture. The mixture was allowed to stir for 20 mins and was filtered over a glass frit, where the resulting solid was washed with additional water (30 mL) and diethyl ether (20 mL). The solid was dried under vacuum at 100 °C for 2 h. The product was recrystallized from a mixture of hexane/toluene and was obtained in 81% yield (8.6 g, 16.7 mmol.) **^{1}H NMR** (400 MHz, $CDCl_3$): δ 7.06–7.47 (m, 20H); 0.98–2.66 (broad, 10H). ^{11}B NMR (400 MHz, $CDCl_3$): δ –0.40; –9.42. **^{11}B{^{1}H} NMR** (400 MHz, $CDCl_3$): δ –0.40; –7.21; –9.42. **^{31}P{^{1}H} NMR** (400 MHz, $CDCl_3$): δ 7.88.

Step 2: A solution of H_2O_2 (30% in water, 1.8 mL, 58.7 mmol) was added dropwise to a solution of [*closo*–(1,2–$(Ph_2P)_2$–1,2–$C_2B_{10}H_{10}$)] (from step 1) (2.1 g, 4.1 mmol) in THF (50 mL). The reaction was stirred for 3 h at room temperature. The reaction was monitored by ^{31}P NMR spectroscopy for formation of an unwanted side–product at 49 ppm. Once this product formed, the reaction was discontinued by addition of chloroform. The mixture was washed with water and brine, the phases separated, and the organic layer dried with Na_2SO_4. The solvent was removed, and the solid was slowly recrystallized from acetonitrile to yield a colourless crystalline solid. The solid was dried under vacuum at 80 °C for several hours. (1.4 g, 2.6 mmol, 60% yield). Single crystals suitable for X–ray crystallography were obtained by vapour diffusion of pentane in a saturated THF solution of **4.1**. **^{1}H NMR** (400 MHz, MeCN–d_3): δ 7.99 (m, 8H); 7.63 (m, 4H); 7.54 (m, 8H); 2.5 (broad s, 10H). **^{11}B** and **^{11}B{^{1}H} NMR**

(400 MHZ, MeCN–d_3): δ 0.66; –8.75. **^{31}P{^{1}H} NMR** (400 MHz, MeCN–d_3): δ 22.8. *Anal. Calcd*. for $C_{26}H_{30}B_{10}O_2P_2$: C, 57.35; H, 5.55. Found: C, 57.33; H, 5.66. Selected interatomic distances for **4.1** where C···C: 1.688(4) Å; P···P: 3.537 Å.

Synthesis of UO_2Cl_2(4.1)$_2$: A 20 mL vial equipped with a magnetic stirbar was charged with **4.1** (54.4 mg, 0.1 mmol) and 2 mL of DCM. In a separate vial, $[UO_2Cl_2(THF)_2]_2$ (24.2 mg, 0.025 mmol) was dissolved in 2 mL of DCM and added to the stirring solution of **4.1**, resulting in the formation of a light–yellow suspension. After 1 h, the reaction mixture became homogeneous. This was stirred for an additional 24 h at room temperature. The solvent was removed, yielding a yellow solid (62.5 mg). Multiple attempts were made to obtain single crystals suitable for XRD studies but failed. **^{1}H NMR** (400 MHz, DCM–d_2): δ 8.32–6.29 (m, 20H); 2.5 (broad s, 10H). **^{11}B** and **^{11}B{^{1}H} NMR** (400 MHz, DCM–d_2): δ 5.84; –8.46. **^{31}P{^{1}H} NMR** (400 MHz, DCM–d_2): δ 38.8 (s); 38.4 (s). *Anal. Calcd*. for $C_{52}H_{60}B_{20}Cl_2O_6P_4U$•1/2$CH_2Cl_2$: C, 43.05; H, 4.16. Found: C, 42.76; H, 4.32.

Synthesis of [CoCp$^*_2$]$_2$[(*nido*–1,2–(Ph$_2$PO)$_2$–1,2–$C_2B_{10}H_{10}$)] (4.2a): A 20 mL vial equipped with a magnetic stirbar was charged with **4.1** (54.4 mg, 0.1 mmol) and 6 mL of benzene. In a separate vial, $CoCp^*_2$ (69.1 mg, 0.2 mmol, 2.0 equiv) was dissolved in 4 mL of benzene and added dropwise to the stirring solution of **4.1**. Upon addition, a yellow solid immediately precipitated from the reaction mixture and the mixture was stirred for an additional 4 h at room temperature. Stirring was discontinued and the solid was allowed to settle to the bottom of the vial. The supernatant was decanted and filtered on a plug of Celite. The solids were washed with benzene (3 x 6 mL) and each washing was filtered over the same Celite plug. The remaining solids were then dissolved in a minimal amount of MeCN (2 mL) and filtered on the same Celite plug into a new vial. The MeCN filtrate was collected and the volatiles were

removed *in vacuo,* yielding a shiny golden–yellow solid (114.3 mg, 0.95 mmol, 95% yield). Single crystals suitable for X–ray crystallography were obtained by vapour diffusion of Et_2O in a saturated MeCN solution of **4.2a** at –38 °C. **^{1}H NMR** (400 MHz, MeCN–*d_3*): δ 8.05 (broad m, 8H); 7.24 (broad s, 12H); 1.62 (s, 60H). Note: Carborane B–**H** resonances are too broad to be observed. **^{11}B** and **^{11}B{^{1}H} NMR** (400 MHZ, MeCN–*d_3*): δ 20.24; –0.62; –18.46; –22.06. **^{31}P{^{1}H} NMR** (400 MHz, MeCN–*d_3*): δ 29.8. *Anal. Calcd*. for $C_{66}H_{90}B_{10}Co_2O_2P_2$: C, 65.88; H, 7.54. Found: C, 65.57; H, 7.67. Selected interatomic distances for **4.2a** where C···C: 2.860 Å; P···P: 5.036 Å.

Synthesis of $[Bu_4N]_2[(nido–1,2–(Ph_2PO)_2–1,2–C_2B_{10}H_{10})]$ (4.2b): The synthesis of compound **4.2b** was accomplished in two steps.

Step 1: In the glovebox, a 250 mL round bottom equipped with a magnetic stirbar was charged with **4.1** (272.2 mg, 0.5 mmol), 20 mL of THF, and cooled to –78 °C. In a separate vial, KC_8 (182.4 mg, 1.35 mmol, 2.7 equiv) was suspended in 20 mL of THF and added slowly dropwise to the stirring solution of **4.1**. Upon addition, the KC_8 suspension began to turn grey in colour and was stirred for 30 mins at room temperature. Stirring was discontinued and the mixture was filtered over a pad of Celite on a fine glass frit. The graphite pad was washed additionally with MeCN (3 x 5 mL). The filtrate was collected and the volatiles were removed *in vacuo,* yielding a pale–yellow oil. The oil was redissolved in THF (5 mL) and layered with 5 mL of pentane and was recrystallized at –38 °C, yielding a white solid (234.1 mg, 0.38 mmol, 75% yield). **^{1}H NMR** (400 MHz, MeCN–*d_3*): δ 7.81 (broad m, 8H); 7.28 (broad m, 12H). Note: Carborane B–**H** resonances are too broad to be observed. **^{11}B and ^{11}B{^{1}H} NMR** (400 MHZ, MeCN–*d_3*): δ 20.24; –0.62; –18.46; –22.06. **^{31}P{^{1}H} NMR** (400 MHz, MeCN–*d_3*): δ 31.8. *Anal. Calcd*. for $C_{26}H_{30}B_{10}K_2O_2P_2$•THF: C, 51.86; H, 5.51. Found: C, 51.09; H, 5.47.

Step 2: A 20 mL vial equipped with a magnetic stirbar was charged with $[K]_2$[(*nido*–1,2–$(Ph_2PO)_2$–1,2–$C_2B_{10}H_{10}$)•THF] (655.4 mg, 0.94 mmol) (Step 1), 15 mL of DCM, and was cooled to –78 °C. In a separate vial, $[Bu_4N][Cl]$ (528 mg, 1.88 mmol, 2.0 equiv) was dissolved in 10 mL of DCM and added dropwise to the stirring carborane suspension. Upon addition, the reaction mixture became homogenous and after 1 h, a white precipitate began to crash out. This mixture was stirred for 2 h at room temperature. Stirring was discontinued and all volatiles were removed, yielding a pale–yellow solid. A minimal amount of DCM (3 mL) was added and the mixture was filtered on a plug of Celite. The solids were washed with chilled DCM (3 x 2 mL) and each washing was filtered over the same Celite plug. The DCM filtrate was collected and the volatiles were removed *in vacuo,* yielding a pale–yellow residue which was triturated with pentane (10 mL) and dried in vacuo to yield an off–white solid which was recrystallized from DCM and pentane (690.4 mg, 0.67 mmol, 71 % yield). **^{1}H NMR** (400 MHz, MeCN–d_3): δ 8.03 (m, 8H); 7.25 (broad s, 12H); 3.08 (m, 16H); 1.59 (m, 16H); 1.35 (m, 16H); 0.96 (t, 24H). Note: Carborane B–**H** resonances are too broad to be observed. **^{11}B** and **^{11}B{^{1}H} NMR** (400 MHZ, MeCN–d_3): δ 20.25; –0.65; –18.42; –22.05. **^{31}P{^{1}H }NMR** (400 MHz, MeCN–d_3): δ 30.1. *Anal. Calcd*. for $C_{58}H_{102}B_{10}N_2O_2P_2$: C, 67.67; H, 9.99. Found: C, 66.81; H, 10.29.

Synthesis of [$UO_2Cl(THF)_2$][*nido*–7,8–$(Ph_2PO)_2$–7,8–$C_2B_9H_{10}$] (4.3): A 20 ml vial equipped with a magnetic stirbar was charged with **4.1** (65.2 mg, 0.12 mmol) and 4 ml of THF. In a separate vial, $[UO_2Cl_2(THF)_2]_2$ (24.2 mg, 0.025 mmol) was dissolved in 4 ml of THF and added to the stirring solution of **4.1**. Upon addition, the solution became yellow in color. The solution stirred overnight (20 hrs) at room temperature. The solvent was removed yielding a shiny yellow solid. The product was recrystallized from THF/hexanes yielding yellow crystals

(63.7 mg, 0.065 mmol, 65% yield). **^{1}H NMR** (400 MHz, *d_3*–MeCN): δ 7.9–7.2 (m, 20H). **^{31}P{^{1}H} NMR** (400 MHz, *d_3*–MeCN): δ 48.5 ppm. **^{11}B{^{1}H} NMR** (400 MHZ, *d_3*–MeCN): δ 19.9; –9.7; –18.3; –31.6; –34.4. *Anal. Calcd*. for $C_{34}H_{44}B_9O_6P_2U$: C, 41.61; H, 4.52. Found: C, 42.05; H, 4.95.

Synthesis of [CoCp$^*_2$]$_2$[UO$_2$Cl$_2$(*nido*–1,2–(Ph$_2$PO)$_2$–1,2–C$_2$B$_{10}$H$_{10}$)] (4.4): A 20 mL vial equipped with a magnetic stirbar was charged with $[UO_2Cl_2(THF)_2]_2$ (16.9 mg, 0.018 mmol) and 4 mL of MeCN. In a separate vial, **4.2a** (42.2 mg, 0.035 mmol) was dissolved in 4 mL of MeCN and then added dropwise to the stirring solution of $[UO_2Cl_2(THF)_2]_2$, turning dark yellow in colour. After stirring for 5 mins, a yellow solid began to precipitate from the reaction mixture and this was stirred at room temperature for 4 h. Stirring was discontinued and the mixture was passed over a plug of Celite, collecting a yellow solid and a yellow filtrate. The solvent was removed from the yellow filtrate yielding a yellow solid which was washed with THF (3 x 2 mL) and passed over another plug of Celite. The filtrate was collected and the volatiles were removed *in vacuo,* yielding a yellow powder. Residual [CoCp$^*_2$][Cl] was removed by selectively recrystallizing the mixture by vapor diffusion of pyridine/Et_2O at –38 °C. The supernatant was transferred and volatiles removed collecting a yellow solid (36.3 mg, 0.024 mmol, 69 % yield). Single crystals suitable for XRD studies were grown by vapour diffusion of Et_2O into a saturated MeCN solution of **4.4** at room temperature. **^{1}H NMR** (400 MHz, MeCN–*d_3*): δ 8.13 (m, 10H); 7.35 (m, 10H); 1.66 (s, 60H). Note: Carborane B–**H** resonances are too broad to be observed. **^{11}B** and **^{11}B{^{1}H} NMR** (400 MHZ, MeCN–*d_3*): δ 0.27; –16.90; –19.69. **^{31}P{^{1}H} NMR** (400 MHz, MeCN–*d_3*): δ 51.12. *Anal. Calcd*. for $C_{66}H_{90}B_{10}Cl_2Co_2O_4P_2U$•2MeCN: C, 51.70; H, 5.95; N, 1.72. Found: C, 51.91; H, 5.88; N, 1.74.

Selected interatomic distances (Å) and angles (º) for **4.4** where C···C: 2.855 Å; P···P: 4.697 Å; O1–U–O2: 86.5(3)º.

Synthesis of $[CoCp^*_2]_2[UO_2(nido\text{–}1,2\text{–}(Ph_2PO)_2\text{–}1,2\text{–}C_2B_{10}H_{10})_2]$ (4.5): A 20 mL vial equipped with a magnetic stirbar was charged with **4.2a** (26.6 mg, 0.022 mmol) and 1.5 mL of MeCN. In a separate vial, $[UO_2Cl_2(THF)_2]_2$ (5.3 mg, 0.0055 mmol) was dissolved in 1.5 mL of MeCN and then added dropwise to the stirring solution of **4.2a**. After stirring for 5 mins, a yellow solid began to precipitate from the reaction mixture and this was stirred at room temperature for 24 h. Stirring was discontinued and the solid was allowed to settle to the bottom of the vial. The supernatant was decanted and filtered on a plug of Celite. The solids were washed with MeCN (3 x 2 mL) and each washing was filtered over the same Celite plug. The remaining solids were then dissolved in a minimal amount of pyridine and filtered on the same Celite plug into a new vial. The pyridine filtrate was collected and the volatiles removed *in vacuo,* yielding a light–yellow powder (35.5mg, 0.018 mmol, 80% yield). Single crystals suitable for XRD analysis were grown from a small–scale reaction in a J–young NMR tube which was charged with a solution of **4.2a** (12.0 mg, 0.01 mmol) in MeCN–d_3 (0.25 mL). A solution of $[UO_2Cl_2(THF)_2]_2$ (2.4 mg, 0.0025 mmol) in MeCN–d_3 (0.25 mL) was added to this whereupon crystals suitable for XRD analysis slowly formed on the walls of the NMR tube. **^{1}H NMR** (400 MHz, MeCN–d_3): δ 8.13 (m, 15H); 7.38 (m, 10H); 7.24 (m, 15H); 1.68 (s, 60H). Note: Carborane B–**H** resonances are too broad to be observed. **^{11}B** and **^{11}B{^{1}H} NMR** (400 MHZ, MeCN–d_3): δ 0.26; –17.15; –20.66. **^{31}P{^{1}H} NMR** (400 MHz, MeCN–d_3): δ 52.0. *Anal. Calcd*. for $C_{92}H_{120}B_{20}Co_2O_6P_4U$: C, 54.76; H, 5.99. Found: C, 55.22; H, 6.36. Selected interatomic distances (Å) and angles (º) for **4** where C···C: 2.857 Å; P···P: 4.806 Å; O1–U–O2: 89.7(17)º.

4.4.3 Cyclic voltammograms

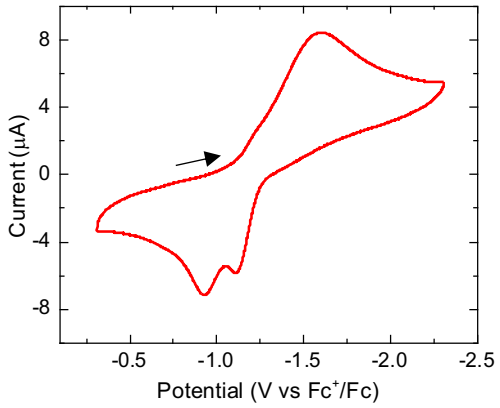

Figure 4.13. CV of **4.1** (0.5 mM) in a 0.1 M [Bu_4N][PF_6] THF solution using a 3 mm diameter glassy–carbon working electrode and platinum–wire counter electrode, referenced to the Fc^+/Fc redox couple (scan rate = 100 mV/s). The quasi–reversible redox event exhibits two cathodic waves at –0.93 and –1.11 V.

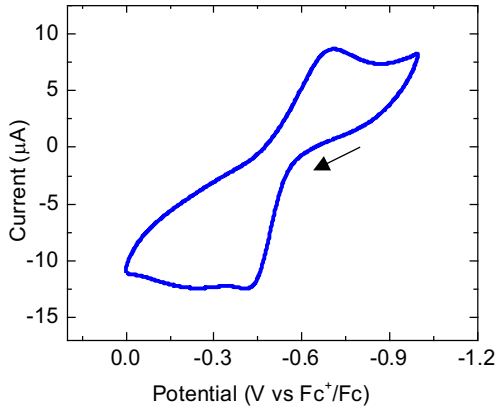

Figure 4.14. CV of **4.5** (1.0 mM) in a 0.1 M [Bu_4N][PF_6] PC solution using a 3 mm diameter glassy–carbon working electrode and platinum–wire counter electrode, referenced to the Fc^+/Fc couple (scan rate = 100 mV/s). The quasi–reversible redox event exhibits one anodic wave at –0.42 V.

4.4.4 Monophasic chemical capture and release of UO_2^{2+}

Formation of *in–situ* generated [$(UO_2)(TPO)_2Cl_2$]: A 20 mL vial equipped with a magnetic stirbar was charged with **4.1** (2.0 equiv, 5.4 mg, 0.01 mmol), TPO (4.0 equiv, 5.6 mg, 0.02 mmol), and Mes_3P (4.0 equiv, 7.7 mg, 0.02 mmol) and dissolved in a 3:1 PC:benzene (3 mL) solvent system. A 500 μL aliquot was taken from this mixture and placed in an NMR tube equipped with a MeCN–d_3 capillary tube. A $^{31}P\{^1H\}$ NMR spectrum was collected and the relative integrations recorded (a, **Figure 4.8**). The NMR solution was returned to the vial and $[UO_2Cl_2(THF)_2]_2$ (0.5 equiv, 2.4 mg, 0.0025 mmol) was added. The mixture was stirred vigorously until all the solids were dissolved (~20 mins), resulting in a light–yellow coloured solution. After 1 h, a 500 μL aliquot was taken from the reaction mixture and placed in an NMR tube equipped with a MeCN–d_3 capillary tube. A $^{31}P\{^1H\}$ NMR spectrum was obtained (b, **Figure 4.8**). After the spectrum was recorded, the NMR sample was transferred back into the reaction mixture.

Reduction: To the solution generated above, $CoCp^*_2$ (4.0 equiv, 6.6 mg, 0.02 mmol) in 100 μL of benzene was added to the solution dropwise. Upon addition, the solution turned golden in colour and was stirred for 1 h at room temperature. A 500 μL aliquot was then taken from the reaction mixture and placed in an NMR tube equipped with a MeCN–d_3 capillary tube. A $^{31}P\{^1H\}$ NMR spectrum was obtained (c, **Figure 4.8**). After the spectrum was obtained, the NMR solution was transferred back into the reaction mixture.

Oxidation: To the reduced solution above, $[Fc][PF_6]$ (4.0 equiv, 6.6 mg, 0.02 mmol) was added. Upon addition, the solution turned green in colour, and then turned a golden colour. This was stirred for 1 h at room temperature after which a 500 μL aliquot was taken from the reaction mixture and placed in an NMR tube equipped with a MeCN–d_3 capillary tube. A

$^{331}P\{^{1}H\}$ NMR spectrum was obtained (d, **Figure 4.8**). After the spectrum was obtained, the NMR sample was transferred back into the reaction mixture.

4.4.5 Monophasic electrochemical capture and release of UO_2^{2+}

4.4.5.1 Experimental Conditions

Galvanostatic bulk electrolysis experiments were carried out in a divided glass H–cell (a and b, **Figure 4.15**). The physical barrier between each component of the cell, and the respective two Bio–Logic high–surface coiled Pt electrodes, was an anion exchange membrane (Membranes International, AMI–7001) held in place by two FEP–encapsulated silicon o–rings with a metal clamp. The electrodes were cleaned by rinsing with distilled water and acetone and then heating white–hot with a butane torch prior to use. The anion exchange membrane was soaked in a 0.1 M $[Bu_4N][PF_6]$ solution of PC/benzene (3:1) over 3 Å molecular sieves for 24 hours prior to use.

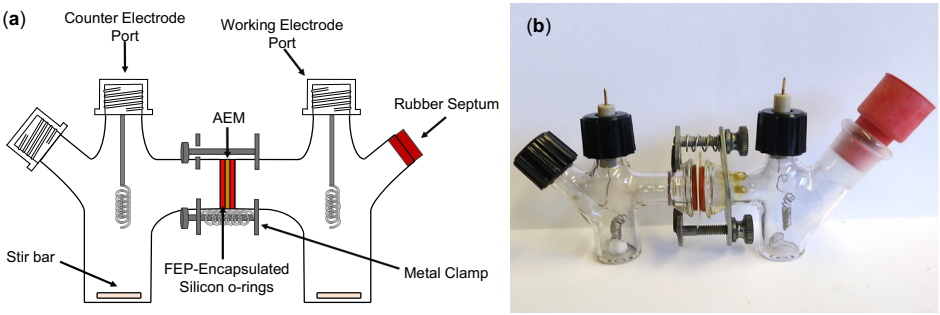

Figure 4.15. (**a**) Schematic of the divided H–cell used for the monophasic galvanostatic bulk electrolysis cycling experiments with UO_2^{2+}. (**b**) Picture of the divided H–cell for the monophasic galvanostatic bulk electrolysis cycling experiments with UO_2^{2+}.

The left compartment, containing the counter electrode, consisted of Fc (41.9 mg, 0.225 mmol) and $[Fc][PF_6]$ (74.5 mg, 0.225 mmol) in 7.0 mL of a 0.1 M $[Bu_4N][PF_6]$ PC:benzene solution. The right compartment, containing the working electrode, contained **4.1** (5 equiv, 40.8 mg,

0.075 mmol), TPO (6 equiv, 25.0 mg, 0.09 mmol), $[UO_2Cl_2(THF)_2]_2$ (0.5 equiv, 7.3 mg, 0.0075 mmol of dimer (1.0 equiv of U monomer)), and $[Ph_3PNPPh_3][PF_6]$ (1.0 equiv, 10.2 mg, 0.015 mmol) in a 0.1 M $[Bu_4N][PF_6]$ PC:benzene solution (7.0 mL).

4.4.5.2 Experimental Parameters

Reduction (UO_2^{2+} capture): to initiate UO_2^{2+} capture, the first cycle was charged with an applied current of –201.0 μA over the course of 6 h to a 75 % state of charge (SOC) relative to the $[UO_2Cl_2(THF)_2]_2$ concentration. After the cell was charged, a wait period of 2 h was incorporated in between charge/discharge cycling (**Figure 4.9**).

Oxidation (UO_2^{2+} release): UO_2^{2+} release was achieved by discharging the cell galvanostatically at an applied current of 68.94 μA over the course of 13 h, utilizing voltage cutoffs (0.0 V), to a final SOC of approximately 15 % relative to the initial $[UO_2Cl_2(THF)_2]_2$ concentration. After each cell discharge, a wait period ranging between 4–5 h was incorporated (depending on when the voltage cutoffs were applied) in between discharging/charging cycles (**Figure 4.9**).

Cycling (capture and release): the cell was charged/discharged over the course of six cycles. Each additional cycle thereafter was charged and discharged galvanostatically at currents of –160.87 μA and 68.94 μA, respectively. This resulted in charging cycles from ~15 to ~75% SOC, and between ~75 to ~15% SOC, respectively. Between each charge/discharge a $^{31}P\{^1H\}$ NMR spectrum was obtained (**Figure 4.10**) using a 40 s relaxation delay (see NMR details above, **Figure 4.12**) with $[Ph_3PNPPh_3][PF_6]$ as the standard. We note that an excess of **4.1** was used to keep the applied current (I_{app}) below the limiting current at any given time ($I_l(t)$) for the presumed EC mechanism involving reduction of **4.1** followed by uranyl ligation. This allows the use of a galvanostatic charge/discharge procedure operating close to the mass–

transfer–controlled plateau (similar to potentiostatic methods) but with the added benefit of not requiring prior knowledge of the optimal applied voltage, which will be a function of both the onset of the reductive process and total cell impedance[68]. Attempts at GBE with stoichiometric equivalents of **4.1**, revealed an earlier than expected onset of $I_{app} > I_l(t)$, clearly indicating that additional and unwanted electrochemical processes were being accessed, perhaps indicating an initial degradation of **4.1** within the system. Therefore, an initial ratio of 0.5:6:8 for $[UO_2Cl_2(THF)_2]_2$:**4.1**:TPO reagents was utilized.

4.4.6 Biphasic electrochemical capture and release of UO_2^{2+}

4.4.6.1 Experimental Conditions

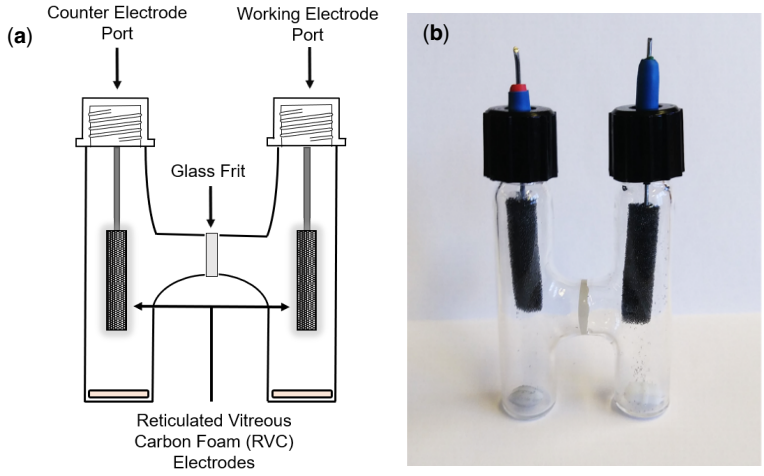

Figure 4.16. (a) Schematic of the two–compartment H–cell used for the biphasic electrochemical capture and release of UO_2^{2+}. (**b**) Picture of the two–compartment H–cell used for the biphasic electrochemical capture and release of UO_2^{2+}.

A complete, stepwise, half–cell figure of the experiments conducted in this section, along with spectroscopic data is shown in **Figure 4.11**. Two–electrode galvanostatic bulk electrolysis was performed in an argon glovebox utilizing a two compartment H–cell with a glass frit separator, a stir bar in each compartment, and reticulated vitreous carbon (RVC) foam electrodes for both

the working and counter electrodes (a and b, **Figure 4.16**). The RVC foam electrodes consisted of a ~5 cm steel rod inserted into 100 PPI Duocel® RVC foam core (length ~2.5 cm; diameter ~3 mm), with a tap bore (length ~5 mm; diameter ~2 mm), which was filled with molten gallium to fuse the steel connector to the RVC foam. Each electrode has an end–to–tip resistance of < 5 Ω. The RVC electrodes were rinsed with methanol and dried under reduced pressure overnight prior to use. The Ketjenblack used was dried for 48 h in a 175 °C oven and ground in a glass mortar and pestle under inert atmosphere prior to use.

4.4.6.2 Experimental Parameters

Reduction (charging): The counter compartment consisted of 400 mg of Ketjenblack suspended in 6 mL of a 0.1 M solution of $[Bu_4N][PF_6]$ in DCE. The working compartment consisted of **4.1** (34 mg, 0.0625 mmol, 1.0 equiv) dissolved in 6 mL of a 0.1 M solution of $[Bu_4N][PF_6]$ in DCE. A charging current of –107.1 μA with a –9.25 C charge cutoff was utilized, resulting in a ~ 75% SOC after 24 h assuming 100% columbic efficiency. Upon completion, the working compartment solution was analysed by $^{31}P\{^1H\}$ NMR spectroscopy to reveal the formation of **4.2b** (a→b, **Figure 4.11**; a, **Figure 4.17**). The working compartment solution was then removed from the H–cell and placed in a 20 mL vial for subsequent capture chemistry.

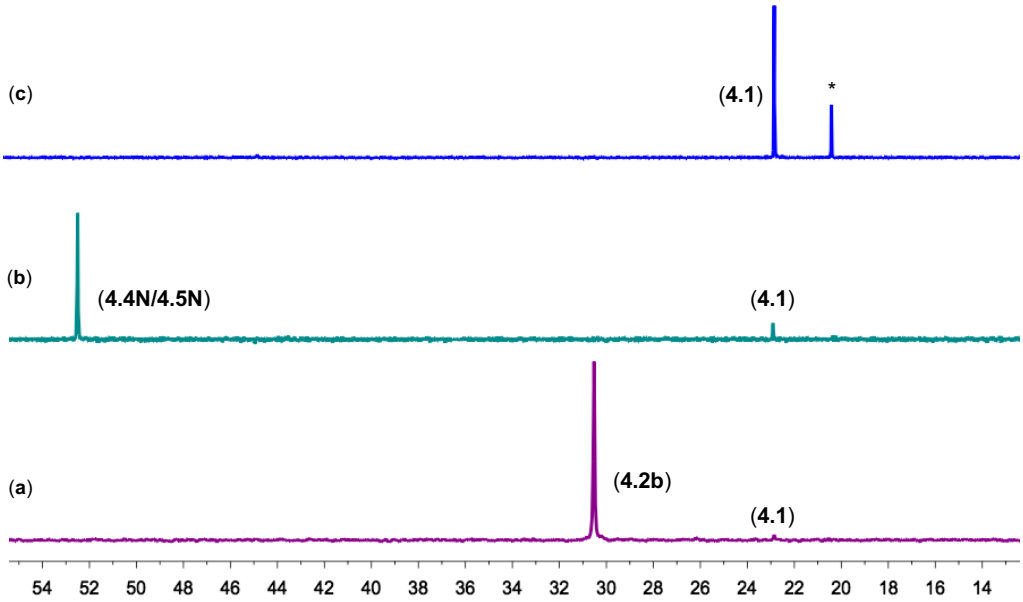

Figure 4.17. (**a**) $^{31}P\{^{1}H\}$ NMR spectrum in DCE of electrochemically reduced **4.1** to produce **4.2b**. (**b**) $^{31}P\{^{1}H\}$ NMR spectrum of DCE layer following UO_2^{2+} capture from the aqueous layer containing $UO_2(NO_3)_2(THF)_2$ in 0.1 M sodium acetate buffer. (**c**) $^{31}P\{^{1}H\}$ NMR spectrum of electrochemically oxidized DCE layer containing **4.4N/4.5N** following extraction of UO_2^{2+} into 0.1 M sodium acetate buffer. Minor unknown by–products (*) are also observed.

UO_2^{2+} capture: A 5 mL vial was charged with excess $UO_2(NO_3)_2(THF)_2$ (42 mg, 0.078 mmol, 1.25 equiv), and dissolved in 3 mL of a 0.1 M sodium acetate buffer adjusted to pH 5.4 (0.026 M UO_2^{2+}). An aliquot of the resulting pale–yellow solution was used to record an initial UV–Vis spectrum (b, **Figure 4.11**; blue, **Figure 4.18**). The aliquot was transferred back to the 5 mL vial and this solution was added slowly dropwise without stirring to the DCE solution containing the electrochemically reduced **4.1** (forming **4.2b**). After addition, the mixture was allowed to stir for 2 hours, resulting in a bright yellow organic phase and a very pale–yellow aqueous phase. Stirring was discontinued and the organic and aqueous phases were separated using a small separatory funnel. An aliquot of the aqueous phase was used to record a UV–Vis

spectrum (d, **Figure 4.11**; red, **Figure 4.18**), indicating that 0.022 mmol of UO_2^{2+} remained, which is equivalent to the capture of 0.056 mmol (~0.9 equiv) to the organic phase. A 1 mL aliquot was taken from the pale yellow dichloroethane layer and transferred to an NMR tube. An unlocked $^{31}P\{^1H\}$ NMR spectrum was collected indicating the formation of **4.4N/4.5N** (d, **Figure 4.11**; b, **Figure 4.17**). The NMR solution was returned to the 20 mL vial.

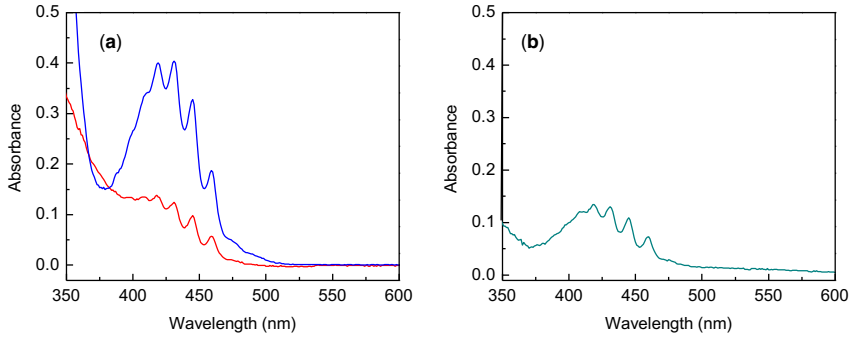

Figure 4.18. (**a**) (blue) Initial UV–Vis spectrum of $UO_2(NO_3)_2(THF)_2$ (0.042 g, 0.078 mmol, 0.026 M, 1.25 equiv) in 3 mL of 0.1 M sodium acetate buffer at pH 5.4. (red) UV–Vis spectrum taken after mixing the aqueous layer with the DCE layer of electrochemically reduced **4.1** (to generate **4.2b**) in a 0.1 M $[Bu_4N][PF_6]$ DCE solution for 2 hours indicating a residual concentration of 0.0073 M consistent with a total quantity of captured UO_2^{2+} to the DCE layer of 0.056 mmol. (**b**) UV–Vis spectrum of 0.1 M aqueous sodium acetate buffer layer at pH 5.4 after mixing for 12 hours with electrochemically oxidized **4.4N/4.5N** in DCE. The concentration of UO_2^{2+} was calculated to be 0.010 M consistent with a total quantity of released UO_2^{2+} from the DCE layer to the aqueous phase of 0.031 mmol.

Oxidation (discharging): Two–electrode galvanostatic bulk electrolysis (discharging) of the captured DCE solution was performed using the same cell utilized for charging. A discharging current of 107.1 μA was applied until 9.49 C of charge was transferred resulting in a final SOC of ~ 0 % (assuming 100% columbic efficiency and no loss of material during the biphasic

capture). Upon completion, the working compartment solution was removed and placed in a 20 mL vial for subsequent release chemistry.

UO_2^{2+} release: The 20 mL vial containing the electrochemically oxidized **4.4N/4.5N** yellow DCE solution was equipped with a stirbar and a solution of 0.1 M sodium acetate buffer adjusted to pH 5.4 (3 mL) was added dropwise to it. The mixture was allowed to stir for 12 hours, resulting in a pale–yellow aqueous phase and a colourless organic layer. The organic and aqueous phases were separated using a small separatory funnel, and an aliquot of the aqueous layer was used to take a UV–Vis spectrum indicating the presence of released UO_2^{2+} (0.031 mmol, ~0.5 equiv) (f, **Figure 4.11**; b, **Figure 4.18**). A 1 mL aliquot was taken from the yellow DCE layer and transferred to an NMR tube. An unlocked $^{31}P\{^1H\}$ NMR spectrum was collected indicating the clean formation of **4.1** and a small unknown by–product at 20.1 ppm. (f, **Figure 4.11**; c, **Figure 4.17**).

4.4.6.3 Biphasic control experiments

UO_2^{2+} migration from water to DCE in the absence of carborane (4.1 or 4.2a/b): A 5 mL vial was charged with $UO_2(NO_3)_2(THF)_2$ (14.0 mg, 0.026 mmol), and dissolved in 1.5 mL of 0.1 M sodium acetate buffer adjusted to pH 5.4 (0.017 M UO_2^{2+}). An aliquot of the resulting pale–yellow solution was used to record an initial UV–Vis spectrum (a, blue, **Figure 4.19**). The aliquot was transferred back to the 5 mL vial. A separate 20 mL vial charged with a stirbar, and $[Bu_4N][PF_6]$ (0.2324 g, 0.1 M) dissolved in DCE (6.0 mL). To the clear DCE solution, the pale–yellow aqueous solution was added slowly dropwise over the course of two minutes without stirring. After addition, the mixture was allowed to stir for 4 hours and the organic phase remained clear. Stirring was discontinued and the organic and aqueous phases were separated using a small separatory funnel. Small aliquots of the aqueous (a, red, **Figure 4.19**)

and organic (b, **Figure 4.19**) phases were used to record UV–Vis spectra which together clearly indicated that the UO_2^{2+} had remained in the aqueous phase.

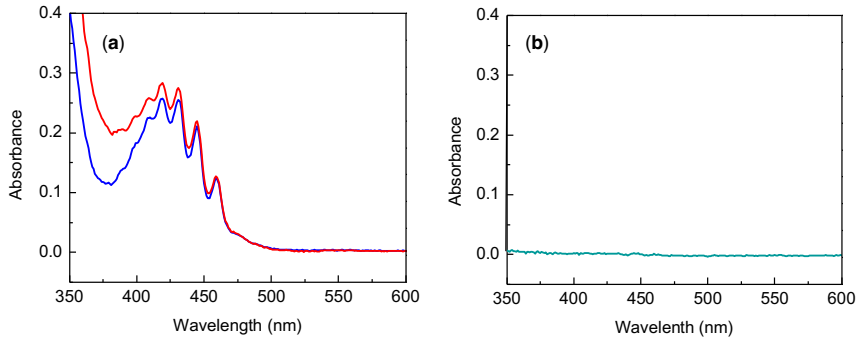

Figure 4.19. (**a**) Control for UO_2^{2+} migration from water to DCE in the absence of carborane **(4.1** or **4.2a/b)**. (blue) Initial UV–Vis spectrum of UO_2^{2+} in 0.1 M sodium acetate buffered solution at pH 5.4. (red) UV–Vis spectrum of aqueous layer after mixing for 4 h with DCE solution containing $[Bu_4N][PF_6]$ (0.1 M). (**b**) Corresponding UV–Vis spectrum of DCE layer after mixing for 4 h with the aqueous layer containing UO_2^{2+} in (**a**).

UO_2^{2+} migration from water to DCE in the presence of 4.1: A 5 mL vial was charged with $UO_2(NO_3)_2(THF)_2$ (14.0 mg, 0.026 mmol, 1.0 equiv), and dissolved in 1.5 mL of 0.1 M sodium acetate buffer adjusted to pH 5.4 (0.017 M UO_2^{2+}). An aliquot of the resulting pale–yellow solution was used to record an initial UV–Vis spectrum (a, blue, **Figure 4.20**). The aliquot was transferred back to the 5 mL vial. A separate 20 mL vial was charged with a stirbar, **4.1** (14.1 mg, 0.026 mmol, 1.0 equiv), $[Bu_4N][PF_6]$ (0.2324 g, 0.1 M), and DCE (6.0 mL). To the clear DCE solution, the pale–yellow aqueous solution was added slowly dropwise over the course of two minutes without stirring. After addition, the mixture was allowed to stir for 3 hours and the organic phase remained clear. Stirring was discontinued and the organic and aqueous phases were separated using a small separatory funnel. Small aliquots of the aqueous (a, red,

Figure 4.20) and organic (b, **Figure 4.20**) phases were used to record UV–Vis spectra which together clearly indicated negligible transfer of UO_2^{2+} from the aqueous to the organic phase.

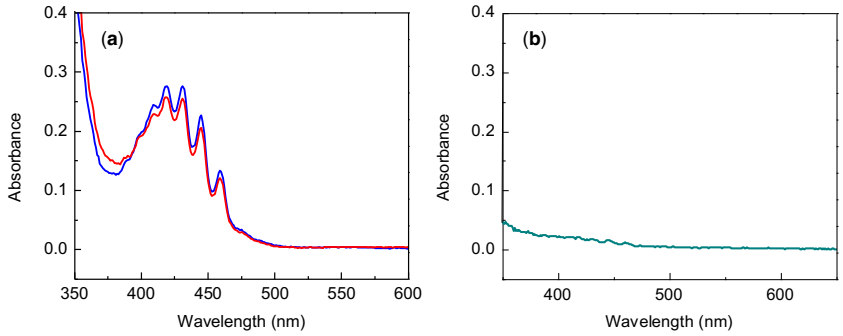

Figure 4.20. (**a**) Control for UO_2^{2+} migration from water to DCE in the presence of neutral carborane (**4.1**). (blue) Initial UV–Vis spectrum of UO_2^{2+} (1.0 equiv) in 0.1 M sodium acetate buffered solution at pH 5.4. (red) UV–Vis spectrum of aqueous layer after mixing for 3 h with DCE solution containing $[Bu_4N][PF_6]$ (0.1 M) and **4.1** (1.0 equiv). (**b**) Corresponding UV–Vis spectrum of DCE layer containing **4.1** after mixing for 3 h with the aqueous layer containing UO_2^{2+} in (**a**). The UO_2^{2+} extinction coefficient was experimentally determined to be 7.715 $L \bullet mol^{-1} \bullet cm^{-1}$ (460 nm) at pH 5.4.

4.4.7 DFT calculations and parameters

To get a theoretical support for the relative basicity of **4.1**, **4.2**, TPO and PC, we performed the density functional theory (DFT) calculation on isodesmic reactions of proton transfer between these molecules at B3LYP/def2–SVP[79-80] level of theory in DCM using conductor–like polarizable continuum model (CPCM).[81]

(**a**) **4.2**·H^+ + 2TPO ⇌ **4.2** + TPO_2·H^+ ΔH = 21.89; ΔG = 33.99; K_{eq} = 1.21E^{-25}

(**b**) TPO_2·H^+ + **4.1** ⇌ 2TPO + **4.1**·H^+ ΔH = 16.45; ΔG = 5.76; K_{eq} = 5.96E^{-25}

(**c**) **4.1**·H^+ + 2PC ⇌ **4.1** + PC_2H^+ ΔH = 5.49; ΔG = 15.06; K_{eq} = 9.20E^{-25}

Scheme 4.1. DFT calculated isodesmic proton transfer reactions (**a**) from **4.2**·H^+ to two TPOs (**b**) from 2TPO·H^+ to **4.1** (**c**) from **4.1**·H^+ to two PCs. ΔH and ΔG are given in kcal·mol^{-1}.

Since **4.1** and **4.1** have two P=O units the comparison was made versus two TPO and two PC molecules. The calculations have the same trend obtained from competition experiments, where **4.2** is much more basic than 2TPOs with the calculated equilibrium constant (K_{eq}) for the proton transfer from **4.2**·H^+ to two TPOs of 1.21E^{-25} (a, **Scheme 4.1**; **Figure 4.21**). The K_{eq} for the proton transfer from 2TPO·H^+ to **4.1** is 5.96E^{-5}, making 2TPOs more basic than **4.1** (b, **Scheme 4.1**). Finally, **4.1** is more basic than 2PCs with K_{eq} = 9.20E^{-12} for proton transfer from **4.1**·H^+ to two PCs molecules (c, **Scheme 4.1**). Overall the calculated relative basicity is similar to the experimental one with **4.2** > 2TPOs > **4.1** > 2PCs.

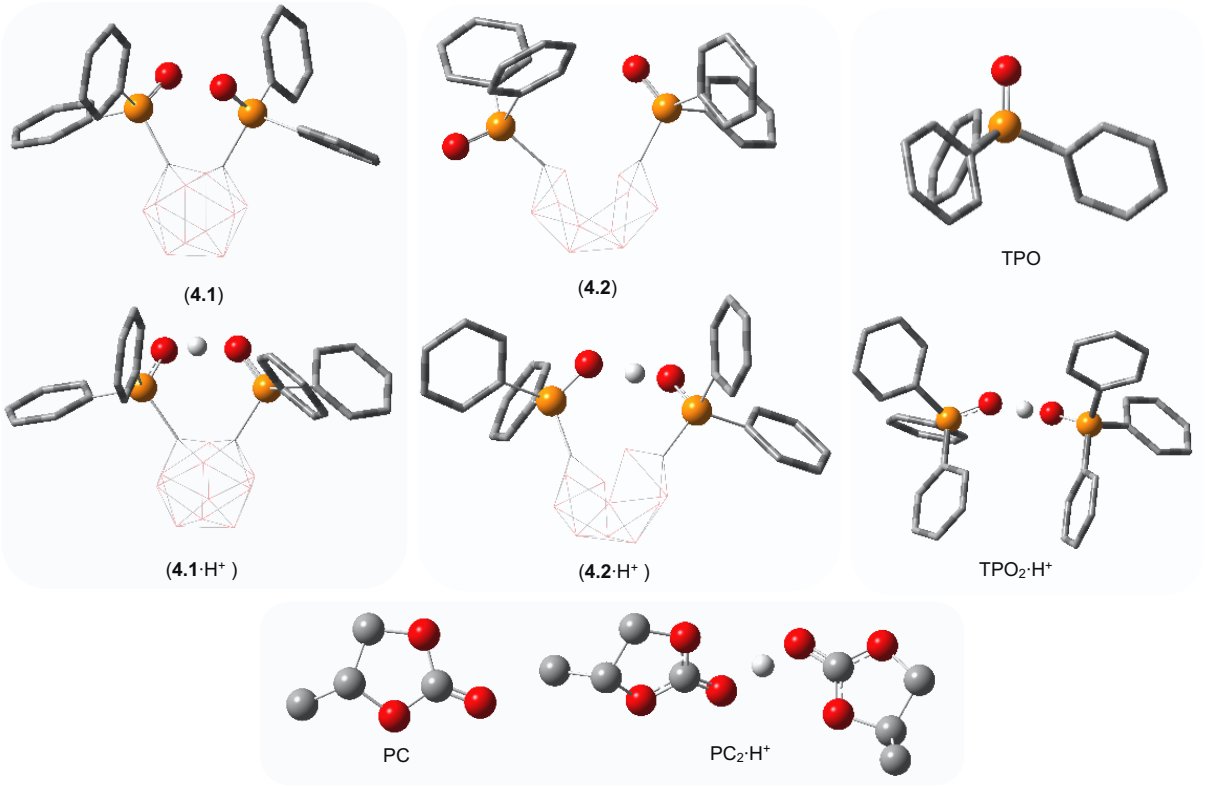

Figure 4.21. Physical computational representation of various compounds and H^+ transfer reactions to determine relative basicity's.

The electron density (ED) surface with electrostatic potentials (ESP) was extracted from optimized **4.1** and **4.1** and clearly shows that **4.2** has a significantly larger negative electron density located at the oxygen atoms of the P=O moieties (**Figure 4.2**). DFT calculations were performed using Gaussian 09.2. Geometry optimization of all the molecules was carried out using the B3LYP/def2–SVP basis sets in dichloromethane using the conductor–like polarizable continuum model (CPCM)[81-83] implemented in the Gaussian 09 software.

Thermal energy corrections were extracted from the results of frequency analysis performed at the same level of theory (**Figure 4.21**). Frequency analysis of all the molecules and intermediates contained no imaginary frequency showing that these are energy minima. The

equilibrium constants were calculated from Gibbs free energy values for the proton transfer reactions ($K_{eq} = e^{(-\Delta G/RT)}$) (**Scheme 4.1**; **Table 4.3**).

Table 4.3. Calculated values for the H^+ transfer reactions.

Compound	Sum of electronic and zero–point Energies	Sum of electronic and thermal Energies	Sum of electronic and thermal Enthalpies	Sum of electronic and thermal Free Energies
4.1	–2088.959472	–2088.926555	–2088.925611	–2089.023300
4.1·H^+	–2089.712218	–2089.678373	–2089.677429	–2089.779778
4.2	–2089.226219	–2089.192596	–2089.191652	–2089.291386
4.2·H^+	–2089.712218	–2089.678373	–2089.677429	–2089.779778
TPO	–1110.637439	–1110.620695	–1110.619751	–1110.684532
TPO_2·H^+	–2221.726815	–2221.691121	–2221.690177	–2221.802940
PC	–381.346082	–381.339865	–381.338921	–381.376432
PC_2·H^+	–763.108811	–763.094497	–763.093553	–763.153562

4.5 References

1. Adamantiades, A.; Kessides, I., Nuclear power for sustainable development: Current status and future prospects. *Energ. Policy* **2009,** *37* (12), 5149-5166.

2. Abu-Qare, A. W.; Flaherty, M. M.; Garofolo, M. C.; Rincavage, H. L.; Abou-Donia, M. B., Depleted and Natural Uranium: Chemistry and Toxicological Effects. *J. Toxicol. Env. Heal. B* **2004,** *7* (4), 297-317.

3. Jungseung, K.; Tsouris, C.; Mayes, R. T.; Oyola, Y.; Saito, T.; Janke, C. J.; Dai, S.; Schneider, E.; Sachde, D., Recovery of Uranium from Seawater: A Review of Current Status and Future Research Needs. *Sep. Sci. Technol.* **2013,** *48* (3), 367-387.

4. Parker, B. F.; Zhang, Z.; Rao, L.; Arnold, J., An overview and recent progress in the chemistry of uranium extraction from seawater. *Dalton Trans.* **2018,** *47* (3), 639-644.

5. Xiong, L.-p.; Lv, K.; Gu, M.; Yang, C.-t.; Wu, F.-c.; Han, J.; Hu, S., Efficient capture of actinides from strong acidic solution by hafnium phosphonate frameworks with excellent acid resistance and radiolytic stability. *Chem. Eng. J.* **2019,** *355*, 159-169.

6. Sun, Q.; Aguila, B.; Perman, J.; Ivanov, A. S.; Bryantsev, V. S.; Earl, L. D.; Abney, C. W.; Wojtas, L.; Ma, S., Bio-inspired nano-traps for uranium extraction from seawater and recovery from nuclear waste. *Nat. Commun.* **2018,** *9* (1), 1644.

7. Jang, J.-H.; Dempsey, B. A.; Burgos, W. D., A Model-Based Evaluation of Sorptive Reactivities of Hydrous Ferric Oxide and Hematite for U(VI). *Environ. Sci. Technol.* **2007,** *41* (12), 4305-4310.

8. Mellah, A.; Chegrouche, S.; Barkat, M., The removal of uranium(VI) from aqueous solutions onto activated carbon: Kinetic and thermodynamic investigations. *J. Colloid Interf. Sci.* **2006,** *296* (2), 434-441.

9. Kim, J. H.; Lee, H. I.; Yeon, J.-W.; Jung, Y.; Kim, J. M., Removal of uranium(VI) from aqueous solutions by nanoporous carbon and its chelating polymer composite. *J. Radioanal. Nucl. Ch.* **2010,** *286* (1), 129-133.

10. Mehio, N.; Ivanov, A. S.; Williams, N. J.; Mayes, R. T.; Bryantsev, V. S.; Hancock, R. D.; Dai, S., Quantifying the binding strength of salicylaldoxime–uranyl complexes relative to competing salicylaldoxime–transition metal ion complexes in aqueous solution: a combined experimental and computational study. *Dalton Trans.* **2016,** *45* (22), 9051-9064.

11. Kuo, L.-J.; Pan, H.-B.; Wai, C. M.; Byers, M. F.; Schneider, E.; Strivens, J. E.; Janke, C. J.; Das, S.; Mayes, R. T.; Wood, J. R.; Schlafer, N.; Gill, G. A., Investigations into the Reusability of Amidoxime-Based Polymeric Adsorbents for Seawater Uranium Extraction. *Ind. Eng. Chem. Res.* **2017,** *56* (40), 11603-11611.

12. Ren, Y.; Lin, Z.; Mao, X.; Tian, W.; Van Voorhis, T.; Hatton, T. A., Superhydrophobic, Surfactant-doped, Conducting Polymers for Electrochemically Reversible Adsorption of Organic Contaminants. *Adv. Funct. Mater.* **2018,** *28* (32), 1801466.

13. Kim, Y.; Lin, Z.; Jeon, I.; Van Voorhis, T.; Swager, T. M., Polyaniline Nanofiber Electrodes for Reversible Capture and Release of Mercury(II) from Water. *J. Am. Chem. Soc.* **2018,** *140* (43), 14413-14420.

14. Mendecki, L.; Ko, M.; Zhang, X.; Meng, Z.; Mirica, K. A., Porous Scaffolds for Electrochemically Controlled Reversible Capture and Release of Ethylene. *J. Am. Chem. Soc.* **2017,** *139* (48), 17229-17232.

15. Cheng, H. F.; d'Aquino, A. I.; Barroso-Flores, J.; Mirkin, C. A., A Redox-Switchable, Allosteric Coordination Complex. *J. Am. Chem. Soc.* **2018,** *140* (44), 14590-14594.

16. Singewald, E. T.; Mirkin, C. A.; Stern, C. L., A Redox-Switchable Hemilabile Ligand: Electrochemical Control of the Coordination Environment of a RhI Complex. *Angew. Chem. Int. Ed.* **1995,** *34* (15), 1624-1627.

17. Keener, M.; Hunt, C.; Carroll, T. G.; Kampel, V.; Dobrovetsky, R.; Hayton, T. W.; Ménard, G., Redox-switchable carboranes for uranium capture and release. *Nature* **2020**.

18. Heying, T. L.; Ager, J. W.; Clark, S. L.; Mangold, D. J.; Goldstein, H. L.; Hillman, M.; Polak, R. J.; Szymanski, J. W., A New Series of Organoboranes. I. Carboranes from the Reaction of Decaborane with Acetylenic Compounds. *Inorg. Chem.* **1963,** *2* (6), 1089-1092.

19. Fisher, S. P.; Tomich, A. W.; Lovera, S. O.; Kleinsasser, J. F.; Guo, J.; Asay, M. J.; Nelson, H. M.; Lavallo, V., Nonclassical Applications of closo-Carborane Anions: From Main Group Chemistry and Catalysis to Energy Storage. *Chem. Rev.* **2019**, DOI: 10.1021/acs.chemrev.8b00551.

20. Núñez, R.; Tarrés, M.; Ferrer-Ugalde, A.; de Biani, F. F.; Teixidor, F., Electrochemistry and Photoluminescence of Icosahedral Carboranes, Boranes, Metallacarboranes, and Their Derivatives. *Chem. Rev.* **2016,** *116* (23), 14307-14378.

21. Saxena, A. K.; Hosmane, N. S., Recent advances in the chemistry of carborane metal complexes incorporating d- and f-block elements. *Chem. Rev.* **1993,** *93* (3), 1081-1124.

22. Plesek, J., Potential applications of the boron cluster compounds. *Chem. Rev.* **1992,** *92* (2), 269-278.

23. Fronczek, F. R.; Halstead, G. W.; Raymond, K. N., The synthesis, crystal structure, and reactions of an actinide metallocarborane complex, bis(.eta.5-(3)-1,2-dicarbollyl)dichlorouranium(IV) dianion, [U(C2B9H11)2Cl2]2. *J. Am. Chem. Soc.* **1977,** *99* (6), 1769-1775.

24. Axtell, J. C.; Saleh, L. M. A.; Qian, E. A.; Wixtrom, A. I.; Spokoyny, A. M., Synthesis and Applications of Perfunctionalized Boron Clusters. *Inorg. Chem.* **2018,** *57* (5), 2333-2350.

25. Barton, J. L.; Wixtrom, A. I.; Kowalski, J. A.; Brushett, F.; Spokoyny, A. M., Perfunctionalized Dodecaborate Clusters as Stable Metal-Free Active Materials for Charge Storage. *ChemRxiv* **2018**, DOI: 10.26434/chemrxiv.7472921.v1.

26. Fisher, S. P.; Tomich, A. W.; Lovera, S. O.; Kleinsasser, J. F.; Guo, J.; Asay, M. J.; Nelson, H. M.; Lavallo, V., Nonclassical Applications of closo-Carborane Anions: From Main Group Chemistry and Catalysis to Energy Storage. *Chem. Rev.* **2019**.

27. Weber, L.; Kahlert, J.; Böhling, L.; Brockhinke, A.; Stammler, H.-G.; Neumann, B.; Harder, R. A.; Low, P. J.; Fox, M. A., Electrochemical and spectroelectrochemical studies of C-benzodiazaborolyl-ortho-carboranes. *Dalton Trans.* **2013,** *42* (6), 2266-2281.

28. Charmant, J. P. H.; Haddow, M. F.; Mistry, R.; Norman, N. C.; Orpen, A. G.; Pringle, P. G., A simple entry into nido-C2B10clusters: HCl promoted cleavage of the C–C bond in ortho-carboranyl diphosphines. *Dalton Trans.* **2008,** (11), 1409-1411.

29. Deng, L.; Cheung, M.-S.; Chan, H.-S.; Xie, Z., Reduction of 1,2-(CH2)n-1,2-C2B10H10 by Group 1 Metals. Effects of Bridge Length/Rigidity on the Formation of Carborane Anions. *Organometallics* **2005,** *24* (25), 6244-6249.

30. Wade, K., The structural significance of the number of skeletal bonding electron-pairs in carboranes, the higher boranes and borane anions, and various transition-metal carbonyl cluster compounds. *J. Chem. Soc. D.* **1971,** (15), 792-793.

31. Popescu, A.-R.; Laromaine, A.; Teixidor, F.; Sillanpää, R.; Kivekäs, R.; Llambias, J. I.; Viñas, C., Uncommon Coordination Behaviour of P(S) and P(Se) Units when Bonded to Carboranyl Clusters: Experimental and Computational Studies on the Oxidation of Carboranyl Phosphine Ligands. *Chem. Eur. J.* **2011,** *17* (16), 4429-4443.

32. Weiss, R.; Grimes, R. N., Nuclear magnetic resonance relaxation in complex spin systems. Proton and boron-11 spin-lattice relaxation studies of carboranes and metallocarboranes. *J. Am. Chem. Soc.* **1977,** *99* (4), 1036-1042.

33. Sundberg, M. R.; Uggla, R.; Viñas, C.; Teixidor, F.; Paavola, S.; Kivekäs, R., Nature of intramolecular interactions in hypercoordinate C-substituted 1,2-dicarba-closo-dodecaboranes with short P···P distances. *Inorg. Chem. Commun.* **2007,** *10* (6), 713-716.

34. Teixidor, F.; Núñez, R.; Viñas, C.; Sillanpää, R.; Kivekäs, R., Contribution of the nido-[7,8-C2B9H10]- Anion to the Chemical Stability, Basicity, and 31P NMR Chemical Shift in nido-o-Carboranylmonophosphines. *Inorg. Chem.* **2001,** *40* (11), 2587-2594.

35. Fox, M. A.; Nervi, C.; Crivello, A.; Low, P. J., Carborane radical anions: spectroscopic and electronic properties of a carborane radical anion with a 2n + 3 skeletal electron count. *Chem. Commun.* **2007,** (23), 2372-2374.

36. Zhang, J.; Fu, X.; Lin, Z.; Xie, Z., Supercarborane Radical Anions with 2n + 3 Electron Counts: A Combined Experimental and Theoretical Study. *Inorg. Chem.* **2015,** *54* (4), 1965-1973.

37. Mercer, G. D.; Lang, J.; Reed, R.; Scholer, F. R., Electrolytic reduction of B-oxy derivatives of 2,3-dicarba-closo-undecaborane(11). *Inorg. Chem.* **1975,** *14* (4), 761-763.

38. Fu, X.; Chan, H.-S.; Xie, Z., Synthesis and Crystal Structure of a 13-Vertex Carborane Radical Anion with 2n + 3 Framework Electrons. *J. Am. Chem. Soc.* **2007,** *129* (29), 8964-8965.

39. Hosoi, K.; Inagi, S.; Kubo, T.; Fuchigami, T., o-Carborane as an electron-transfer mediator in electrocatalytic reduction. *Chem. Commun.* **2011,** *47* (30), 8632-8634.

40. Fox, M. A.; Nervi, C.; Crivello, A.; Batsanov, A. S.; Howard, J. A. K.; Wade, K.; Low, P. J., Structural, spectroscopic, electrochemical and computational studies of C,C′-diaryl-ortho-carboranes, 1-(4-XC6H4)-2-Ph-1,2-C2B10H10 (X = H, F, OMe, NMe2, NH2, OH and O−). *Journal of Solid State Electrochemistry* **2009,** *13* (10), 1483-1495.

41. Tricas, H.; Colon, M.; Ellis, D.; Macgregor, S. A.; McKay, D.; Rosair, G. M.; Welch, A. J.; Glukhov, I. V.; Rossi, F.; Laschi, F.; Zanello, P., Spectroscopic, structural, computational and (spectro)electrochemical studies of icosahedral carboranes bearing fluorinated aryl groups. *Dalton Trans.* **2011,** *40* (16), 4200-4211.

42. Wee, K. R.; Han, W. S.; Cho, D. W.; Kwon, S.; Pac, C.; Kang, S. O., Carborane Photochemistry Triggered by Aryl Substitution: Carborane-Based Dyads with Phenyl Carbazoles. *Angew. Chem. Int. Ed.* **2012,** *51* (11), 2677-2680.

43. Chui, K.; Li, H.-W.; Xie, Z., Synthesis and Structural Characterization of closo-exo, exo-nido, and pseudocloso Group 1 Carborane Compounds of the C2B10 System. *Organomet.* **2000,** *19* (25), 5447-5453.

44. Xie, Z.; Yan, C.; Yang, Q.; Mak, T. C. W., [{[(η7-C2B10H12)(η6-C2B10H12)U][K2(thf)5]}2]: A Metallacarborane Containing the Novel η7-C2B10H124− Ligand. *Angew. Chem. Int. Ed.* **1999,** *38* (12), 1761-1763.

45. Deng, L.; Xie, Z., Advances in the chemistry of carboranes and metallacarboranes with more than 12 vertices. *Coord. Chem. Rev.* **2007,** *251* (17), 2452-2476.

46. Deng, L.; Xie, Z., A Journey from 12-Vertex to 14-Vertex Carboranes and to 15-Vertex Metallacarboranes. *Organomet.* **2007,** *26* (8), 1832-1845.

47. Charmant, J. P. H.; Haddow, M. F.; Mistry, R.; Norman, N. C.; Orpen, A. G.; Pringle, P. G., A simple entry into nido-C2B10clusters: HCl promoted cleavage of the C-C bond in ortho-carboranyl diphosphines. *Dalton Trans.* **2008,** (11), 1409-1411.

48. Connelly, N. G.; Geiger, W. E., Chemical Redox Agents for Organometallic Chemistry. *Chem. Rev.* **1996,** *96* (2), 877-910.

49. Teixidor, F.; Vinas, C.; Mar Abad, M.; Lopez, M.; Casabo, J., Synthesis of [7,8-(PPh2)2-7,8-C2B9H10]-: a ligand analogous to 1,2-bis(diphenylphosphino)ethane with a "built-in" negative charge. *Organomet.* **1993,** *12* (9), 3766-3768.

50. Teixidor, F.; Viñas, C.; Abad, M. M.; Kivekäs, R.; Sillanpää, R., The formation of nido [7,8-(PR2)2-7,8-C2B9H10]− from closo 1,2−(PR2)2−1,2−C2B10H10 (R = Ph, Et, iPr or OEt): a process enhanced by complexation. *J. Organomet. Chem.* **1996,** *509* (2), 139-150.

51. Teixidor, F.; Viñas, C.; Mar Abad, M.; Nuñez, R.; Kivekäs, R.; Sillanpäa, R., Procedure for the degradation of 1,2-(PR2)2-1,2-dicarba-closo-dodecaborane(12) and 1-(PR2)-2-R′-1,2-dicarba-closo-dodecaborane(12). *J. Organomet. Chem.* **1995,** *503* (2), 193-203.

52. Wiesboeck, R. A.; Hawthorne, M. F., Dicarbaundecaborane(13) and Derivatives. *J. Am. Chem. Soc.* **1964,** *86* (8), 1642-1643.

53. Hawthorne, M. F.; Young, D. C.; Garrett, P. M.; Owen, D. A.; Schwerin, S. G.; Tebbe, F. N.; Wegner, P. A., Preparation and characterization of the (3)-1,2- and (3)-1,7-dicarbadodecahydroundecaborate(-1) ions. *J. Am. Chem. Soc.* **1968,** *90* (4), 862-868.

54. Zakharkin, L. I.; Kirillova, V. S., Cleavage of o-carboranes to (3)-l,2-dicarbaundecarborates by amines. *Bulletin of the Academy of Sciences of the USSR, Division of chemical science* **1975,** *24* (11), 2484-2486.

55. Fox, M. A.; Gill, W. R.; Herbertson, P. L.; MacBride, J. A. H.; Wade, K.; Colquhoun, H. M., Deboronation of C-substituted ortho- and meta-closo-carboranes using "wet" fluoride ion solutions. *Polyhedron* **1996,** *15* (4), 565-571.

56. Fox, M. A.; Wade, K., Cage-fluorination during deboronation of meta-carboranes. *Polyhedron* **1997,** *16* (14), 2517-2525.

57. G. Davidson, M.; A. Fox, M.; G. Hibbert, T.; A. K. Howard, J.; Mackinnon, A.; S. Neretin, I.; Wade, K., Deboronation of ortho-carborane by an iminophosphorane: crystal structures of the novel carborane adduct nido-C2B10H12·HNP(NMe2)3 and the borenium salt [(Me2N)3PNHBNP(NMe2)3]2O2+(C2B9H12–)2. *Chem. Commun.* **1999,** (17), 1649-1650.

58. Hayton, T. W.; Wu, G., Synthesis, Characterization, and Reactivity of a Uranyl β-Diketiminate Complex. *J. Am. Chem. Soc.* **2008,** *130* (6), 2005-2014.

59. Wilkerson, M. P.; Burns, C. J.; Paine, R. T.; Scott, B. L., Synthesis and Crystal Structure of UO2Cl2(THF)3: A Simple Preparation of an Anhydrous Uranyl Reagent. *Inorg. Chem.* **1999,** *38* (18), 4156-4158.

60. Copping, R.; Jeon, B.; Pemmaraju, C. D.; Wang, S.; Teat, S. J.; Janousch, M.; Tyliszczak, T.; Canning, A.; Grønbech-Jensen, N.; Prendergast, D.; Shuh, D. K., Toward Equatorial Planarity about Uranyl: Synthesis and Structure of Tridentate Nitrogen-Donor {UO2}2+ Complexes. *Inorg. Chem.* **2014,** *53* (5), 2506-2515.

61. Pedrick, E. A.; Assefa, M. K.; Wakefield, M. E.; Wu, G.; Hayton, T. W., Uranyl Coordination by the 14-Membered Macrocycle Dibenzotetramethyltetraaza[14]annulene. *Inorg. Chem.* **2017,** *56* (11), 6638-6644.

62. Pedrick, E. A.; Wu, G.; Hayton, T. W., Reductive Silylation of the Uranyl Ion with Ph3SiOTf. *Inorg. Chem.* **2014,** *53* (23), 12237-12239.

63. Sutton, A. D.; John, G. H.; Sarsfield, M. J.; Renshaw, J. C.; May, I.; Martin, L. R.; Selvage, A. J.; Collison, D.; Helliwell, M., Spectroscopic Evidence for the Direct Coordination of the Pertechnetate Anion to the Uranyl Cation in [UO2(TcO4)(DPPMO2)2]+. *Inorg. Chem.* **2004,** *43* (18), 5480-5482.

64. Fortier, S.; Hayton, T. W., Oxo ligand functionalization in the uranyl ion (UO22+). *Coord. Chem. Rev.* **2010,** *254* (3), 197-214.

65. Bombieri, G.; Forsellini, E.; Day, J. P.; Azeez, W. I., Crystal and molecular structure of dichlorodioxobis(triphenylphosphine oxide)uranium(VI). *J. Chem. Soc. Dalton Trans.* **1978,** (6), 677-680.

66. Brighli, M.; Fux, P.; Lagrange, J.; Lagrange, P., Discussion on the complexing ability of the uranyl ion with several crown ethers and cryptands in water and in propylene carbonate. *Inorg. Chem.* **1985,** *24* (1), 80-84.

67. Akona, S. B.; Fawcett, J.; Holloway, J. H.; Russell, D. R.; Leban, I., Structures of cis- and trans-dichlorodioxobis(triphenylphosphine oxide)uranium(VI). *Acta Cryatallogr. C* **1991,** *47* (1), 45-48.

68. Bard, A. J.; Faulkner, L. R., *Electrochemical Methods: Fundamentals and Applications*. 2nd ed.; Wiley: 2000.

69. Liu, C.; Hsu, P.-C.; Xie, J.; Zhao, J.; Wu, T.; Wang, H.; Liu, W.; Zhang, J.; Chu, S.; Cui, Y., A half-wave rectified alternating current electrochemical method for uranium extraction from seawater. *Nat. Energy* **2017,** *2*, 17007.

70. Chi, F.; Zhang, S.; Wen, J.; Xiong, J.; Hu, S., Highly Efficient Recovery of Uranium from Seawater Using an Electrochemical Approach. *Ind. Eng. Chem. Res.* **2018,** *57* (23), 8078-8084.

71. Paiva, A. P.; Malik, P., Recent advances on the chemistry of solvent extraction applied to the reprocessing of spent nuclear fuels and radioactive wastes. *J. Radioanal. Nucl. Ch.* **2004,** *261* (2), 485-496.

72. Hunt, C.; Mattejat, M.; Anderson, C.; Sepunaru, L.; Ménard, G., Symmetric Phthalocyanine Charge Carrier for Dual Redox Flow Battery/Capacitor Applications. *ACS Appl. Energy Mater.* **2019,** *2*, 5391-5396.

73. Quilès, F.; Nguyen-Trung, C.; Carteret, C.; Humbert, B., Hydrolysis of Uranyl(VI) in Acidic and Basic Aqueous Solutions Using a Noncomplexing Organic Base: A Multivariate Spectroscopic and Statistical Study. *Inorg. Chem.* **2011,** *50* (7), 2811-2823.

74. Pant, D. D.; Khandelwal, D. P., The absorption and fluorescence spectra of uranyl nitrate solutions at room temperature. *P. Indian Acad. Sci. A* **1959,** *50* (5), 323-335.

75. Reynolds, J. G.; Zalkin, A.; Templeton, D. H., Structure of uranyl nitrate-bis(tetrahydrofuran). *Inorg. Chem.* **1977,** *16* (12), 3357-3359.

76. Lalancette, J. M.; Rollin, G.; Dumas, P., Metals Intercalated in Graphite. I. Reduction and Oxidation. *Can. J. Chem.* **1972,** *50* (18), 3058-3062.

77. Liu, Y.; Ren, W.-M.; Liu, C.; Fu, S.; Wang, M.; He, K.-K.; Li, R.-R.; Zhang, R.; Lu, X.-B., Mechanistic Understanding of Dinuclear Cobalt(III) Complex Mediated Highly Enantioselective Copolymerization of meso-Epoxides with CO2. *Macromolecules* **2014,** *47* (22), 7775-7788.

78. Alexander, R. P.; Schroeder, H., Chemistry of Decaborane-Phosphorus Compounds. IV. Monomeric, Oligomeric, and Cyclic Phosphinocarboranes. *Inorg. Chem.* **1963,** *2* (6), 1107-1110.

79. Lee, D. W.; Kaska, W. C.; Jensen, C. M., Mechanistic Features of Iridium Pincer Complex Catalyzed Hydrocarbon Dehydrogenation Reactions: Inhibition upon Formation of a μ-Dinitrogen Complex. *Organometallics* **1998,** *17* (1), 1-3.

80. Weigend, F., Accurate Coulomb-fitting basis sets for H to Rn. *Physical Chemistry Chemical Physics* **2006,** *8* (9), 1057-1065.

81. Cossi, M.; Rega, N.; Scalmani, G.; Barone, V., Energies, structures, and electronic properties of molecules in solution with the C-PCM solvation model. *Journal of Computational Chemistry* **2003,** *24* (6), 669-681.

82. Barone, V.; Cossi, M., Quantum Calculation of Molecular Energies and Energy Gradients in Solution by a Conductor Solvent Model. *The Journal of Physical Chemistry A* **1998,** *102* (11), 1995-2001.

83. Andzelm, J.; Kölmel, C.; Klamt, A., Incorporation of solvent effects into density functional calculations of molecular energies and geometries. *The Journal of Chemical Physics* **1995,** *103* (21), 9312-9320.

Chapter 5 – Selective UO_2^{2+} Sequestration and Recovery from Aqueous Mixtures Utilizing *o*–carboranes

5.1 Introduction

5.1.1 Selective UO_2^{2+} sequestration for nuclear waste remediation and reprocessing

Nuclear waste remediation and spent fuel reprocessing is one of the most important issues in nuclear science today. Nuclear power has been shown to be a reliable source of electricity and has been argued to be a crucial energy source in reducing CO_2 emissions and battling the global climate crisis.[1] One barrier in the proliferation of nuclear energy as a primary energy currency includes the management and disposal of spent nuclear waste. Closed and open fuel cycles present many advantages and disadvantages, but it has been shown that nuclear fuel cycles where the actinides are recycled through closed fuel cycles offer substantial benefits. For example, France is one of the major world leaders in providing power to consumers generated nuclear energy, making up roughly 87% of their energy currency.[2] The UK, France, India, and Russia have been reprocessing their spent fuel on industrial scales for decades through use of the PUREX process, recovering U and Pu for reuse in nuclear fuels; MOX fuel or reprocessed U fuel.[3-8] Removing more than 96% of the recyclable materials also reduces the long–term radiotoxicity and quantity of nuclear waste stored in geological repositories.[9] Additionally, due to U being a finite resource on terrestrial surfaces – in which U ores have been projected to be depleted within the next century[10-11] – extraction and reuse of U from spent fuel can reduce the mining of U ore, increasing the longevity of this natural resource.[5]

Civil reprocessing plants for nuclear fuel in the US have been non–operational since 1977 under the US Non–Proliferation Policy. The primary reason for foregoing reprocessing

and utilizing open fuel cycles, involves the ease of extraction and isolation of pure Pu waste streams from the PUREX process. This has caused national security concerns with fear that pure Pu recovered could be diverted from civil use and into nuclear weapon manufacturing (not technologically likely without advanced facilities) or through a dispersal device (more likely due to radiological toxicity), thereby increasing proliferation resistance for closed fuel cycles.[8] In 2006, the US government announced the Global Nuclear Partnership (GNEP) in which it would "work with other nations possessing advanced nuclear technologies to develop new proliferation–resistant recycling technologies in order to produce more energy, reduce waste and minimize proliferation concerns".[12]

Between 2006–2008, the GNEP (now known as International Framework for Nuclear Energy – IFNEC) had focused on developing new reprocessing strategies which center around selectively separating uranium from all other TRU elements and fission products in waste. The central feature of these extraction schemes was to ease resistance by eliminating pure Pu streams and separating the Pu with U or Pu with all other TRU elements and fission products – which could then be transmutated and destroyed in fast neutron reactors. Various iterations of UREX processes (**UR**anium **EX**traction) had been developed, but safety issues surrounding the extraction scheme and defunding from political entities caused the project to be abandoned in 2008.[12-13] A few examples of the more relevant technologies include NUEX (similar to UREX+1a; separates U, then TRUs, without carrying fission products through), COEX (separates U and Pu; can be modified for Np together from minor An's and fission products) and GANEX (separates U and Pu as in COEX, then An's and Ln's from fission products). All these systems have shown promise, but unlike the PUREX process, none are industrially viable, suffering due to complexity and lack of understanding.[7, 9, 14-17] The most promising

technique such as COEX, which co–extracts U and Pu together, limits the recycled material to usage in MOX fuels, which presents its own additional complications due to reactor modifications (i.e. going from a U fuel to a MOX fuel).[18] Additionally, the theft of separated Pu is still considered a great national security concern at reprocessing and fabrication facilities, specifically in the US If stolen, the threat corresponding to the non–civil usage of Pu contributes largely to the barrier impeding us from remediating and reprocessing our nuclear waste. Therefore, means of improving reprocessing techniques for selective UO_2^{2+} sequestration and generating pure U streams from wastes, need to be realized to improve technological and proliferation concerns.

5.1.2 Progress toward selective UO_2^{2+} recovery from seawater

The recovery of uranium from seawater has received considerable attention recently due to the size of this yet untapped source for nuclear fuels.[19] Uranyl (UO_2^{2+}, U^{VI} oxidation state), the most common form of uranium, is found both in terrestrial ores and is dissolved in our oceans, containing 4.5 billion tons, roughly a thousand times more than the known terrestrial supply. Although plentiful, the concentration of UO_2^{2+} in the ocean is low (3.3 ppb or 3.3 g/mL), with seawater containing trace amounts of almost every naturally occurring element, making systems selective for UO_2^{2+} necessary for efficient extraction.[20] Uranium extraction from seawater has been extensively studied and developed over the past several decades, but most systems present low selectivity toward UO_2^{2+} over other metals, meaning practical application is far from being realized. Currently, the most developed system, an amidioxime–based sorbent, shows selectivity toward vanadium (V^V) (14.9%) >> iron (Fe^{III}) (1.6%) > uranyl (U^{VI}) (1.0%),[21] with vanadium occupying almost 15 times as many sites as uranyl, even though the concentrations of each ion are comparable in solution.[20-25] Multiple

structural and speciation studies have been utilized in order to better understand the ligand–uranyl, –V, and –Fe binding processes of amidoxime–based ligands in order to design selective ligands and sorbents for U.[26-31]

Historically, the design of selective sorbents for UO_2^{2+} capture are based on soft–hard acid–base properties of metal ions and their geometric preferences. Generally, strong and selective coordination requires hard–donor atoms with planar geometries that can occupy the equatorial open coordination sites of UO_2^{2+}, which has been widely shown with amidoxime ligands.[30-34] In 2018, Kabanos and Keramidas reported a structurally similar framework to amidioximes, H_2bihyat (2,6–bis[hydroxy(methyl)amino]–4–morpholino–1,3,5–triazine) ligand, that has two hard deprotonated hydroxylamine oxygens and a negatively charged heterocyclic nitrogen donor atom with a planar coordination geometry. Utilizing this framework, they demonstrated the strongest and most selective binding of UO_2^{2+} in both UO_2^{2+}/Fe^{III} or $UO_2^{2+}/V^VO_4^{3-}$ aqueous solutions at alkaline pHs.[35] Although this is significant progress for capture and selectivity chemistry, the controlled release remains challenging with these materials and the recyclability is generally poor. In this present study, they did not study release of UO_2^{2+} from the ligand, but in most of the amidioxime–based systems, coordination tends to be very strong and dissociation from the ligand becomes challenging for not only UO_2^{2+}, but also other metal ions that complex with the materials – which tend to be in higher concentrations. For example, the stripping conditions required to elute adsorbed V^V from sorbent systems for reuse requires harsh conditions that ultimately destroy the sorbent.[23, 36] Developing systems that are capable of performing the selective capture and release of UO_2^{2+} with regeneration of all materials is of great interest in extraction chemistry today.

5.1.3 Scope of Chapter 5

First, we were curious if we could employ our previously developed system, outlined in Chapter 4, by exploiting the redox–switchable capabilities of our *o*–carborane ligand for the selective capture and release in terms of nuclear waste remediation or seawater extraction. Previously, we found by harnessing the redox–switchable properties of substituted *ortho*–1,2–$(Ph_2PO)_2$–carboranes (**4.1**) (**Scheme 5.1**), we could promote the controlled chemical or electrochemical capture and release of UO_2^{2+} in monophasic (organic) or biphasic (organic/aqueous) solvents systems. This was accomplished by exploiting the increase in the ligand bite (θ1→ θ2; **Scheme 5.1**) angle when *closo*–carborane is reduced to *nido*–carborane, resulting in C–C bond rupture with cage opening, capturing UO_2^{2+} (**4.1→4.4N/4.5N**; **Scheme 5.1**).

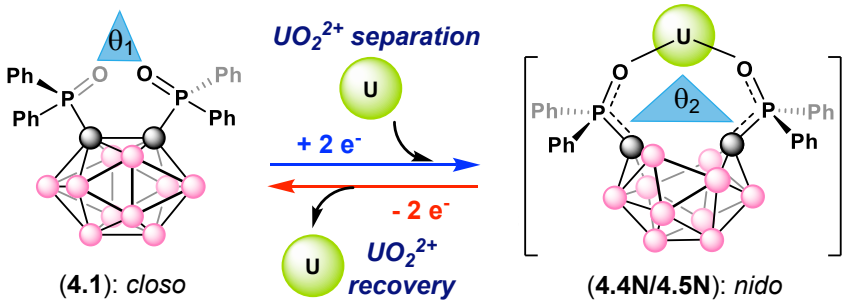

Scheme 5.1. Redox–controlled capture and release of UO_2^{2+} by exploiting differences in bite angle (θ1 and θ2).

Subsequent release of UO_2^{2+} occurs by re–oxidation of *nido*–carborane, restoring the C–C bond, and closing the cage to the *closo* conformation (**4.1**). Building on these results, we have investigated UO_2^{2+} selectivity and recovery for nuclear waste remediation and selective seawater extraction of UO_2^{2+} over problematic ions found in seawater such as V and Fe.

5.2 Results and Discussion

5.2.1 Selective separation and recovery of UO_2^{2+} from an aqueous mixture of actinides(IV), lanthanides(III), and alkali metals for nuclear waste remediation

Aqueous waste generated in nuclear fission contains more than 40 elements of the periodic table, including but not limited to lanthanides (Ln), actinides (An), and alkali metals.[37] Developing systems for the selective sequestration of UO_2^{2+} from the minor actinides and fission products found in nuclear raffinate are crucial for nuclear waste reprocessing and remediation. One of the biggest concerns in waste remediation and reprocessing sciences today is proliferation concerns by generating pure Pu waste streams. Within recent years, there have been systems developed in order to mitigate these concerns by co–extracting U and Pu – eliminating separation of pure Pu – to then be used in MOX fuels, but this limits the fuel to technologically developed MOX reactors.[18] Instead, it would be beneficial to develop an extraction scheme that is capable of selectively extracting UO_2^{2+}, keeping the Pu^{IV} and other fission products in the nuclear raffinate, which could then further separate the minor actinides and fission products to be transmutated to reduce the long–lived actinide radiotoxicity found in HLW. From a chemical point of view, UO_2^{2+} and Pu^{IV} are hard acids and tend to exhibit an affinity toward hard bases such as deprotonated carboxylic and phosphoric acids.[38-40] In the PUREX process, the UO_2^{2+} and Pu^{IV} nitrates exhibit almost identical chemistry and there is no selectivity between them in these oxidation states. In selectivity chemistry, most alternative systems have been investigated in terms of chelation from blood due to adverse human exposure,[40] where several methods are known for U separation from aqueous mixtures,[41-48] but few systems have been investigated in terms of UO_2^{2+} selectivity in the presence of fission products found in waste.[45, 49-55] Ultimately, this presents an interesting opportunity to

investigate the selectivity of UO_2^{2+} in the presence of fission products commonly found in nuclear waste.

Building on our previous report for biphasic electrochemical UO_2^{2+} capture and release utilizing redox–switchable *o*–carboranes (**4.1→4.2a/b**),[56] we sought to investigate the selective extraction of UO_2^{2+} in aqueous mixtures containing An (Th^{IV}), Ln (Nd^{III} and Sm^{III}), and alkali (Cs^{I}) metals (**Scheme 5.2**). Due to the difficulty in handling Pu, Th will instead be used as an analogue, as previously done,[33, 40, 57-59] but caution must be taken as Th^{IV} reactivity is not always analogues to Pu^{IV}. With this in mind, Th is considered a good preliminary step for this first study, with hopes of performing selectivity chemistry with Pu in the future. From an array of lanthanides, Nd^{III} and Sm^{III} were chosen due to being two of the most prevalent lanthanides in nuclear waste raffinate in a UO_2 fuel and are the lanthanide analogues of U and Pu respectively.[37]

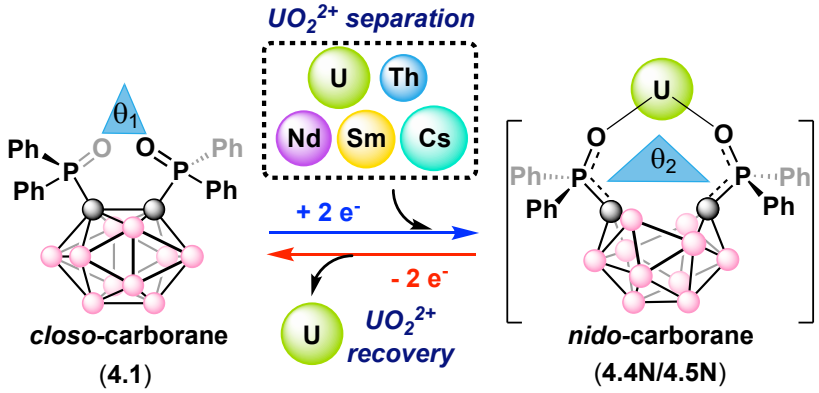

Scheme 5.2. Redox–controlled selective sequestration and recovery of UO_2^{2+} in aqueous mixtures of Th^{IV}, Nd^{III}, Sm^{III}, Cs^{I}.

Lastly, Cs was of interest because it is an alkali metal and presents a different bonding scheme in comparison to Th^{IV} and the Ln^{III} ions. Additionally, from a nuclear waste perspective, ^{137}Cs (one of the many isotopes of Cs in waste) is one of the most prevalent and radiotoxic alkali

metals, which is partially responsible for the long-lasting radioactivity of spent fuel. There have been many systems developed in order to separate Cs (and in some cases with Sr) from other fission products and minor actinides in waste to reduce radiotoxicity for storage. Most systems for Cs or Sr separation (CSEX, SREX, CCD–PEG)[60-61] have been developed assuming U has already been separated from the raffinate through previously proposed UREX schemes. Therefore, if pure UO_2^{2+} could be selectively separated and recovered in these complicated waste streams, it can help reduce the quantity of waste (U comprises >96% of spent fuel) for further remediation of the long–lived actinides. Additionally, recovered U can be recycled for fuel, mitigating depletion of natural U resources.[5] Thus, selective UO_2^{2+} sequestration from aqueous mixtures with these elements is desirable. Herein, we describe our investigation for the selective sequestration and recovery of UO_2^{2+} in aqueous mixtures of metal ions commonly found in nuclear waste

5.2.1.1 Coordination chemistry of redox–active *o*–carboranes

We first investigated the coordination chemistry of **4.2a** with nitrate complexes of Th^{IV}, Nd^{III}, Sm^{III}, and Cs^{I}. Addition of three equivalents of **4.2a** to $Th(NO_3)_4•H_2O$ in MeCN resulted in a bright yellow solution with consumption of **4.2a** and formation of a diamagnetic product with a single resonance at 51.2 ppm in the $^{31}P\{^1H\}$ NMR spectrum.[62] The ^1H NMR spectrum displayed multiple new C–H aryl resonances and the $–CH_3$ resonances of $[CoCp^*_2]^+$ counter ion. After separation of $[CoCp^*_2][NO_3]$, , the diamagnetic product was isolated and recrystallized by diffusion of Et_2O into a concentrated MeCN solution at room temperature to give large block, yellow single crystals suitable for XRD analysis. The solid–state structure revealed coordination of three equivalents of **4.2a** with subsequent loss of four $[CoCp^*_2]^+$ counterions, isolating the diamagnetic Th^{IV} complex, $[CoCp^*_2]_2[Th(nido–1,2–(Ph_2PO)_2–1,2–$

$C_2B_{10}H_{10})_3$] (**5.1**) in a 44% yield (a, **Figure 5.1**). The C1···C2 (2.854 Å) and P1···P2 (4.858 Å) bond distances are consistent with our previous report for complexes **4.4** and **4.5**.

Similar to **5.1**, addition of three equivalents of **4.2a** to individual solutions of $Nd(NO_3)_3THF_3$ and $Sm(NO_3)_3THF_3$ in MeCN resulted in consumption of **4.2a**, with formation of single resonances in the $^{31}P\{^1H\}$ NMR spectra, displaying signals at 140.6 ppm and 27.9 ppm, respectively.[63-64] The markedly shifted resonances are likely due to the paramagnetic nature of these metals. After separation of $[CoCp^*_2][NO_3]$, the following Ln products were isolated by diffusion of Et_2O into concentrated MeCN solutions at room temperature. Large block, yellow single crystals suitable for XRD analysis were obtained isolating $[CoCp^*_2]_3[Nd(nido\text{–}1,2\text{–}(Ph_2PO)_2\text{–}1,2\text{–}C_2B_{10}H_{10})_3]$ (**5.2**) and $[CoCp^*_2]_3[Sm(nido\text{–}1,2\text{–}(Ph_2PO)_2\text{–}1,2\text{–}C_2B_{10}H_{10})_3]$ (**5.3**) in 66 and 66% yields, respectively (b and c, **Figure 5.1**).

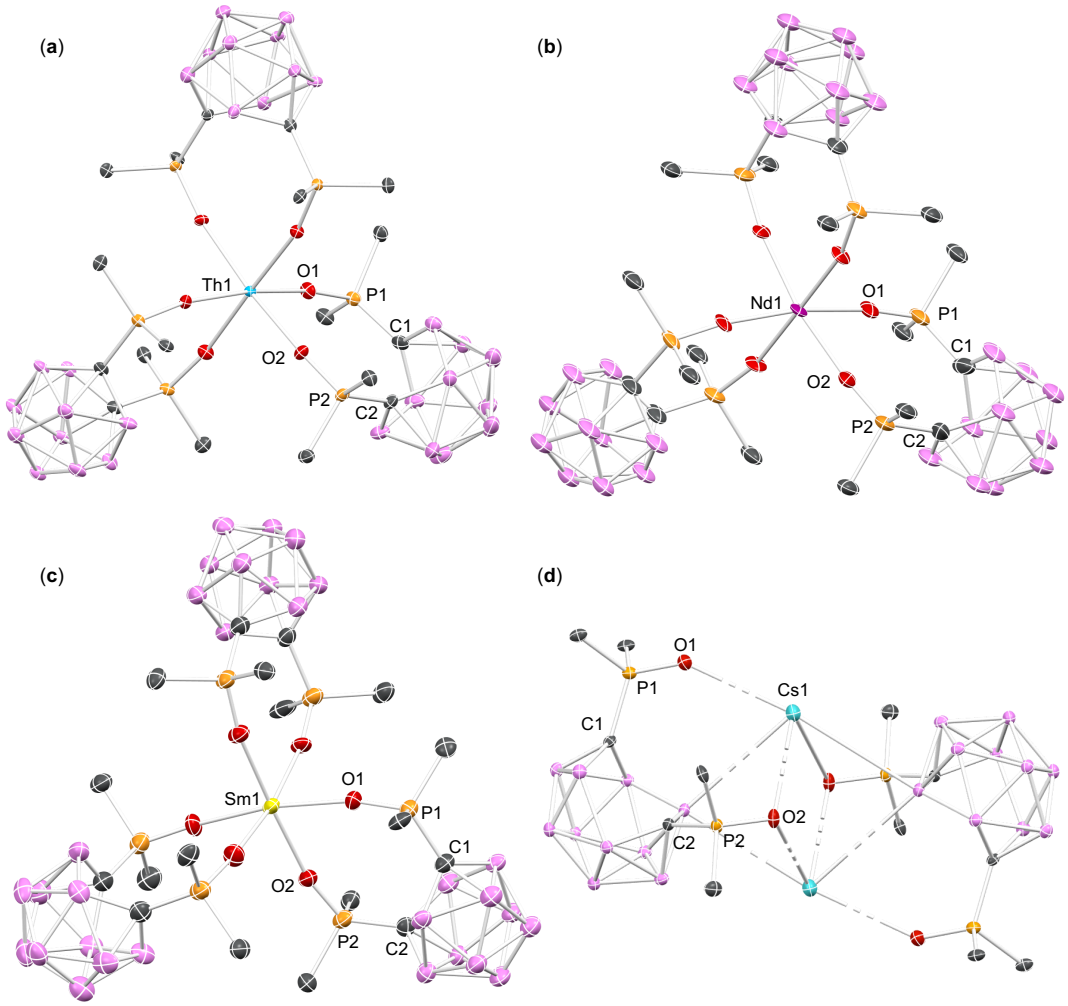

Figure 5.1. Solid–state molecular structures of **5.1** (**a**), **5.2** (**b**), **5.3** (**c**), **5.4** (**d**) obtained from X–ray diffraction studies. H atoms, $[CoCp^*_2]^+$ counter cations, phenyl C–H linkages, and all co–crystallized solvent molecules are omitted for clarity.

The C1···C2 (2.853 Å) and P1···P2 (4.785 Å) bond distances for **5.2** and C1···C2 (2.810 Å) and P1···P2 (4.762 Å) for **5.3** are consistent with each other and **5.1**.

Lastly, addition of one equivalent of **4.2a** to a solution of $CsNO_3$ in pyridine resulted in a slightly shifted, single resonance at 31.7 ppm in the $^{31}P\{^1H\}$ NMR spectrum, with two slightly shifted aryl C–H resonances and –CH_3 resonances of the $[CoCp^*_2]^+$ counter ion in the ^1H NMR spectrum. After separation of $[CoCp^*_2][NO_3]$, $[CoCp^*_2][Cs(nido\text{–}1,2\text{–}(Ph_2PO)_2\text{–}1,2\text{–}$

$C_2B_{10}H_{10}$)] (**5.4**), was isolated as a yellow crystalline solid in 51 % yield. Single crystals suitable for XRD analysis were grown by evaporation of Et_2O into a saturated MeCN solution of **5.4** (d, **Figure 5.1**). The solid–state molecular structure reveals **5.4** is dimeric with C1···C2 (2.862 Å) and P1···P2 (5.089 Å) bond distances similar to complexes **4.5** (UO_2^{2+}), **5.1** (Th^{IV}), **5.2** (Nd^{III}), and **5.3** (Sm^{III}).

5.2.1.2 Model system for UO_2^{2+} sequestration from aqueous mixtures

Building on our previous report for the biphasic capture and release of UO_2^{2+} by galvanostatic bulk electrolysis (GBE), we next targeted the selective sequestration and recovery of UO_2^{2+} in aqueous mixtures containing Th^{IV}, Nd^{III}, Sm^{III}, and Cs^{I}. This was accomplished in a biphasic (organic/aqueous) extraction scheme utilizing the analogous salt of **4.2a**, $[Bu_4N]_2[(nido–1,2–(Ph_2PO)_2–1,2–C_2B_{10}H_{10})]$ (**4.2b**), as the extractant, which is relevant for the electrochemical experiments described below. To probe **4.2b** as a selective extractant, we first developed a model biphasic extraction system by dissolving UO_2^{2+}, Th^{IV}, Nd^{III}, Sm^{III}, and Cs^{I} in an aqueous sodium acetate buffered solution and layering with the organic DCE phase containing the independently synthesized extractant **4.2b** (a→b, **Figure 5.2**). As seen in our previous report, we note the vibronic ligand–to–metal charge transfer (LMCT) absorption of UO_2^{2+} (425 nm) is pH–dependent, resulting in a variable extinction coefficient (ε)[65-66]; therefore, a buffered solution was used. Additionally, absorptions for Nd^{III} (797, 746, 538, and 525 nm) and Sm^{III} (404 nm) were also monitored by UV–Vis spectroscopy (**Figure 5.25**).[67] Th^{IV} and Cs^{I} do not exhibit optical absorption in the visible region,[68] instead complex formation was monitored by $^{31}P\{^1H\}$ NMR spectroscopy upon analysis of the organic layer.

1.0 equivalent of **4.2b** was dissolved in DCE and an initial unlocked $^{31}P\{^1H\}$ NMR spectrum was obtained (a, bottom inset, **Figure 5.2**; a, **Figure 5.17**). Next, a sodium acetate

(NaOAc)–buffered (0.5 M, pH = 5.4) water solution containing equimolar amounts (1.5 equivalents relative to **4.2b**; 0.02 M for each ion; 0.1 M total ion concentration) of $UO_2(NO_3)_2THF_2$, $Th(NO_3)_4•H_2O$, $Nd(NO_3)_3THF_3$, $Sm(NO_3)_3THF_3$, and $CsNO_3$ (a, top inset, **Figure 5.2**; blue, **Figure 5.16**) were next added to the DCE layer with mixing (a→b, **Figure 5.2**).

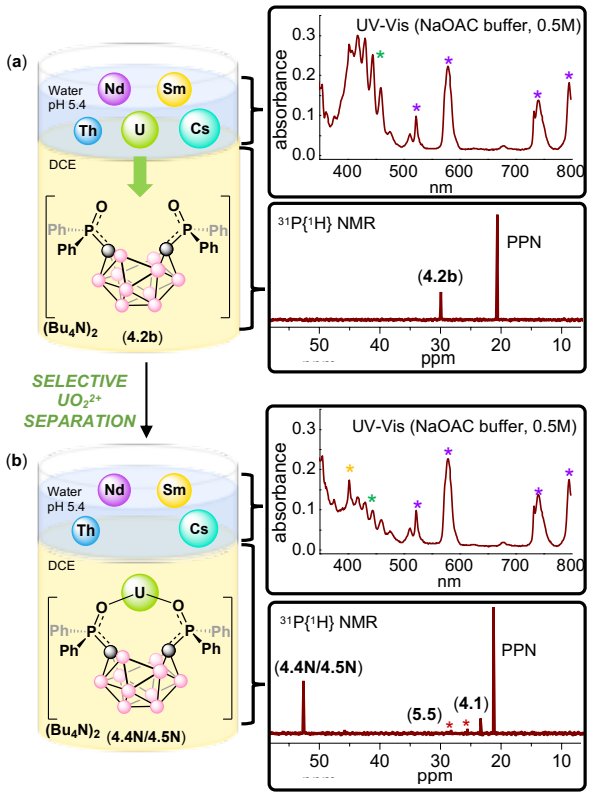

Figure 5.2. Model biphasic extraction scheme for selective sequestration of UO_2^{2+} in an aqueous mixture of Th^{VI}, Nd^{III}, Sm^{III}, and Cs^{I}. (**a**) Top inset, UV–Vis spectrum of aqueous phase (NaOAc buffer 0.5 M, pH 5.4) containing 1.5 equiv. $UO_2(NO_3)_2(THF)_2$ (*), $Th(NO_3)_4•H_2O$, $Nd(NO_3)_3THF_3$ (*), $Sm(NO_3)_3THF_3$ (*), and $CsNO_3$ before mixing with the DCE phase. Bottom inset, $^{31}P\{^1H\}$ NMR spectrum of DCE layer containing **4.2b**. (**b**) Mixing of the phases in **a** for 1.5 hours. Top inset, UV–Vis spectrum of aqueous phase after mixing with the DCE phase, revealing approximately ~0.95 equiv. of UO_2^{2+} were selectively extracted.

Bottom inset, $^{31}P\{^{1}H\}$ NMR spectrum of the DCE layer after mixing with aqueous phase, showing captured products **4.4N**/**4.5N** (major), with **5.5** (denoted *) and **4.1** as minor products.

Monitoring the biphasic extraction by UV–vis and $^{31}P\{^{1}H\}$ NMR spectroscopy indicated the selective sequestration of UO_2^{2+}, forming our previously reported **4.4N/4.5N** (b, bottom inset, **Figure 5.2**; b, **Figure 5.17**),[56] suggesting Th^{IV}, Nd^{III}, Sm^{III}, and Cs^{I} remained in the aqueous phase (a, top inset, **Figure 5.2**). Approximately 0.95 equivalents of UO_2^{2+} (relative to **4.2b**) was selectively separated from the aqueous mixture as evidenced by the UV–vis spectra over 1.5 hours (b, top inset, **Figure 5.2**; red, **Figure 5.16**). The Nd^{III} concentration is unchanged, with the overlapping Sm^{III} absorbance becoming more prevalent as UO_2^{2+} concentration decreases during sequestration. The reaction was monitored by $^{31}P\{^{1}H\}$ NMR spectroscopy and compared to the known chemical shift values for independently synthesized Th^{IV} (**5.1**), Nd^{III} (**5.2**), Sm^{III} (**5.3**), and Cs^{I} (**5.4**) complexes detailed above. Analysis of the DCE solution by ^{31}P NMR spectroscopy revealed formation of the resonance at 51.5 ppm corresponding to **4.4N/4.5N**, with two smaller–intensity resonances at 27.1 and 24.7 ppm, **4.1**. No apparent formation of additional complexes (b, bottom inset, **Figure 5.2**; b, **Figure 5.17**) were seen and were further supported by control experiments in the absence of UO_2^{2+} (see below).

The two smaller–intensity resonances were observed with the increased concentration of NaOAc buffer (0.5 M) in the aqueous layer compared to our previous system (0.1 M). A higher concentration was used due to the increased concentration of ions in solution (0.1 M total ion concentration), as the buffer was no longer able to maintain a consistent pH at this increased concentration. We were able to independently synthesize and characterize this byproduct by dissolving **4.2b** in DCE and layering the organic phase with the aqueous NaOAc

buffer solution (0.5 M). After 2.5 hours, the DCE layer was separated and a $^{31}P\{^{1}H\}$ NMR spectrum was obtained showing the two resonances at 27.1 and 24.7 ppm, and **4.1** (**Figure 5.13**). The unknown product can be selectivity isolated through recrystallization by diffusion of pentane into a concentrated THF solution of the reaction mixture at room temperature. Removal and characterization of the THF supernatant reveals isolation of **4.1** (a, **Figure 5.12**). Alternatively, a $^{31}P\{^{1}H\}$ NMR spectrum of the crystals reveals the unknown resonances at 27.1 and 24.7 ppm (b, **Figure 5.12**). Analysis of the colorless crystals by XRD studies reveals formation of a by–product of **4.2a**, mono–anionic protonated complex in a 60 % yield (**5.5**; **Figure 5.3**). Mono–anionic carboranes are exceedingly rare,[69-76] with no current examples reported for mono–anionic *ortho*–$[C_2B_{10}H_{10}]^-$ clusters.

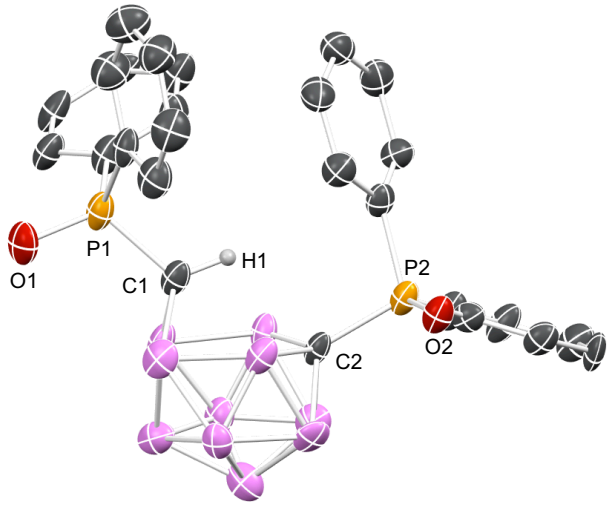

Figure 5.3. Solid–state molecule structure of the mono–anionic $[Bu_4N][(nido–1,2–(Ph_2PO)_2–1,2–C_2B_{10}H_{10})H]$ (**5.5**). H atoms on the phenyl rings and the $[NBu_4]^+$ counter ion are omitted for clarity. Pertinent bond distances; C1···C2 (2.791Å); P1···P2 (5.627 Å); O2–P2 (1.497(6) Å); O1–P1 (1.474(5) Å); C2–P2 (1.810(8) Å); C1–P1 (1.817(8) Å).

Therefore, complex **5.5** is to the best of our knowledge, the first example of an isolated mono–anionic *ortho*–$[C_2B_{10}H_{10}]$ cluster. The solid–state molecular structure of **5.5** displays a basket–

cage structure with C1 puckering out of the plane, resulting in an asymmetric cluster. This is consistent with the $^{31}P\{^{1}H\}$ NMR spectrum which displays two asymmetric resonances in a 1:1 ratio. The C1–H1 was further probed by obtaining $^{1}H–^{13}C$ heteronuclear single quantum coherence (HSQC) and $^{1}H–^{13}C$ heteronuclear multiple bond correlation (HMBC) NMR spectra. The $^{1}H–^{13}C$ HSQC spectrum displayed a correlation between a H–signal at 4.3 ppm (assignment to 1H by integration) and a very broad C–signal at 80 ppm (**Figure 5.4**). Analysis of the ^{13}C NMR spectrum displayed a broadened C–signal at 80 ppm, most likely corresponding to the C1 carbon in the cluster (inset, **Figure 5.4**). The broadening in the ^{13}C NMR spectrum is most likely due to the coupling to the quadrapolar (S = 3/2) ^{11}B nuclei in the carborane cage.[77]

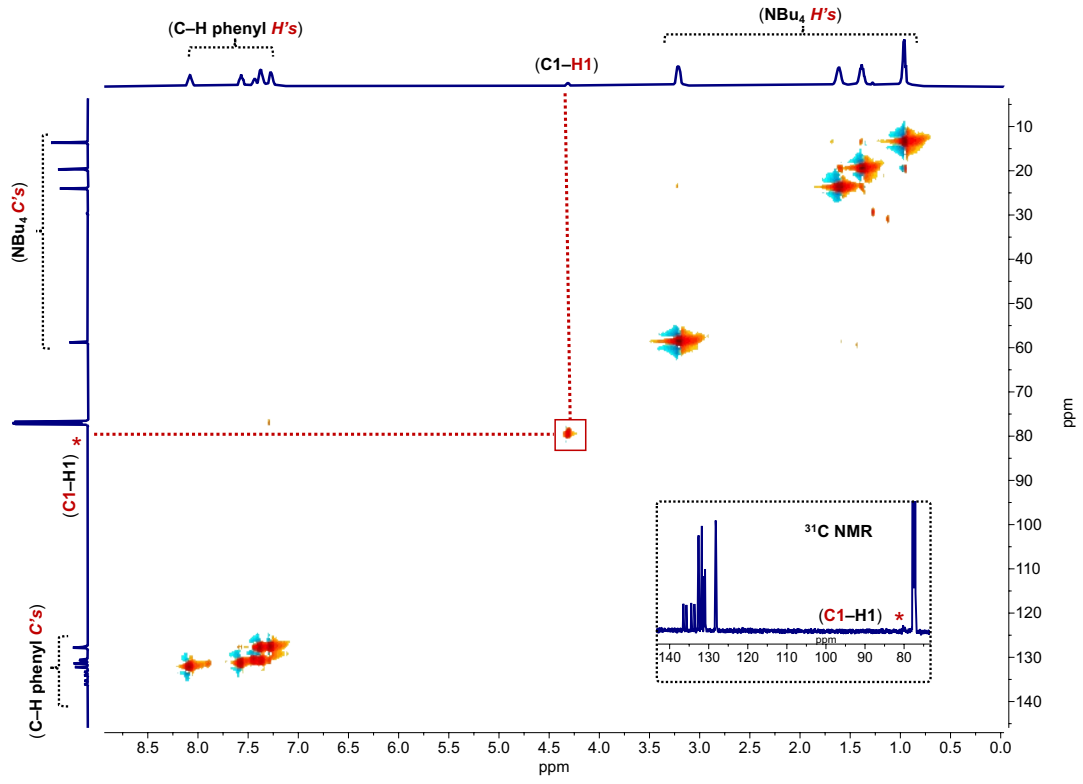

Figure 5.4. $^{1}H–^{13}C$ heteronuclear single quantum coherence (HSQC) spectrum for complex **5.5**.

Additionally, a $^{1}H–^{13}C$ HMBC spectrum was obtained (**Figure 5.5**). The spectrum does not display multiple–bond correlation between the assigned H–signal and other H– or C–signals in the molecule, further supporting the following assignment.

Further control experiments for the extraction of Th^{IV}, Nd^{III}, Sm^{III}, and Cs^{I} in the absence of UO_2^{2+} were carried out revealing no biphasic sequestration of the following ions in NaOAc buffer solution in the presence of **4.2b** (**Figure 5.14**). Analysis of the DCE layer by $^{31}P\{^{1}H\}$ NMR spectroscopy after 1.5 hours indicated the formation of major by–products **5.5** and **4.1** (**Figure 5.15**), suggesting Th^{IV}, Nd^{III}, Sm^{III}, and Cs^{I} were not extracted into the DCE layer.

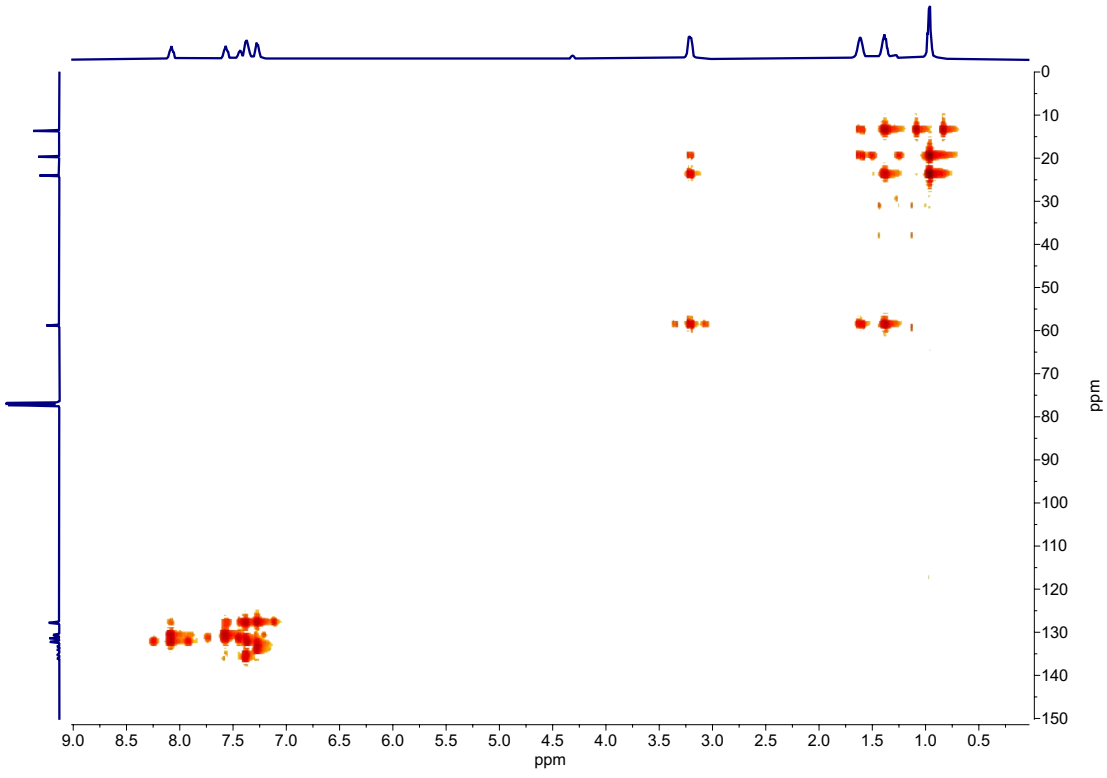

Figure 5.5. $^{1}H–^{13}C$ heteronuclear multiple bond correlation (HMBC) spectrum for complex **5.5**.

5.2.1.3 Biphasic electrochemical selective sequestration and recovery of UO_2^{2+}

Lastly, we wanted to employ our previously reported biphasic electrochemical GBE system (**Figure 5.18**) for selective sequestration and recovery of UO_2^{2+}.[56] A DCE solution of **4.1** (1.0 equivalent) with $[Bu_4N][PF_6]$ as supporting electrolyte was galvanostatically charged to a ~75% theoretical SOC (**Figure 5.19**). Analysis of the solution by $^{31}P\{^1H\}$ NMR spectroscopy revealed the clean conversion of most of **4.1** to **4.2b** (a→b, **Figure 5.20** and **Figure 5.24**). A sodium acetate (NaOAc)–buffered (pH = 5.4) water solution containing 1.25 equivalents (relative to **4.1**) of $UO_2(NO_3)_2(THF)_2$, $Th(NO_3)_4•H_2O$, $Nd(NO_3)_3THF_3$, $Sm(NO_3)_3THF_3$, and $CsNO_3$ (0.1 M total concentration) was next added to the DCE layer with mixing (b→c, **Figure 5.24**). Approximately 0.9 equivalent of UO_2^{2+} (relative to **4.2b** formed at 75 % SOC) was selectivity separated from the aqueous phase as evidenced by comparing the before and after UV–Vis spectra (b→d, top insets, **Figure 5.24**; **Figure 5.21**). Analysis of the DCE solution by $^{31}P\{^1H\}$ NMR spectroscopy revealed the clean formation of a single resonance at 51.5 ppm corresponding to **4.4N/4.5N**, with minor product formation of **5.5** and **4.1** (b→d, bottom insets, **Figure 5.24**; c, **Figure 5.20**). The aqueous phase was next removed, and the cell was galvanostatically discharged to achieve a theoretical final SOC of ~0 % (**Figure 5.22**). Mixing a fresh NaOAc–buffered solution (0.1 M, pH = 5.4) to this solution led to the release of approximately 0.03 mmol of UO_2^{2+} (77 % recovery based on extraction of **4.4N**/**4.5N**) from the DCE layer as confirmed by UV–Vis spectroscopy (e→f, **Figure 5.24**; **Figure 5.23**). Analysis of the DCE layer by $^{31}P\{^1H\}$ NMR spectroscopy revealed conversion to **4.1**, as well as the formation of a minor unknown byproduct at 20 ppm (f, bottom inset, **Figure 5.24**; e, **Figure 5.20**). Together, these biphasic extraction schemes demonstrate the

potential applicability of this redox–switchable selective UO_2^{2+} sequestration and recovery in aqueous mixtures of ions commonly found in nuclear waste raffinate.

5.2.2 Targeting selective UO_2^{2+} extraction and recovery in aqueous mixtures of vanadium (V) for seawater extraction

Currently, amidoxime–based sorbents are considered to be the most promising materials for UO_2^{2+} extraction from seawater.[20, 26-27, 78-81] However, amidoximes lack selectivity for uranyl in the presence of vanadium and iron.[24, 26] Building on our previous results in section 5.2.1, we sought to further probe our previously reported biphasic system by utilizing $[Bu_4N]_2[(nido–1,2–(Ph_2PO)_2–1,2–C_2B_{10}H_{10})]$ (**4.2b**) for the selective extraction and recovery of UO_2^{2+} in aqueous mixtures containing vanadium(V) for seawater extraction chemistry. First, we investigated the coordination chemistry of **4.2b** with sodium orthovanadate (Na_3VO_4) – which is the most common V^V starting reagent in most selectivity experiments.[26, 35, 82-83] Addition of 1.0 equivalent of Na_3VO_4 to a solution of **4.2b** in d_3–MeCN or $CDCl_3$ resulted in an insoluble Na_3VO_4 suspension. Monitoring the reaction by ^1H, $^{31}P\{^1H\}$, and ^{51}V NMR spectroscopies indicated unreacted **4.2b** with no signal in the ^{51}V spectrum – indicating the V–salt was not soluble in the following solvents. Additionally, we attempted reacting 1.0 equivalent of Na_3VO_4 dissolved in D_2O with a suspension of **4.2b** in D_2O. An initial ^{51}V NMR spectrum was obtained for the Na_3VO_4 showing an upfield shifted signal at –533.7 ppm, corresponding to a V^V center. Monitoring the reaction mixture by NMR indicated the VO_4^{3-} was unreacted and **4.2b** was completely insoluble in D_2O. Based on these results, we were curious if we could perform a biphasic extraction scheme for selective UO_2^{2+} (similar to the bisphasic chemistry in section 5.2.1). First, we performed control experiments in which we added 1.5 equivalents of Na_3VO_4 to 3 ml of a NaOAc buffer solution to a 5 ml vial (0.1 M,

pH was adjusted to 5.4). An initial unlocked ^{51}V NMR spectrum indicated the V^V species in solution (a, **Figure 5.6**).

In separate 20 ml vial, **4.2b** was added and dissolved in 6 ml of DCE where a $^{31}P\{^1H\}$ and ^{51}V NMR spectrum (c, **Figure 5.6**) was obtained. The aqueous solution of VO_4^{3-} was layered over the DCE solution over the course of 2 minutes without stirring or agitating the mixture. Upon addition, the biphasic solution was allowed to stir at low speed and the aqueous and DCE layer were monitored by ^{51}V and $^{31}P\{^1H\}$ NMR spectroscopies. The ^{51}V NMR spectra of the aqueous solution shows the presence of VO_4^{3-} (b, **Figure 5.6**). The $^{31}P\{^1H\}$ and ^{51}V NMR spectra for the DCE solution indicate the decomposition of **4.2b** (which had been previously seen in biphasic experiments with absence of UO_2^{2+}) displaying two signals consistent with complex **5.5** (b, **Figure 5.12**) and formation of the neutral ligand (**4.1**) and no signal for a V^V species in the DCE solution and (d, **Figure 5.6**), respectively.

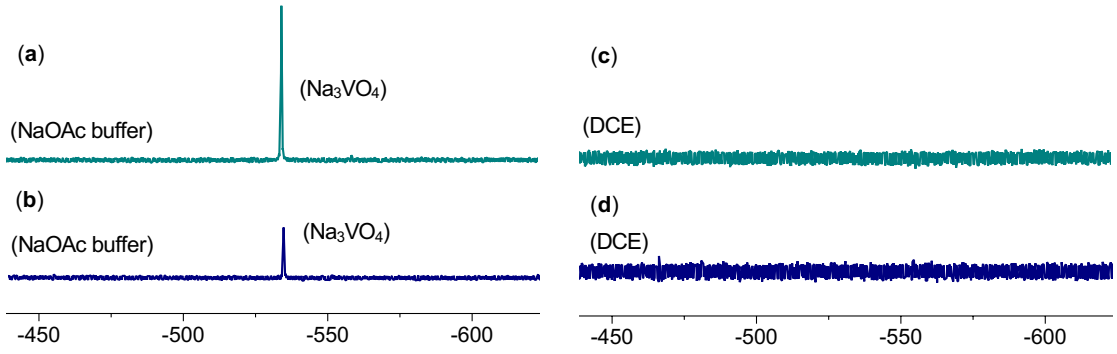

Figure 5.6. ^{51}V NMR spectra for (**a**) initial spectrum for Na_3VO_4 in NaOAc buffer solution, (**b**) 12 hour biphasic reaction for Na_3VO_4 in NaOAc buffer solution, (**c**) initial spectrum in DCE solution; no ^{51}V signal, (**d**) 12 hour biphasic reaction in DCE solution; no ^{51}V signal.

It is important to note that no display of new signals in the following spectrum do not exclude formation of a new V–containing product. For example, V^V could be reduced to a V^{IV} under

aqueous conditions,[20] and could be paramagnetic and not spectroscopically observable by NMR spectroscopy. For future experiments, it would be useful to utilize EPR spectroscopy to exclude extraction with formation of a new V^{IV}–containing species.

Based on these strong preliminary results, we wanted to probe selective UO_2^{2+} extraction in the presence of VO_4^{3-} in an aqueous mixture. Addition of 1.5 equivalents of $UO_2(NO_3)_2(THF)_2$ in 1.5 ml of NaOAc buffer (0.1M adjusted to pH of 5.4) was added to a solution of Na_3VO_4 (1.5 equivalent in 1.5 ml of NaOAc buffer). It is important to note that $Ca(UO_2)(CO_3)_3$ is the known primary UO_2^{2+} species under seawater conditions,[84-86] but was not utilized in these preliminary experiments. Upon addition of UO_2^{2+} to VO_4^{3-}, a bright yellow solid immediately crashed out of solution and was identified to be previously published uranyl vanadate, $(UO_2)_3(VO_4)_2$.[87]

Table 5.1. Solubility of $(UO_2)_3(VO_4)_2 \cdot 4H_2O$ in aqueous solutions of $HClO_4$ or NaOH.

pH ($HClO_4$ or NaOH)	Solubility (M)	Prominent Species (not balanced)
< 2.0	—	V_2O_5 (s) + UO_2^{2+}
2.39–2.84	$8.8–1.5x10^{-4}$	—
3.39–3.78	$3.6–1.0x10^{-5}$	—
4.21–4.35	$4.0–3.4x10^{-6}$	—
5.50	$6.1x10^{-7}$	—
>7	—	UO_3 (s) + $NaVUO_6$ (s)
>12	—	$Na_2U_2O_7$ (s) + VO_4^{3-}

Uranyl vanadate is the favoured product formed when UO_2^{2+} and VO_4^{3-} are reacted. The neutral complex has been previously shown to have very poor solubility at standard working concentrations (ie. 10^{-3} to 10^{-5} M) and in most solvents, including water, in which solubility is determined primarily by pH. Studies carried out in perchloric acid ($HClO_4$ and NaOH) indicated the species at various pH's indicated various types of prominent species in aqueous

solutions (**Table 5.1**).[87] To achieve monomeric forms of the ions, the optimal pH < 6 with concentrations around 6 x 10^{-7} M. Correlating this to our system, we found the working concentration of ions in solution must not exceed concentrations of (10^{-3} M) due to the increased rate in decomposition of **4.2b** to byproducts **5.5** and **4.1** (section 5.2.1). Instead, we focused our attention toward lowering the pH in order to establish monomeric forms for UO_2^{2+} separation. **Table 5.2** shows the qualitative solubility experiments performed with various acids (pH = 3.0) and buffers in order to attempt to solubilize the uranyl vanadate solid that forms *in situ*.

First, we attempted solubilizing uranyl vanadate by using known buffers that can access the desired pH range < 6. Citrate buffer was the only buffer capable of fully solubilizing the uranyl product that forms, but unfortunately, the solubility was too great and UO_2^{2+} extraction did not occur. This is most likely because the ligand has a comparable basicity to **4.2b**, due to the negatively charged oxygen donors – causing it to selectively remain in the aqueous layer.

Table 5.2. Qualitative solubility experiments for mixtures of UO_2^{2+} and VO_4^{3-} in aqueous solutions of various acids and buffers.

Buffer (2 ml)	pH	UO_2^{2+} ($7.5x10^{-3}$ M) soluble? Extraction?	VO_4^{3-} ($7.5x10^{-3}$ M) soluble? Extraction?	$(UO_2)_3(VO_4)_2$ soluble?	UO_2^{2+} capture from mixture?
Citrate	2.60	Yes/no	Yes/no	Yes	No
Phosphate	2.66	No/no[88-89]	Yes/no	Forms suspension	No
NaOAc	5.8	Yes/yes	Yes/no	Forms suspension	No
Acid (2 ml)	**pH**	**UO_2^{2+} ($7.5x10^{-3}$ M) soluble? Extraction?**	**VO_4^{3-} ($7.5x10^{-3}$ M) soluble? Extraction?**	**$(UO_2)_3(VO_4)_2$ soluble?**	**UO_2^{2+} capture from mixture?**
HOAc	3.0	Yes/yes	Yes/no	Forms suspension	Small quantity
HNO_3	3.0	Yes/yes	Yes/no	Forms suspension	No

HCl	3.0	Yes/yes	Yes/no	Forms suspension	No
$HClO_4$[87]	2.5	Yes/yes	Yes/no	Forms suspension	No

Alternatively, phosphate buffer led to completely insoluble UO_2^{2+} species, which is known to occur in aqueous solutions at this pH range.[88-90] Shifting our focus toward primarily acid solutions, we found 1.5 equivalents of UO_2^{2+} to 1.5 equivalents of VO_4^{3-} in acetic acid (HOAc) resulted in a fully soluble solution, but after sitting for 1 hour at room temperature or by agitating the acidic solution over a layer of DCE with **4.2b** for 15 mins resulted in formation of a bright yellow suspension. In the biphasic sequestration experiments, we found that in some instances we were able to achieve a small amount of UO_2^{2+} sequestration by forming complex **4.4N/4.5N** and monitoring by $^{31}P\{^1H\}$ NMR spectroscopy (Chapter 4 and section 5.2.1), resulted in the most promising results (**Table 5.2**).

In order to try and prevent formation of a suspension, we attempted to alter the solubility by slightly changing the amount of aqueous acid solution added (pH = 3.0; 2–4 ml). We found that by slightly varying the concentration of the aqueous layer ($7.5x10^{-3}$ to $3.8x10^{-3}$ M) dramatically affected the UO_2^{2+} extraction. At higher concentrations there was a small amount of UO_2^{2+} sequestration from the mixture (**4.4N/4.5N**), with subsequent formation of by–products **5.5** and **4.1** (section 5.2.1) (a, **Figure 5.7**), while at lower concentrations there was none with subsequent increased formation of the by–products **5.5** and **4.1**. Additionally, at these highly acidic conditions (pH = 3.0), we found that the UO_2^{2+} sequestrated product, **4.4N/4.5N**, decomposes in the biphasic mixture over the course of 3 hours to form a large quantities of **4.1** (b, **Figure 5.7**).

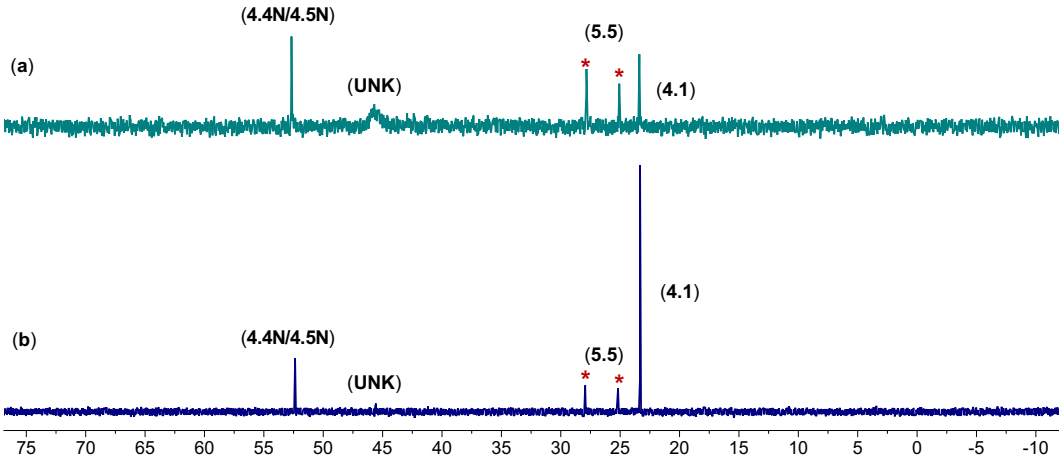

Figure 5.7. $^{31}P\{^{1}H\}$ NMR spectrum for biphasic UO_2^{2+} sequestration in the presence of VO_4^{3-} after (**a**) 15mins and (**b**) 3 hours.

Unfortunately, due to the difficultly in solubilizing uranyl vanadate in the desired pH range and concentrations of ions in the aqueous solution, we were unable to further carry out or optimize this chemistry in the time allotted of the PhD award date. For future work, we have postulated alternating the counterions present in the aqueous layer. For example, previous reports have indicated uranyl vanadate can be solubilized with carbonate (CO_3^{2-}),[85-86] which is correlated to the chemical composition present in seawater. Additionally, tuning the ligand in order to make a more robust ligand toward acidic solutions is of upmost importance in performing this chemistry. We found highly acidic aqueous solutions and higher concentrations of OAc^- led to the decomposition of the mono–anionic complex **5.5** (section 5.2.1) and **4.1**. We are still unsure of why increased concentrations of OAc^- causes the rate in decomposition but should be carried out in further work in order to optimize these conditions.

5.2.3 Supplementary reactivity of various derivatized *o*–carboranes

5.2.3.1 Reactivity of $[CoCp^*_2]_2[(nido–1,2–(Ph_2PO)_2–1,2–C_2B_{10}H_{10})]$ with Fe^{II} and Co^{II}

In our investigations into selective nuclear waste remediation and seawater extraction chemistry, we were also interested in probing alternative transition metals complexes for reactivity. Iron(II) and cobalt(II) initially were investigated as the preliminary reactions due to the readily available starting materials in the lab. Interestingly, iron is extremely relevant in terms of both seawater and nuclear waste sequestration chemistry. For example, amidoximes – the most widely used UO_2^{2+} sequestration – lack selectivity for uranyl in the presence of vanadium and iron.[24, 26] Additionally, in nuclear waste, there are high concentrations of iron in the waste streams due to the corrosion of the steel over time. Due to the high content of iron compared to fission products, it adds an extra level of difficulty to selectively remove the desired ions for remediation. This presented an opportunity to investigate iron coordination to our derivatized *o*–carborane system. Alternatively, cobalt does not represent any specific relevance to this sequestration chemistry but was originally synthesized and characterized for potential small molecule activation – which has not since been probed further. Addition of 2.0 equivalent of $[CoCp^*_2]_2[(nido–1,2–(Ph_2PO)_2–1,2–C_2B_{10}H_{10})]$ (**4.2a**) to a suspension of $Fe^{II}(OAc)_2$ resulted in a heterogenous solution which over the course of 1 hour became homogenous. The ^1H NMR spectrum in d_3–MeCN exhibits paramagnetically shifted signals at 32.1 and 10.2 ppm for the aryl C–H resonances compared to **4.2a**, at 7.24 and 8.05 ppm. The $^{31}P\{^1H\}$ NMR spectrum no longer displays a signal for **4.2a** at 29.8 ppm and is silent, most likely resulting for the paramagnetic Fe^{II} center. Recrystallization from a concentrated MeCN solution at room temperature resulted in large block yellow crystals suitable for XRD analysis,

affording $[CoCp^*_2]_2[Fe(nido\text{–}1,2\text{–}(Ph_2PO)_2\text{–}1,2\text{–}C_2B_{10}H_{10})_2]$ (**5.6**) in a 62% yield (a, **Figure 5.8**).

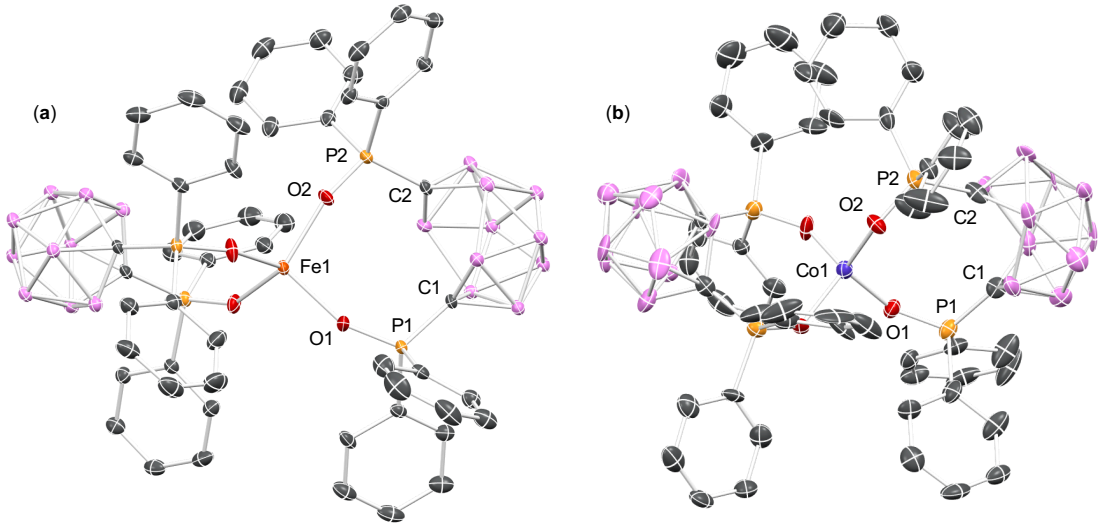

Figure 5.8. Solid–state molecular structures of complexes **5.6** (**a**) and **5.7** (**b**). H atoms, $[CoCp^*_2]^+$ counter cations, and all co–crystallized solvent molecules are omitted for clarity.

The solid–state molecular structure revealed coordination of two bidentate direduced *nido*–carborane ligands with a tetrahedral core about the Fe^{II} center. The *nido*–carborane displays a cleaved C···C bond (2.830 Å) and a slightly contracted P···P distance (4.667 Å) relative to the direduced ligand, **4.2a** (**Table 5.3**). Biphasic sequestration chemistry has not yet been performed with **5.5**, but this could be an interesting structure to probe in building on the work outlined in sections 5.2.1 and 5.2.2. Next, we sought reactivity with cobalt(II). Addition of 2.0 equivalents of a gold solution of **4.2a** in MeCN to a blue solution of $CoCl_2$ in MeCN resulted in a seafoam green homogenous solution in which the diamagnetic starting material **4.2a** was consumed and two new broad aryl C–H resonances appeared at 8.8 and 7.4 ppm with additional broad paramagnetically shifted signals at 186, 16.8, and 9.3 ppm. The $^{31}P\{^1H\}$ NMR spectrum was silent at the starting material was fully consumed, with the ^{11}B NMR spectrum displaying

broadened signals at 1.1, –15.0 and –17.7 ppm. Single crystals suitable for XRD analysis of $[CoCp^*_2]_2[Co(nido\text{–}1,2\text{–}(Ph_2PO)_2\text{–}1,2\text{–}C_2B_{10}H_{10})_2]$ (**5.7**) (b, **Figure 5.8**) were obtained by vapor diffusion of Et_2O into a concentrated MeCN solution at –38 ºC in a 77% yield. Similar to **5.6**, the solid–state molecular structure of **5.7** revealed coordination of two bidentate direduced *nido*–carborane ligands with a tetrahedral core about the Co^{II} center. The *nido*–carborane displays a cleaved C–C bond of 2.879 Å and a slightly contracted P···P distance (4.822 Å) relative to the direduced ligand, **4.2a** (**Table 5.3**).

Table 5.3. Selected interatomic distances (Å) for **4.2a**, **5.6**, and **5.7**.

	4.2a	**5.6**	**5.7**
P···P	5.036Å	4.667Å	4.822Å
C···C	2.860Å	2.830Å	2.879Å

5.2.3.2 Reactivity of $[Me_3Si]_2[(nido\text{–}1,2\text{–}(Ph_2PO)_2\text{–}1,2\text{–}C_2B_{10}H_{10})]$

In developing systems for selective capture and release chemistry we sought to investigate alternative ligand frameworks to perform the desired transformations. In all our current chemistry, we have utilized the starting materials, $[CoCp^*_2]_2[(nido\text{–}1,2\text{–}(Ph_2PO)_2\text{–}1,2\text{–}C_2B_{10}H_{10})]$ (**4.2a**) or $[Bu_4N]_2[(nido\text{–}1,2\text{–}(Ph_2PO)_2\text{–}1,2\text{–}C_2B_{10}H_{10})]$ (**4.2b**) for the synthesis of UO_2^{2+}–containing complexes. Due to the relatively high reduction potential of at –0.91 and –1.11 V, these complexes were synthesized by reacting neutral derivatized *o*–carborane (**4.1**) with known strong reducing agents, such as $CoCp^*_2$ and KC_8. Further reactivity of these compounds with various d– and f–block metal salts such as $[UO_2Cl_2(THF)_2]_2$, $Nd(NO_3)_3(THF)_2$, $CoCl_2$, and $Fe(OAc)_2$ have shown to undergo transmetallation with subsequent release of either $[CoCp^*_2][Cl]$, $[CoCp^*_2][NO_3]$, $[CoCp^*_2][OAc]$, or $[Bu_4N][Cl]$ as byproducts. Removal of these byproducts from a synthetic perspective has proven difficult and either requires selective bulk recrystallization of material or multiple solvent purification steps

to remove the salts, which lowers yield due to similar solubility of the products. Metal–free, organic–based reductants have gained considerable attention within recent years for isolation of low–valent metal complexes with easy removal of the organic byproducts with washes or evaporation under high vacuum.[91-93] Saito *et. al*. in 2014 reported a series of organosilicon compounds that are capable of undergoing controlled $1e^-$ reduction of Ti^{IV} to various Ti^{III} complexes, with subsequent elimination of Me_3SiCl and pyrazine–derivatized byproducts.

The benefits in utilizing these organic reductants stems from ease of workup and removal of the byproducts formed as a result of the reduction. Expanding on this chemistry, our group has previously shown use of these organosilicon compounds, 1,4–bis(trimethylsilyl)–1–aza–2,5–cyclohexadiene (TMS_2–pyz), for PCET chemistry, probing HAT at a P^V=O using Me_3Si• as a "bulky hydrogen atom" surrogate, with elimination of pyrazine as a byproduct.[94] Taking a similar approach in this chemistry, we were curious if we could utilize an organosilicon reductant, TMS_2–pyr, to generate an analogous direduced "capped" *o*–carborane species as **4.2a/b**, which could then undergo subsequent transmetallation reactions, generating byproducts that were simple to remove by solvent washes or evaporation by high vacuum.

Reduction of **4.1** using 1.1 equivalents of TMS_2–pyr in benzene afforded a white suspension from which the direduced *nido*–carborane, $[Me_3Si_2]_2[(nido–1,2–(Ph_2PO)_2–1,2–C_2B_{10}H_{10})]$ (**5.8**) could be isolated as a diamagnetic, white crystalline solid in 87% yield (**Figure 5.9**).

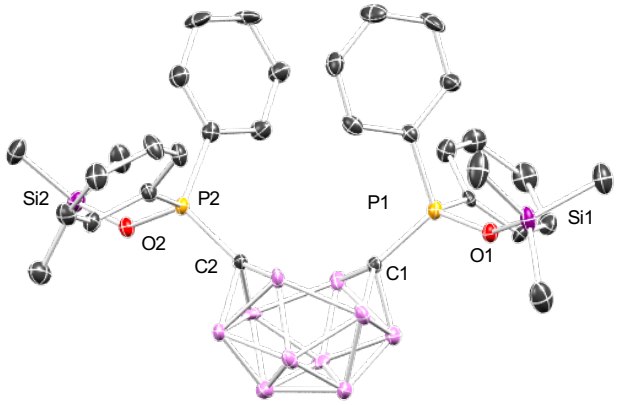

Figure 5.9. Solid–state molecular structures of complexes **5.8**. H atoms and all co–crystallized solvent molecules are omitted for clarity.

The ^{1}H NMR spectrum of **5.8** in d_3–MeCN exhibits a sharp singlet at 0.91 ppm, corresponding the the –SiMe$_3$ resonances, with two aryl C–H resonances at 7.37 and 7.51 ppm, compared to three distinct aromatic signals seen in **4.1**. The ^{31}P{^{1}H} NMR spectrum displays a down–shifted singlet at 57.2 ppm, compared to **4.1** and **4.2a/b**, corresponding to a single P–containing species.

Table 5.4. Selected interatomic distances (Å), angles (°), and torsion angles (°) for **4.1**, **4.42a**, and **5.8**.

	4.1	**4.2a**	**5.8**
P···P	3.537 Å	5.036 Å	5.348 Å
C–C	1.688(4) Å	2.860 Å	2.853 Å
P1–O1	1.469(2) Å	1.487(3) Å	1.558(1) Å
C1–P1	1.871(6) Å	1.745(2) Å	1.710(5) Å
C1–P1–O1	109.98°	118.05°	111.57°
C2–C1–P1	119.57°	135.01°	136.42°
P1–C1–C2–P2	10.03°	–19.24°	14.07°

The solid state structure of **5.8** revealed the [$C_2B_{10}H_{10}$] cluster was preserved, similar to reduction of **4.1** to form complexes **4.2a/b**, as an open–cage *nido*–carborane with a cleaved C–

C bond (2.853 Å) and elongated P···P distance (5.348 Å) relative to **4.1**. The bond metrics are comparable relative to the direduced compound **4.2a**, with a slightly more elongated P···P distance and consistent C–C distance (**Table 5.4**).

5.2.3.2.1 Reactivity with UO_2^{2+} salts

We next investigated the coordination chemistry of **5.8**. In probing reactivity, we hypothesized that reactivity with various metal–halides could promote elimination of organosilicon halides, with subsequent coordination of the direduced ligand to the metal center. In hopes of probing this ligand for selective UO_2^{2+} sequestration and recovery, addition of 0.5 equivalent of $[UO_2Cl_2(THF)_2]_2$ in deuterated chloroform ($CDCl_3$) or dichloromethane (d_2–DCM) resulted in no change in the spectrum of **5.8**, monitored by ^{1}H NMR spectroscopy. The reaction was also monitored at various temperatures (30–50 °C) but found that **5.8** is a thermally unstable compound, where over the course of two weeks, **5.8** decomposes at room temperature. Additionally, when heated above room temperature, there is immediate decomposition to unidentifiable products. Due to the unreactive nature of **5.8** with $[UO_2Cl_2(THF)_2]_2$, we postulated the formation of Me_3SiCl, the theoretical driving force of the reaction, was most likely not as strong as the Me_3Si–O–P bond. In order to promote elimination of –$SiMe_3$, we turned to $UO_2(OTf)_2(THF)_2$, where we postulated formation of a new Si–OTf bond could promote reactivity. Addition of 1.0 equivalent of $UO_2(OTf)_2(THF)_2$ to a d_3–MeCN solution of **5.8** at room temperature resulted in large yellow block crystals of [U(*nido*–7,8–$(Ph_2PO)_2$–7,8–$C_2B_9H_{10}$)(*nido*–1,2–$(Ph_2PO)_2$–1,2–$C_2B_{10}H_{10})_2$][Li] (**5.9, Figure 5.10**). The following was isolated in 22% yield by slow evaporation of a concentrated MeCN solution where crystals were suitable for XRD analysis were obtained. The following solid–state molecular structure revealed activation of the O–U–O moiety with preservation of two of the

three clusters, with elimination of a B^+ from one of the three clusters in the system, as seen in one of our previous examples (**4.3**, Chapter 4). Li^+ is incorporated into the structure and is most likely from advantageous Li^+ that was carried through from the original starting materials. O–U–O activation was an unexpected result and has been previously shown extensively through reductive sialylation with organosilicon reagents or metal cation coordination to form activated O–U–O bonds.[95-103] Additionally, Hayton *et. al*. has shown functionalization by use of reducing agents to form U^{VI} with elimination of RSi–O–SiR compounds.[104]

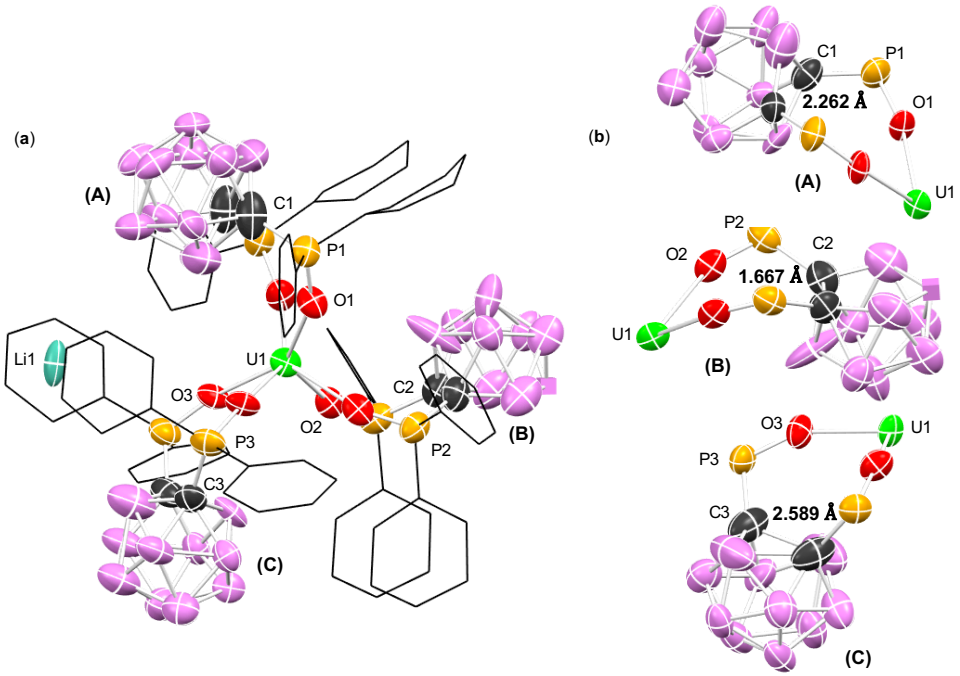

Figure 5.10. Solid–state molecular structure of [U(*nido*–7,8–$(Ph_2PO)_2$–7,8–$C_2B_9H_{10}$)(*nido*–1,2–$(Ph_2PO)_2$–1,2–$C_2B_{10}H_{10})_2$][Li] (**5.9**) obtained fro X–Ray diffraction studies. H atoms, $[CoCp^*_2]^+$ counter cations, phenyl C–H linkages, and all co–crystallized solvent molecules are omitted for clarity. (**a**) Full depiction of structure with labeled individual carborane clusters (A–C). (**b**) Individual carborane clusters (A–C) with pertinent C–C bond distances.

Based on relative bond lengths and distortion of the clusters, oxidation state determination of the U–center is difficult. The U is most likely either U^{IV} or U^{VI}, dependent on

the oxidation state of the carborane clusters. For example, the C–C bond length for the *nido*–[B_9] cluster is 1.667 Å (C), which is consistent with the C–C bond length found in **4.3** (1.622 Å), consistent with a (1^-) formal charge. As for the other two clusters, the C–C bond lengths are 2.262 Å and 2.589 Å (A and C, respectively; **Figure 5.10**). The C–C bond lengths in both clusters [B_{10}] are significantly different, suggesting they may be different oxidation states. Neither C–C bond length suggests a formal charge of (2^-) within the clusters when compared to direduced complexes **4.4** and **4.5**, where the C–C bond lengths average 2.85 Å.

Attempts to reproduce this product with the corresponding synthesis proved to be unsuccessful, seeming that clean **5.8** was resynthesized and Li^+ contamination was thoroughly monitored by ^{7}Li NMR spectroscopy. We attempted to reproduce the previous reactions conditions by addition of a Li salt, Li(OTf). Addition of 1.0 equivalent of $UO_2(OTf)_2(THF)_2$ with varying quantities of Li(OTf) (1.0–4.0 equivalents) to d_3–MeCN solutions containing 3.0 equivalents of **5.8** were monitored by ^{1}H, ^{19}F, ^{11}B, and ^{31}P{^{1}H} NMR spectroscopies. The ^{1}H NMR spectrum displayed formation of HMDSO which is expected for elimination of the –$SiMe_3$ moiety on the ligand, although it is important to note, this was commonly seen upon decomposition of **5.8** with heating or advantageous water present in the solvent. The ^{31}P{^{1}H} NMR spectrum, monitored over the course of 24 hours, displayed formation of 2 new signals at 40 and 41 ppm, with small shifts in the ^{19}F and ^{11}B spectra. After multiple attempts of recrystallization, we were unsuccessful in ascertaining a full chemical structure. In one trial, we were able to obtain needle crystals that had poor diffraction and extreme disorder. The complex displayed hexagonal symmetry and displayed a similar core structure to **5.9**, but we were unable to obtain a full structure. Additionally, we were curious if we could independently synthesize a similar structure to **5.9** through use of $U^{VI}(O^tBu)_6$[105] in order to gain a synthetic

and spectroscopic handle. Addition of 3.0 equivalents of **5.8** to 1.0 equivalent of $U^{VI}(O^tBu)_6$ in d_3–MeCN or d_4–THF resulted in no change by ^1H, $^{31}P\{^1H\}$, or ^{11}B NMR spectra. Lastly, although these reactions were proving unsuccessful, we were interested in probing the role of $–SiMe_3$ in the activation chemistry. Unfortunately, in the time of the allotted of the awarded PhD, we were unsuccessful in further probing this reactivity, but is an interesting direction for suture work.

5.2.3.2.2 Reactivity with transition metal salts (CoF_2 and VOF_3)

In addition to develop systems for UO_2^{2+} salt reactivity with **5.8**, we were curious if we could harness $–SiMe_3$ elimination by use of fluoride salts. The driving force behind $F–SiMe_3$ bond formation is significant compared to other halide–Si (ie. $Cl^–$) and O–Si bonds. Known soluble fluoride salts of the f–block (UO_2F_2) are difficult to obtain (ie. reactivity from HF or UF_6),[106-109] so we turned our attention toward commercially available fluoride transition metal salts. Soluble fluoride salts within the d–block are very limited, but we first tested the reactivity of CoF_2 with **5.8** as we had previously sought reactivity of Co–based *o*–carboranes.Unfortunately, after many attempts in various solvents (MeCN, THF, DCM, $CHCl_3$, PC, and pyridine) we found the CoF_2 was completely insoluble and unable to react with **5.8**. Based on how insoluble these salts generally are, we turned out attention toward VOF_3 which is a relatively soluble fluoride salt. Addition of 1.0 equivalent of a bright orange suspension of VOF_3 to a colorless solution of **5.8** in DCM led to formation of dark green–teal solution with formation of a green crystalline solid. Characterization by ^1H and $^{31}P\{^1H\}$ NMR spectroscopies indicated formation of neutral *o*–carborane (**4.1**) and unreacted **5.8**. Increasing the amount of ligand compared to VOF_3 changed the amount of starting material (**5.8**) that was present in the reaction mixture and was never fully consumed. Instead, we found addition of

2.0 equivalents of VOF_3 to **5.8** at room temperature led to the formation of a bright teal solution with formation of dark green–teal crystalline solid. Analysis of an aliquot from the reaction mixture indicated formation of **4.1** with complete consumption of starting material (**5.8**) seen by the ^{1}H, ^{11}B, and $^{31}P\{^{1}H\}$ NMR spectra. Additionally, the ^{19}F NMR spectrum indicated formation of F–$SiMe_3$ and the ^{51}V NMR spectrum displayed no signal, indicating the species was most likely a paramagnetic species. Slow evaporation of a concentrated DCM solution of **5.8** led to crystals suitable for X–ray analysis isolating, [$V^{IV}O$(*nido*–1,2–$(Ph_2PO)_2$–1,2–$C_2B_{10}H_{10})_2$] (**5.10**) in 52% yield (**Figure 5.11**).

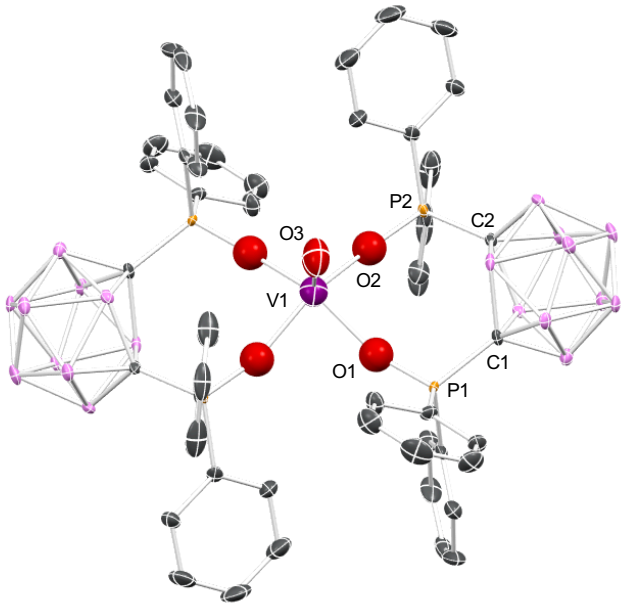

Figure 5.11. Solid–state molecular structure of [$V^{IV}O$(*nido*–1,2–$(Ph_2PO)_2$–1,2–$C_2B_{10}H_{10})_2$] (**5.10**) obtained from XRD analysis. H atoms and all co–crystallized solvent molecules are omitted for clarity.

The solid–state structure indicates the metal is a V^{IV}–center with mono–reduced *o*–carborane clusters, indicative of the paramagnetic NMR spectra, with a cage C–C bond length of 2.420 Å) and interatomic P···P distance of 4.396 Å. While *closo* and *nido* carboranes are widely

known, carboranes with odd numbers of skeletal electrons are rare due to the decreased stability compared to their even–numbered electron counterparts.[70, 72-74, 110-119] The decrease in relative bond length of the C–C bond in the cage is consistent with singly–reduced organic–based *o*–carborane species (**Table 5.5**),[69-76] yet not consistent with our isolated mono–anionic structure (**5.5**) – as this complex has a $C_{cluster}$ atom puckered out of the plane and is asymmetric (**Figure 5.3**).

Table 5.5. Selected interatomic distances (Å), angles (°), and torsion angles (°) for **5.8** and **5.10**.

	5.8	**5.10**
P···P	5.348 Å	4.396 Å
C–C	2.853 Å	2.420 Å
P1–O1	1.558(1) Å	1.512(5) Å
C1–P1	1.710(5) Å	1.787(7) Å
C1–P1–O1	111.57°	110.02°
C2–P2–O2	111.19°	109.97°
C2–C1–P1	136.42°	123.21°
C1–C2–P2	136.22°	123.81°
P1–C1–C2–P2	14.07°	–0.66°

The stoichiometry for this reaction is imbalanced and the mechanism in which the product is formed cleanly with subsequent oxidation of the ligand, **5.8**, is most likely very complicated. VOF_3 has been previously shown to act as a oxidizing–mediator in organic coupling reactions,[120-121] which could be capable of oxidizing the ligand to form the mono–reduced form or undergo $2e^-$ reduction back to neutral *o*–carborane (**4.1**). As for the $–SiMe_3$ elimination, reactivity could occur by PCET elimination of $•SiMe_3$ or as "deprotonation" as a "bulky hydrogen", $^+SiMe_3$. Ultimately, more experiments need to be performed in order to elucidate this chemistry and will provide an interesting for further work.

5.3 Conclusions

In summary, this chapter has outlined methods for selective uranyl separation and recovery by controlled redox–switchable chelation using a derivatized *ortho*–carborane in biphasic (organic/aqueous) environments. We anticipate this fundamentally new direction in cluster carborane chemistry may have a significant impact on nuclear fuel extraction and waste sequestration activities.

5.4 Experimental Section

5.5.1 General Considerations

All manipulations were performed under an atmosphere of dry, oxygen–free N_2 or Ar by means of standard Schlenk or glovebox techniques (MBraun (equipped with a –38 °C freezer) or VAC gloveboxes). Hexanes, pentane, dichloromethane (DCM), and benzene were dried on an MBraun solvent purification system. Acetonitrile ($–H_3$ and $–D_3$) was dried over CaH_2 for several days prior to distillation. THF was dried over sodium benzophenone and distilled. 1,2–Dichloroethane (DCE) was initially distilled followed by drying over CaH_2 for several days prior to a second distillation and subsequent storage on activated 4 Å molecular sieves. VOF_3, Na_3VO_4, $CoCl_2$, $FeCl_2$, $[Bu_4N][Cl]$ was purchased from Fisher Scientific. $[Th(NO_3)_4•H_2O]$ was purchased from Stream Chemicals. *Ortho*–carborane was purchased from Boron Specialties and sublimed before use. Ph_2PCl was purchased from Aldrich and vacuum distilled prior to use. $CsNO_3$ and decamethylcobaltocene ($CoCp^*_2$) and was purchased from Aldrich; $CoCp^*_2$ was purified by filtration through Celite using pentane, followed by recrystallization from pentane at –38 °C over several days. $[Bu_4N][PF_6]$ was purchased from Oakwood Chemicals and purified by twice recrystallizing from hot ethanol. The recrystallized product was then washed with cold water, cold ethanol, and pentane prior to drying at 100 °C under vacuum for 24 h.

Sodium acetate (NaOAc) buffer's (0.1 and 0.5 M) were prepared from a stock solution purchased from Aldrich (pH 4.9) and adjusted to pH 5.4 using NaOH. The pH value was confirmed using a pH meter. Ketjenblack® EC–600JD (KB) was purchased from a private supplier. $[UO_2(NO_3)_2(THF)_3]$,[122] $[Nd(NO_3)_3(THF)_3]$,[123] KC_8,[124] bis(triphenyl–phosphoranylidene)ammonium hexafluorophosphate ($[Ph_3PNPPh_3][PF_6]$)[125], and complexes (**4.1**), (**4.2a/b**), (**4.4**), and (**4.5**)[56] were prepared by literature procedures. $[Sm(NO_3)_3(THF)_3]$ synthesis was adapted from the synthesis of $[Nd(NO_3)_3(THF)_3]$.[123]

NMR spectra were obtained on a Varian Unity Inova 500 MHz or Agilent Technologies 400 MHz spectrometer, and referenced to residual solvent resonances of acetonitrile (MeCN–d_3) or externally (^{11}B: 85% $(Et_2O)BF_3$, ^{31}P: 85% H_3PO_4,). Unlocked spectra were collected with the 2H lock turned off. Gradient shimming including Z1 to Z5 was done with the strong 1H signal in the samples using a shim map generated with the same or similar sample with equal sample volume. Chemical shifts (δ) are recorded in ppm. All ^{11}B NMR spectra were processed using MestReNova software in order to reduce background signal with a linewidth of approximately 3000 Hz from the Pyrex NMR tubes. The NMR time–domain data were first left–shifted to discard the first ~0.1 ms. To correct the linear phase change, linear prediction (LP) is used to fill the initial discarded data before Fourier transform or an appropriate linear phase correction is applied to the frequency domain data after Fourier transform. T_1 relaxation values for ^{31}P nuclei were determined using the inversion–recovery method. The delay times after the 180–degree inversion pulse were varied up to the maximum of 5 times of the expected T_1 values. T_1's for complexes **4.1**, **4.2a/b**, **4.4**, **4.5**, and $[Ph_3PNPPh_3][PF_6]$ were determined in our previous report.[56]

UV/Vis absorption spectra were collected on a Shimadzu UV–2401PC spectrophotometer. The UO_2^{2+} extinction coefficient (Ɛ) was experimentally determined to be 7.715 $L•mol^{-1}•cm^{-1}$ (460 nm) at pH 5.4. $Nd(NO_3)_3THF_3$ (797, 746, 583, and 525 nm) and $Sm(NO_3)_3THF_3$ (404 nm) display multiple absorbances at pH 5.4. $CsNO_3$ and $Th(NO_3)_4•H_2O$ do not display optical absorbances in the visible region.

Elemental analyses (C, N, H) were recorded at the University of California, Berkeley using a Perkin Elmer 2400 Series II combustion analyser.

Galvanostatic Bulk Electrolysis cycling experiments were carried out using a Metrohm Autolab PGSTAT128N potentiostat/galvanostat and carried out inside an Ar glovebox. The full experimental setup for both the mono– and biphasic cycling experiments are described below.

X–ray crystallography data for complexes **5.1, 5.2, 5.3, 5.6, 5.7, 5.8, 5.9,** and **5.10** were collected at University of California, Santa Barbara on a Bruker KAPPA APEX II diffractometer equipped with an APEX II CCD detector using a TRIUMPH monochromator with a Mo Kα X–ray source (α = 0.71073 Å). The crystals were mounted on a cryoloop under Paratone–N oil, and all data were collected at 100(2) K using an Oxford nitrogen gas cryostream system. A hemisphere of data was collected using ω scans with 0.5° frame widths. Data collection and cell parameter determination were conducted using the SMART program. Integration of the data frames and final cell parameter refinement were performed using SAINT software. Absorption correction of the data was carried out using SADABS. Structure determination was done using direct or Patterson methods and difference Fourier techniques. All hydrogen atom positions were idealized and rode on the atom of attachment. Structure solution, refinement, graphics, and creation of publication materials were performed using

SHELXTL or OLEX.[2] X–ray studies for complexes **5.3** and **5.5** were carried out at Harvard University and the data was collected at 298 K. The intensities of the reflections were collected by means of a Bruker D8 Venture diffractometer (MoKα radiation, λ=0.71073 Å), and equipped with an Oxford Cryosystems nitrogen flow apparatus. The collection method involved 0.5° scans in ω at 0, and 29° in 2θ with a Photon100 detector distance at 10 cm. Data integration down to 0.84 Å resolution was carried out using SAINT V8.37A with reflection spot size optimization. Absorption corrections were made with the program SADABS. The structure was solved by the Intrinsic Phasing methods and refined by least–squares methods again F2 using SHELXT–2014 and SHELXL–2014[126-127] with OLEX 2 interface[128]. Non–hydrogen atoms were refined anisotropically, and hydrogen atoms were allowed to ride on the respective atoms. The Ortep plots produced with SHELXL–2014 program.

5.5.2 Synthesis of Compounds

Synthesis of $[CoCp^*_2]_2[Th(nido\text{–}1,2\text{–}(Ph_2PO)_2\text{–}1,2\text{–}C_2B_{10}H_{10})_3]$ (5.1): A 20 mL vial equipped with a magnetic stirbar was charged with **4.2a** (24.0 mg, 0.02 mmol) and 2 mL of MeCN. In a separate vial, $[Th(NO_3)_4{\bullet}H_2O]$ (3.4 mg, 0.0066 mmol) was dissolved in 1 mL of MeCN and then added dropwise to the stirring solution of **4.2a**, where the solution went from golden to bright yellow. After stirring for 5 mins, a yellow solid began to precipitate from the reaction mixture and this was stirred at room temperature for 2 hours. Stirring was discontinued and the mixture was passed over a plug of Celite, collecting a yellow solid and a yellow filtrate. The solvent was removed from the yellow filtrate yielding a yellow solid. Residual $[CoCp^*_2][NO_3]$ was removed by selectively recrystallizing the mixture by vapor diffusion of pyridine/Et_2O at –38 °C in 2–3 crops. The supernatant was transferred and volatiles removed collecting a yellow solid (7.1 mg, 0.0029 mmol, 44 % yield). Single crystals suitable for XRD

studies were grown by vapour diffusion of Et_2O into a saturated MeCN solution of **5.1** at room temperature. **^{1}H NMR** (400 MHz, MeCN–*d_3*): δ 7.95 (m, 12H); 7.84 (m, 12H); 7.09 (m, 18H); 6.87 (t, 6H); 6.15 (m, 12H); 1.69 (s, 60H). Note: Carborane B–**H** resonances are too broad to be observed. **^{11}B** and **^{11}B{^{1}H} NMR** (400 MHZ, MeCN–*d_3*): δ 0.85; –17.57. **^{31}P{^{1}H} NMR** (400 MHz, MeCN–*d_3*): δ 51.32.

Synthesis of [CoCp$^*_2$]$_3$[Nd(nido–1,2–(Ph$_2$PO)$_2$–1,2–C$_2$B$_{10}$H$_{10}$)$_3$] (5.2): A 20 mL vial equipped with a magnetic stirbar was charged with **4.2a** (36.0 mg, 0.03 mmol) and 2 mL of MeCN. In a separate vial, [Nd(NO$_3$)$_3$(THF)$_3$] (5.4 mg, 0.01 mmol) was dissolved in 2 mL of MeCN and then added dropwise to the stirring solution of **4.2a**, where the solution went from golden to bright yellow. The solution remained homogenous and the reaction was stirred at room temperature for 2 hours. The volatiles were removed *in vacuo,* yielding a yellow powder. THF (8 mL) were added and the solids were allowed to settle to the bottom where the filtrate was passed over a plug of Celite. The yellow solid was washed with THF (3 x 2mL) and passed over the same plug of Celite. The remaining solids were then dissolved in MeCN and filtered on the same Celite plug into a new vial. The MeCN filtrate was collected and the volatiles removed in vacuo, yielding a yellow powder. Residual [CoCp$^*_2$][NO$_3$] was removed by selectively recrystallizing the mixture by vapor diffusion of pyridine/Et_2O at –38 °C in two crops. The supernatant was transferred and volatiles removed collecting a yellow solid (18.2 mg, 0.0066 mmol, 66 % yield). Single crystals suitable for XRD studies were grown by vapour diffusion of Et_2O into a saturated MeCN solution of **5.2** at room temperature. **^{1}H NMR** (400 MHz, MeCN–*d_3*): δ 9.82 (broad m, 14H); 7.64 (m, 15H); 7.34 (m, 8H); 5.42 (s, 8H); 4.13 (s, 15H); 1.68 (s, 90H). Note: Carborane B–**H** resonances are too broad to be observed. **^{11}B** and

$^{11}B\{^1H\}$ NMR (400 MHZ, MeCN–d_3): δ 0.17; –17.57. **$^{31}P\{^1H\}$ NMR** (400 MHz, MeCN–d_3): δ 140.6.

Synthesis of $[CoCp^*_2]_3[Sm(nido\text{–}1,2\text{–}(Ph_2PO)_2\text{–}1,2\text{–}C_2B_{10}H_{10})_3]$ (5.3): A 20 mL vial equipped with a magnetic stirbar was charged with **4.2a** (24.0 mg, 0.02 mmol) and X mL of MeCN. In a separate vial, $[Sm(NO_3)_3(THF)_3]$ (3.6 mg, 0.0066 mmol) was dissolved in 2 mL of MeCN and then added dropwise to the stirring solution of **4.2a**, where the solution went from golden to bright yellow. The solution remained homogenous and the reaction was stirred at room temperature for 2 hours. The volatiles were removed *in vacuo,* yielding a yellow powder. THF (8 mL) were added and the solids were allowed to settle to the bottom where the filtrate was passed over a plug of Celite. The yellow solid was washed with THF (3 x 2mL) and passed over the same plug of Celite. The remaining solids were then dissolved in MeCN and filtered on the same Celite plug into a new vial. The MeCN filtrate was collected and the volatiles removed in vacuo, yielding a yellow powder. Residual $[CoCp^*_2][NO_3]$ was removed by selectively recrystallizing the mixture by vapor diffusion of pyridine/Et_2O at –38 °C in two crops. The supernatant was transferred and volatiles removed collecting a yellow solid (12.1 mg, 0.0044 mmol, 66 % yield). Single crystals suitable for XRD studies were grown by vapour diffusion of Et_2O into a saturated MeCN solution of **5.3** at room temperature. **^1H NMR** (400 MHz, MeCN–d_3): δ 8.86 (t, 12H); 7.24 (t, 12H); 7.12 (t, 8H); 6.25 (t, 6H); 5.84 (t, 12H); 5.35 (t, 12H); 1.69 (s, 90H). Note: Carborane B–**H** resonances are too broad to be observed. **^{11}B** and **$^{11}B\{^1H\}$ NMR** (400 MHZ, MeCN–d_3): δ 0.04; –17.00; –18.15. **$^{31}P\{^1H\}$ NMR** (400 MHz, MeCN–d_3): δ 27.87.

Synthesis of $[CoCp^*_2][Cs(nido\text{–}1,2\text{–}(Ph_2PO)_2\text{–}1,2\text{–}C_2B_{10}H_{10})]$ (5.4): A 20 mL vial equipped with a magnetic stirbar was charged with $CsNO_3$ (4.0 mg, 0.02 mmol) and 1 mL of MeCN. In

a separate vial, **4.2a** (24.0 mg, 0.02 mmol) was dissolved in 2 mL of MeCN and then added dropwise to the stirring solution of $CsNO_3$, where the solution went from golden to bright yellow. The solution remained homogenous and the reaction was stirred at room temperature for 2 hours. The solution was filtered over a plug of Celite and the volatiles were removed *in vacuo,* yielding a shiny golden solid. $[CoCp^*_2][NO_3]$ was removed by selectively recrystallizing the mixture by vapor diffusion of pyridine/Et_2O at –38 °C in two crops. The supernatant was transferred and volatiles removed collecting a yellow solid (10.3 mg, 0.010 mmol, 51 % yield). Single crystals suitable for XRD studies were grown by vapour diffusion of Et_2O into a saturated MeCN solution of **5.4** at room temperature yielding golden large blocks. **^{1}H NMR** (400 MHz, MeCN–*d_3*): δ 7.88 (m, 8H); 7.26 (m, 12H); 1.69 (s, 30H). Note: Carborane B–**H** resonances are too broad to be observed. **^{11}B** and **^{11}B{^{1}H} NMR** (400 MHZ, MeCN–*d_3*): δ –0.49; –18.91; –21.60. **^{31}P{^{1}H} NMR** (400 MHz, MeCN–*d_3*): δ 31.66.

Synthesis of $[Bu_4N][(nido–1,2–(Ph_2PO)_2–1,2–C_2B_{10}H_{10})H]$ (5.5): A 1.5 mL NaOAc buffer solution (0.5 M, pH 5.4) was added slowly dropwise without stirring to the DCE solution (4 mL) containing independently synthesized **4.2a** (20.5 mg, 0.02 mmol). After addition, the mixture was allowed to stir for 2.5 hours, where stirring was discontinued and the organic and aqueous phases were separated using a small separatory funnel. The DCE fraction was collected and volatiles removed in vacuo, yielding a colorless oil. The product was selectively recrystallized by diffusion of pentane into a saturated THF solution containing a mixture of **5.5** and **4.1** at room temperature. The filtrate, containing **4.1**, was removed (a, **Figure 5.12**) and the colorless crystalline solid was collected, obtaining **9** (9.4 mg, 0.012 mmol, 60 % yield) (b, **Figure 5.12**). Crystals suitable for X–ray diffraction studies were obtained in a second crop by diffusion of pentane into a saturated solution of **9** in THF at room temperature. **^{1}H NMR** (400

MHz, $CDCl_3$): δ 8.05 (m, 4H); 7.56 (m, 4H); 7.35 (m, 8H); 7.24 (m, 4H); 4.27 (m, 1H); 3.19 (broad m, 8H); 1.58 (broad m, 8H); 1.38 (broad m, 8H); 0.94 (m, 12H). Note: Carborane B–**H** resonances are too broad to be observed. **^{11}B** and **^{11}B{^{1}H} NMR** (400 MHZ, $CDCl_3$): δ 16.58; 2.18; -5.29; -14.79, -20.64. **^{31}P{^{1}H} NMR** (400 MHz, $CDCl_3$): δ 27.08 (s, 1P); 24.75 (s, 1P).

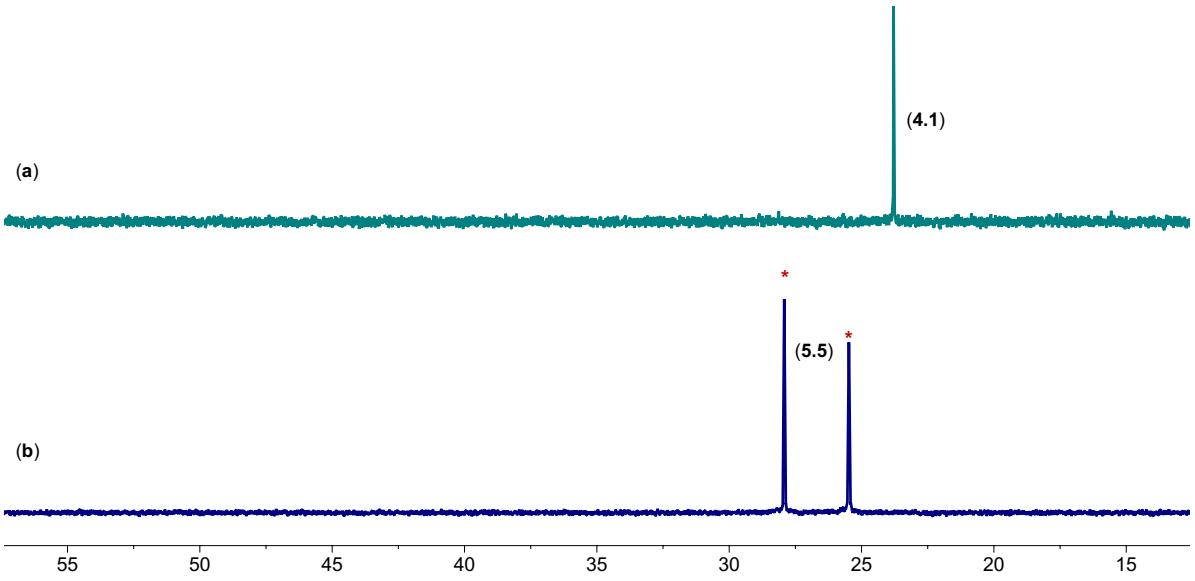

Figure 5.12. ^{31}P{^{1}H} NMR Spectra for Purification of Complex 5.5. (**a**) ^{31}P{^{1}H} NMR spectrum of the supernatant from purification containing **4.1** in $CDCl_3$. (**b**) ^{31}P{^{1}H} NMR spectrum of the crystals isolated from the selective recrystallization of complex **5.5** in $CDCl_3$.

Synthesis of [CoCp$^{*}_2$]$_2$[Fe(*nido*–1,2–(Ph$_2$PO)$_2$–1,2–C$_2$B$_{10}$H$_{10}$)$_2$] (5.6): A 20 mL vial equipped with a magnetic stirbar was charged with $Fe(OAc)_2$ (1 equiv.) and 1 mL of MeCN. In a separate vial, **4.2a** (24.0 mg, 0.02 mmol) was dissolved in 2 mL of MeCN and then added dropwise to the stirring solution of $Fe(OAc)_2$, where the solution went to bright yellow. The solution went from a suspension to homogenous and the reaction was stirred at room temperature for 2 hours. The solution was filtered over a plug of Celite and the volatiles were removed *in vacuo,*

yielding a golden solid. [$CoCp^*_2$][OAc] was removed by selectively recrystallizing the mixture by vapor diffusion of pyridine/Et_2O at –38 °C in two crops. The supernatant was transferred and volatiles removed collecting a yellow solid (62 % yield). Single crystals suitable for XRD studies were grown by vapour diffusion of Et_2O into a saturated MeCN solution of **5.6** at room temperature yielding golden large blocks. **^{1}H NMR** (400 MHz, MeCN–d_3): δ 32.1; 10.2; 1.69 ppm. Note: Carborane B–**H** resonances are too broad to be observed. **^{11}B** and **^{11}B{^{1}H }NMR** (400 MHZ, MeCN–d_3): δ –0.49; –18.91; –21.60.

Synthesis of [$CoCp^*_2$]$_2$[Co(*nido*–1,2–(Ph_2PO)$_2$–1,2–$C_2B_{10}H_{10}$)$_2$] (5.7): A 20 mL vial equipped with a magnetic stirbar was charged with $CoCl_2$ (1 mmol, 1 equiv.) and 1 mL of MeCN. In a separate vial, **4.2a** (24.0 mg, 0.02 mmol) was dissolved in 2 mL of MeCN and then added dropwise to the stirring solution of $CoCl_2$, where the solution went from blue to seafoam green. The solution remained homogenous and the reaction was stirred at room temperature for 2 hours. The solution was filtered over a plug of Celite and the volatiles were removed *in vacuo,* yielding a seafoam green powder. [$CoCp^*_2$][Cl] was removed by selectively recrystallizing the mixture by vapor diffusion of pyridine/Et_2O at –38 °C in two crops. The supernatant was transferred and volatiles removed collecting a seafoam green solid (77 % yield). Single crystals suitable for XRD studies were grown by vapour diffusion of Et_2O into a saturated MeCN solution of **5.7** at room temperature yielding large blue blocks. **^{1}H NMR** (400 MHz, MeCN–d_3): δ 186; 16.8, 9.3 ppm. Note: Carborane B–**H** resonances are too broad to be observed. **^{11}B** and **^{11}B{^{1}H} NMR** (400 MHZ, MeCN–d_3): δ 1.1; –15.0; –17.7.

Synthesis of [Me_3Si_2]$_2$[(nido–1,2–(Ph_2PO)$_2$–1,2–$C_2B_{10}H_{10}$)] (5.8): A 250 mL round bottom flask equipped with a magnetic stirbar was charged with **4.1** (54.5 mg, 1 mmol) and 40 mL of benzene. In a separate vial, TMS_2–pyz (22.6 mg, 1 mmol, 1.0 equiv) was dissolved in 5 mL of

benzene and added dropwise to the stirring solution of **4.1**. Upon addition, a white solid immediately precipitated from the reaction mixture and the mixture was stirred for 4 hours at room temperature. Stirring was discontinued and the solid was allowed to settle to the bottom of the flask. The supernatant was decanted and filtered over a fritted glass filter with a layer of Celite (0.5 inch). The solids were washed with benzene (3 x 6 mL) and each washing was filtered over the same Celite plug. The remaining solids were then dissolved in a minimal amount of DCM (5 mL) and filtered on the same Celite plug into a flask. The volatiles were removed *in vacuo,* yielding a white solid (95% yield). Single crystals suitable for X–ray crystallography were obtained by vapour diffusion of pentane in a saturated DCM solution of **5.8** at room temperature. **^{1}H NMR** (400 MHz, $CDCl_3$): δ 7.51 (m, 12H); 7.30 (m, 8H); 0.11 (s, 18H). Note: Carborane B–**H** resonances are too broad to be observed. **^{11}B** and **^{11}B{^{1}H} NMR** (400 MHZ, $CDCl_3$): δ 23.4; 3.66; –17.3. **^{31}P{^{1}H} NMR** (400 MHz, $CDCl_3$): δ 57.7. Selected interatomic distances for **5.8** where C···C: 2.853 Å; P···P: 5.348 Å.

5.5.3 Supplemental Figures and Methods for Selective Separation and Recovery of UO_2^{2+} from an Aqueous Mixture of Actinides(IV), Lanthanides(III), and Alkali metals(I) for Nuclear Waste Remediation

5.5.3.1 Biphasic Control Reaction of 2b with NaOAc buffer solution (0.5 M)

A 1.5 mL NaOAc buffer solution (0.5 M, pH 5.4) was added slowly dropwise without stirring to the DCE solution (4 mL) containing independently synthesized **4.2b** (20.5 mg, 0.02 mmol). After addition, the mixture was allowed to stir for 1.5 hours, resulting in a colorless organic phase and a colorless aqueous phase. A 1mL aliquot was removed from the organic layer and transferred to an NMR tube. An unlocked ^{31}P{^{1}H} NMR spectrum was collected indicating the formation of **4.1** and **5.5**, with formation of an unknown intermediate at 45 ppm (a, **Figure**

5.13). The sample was transferred back to the biphasic reaction and stirred for an additional hour. After 2.5 hours, stirring was discontinued and the organic and aqueous phases were separated using a small separatory funnel. A 1 mL aliquot was taken again from the colorless dichloroethane layer and transferred to an NMR tube. An unlocked $^{31}P\{^{1}H\}$ NMR spectrum was collected indicating the formation of **4.1** and **5.5** with disappearance of the intermediate at 45 ppm (b, **Figure 5.13**).

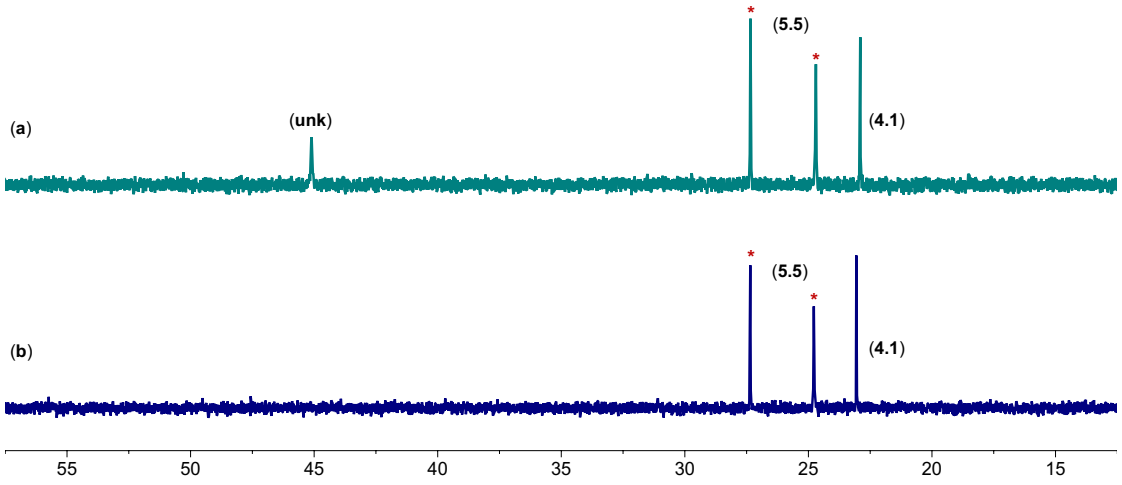

Figure 5.13. $^{31}P\{^{1}H\}$ NMR Spectra for Biphasic Control Reaction of 2b with NaOAc Buffer Solution (0.5 M, pH 5.4). $^{31}P\{^{1}H\}$ NMR spectrum of DCE layer after mixing 1.5 mL of 0.5 M sodium acetate buffer (pH 5.4) with **4.2b** in DCE (4 mL). (**a**) After 1.5 hours, indicating the formation of **4.1**, **5.5** (denoted as *), and unknown at 45 ppm as by–products and (**b**) After 2.5 hours, indicating the formation of **4.1** and **5.5** (denoted as *) with disappearance of unknown at 45 ppm.

5.5.3.2 Selectivity Control Experiments with Th^{IV}, Nd^{III}, Sm^{III}, and Cs^{I}

A 5 mL vial was charged with $Th(NO_3)_4 \cdot H_2O$ (14.4 mg, 0.03 mmol, 1.5 equiv), $Nd(NO_3)_3THF_3$ (16.3 mg, 0.03 mmol, 1.5 equiv), $Sm(NO_3)_3THF_3$ (16.5 mg, 0.03 mmol, 1.5 equiv), and $CsNO_3$ (5.8 mg, 0.03 mmol, 1.5 equiv) and dissolved in 1.5 mL of a 0.5 M sodium acetate buffer (pH

5.4), resulting in a very pale green solution (0.8 M total concentration). An aliquot of the resulting solution was used to record an initial UV–Vis spectrum (a and b, blue; **Figure 5.14**), indicating prominent absorbances for Nd^{III}, Sm^{III}, and overlapping Th^{IV} and Cs^{I} (**Figure 5.25**). The aliquot was transferred back to the 5 mL vial and this solution was added slowly dropwise without stirring to the DCE solution (4 mL) containing independently synthesized **4.2b** (20.5 mg, 0.02 mmol) and $[Ph_3PNPPh_3][PF_6]$ (6.8 mg, 0.01 mmol) as an analytical standard (a, **Figure 5.15**). After addition, the mixture was allowed to stir for 1.5 hours, resulting in a colorless organic phase and a very pale green aqueous phase. Stirring was discontinued and the organic and aqueous phases were separated using a small separatory funnel. An aliquot of the aqueous phase was used to record a UV–Vis spectrum (a and b, red; **Figure 5.14**), indicating all metal ion concentrations remained the same, with no apparent extraction into the DCE phase. A 1 mL aliquot was taken from the colorless dichloroethane layer and transferred to an NMR tube. An unlocked $^{31}P\{^{1}H\}$ NMR spectrum was collected indicating the formation of **4.1** and **5.5** as by–products with absence of the known Th^{IV}, Nd^{III}, Sm^{III}, or Cs^{I} products (b, **Figure 5.15**)

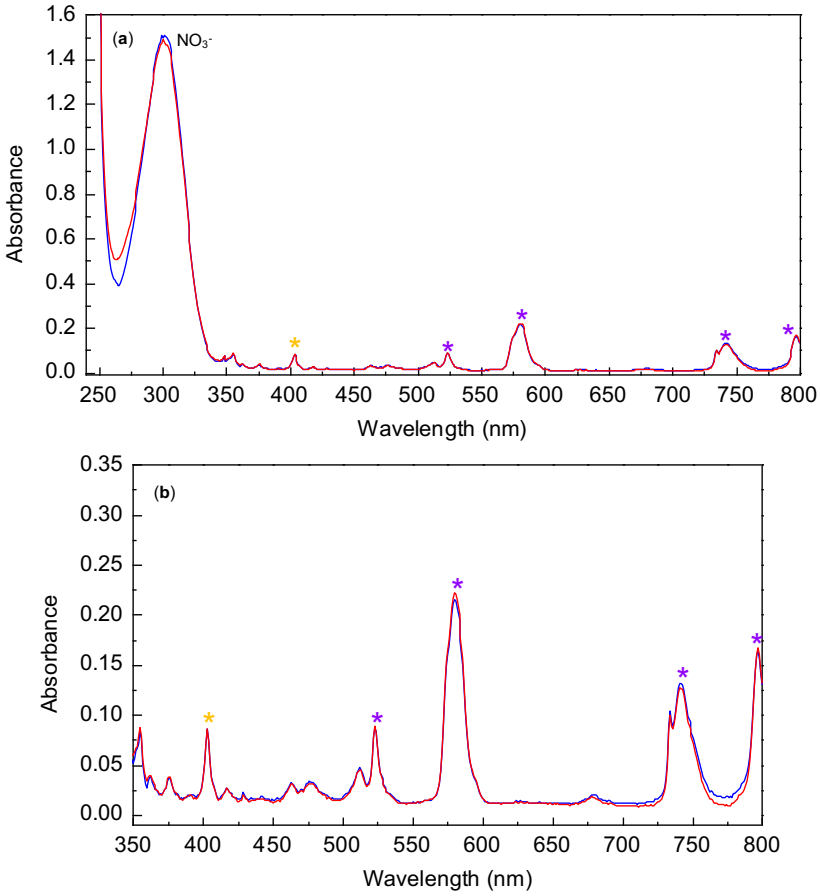

Figure 5.14. UV–Vis Spectra for Selectivity Control Experiments with Th^{IV}, Nd^{III}, Sm^{III}, and Cs^{I}. (**a**) (blue) Initial UV–Vis spectrum of the aqueous layer containing an equimolar mixture of $Th(NO_3)_4$•H_2O, $Nd(NO_3)_3THF_3$ (797, 746, 583, and 525 nm*), $Sm(NO_3)_3THF_3$ (404 nm*), and $CsNO_3$ all dissolved in 1.5 mL of a 0.5 M sodium acetate buffer (pH 5.4; 0.08 M total concentration) (**Figure 5.25**). $Th(NO_3)_4$•H_2O and $CsNO_3$ do not display optical absorbances in the visible region and an absorbance for the NO_3^- anion is observed at 304 nm.[129] (red) UV–Vis spectrum taken after mixing the aqueous layer with the DCE (4 mL) layer of independently synthesized **4.2b** for 1.5 hours indicating Nd^{III}*, Sm^{III}*, and NO_3^- concentrations remained unchanged in solution with no migration to the DCE layer. (**b**) Zoomed–in plot of (**a**), displaying the spectral range used for all further experiments.

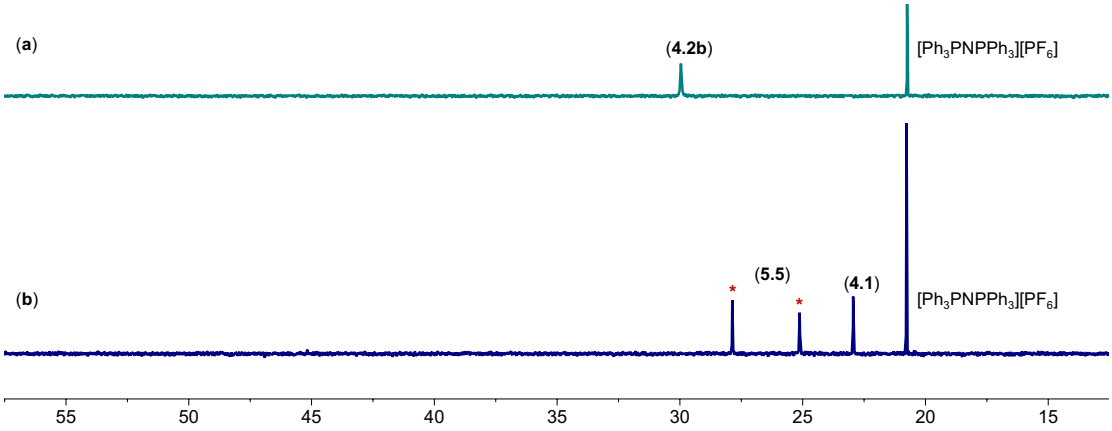

Figure 5.15. $^{31}P\{^{1}H\}$ NMR Spectra for Selectivity Control Experiments with Th^{IV}, Nd^{III}, Sm^{III}, and Cs^{I}. (**a**) $^{31}P\{^{1}H\}$ NMR spectrum in DCE of independently synthesized **4.2b** and $[Ph_3PNPPh_3][PF_6]$ as the analytical standard. (**b**) $^{31}P\{^{1}H\}$ NMR spectrum of DCE layer after mixing the aqueous layer containing $Th(NO_3)_4•H_2O$, $Nd(NO_3)_3THF_3$, $Sm(NO_3)_3THF_3$, and $CsNO_3$ in 1.5 mL of 0.5 M sodium acetate buffer (pH 5.4), indicating the formation of **4.1** and **5.5** (denoted as *) as by–products, with absence of any known Th^{IV}, Nd^{III}, Sm^{III}, or Cs^{I} products.

5.5.3.3 Model Extraction Scheme for UO_2^{2+} Selectivity in Equimolar Aqueous Mixtures of Th^{IV}, Nd^{III}, Sm^{III}, and Cs^{I}

A 5 mL vial was charged with $Th(NO_3)_4•H_2O$ (14.4 mg, 0.03 mmol, 1.5 equiv), $Nd(NO_3)_3THF_3$ (16.3 mg, 0.03 mmol, 1.5 equiv), $Sm(NO_3)_3THF_3$ (16.5 mg, 0.03 mmol, 1.5 equiv), and $CsNO_3$ (5.8 mg, 0.03 mmol, 1.5 equiv) and dissolved in 1.5 mL of a 0.5 M sodium acetate buffer (pH 5.4). This solution was then added to crystalline $UO_2(NO_3)_2(THF)_2$ (16.1 mg, 0.03 mmol, 1.5 equiv), (0.02 M UO_2^{2+}; 0.1 M total ion concentration), resulting in a bright yellow–green solution. An aliquot of the resulting solution was used to record an initial UV–Vis spectrum (a, **Figure 5.16**), indicating UO_2^{2+} and Nd^{III} – with the other absorbances overlapping with

UO_2^{2+} (304 and 400 nm). The aliquot was transferred back to the 5 mL vial and this solution was added slowly dropwise without stirring to the DCE solution (4 mL) containing the independently synthesized **4.2b** (20.5 mg, 0.02 mmol) and $[Ph_3PNPPh_3][PF_6]$ (6.8 mg, 0.01 mmol) as an analytical standard (a, **Figure 5.17**). After addition, the mixture was allowed to stir for 1.5 hours, resulting in a bright yellow organic phase and a pale yellow–green aqueous phase. Stirring was discontinued and the organic and aqueous phases were separated using a small separatory funnel. An aliquot of the aqueous phase was used to record a UV–Vis spectrum (b, **Figure 5.16**), indicating the Nd^{III} concentration remained the same and 0.011 mmol of UO_2^{2+} remained, which is equivalent to the capture of 0.019 mmol (~0.95 equiv) to the organic phase, based on the amount of **4.2b** (0.02 mmol). The UO_2^{2+} concentration was determined by calibration curve (**Figure 5.26**). A 1 mL aliquot was taken from the yellow dichloroethane layer and transferred to an NMR tube. An unlocked $^{31}P\{^1H\}$ NMR spectrum was collected indicating the formation of **4.4N/4.5N** (b, **Figure 5.17**), with formation of **5.5** and **4.1** as by–products with the absence of known Th^{IV}, Nd^{III}, Sm^{III}, or Cs^{I} products.

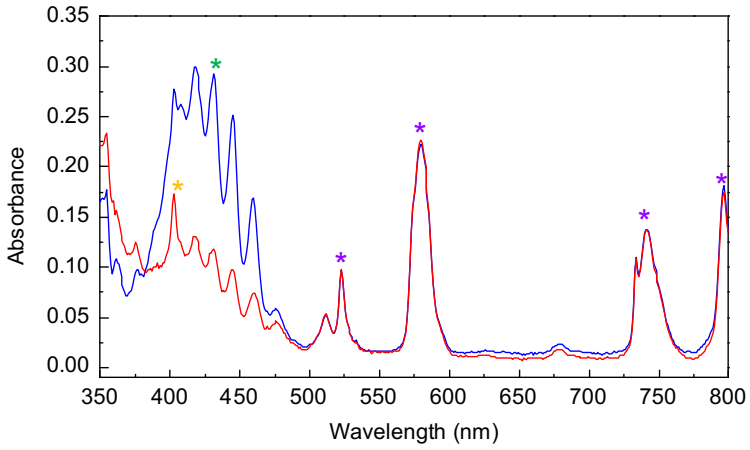

Figure 5.16. (**a**) (blue) Initial UV–Vis spectrum of the aqueous layer containing an equimolar mixture of $UO_2(NO_3)_2(THF)_2$ (*), $Th(NO_3)_4•H_2O$, $Nd(NO_3)_3THF_3$ (*), $Sm(NO_3)_3THF_3$ (*), and

$CsNO_3$ all dissolved in 1.5 mL of a 0.5 M sodium acetate buffer (pH 5.4). (red) UV–Vis spectrum taken after mixing the aqueous layer with the DCE (4 mL) layer of independently synthesized **4.2b** for 1.5 hours indicating the Nd^{III} remained in solution with a residual UO_2^{2+} concentration of 0.0072 M consistent with a total quantity of 0.019 mmol separated from the aqueous layer (~0.95 equiv).

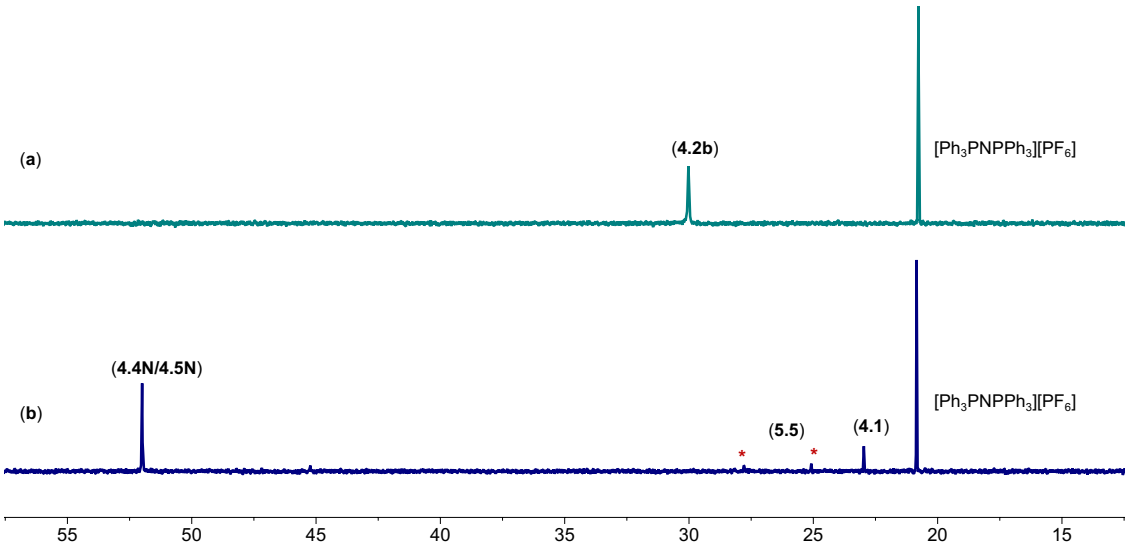

Figure 5.17. (**a**) $^{31}P\{^1H\}$ NMR spectrum in DCE of independently synthesized **4.2b** and $[Ph_3PNPPh_3][PF_6]$ as the analytical standard. (**b**) $^{31}P\{^1H\}$ NMR spectrum of DCE layer following UO_2^{2+} separation from the aqueous layer containing $UO_2(NO_3)_2(THF)_2$, $Th(NO_3)_4•H_2O$, $Nd(NO_3)_3THF_3$, $Sm(NO_3)_3THF_3$, and $CsNO_3$ in 0.5 M sodium acetate buffer (pH = 5.4), indicating the formation of **4.4N/4.5N**, with formation of **5.5** (denoted as *) and **4.1** as by–products

5.5.3.4 Methods for the Electrochemical Biphasic Separation and Recovery of UO_2^{2+}

5.5.3.4.1 Experimental Conditions

A complete, stepwise, half–cell figure of the experiments conducted in this section, along with spectroscopic data is shown in **Figure 5.24**. Two–electrode galvanostatic bulk electrolysis was

performed in an argon glovebox utilizing a two compartment H–cell with a glass frit separator, a stir bar in each compartment, and reticulated vitreous carbon (RVC) foam electrodes for both the working and counter electrodes (a, b, and c; **Figure 5.18**). The RVC foam electrodes consisted of a ~5 cm steel rod inserted into 100 PPI Duocel® RVC foam core (length ~2.5 cm; diameter ~3 mm), with a tap bore (length ~5 mm; diameter ~2 mm), which was filled with molten gallium to fuse the steel connector to the RVC foam. Each electrode has an end–to–tip resistance of < 5 Ω. The RVC electrodes were rinsed with methanol and dried under reduced pressure overnight prior to use. The Ketjenblack used was dried for 48 h in a 175 °C oven and ground in a glass mortar and pestle under inert atmosphere prior to use.[56]

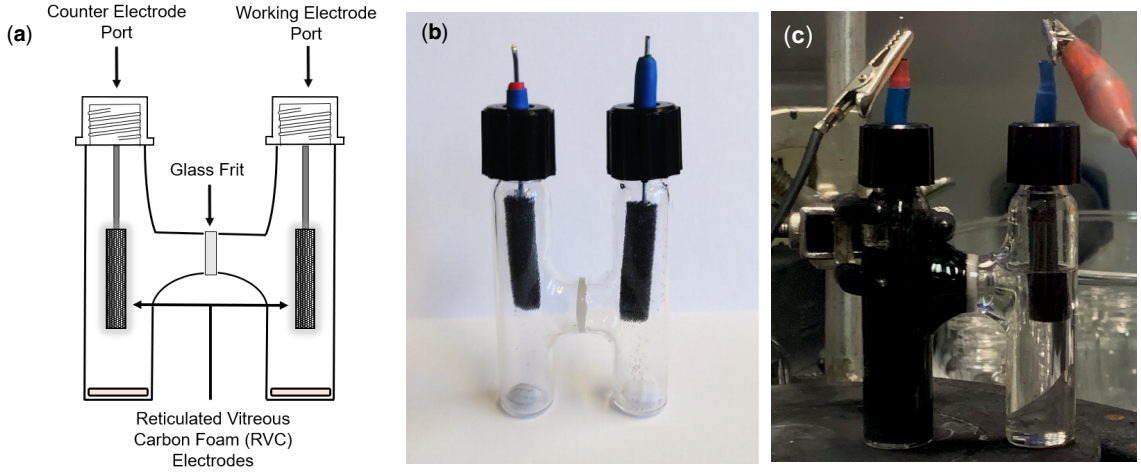

Figure 5.18. (a) Schematic of the two–compartment H–cell used for the biphasic electrochemical separation and recovery of UO_2^{2+}. (**b**) Picture of the two–compartment H–cell used for the biphasic electrochemical separation and recovery of UO_2^{2+}. (**c**) Experimental setup of H–cell (before charging) used for the biphasic separation and recovery.

5.5.3.4.1 Experimental Methods

Reduction (charging): The counter compartment consisted of 400 mg of Ketjenblack suspended in 8 mL of a 0.1 M solution of $[Bu_4N][PF_6]$ in DCE. The working compartment

consisted of **4.1** (34.0 mg, 0.0625 mmol, 1.0 equiv) and $[Ph_3PNPPh_3][PF_6]$ (21.2 mg, 0.031 mmol, 0.5 equiv) dissolved in 6 mL of a 0.1 M solution of $[Bu_4N][PF_6]$ in DCE. An initial $^{31}P\{^1H\}$ NMR spectrum was obtained of the DCE layer (a, **Figure 5.20**). A charging current of –107.1 μA with a –9.25 C charge cutoff was utilized, resulting in a ~75% SOC after 24 h assuming 100% columbic efficiency (**Figure 5.19**). Upon completion, the working compartment solution was analysed by $^{31}P\{^1H\}$ NMR spectroscopy to reveal the formation of **4.2b** with remaining **4.1** (b, **Figure 5.20**). Based on $[Ph_3PNPPh_3][PF_6]$, the amount of **4.2b** was determined to be 0.047 mmol (75% yield), corresponding to the SOC of ~75%. The working compartment solution was then removed from the H–cell and placed in a 15 mL vial for subsequent selective UO_2^{2+} sequestration chemistry.

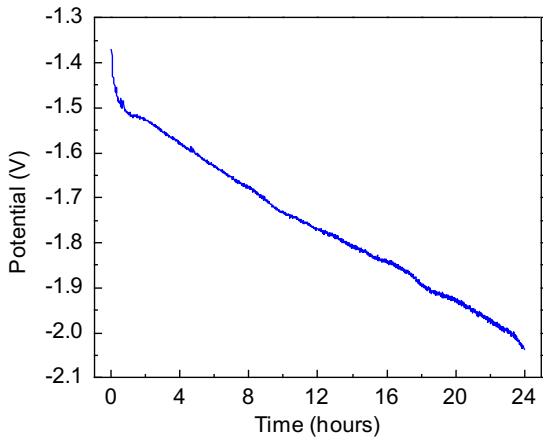

Figure 5.19. Charging curve for the biphasic electrochemical selective seperation of UO_2^{2+}. A charging current of –107.1 μA with –9.25 C of charge transferred, resulting in a 75% SOC after 24 h assuming 100% columbic efficiency.

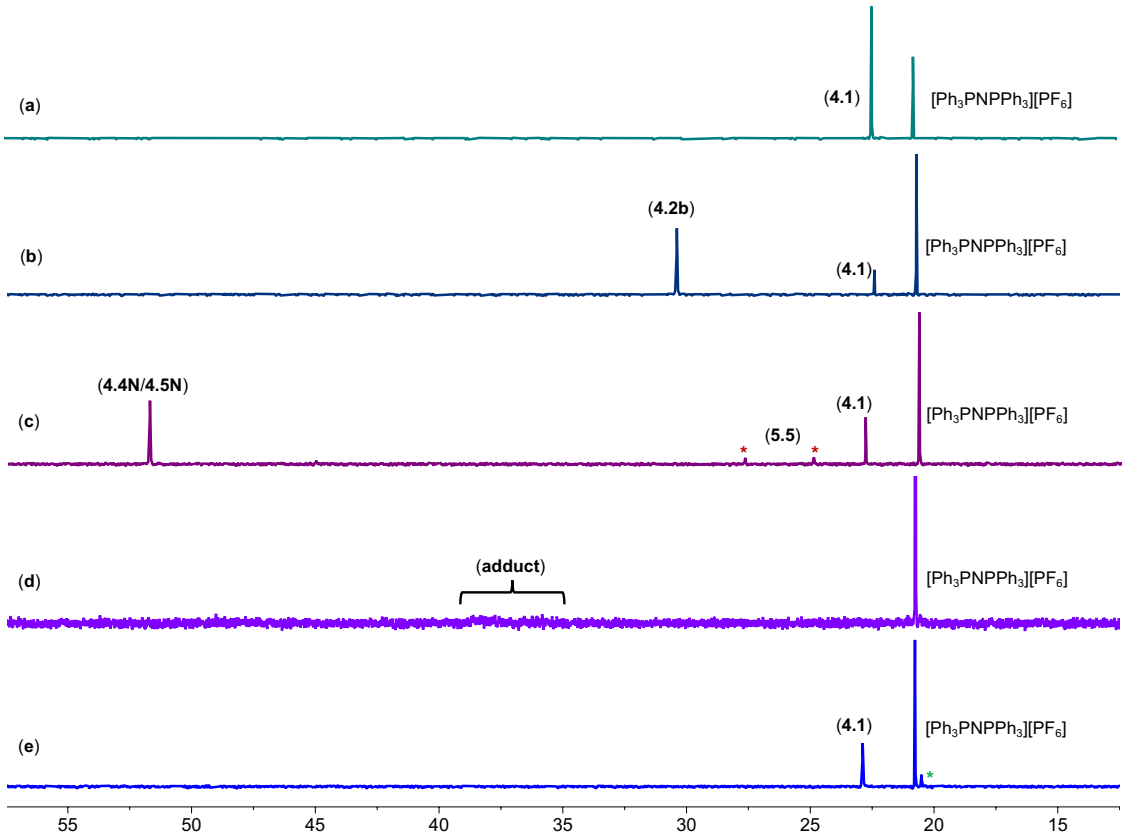

Figure 5.20. $^{31}P\{^{1}H\}$ NMR Spectra for the Electrochemical Biphasic Separation and Recovery of UO_2^{2+}. (**a**) Initial unlocked $^{31}P\{^{1}H\}$ NMR spectrum of **4.1** and $[Ph_3PNPPh_3][PF_6]$ in DCE. (**b**) $^{31}P\{^{1}H\}$ NMR spectrum in DCE of electrochemically reduced **4.1** to produce **4.2b**. (**c**) $^{31}P\{^{1}H\}$ NMR spectrum of DCE layer following UO_2^{2+} separation from the aqueous layer containing $UO_2(NO_3)_2(THF)_2$, $Th(NO_3)_4{\bullet}H_2O$, $Nd(NO_3)_3THF_3$, $Sm(NO_3)_3THF_3$, and $CsNO_3$ in 0.5 M sodium acetate buffer (pH = 5.4), indicating formation of **4.4N/4.5N, 4.1,** and **5.5**. (**d**) $^{331}P\{^{1}H\}$ NMR spectrum of the electrochemically oxidized DCE layer containing **4.4N/4.5N**, following galvanostatic discharge. A very broad signal is observed between 35–40 ppm which we attribute to an adduct of UO_2^{2+} with **4.1**. (**e**) $^{31}P\{^{1}H\}$ NMR spectrum of DCE layer after mixing with fresh NaOAc buffer (0.1 M, pH 5.4) after 15 hours and showing the free carborane **4.1** (major), as well as unknown by–products at 20 ppm, marked by *.

Selective UO_2^{2+} separation: A 10 mL vial was charged with $Th(NO_3)_4•H_2O$ (37.4 mg, 0.078 mmol, 1.25 equiv), $Nd(NO_3)_3THF_3$ (42.3 mg, 0.078 mmol, 1.25 equiv), $Sm(NO_3)_3THF_3$ (42.9 mg, 0.078 mmol, 1.25 equiv), and $CsNO_3$ (15.2 mg, 0.078 mmol, 1.25 equiv) and dissolved in 3.9 mL of a 0.5 M sodium acetate buffer (pH 5.4). This solution was then added to crystalline $UO_2(NO_3)_2(THF)_2$ (42.0 mg, 0.078 mmol, 1.25 equiv), (0.02 M UO_2^{2+}; 0.1 M total ion concentration), resulting in a bright yellow–green solution. An aliquot of the resulting solution was used to record an initial UV–Vis spectrum (blue, **Figure 5.21**), indicating UO_2^{2+} and Nd^{III}, where the absorbances for the other ions are buried under the large UO_2^{2+} signal. The aliquot was transferred back to the 10 mL vial and this solution was added slowly dropwise without stirring to the DCE solution containing the electrochemically reduced **4.1**. After addition, the mixture was allowed to stir for 1.5 hours, resulting in a bright yellow organic phase and a pale yellow–green aqueous phase. Stirring was discontinued and the organic and aqueous phases were separated using a small separatory funnel. An aliquot of the aqueous phase was used to record a UV–Vis spectrum (red, **Figure 5.21**), indicating the Nd^{III} concentration remained the same and 0.034 mmol of UO_2^{2+} remained, which is equivalent to the capture of 0.043 mmol (~0.9 equiv) to the organic phase, based on the amount of **4.2b** that was generated (0.047 mmol). The UO_2^{2+} concentration was determined by calibration curve (**Figure 5.26**). A 1 mL aliquot was taken from the pale yellow dichloroethane layer and transferred to an NMR tube. An unlocked $^{31}P\{^1H\}$ NMR spectrum was collected indicating the formation of **4.4N/4.5N** (c, **Figure 5.20**), with formation of **5.5** and **4.1** as by–products and absence of known Th^{IV}, Nd^{III}, Sm^{III}, or Cs^{I} products. The NMR solution was returned to the 15 mL vial.

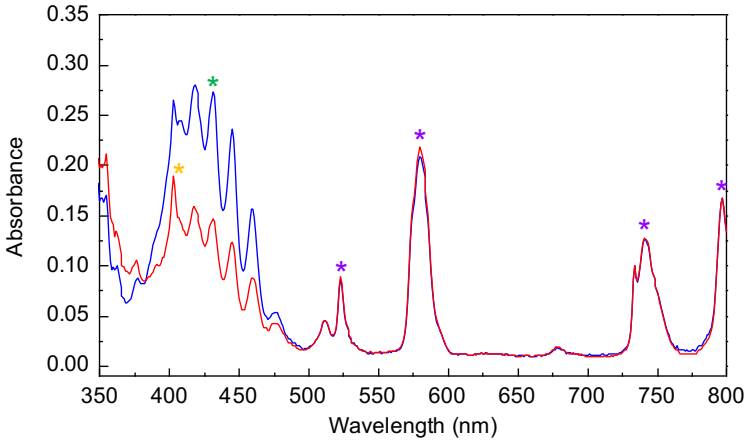

Figure 5.21. UV–Vis for Selective Electrochemical Separation of UO_2^{2+} from an Aqueous Mixture of Th^{IV}, Nd^{III}, Sm^{III}, and Cs^{I}. (blue) Initial UV–Vis spectrum of the aqueous layer containing an equimolar mixture of $UO_2(NO_3)_2(THF)_2$ (*), $Th(NO_3)_4•H_2O$, $Nd(NO_3)_3THF_3$ (*), $Sm(NO_3)_3THF_3$ (*), and $CsNO_3$ and dissolved in 3.9 mL of a 0.5 M sodium acetate buffer (pH 5.4). (red) UV–Vis spectrum taken after mixing the aqueous layer with the DCE layer of electrochemically reduced **4.1** (to generate **4.2b**) in a 0.1 M $[Bu_4N][PF_6]$ DCE solution for 1.5 hours indicating the Nd^{III} remained in solution with a residual UO_2^{2+} concentration of 0.0088 M consistent with a total quantity of selectively separated UO_2^{2+} to the DCE layer of 0.043 mmol (~0.9 equiv).

Oxidation (discharging): Two–electrode galvanostatic bulk electrolysis (discharging) of the captured DCE solution was performed using the same cell utilized for charging. A discharging current of 107.1 μA was applied until 9.49 C of charge was transferred or the voltage cut–off was achieved (2.0 V) resulting in a final SOC of ~0 % (**Figure 5.22**; assuming 100% columbic efficiency and no loss of material during the biphasic capture). Upon completion, a 1 mL aliquot was taken from the pale yellow dichloroethane layer and transferred to an NMR tube. An unlocked $^{31}P\{^{1}H\}$ NMR spectrum was collected indicating a very broad signal between

35–40 ppm which we attribute to an adduct of UO_2^{2+} with **4.1** (d, **Figure 5.20**). The NMR sample was transferred back into the working compartment solution and placed in a 15 mL vial for subsequent release chemistry.

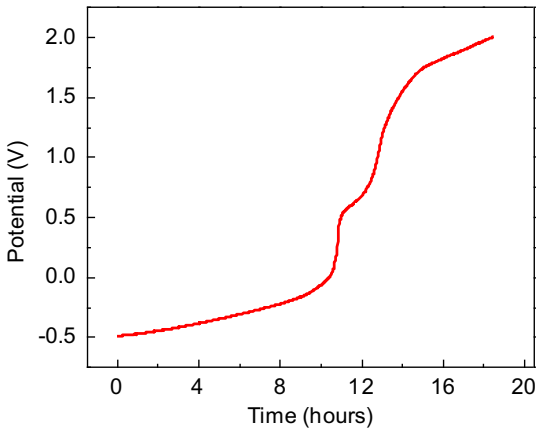

Figure 5.22. Discharging curve for the biphasic electrochemical release of UO_2^{2+}. A discharging current of 107.1 μA until 9.45 C of charge transferred or until 2.0 V cut–off was reached, resulting in a ~0% SOC after ~20 h assuming 100% columbic efficiency.

UO_2^{2+} recovery: The 20 mL vial containing the electrochemically oxidized **4.4N/4.5N** yellow DCE solution was equipped with a stirbar and a solution of 0.1 M sodium acetate buffer adjusted to pH 5.4 (3 mL) was added dropwise to it. The mixture was allowed to stir for 15 hours, resulting in a bright–yellow aqueous phase and a colourless organic layer. The organic and aqueous phases were separated using a small separatory funnel, and an aliquot of the aqueous layer was used to take a UV–Vis spectrum indicating the presence of released UO_2^{2+} (0.033 mmol, ~0.76 equiv) (**Figure 5.23**). A 1 mL aliquot was taken from the colorless DCE layer and transferred to an NMR tube. An unlocked $^{31}P\{^1H\}$ NMR spectrum was collected indicating the clean formation of **4.1**, $[Ph_3PNPPh_3][PF_6]$, and a small unknown by–product at 20.1 ppm (denoted as *) (e, **Figure 5.20**).

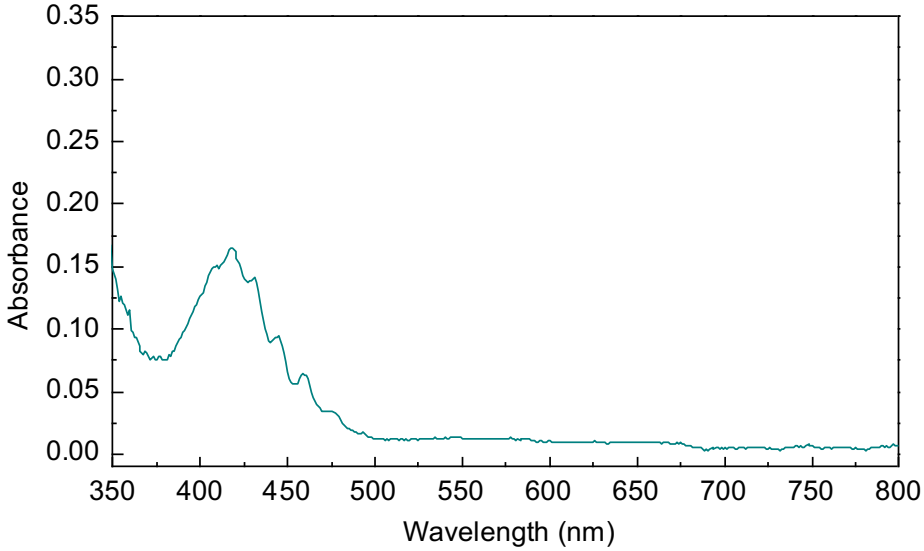

Figure 5.23. UV–Vis Spectrum for Biphasic Electrochemical Recovery of UO_2^{2+}. 0.1 M aqueous sodium acetate buffer layer at pH 5.4 after mixing for 12 hours with electrochemically oxidized **4.4N/4.5N** in DCE. The concentration of UO_2^{2+} was calculated to be 0.011 M consistent with a total quantity of UO_2^{2+} recovered from the DCE layer to the aqueous phase of 0.03 mmol (~0.76 equiv).

5.5.3.5 Half–Cell Depiction of Electrochemical UO_2^{2+} Sequestration in Aqueous Mixtures

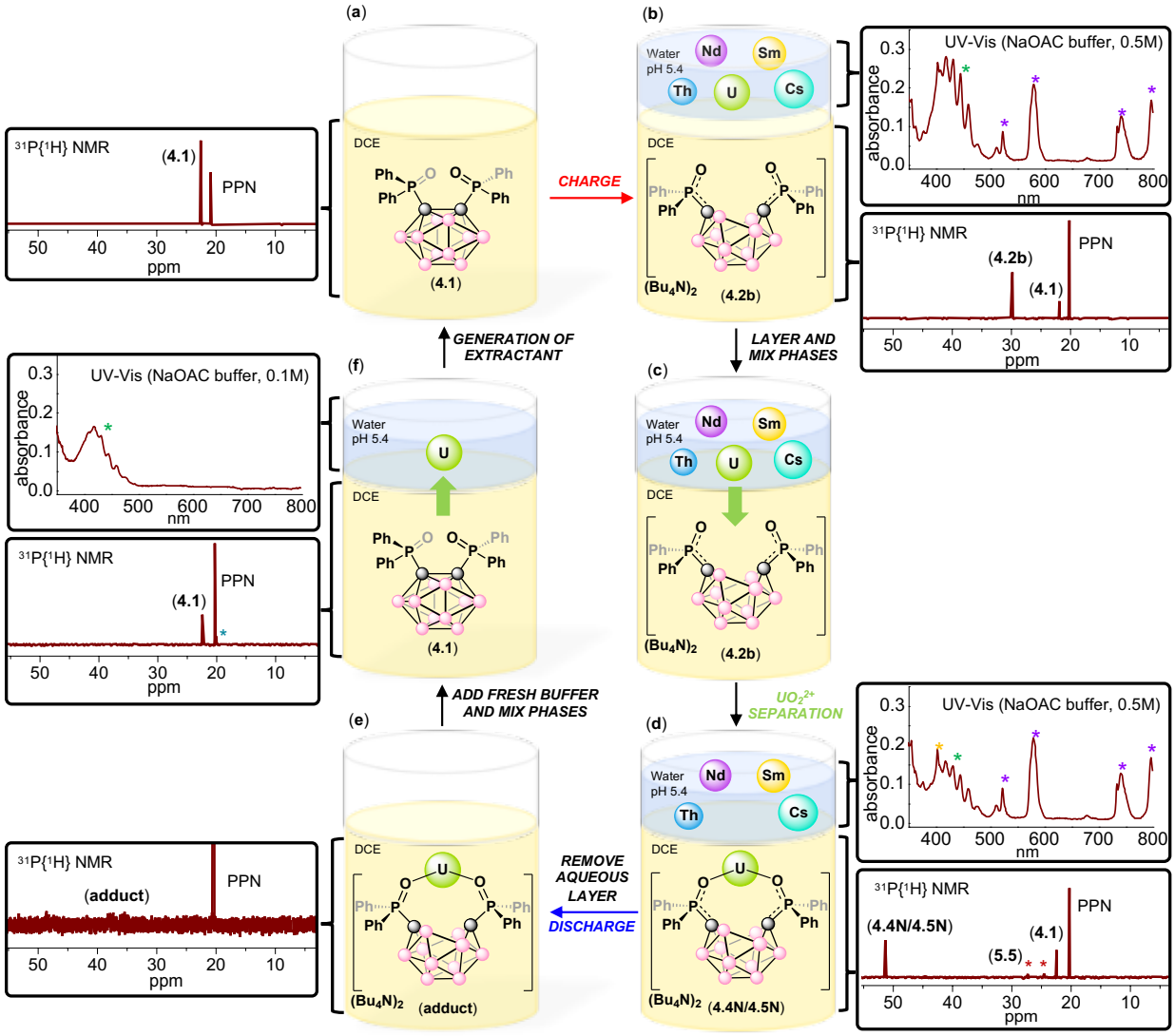

Figure 5.24. Stepwise procedure for the biphasic electrochemical sequestration of UO_2^{2+} in an aqueous mixture of Th^{IV}, Nd^{III}, Sm^{III}, and Cs^{I}. For simplicity, only half of the H–cell is displayed here. For the full cell design, see **Figure 5.18**. (**a**) $^{31}P\{^{1}H\}$ NMR spectrum of DCE layer containing **4.1**, $[Ph_3PNPPh_3][PF_6]$, and $[Bu_4N][PF_6]$ ($[PF_6]^-$ resonance not shown) before charging. (**b**) Top inset, UV–Vis spectrum of aqueous phase (NaOAc buffer 0.5 M, pH 5.4) containing 1.25 equiv. $UO_2(NO_3)_2(THF)_2$ (*), $Th(NO_3)_4{\bullet}H_2O$, $Nd(NO_3)_3THF_3$ (*), $Sm(NO_3)_3THF_3$ (*), and $CsNO_3$ before mixing with the DCE phase. Bottom inset, $^{31}P\{^{1}H\}$

NMR spectrum of DCE layer containing **4.2b** (major) and **4.1** (minor) after charging **4.1** galvanostatically. (**c**) Mixing of the phases in **b** for 1.5 hours. (**d**) Top inset, UV–Vis spectrum of aqueous phase after mixing with the DCE phase, revealing approximately ~0.63 equiv. of UO_2^{2+} were selectively extracted. Bottom inset, $^{31}P\{^1H\}$ NMR spectrum of the DCE layer after mixing with aqueous phase, showing captured products **4.4N**/**4.5N** (major), with **5.5** (denoted *) and **4.1** as minor products. (**e**) $^{31}P\{^1H\}$ NMR spectrum of the DCE layer following phase separation and galvanostatic discharge. A broad peak is observed at 38 ppm, which we attribute to an adduct of UO_2^{2+} with **4.1**. (**f**) Top inset, UV–Vis spectrum of aqueous phase after addition of fresh buffer (0.1 M, pH 5.4) to the discharged DCE solution (in **e**) and mixing for 15 hours. The spectrum reveals the release of approximately ~0.76 equiv. of UO_2^{2+}. Bottom inset, $^{31}P\{^1H\}$ NMR spectrum of the DCE layer after mixing with fresh buffer, showing the free carborane **4.1** (major), as well as unknown byproducts at 20 ppm marked by *.

5.5.3.6 Supplementary Figures for UV–Vis Spectroscopy

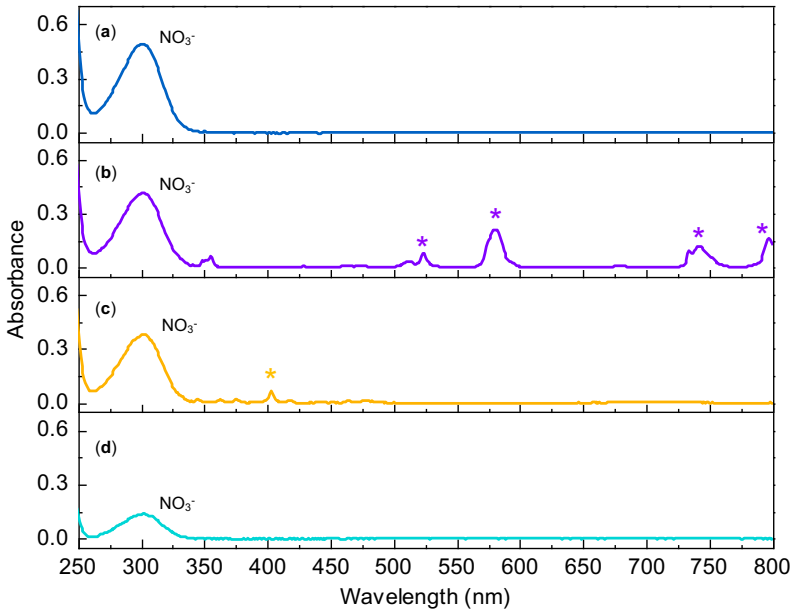

Figure 5.25. UV–Vis Spectra of Individual Solutions of Th^{IV}, Nd^{III}, Sm^{III}, and Cs^{I} in NaOAc buffer. All solutions were prepared at concentrations of 0.02 M in 1.5 mL of NaOAc buffer (0.5 M, pH 5.4) with (**a**) $Th(NO_3)_4•H_2O$, (**b**) $Nd(NO_3)_3THF_3$, (**c**) $Sm(NO_3)_3THF_3$, and (**d**) $CsNO_3$. (**a**) and (**d**) do not display any optical absorptions in the visible region. All spectra display an absorbance at 304 nm consistent with NO_3^- anion.[129]

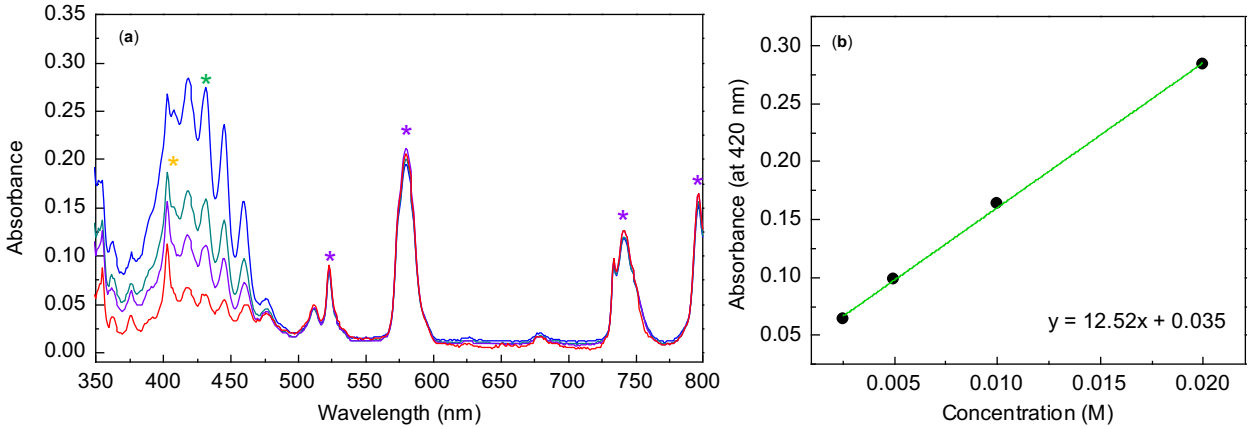

Figure 5.26. Calibration Curve for Varying Concentrations of UO_2^{2+} in an Equimolar Mixtures of Th^{IV}, Nd^{III}, Sm^{III}, and Cs^{I}. The concentrations of Th^{IV}, Nd^{III}, Sm^{III}, and Cs^{I} were kept constant (0.2 M for each ion and 0.08 M total). Varying concentrations of UO_2^{2+} were used (0.0025–0.02 M) and all calibration solutions were prepared in NaOAc buffer (0.5 M at pH 5.4).

5.5 References

1. Rose, D. J., Nuclear Eclectic Power. *Science* **1974,** *184* (4134), 351.

2. Cany, C.; Mansilla, C.; Mathonnière, G.; da Costa, P., Nuclear power supply: Going against the misconceptions. Evidence of nuclear flexibility from the French experience. *Energy* **2018,** *151*, 289-296.

3. Herbst, R. S.; Baron, P.; Nilsson, M., 6 - Standard and advanced separation: PUREX processes for nuclear fuel reprocessing. In *Advanced Separation Techniques for Nuclear Fuel Reprocessing and Radioactive Waste Treatment*, Nash, K. L.; Lumetta, G. J., Eds. Woodhead Publishing: 2011; pp 141-175.

4. Na, C.; Yamagishi, I.; Choi, Y.-J.; Glatz, J.-P.; Hyland, B.; Uhlir, J.; Baron, P.; Warin, D.; De Angelis, G.; Luce, A. *Spent Nuclear Fuel Reprocessing Flowsheet. A Report by the WPFC Expert Group on Chemical Partitioning of the NEA Nuclear Science Committee*; Organisation for Economic Co-Operation and Development: 2012.

5. Poinssot, C.; Bourg, S.; Ouvrier, N.; Combernoux, N.; Rostaing, C.; Vargas-Gonzalez, M.; Bruno, J., Assessment of the environmental footprint of nuclear energy systems. Comparison between closed and open fuel cycles. *Energy* **2014,** *69*, 199-211.

6. Rodríguez-Penalonga, L.; Moratilla Soria, B. Y., A Review of the Nuclear Fuel Cycle Strategies and the Spent Nuclear Fuel Management Technologies. *Energies* **2017,** *10* (8).

7. Borges Silverio, L.; Lamas, W. d. Q., An analysis of development and research on spent nuclear fuel reprocessing. *Energy Policy* **2011,** *39* (1), 281-289.

8. Cashmore, R.; Koppelman, B., 23 - Proliferation resistance, used fuel and multinational approaches to the provision of fuel cycle services. In *Reprocessing and Recycling of Spent Nuclear Fuel*, Taylor, R., Ed. Woodhead Publishing: Oxford, 2015; pp 579-601.

9. Gill, M.; Livens, F.; Peakman, A., Chapter 9 - Nuclear Fission. In *Future Energy (Second Edition)*, Letcher, T. M., Ed. Elsevier: Boston, 2014; pp 181-198.

10. Steiner, G.; Geissler, B.; Haneklaus, N., Making Uranium Recovery from Phosphates Great Again? *Environmental Science & Technology* **2020,** *54* (3), 1287-1289.

11. Srivastava, R. R.; Pathak, P.; Perween, M., Environmental and Health Impact Due to Uranium Mining. In *Uranium in Plants and the Environment*, Gupta, D. K.; Walther, C., Eds. Springer International Publishing: Cham, 2020; pp 69-89.

12. Cooperation, I. F. f. N. E. IFNEC. https://www.ifnec.org/ifnec/.

13. News, W. N., Fatal Blow to GNEP? *Fedearl Register* **2009,** *74* (123), 31017-31018.

14. Association, W. N., Outline history of nuclear energy. *World Nuclear Association* **2010**.

15. Association, N. E., Actinide and Fission Product Partitioning and Transmutation. In *Seventh Information Exchange Meeting*, European Commision and the International Atomic Energy Agency: Jeju, Republic of Korea, 2002.

16. Mathur, J. N.; Murali, M. S.; Nash, K. L., ACTINIDE PARTITIONING—A REVIEW. *Solvent Extraction and Ion Exchange* **2001,** *19* (3), 357-390.

17. Choi, S.; Nam, H. O.; Ko, W. I., Environmental life cycle risk modeling of nuclear waste recycling systems. *Energy* **2016,** *112*, 836-851.

18. Browder, R., *Plant modifications for mixed oxide fuel use in US reactors*. American Society of Mechanical Engineers - ASME: United States, 2004.

19. Sholl, D. S.; Lively, R. P., Seven chemical separations to change the world. *Nature* **2016,** *532* (7600), 435-7.

20. Parker, B. F.; Zhang, Z.; Rao, L.; Arnold, J., An overview and recent progress in the chemistry of uranium extraction from seawater. *Dalton Transactions* **2018,** *47* (3), 639-644.

21. Gill, G. A.; Kuo, L.-J.; Janke, C. J.; Park, J.; Jeters, R. T.; Bonheyo, G. T.; Pan, H.-B.; Wai, C.; Khangaonkar, T.; Bianucci, L.; Wood, J. R.; Warner, M. G.; Peterson, S.; Abrecht, D. G.; Mayes, R. T.; Tsouris, C.; Oyola, Y.; Strivens, J. E.; Schlafer, N. J.; Addleman, R. S.; Chouyyok, W.; Das, S.; Kim, J.; Buesseler, K.; Breier, C.; D'Alessandro, E., The Uranium from Seawater Program at the Pacific Northwest National Laboratory: Overview of Marine Testing, Adsorbent Characterization, Adsorbent

Durability, Adsorbent Toxicity, and Deployment Studies. *Industrial & Engineering Chemistry Research* **2016,** *55* (15), 4264-4277.

22. Wang, D.; Sañudo Wilhelmy, S. A., Vanadium speciation and cycling in coastal waters. *Marine Chemistry* **2009,** *117* (1), 52-58.

23. Kim, J.; Tsouris, C.; Mayes, R. T.; Oyola, Y.; Saito, T.; Janke, C. J.; Dai, S.; Schneider, E.; Sachde, D., Recovery of Uranium from Seawater: A Review of Current Status and Future Research Needs. *Separation Science and Technology* **2013,** *48* (3), 367-387.

24. Leggett, C. J.; Parker, B. F.; Teat, S. J.; Zhang, Z.; Dau, P. D.; Lukens, W. W.; Peterson, S. M.; Cardenas, A. J. P.; Warner, M. G.; Gibson, J. K.; Arnold, J.; Rao, L., Structural and spectroscopic studies of a rare non-oxido V(v) complex crystallized from aqueous solution. *Chemical Science* **2016,** *7* (4), 2775-2786.

25. Sun, X.; Xu, C.; Tian, G.; Rao, L., Complexation of glutarimidedioxime with Fe(iii), Cu(ii), Pb(ii), and Ni(ii), the competing ions for the sequestration of U(vi) from seawater. *Dalton Transactions* **2013,** *42* (40), 14621-14627.

26. Ivanov, A. S.; Leggett, C. J.; Parker, B. F.; Zhang, Z.; Arnold, J.; Dai, S.; Abney, C. W.; Bryantsev, V. S.; Rao, L., Origin of the unusually strong and selective binding of vanadium by polyamidoximes in seawater. *Nature Communications* **2017,** *8* (1), 1560.

27. Kuo, L.-J.; Gill, G. A.; Tsouris, C.; Rao, L.; Pan, H.-B.; Wai, C. M.; Janke, C. J.; Strivens, J. E.; Wood, J. R.; Schlafer, N.; D'Alessandro, E. K., Temperature Dependence of Uranium and Vanadium Adsorption on Amidoxime-Based Adsorbents in Natural Seawater. *ChemistrySelect* **2018,** *3* (2), 843-848.

28. Li, B.; Zhou, J.; Priest, C.; Jiang, D.-e., Effect of Salt on the Uranyl Binding with Carbonate and Calcium Ions in Aqueous Solutions. *The Journal of Physical Chemistry B* **2017,** *121* (34), 8171-8178.

29. Wu, W.; Priest, C.; Zhou, J.; Peng, C.; Liu, H.; Jiang, D.-e., Solvation of the Ca2UO2(CO3)3 Complex in Seawater from Classical Molecular Dynamics. *The Journal of Physical Chemistry B* **2016,** *120* (29), 7227-7233.

30. Xu, C.; Tian, G.; Teat, S. J.; Rao, L., Complexation of U(VI) with Dipicolinic Acid: Thermodynamics and Coordination Modes. *Inorganic Chemistry* **2013,** *52* (5), 2750-2756.

31. Drouza, C.; Gramlich, V.; Sigalas, M. P.; Pashalidis, I.; Keramidas, A. D., Synthesis, Structure, and Solution Dynamics of UO22+−Hydroxy Ketone Compounds [UO2(ma)2(H2O)] and [UO2(dpp)(Hdpp)2(H2O)]ClO4 [ma = 3-Hydroxy-2-methyl-4-pyrone, Hdpp = 3-Hydroxy-1,2-dimethyl-4(1H)-pyridone]. *Inorganic Chemistry* **2004,** *43* (26), 8336-8345.

32. Harrowfield, J. M.; Lugan, N.; Shahverdizadeh, G. H.; Soudi, A. A.; Thuéry, P., Solid-State Luminescence and π-Stacking in Crystalline Uranyl Dipicolinates. *European Journal of Inorganic Chemistry* **2006,** *2006* (2), 389-396.

33. Gorden, A. E. V.; Xu, J.; Raymond, K. N.; Durbin, P., Rational Design of Sequestering Agents for Plutonium and Other Actinides. *Chemical Reviews* **2003,** *103* (11), 4207-4282.

34. Gorden, A. E. V.; DeVore, M. A.; Maynard, B. A., Coordination Chemistry with f-Element Complexes for an Improved Understanding of Factors That Contribute to Extraction Selectivity. *Inorganic Chemistry* **2013,** *52* (7), 3445-3458.

35. Hadjithoma, S.; Papanikolaou, M. G.; Leontidis, E.; Kabanos, T. A.; Keramidas, A. D., Bis(hydroxylamino)triazines: High Selectivity and Hydrolytic Stability of Hydroxylamine-Based Ligands for Uranyl Compared to Vanadium(V) and Iron(III). *Inorganic Chemistry* **2018,** *57* (13), 7631-7643.

36. Vukovic, S.; Watson, L. A.; Kang, S. O.; Custelcean, R.; Hay, B. P., How Amidoximate Binds the Uranyl Cation. *Inorganic Chemistry* **2012,** *51* (6), 3855-3859.

37. Carbol, P.; Wegen, D. H.; Wiss, T.; Fors, P., 5.16 - Spent Fuel as Waste Material. In *Comprehensive Nuclear Materials*, Konings, R. J. M., Ed. Elsevier: Oxford, 2012; pp 389-420.

38. Choppin, G. R., Comparison of the solution chemistry of the actinides and lanthanides. *Journal of the Less Common Metals* **1983,** *93* (2), 323-330.

39. Choppin, G. R., Comparative solution chemistry of the 4f and 5f elements. *Journal of Alloys and Compounds* **1995,** *223* (2), 174-179.

40. Lahrouch, F.; Sofronov, O.; Creff, G.; Rossberg, A.; Hennig, C.; Den Auwer, C.; Di Giorgio, C., Polyethyleneimine methylphosphonate: towards the design of a new class of macromolecular actinide chelating agents in the case of human exposition. *Dalton Transactions* **2017,** *46* (40), 13869-13877.

41. Shen, Y.; Wu, J.; Liu, Z.; Wu, W., Environmentally Friendlier Approach to Nuclear Industry: Recovery of Uranium from Carbonate Solutions Using Ionic Liquids. *Industrial & Engineering Chemistry Research* **2015,** *54* (34), 8624-8628.

42. Takahashi, A.; Ueki, Y.; Igarashi, S., Homogeneous liquid–liquid extraction of uranium(VI) from acetate aqueous solution. *Analytica Chimica Acta* **1999,** *387* (1), 71-75.

43. Krea, M.; Khalaf, H., Liquid–liquid extraction of uranium and lanthanides from phosphoric acid using a synergistic DOPPA–TOPO mixture. *Hydrometallurgy* **2000,** *58* (3), 215-225.

44. Rout, A.; Venkatesan, K. A.; Srinivasan, T. G.; Vasudeva Rao, P. R., Liquid–liquid extraction of Pu(IV), U(VI) and Am(III) using malonamide in room temperature ionic liquid as diluent. *Journal of Hazardous Materials* **2012,** *221-222*, 62-67.

45. Agarwal, R.; Sharma, M. K., Selective Electrochemical Separation and Recovery of Uranium from Mixture of Uranium(VI) and Lanthanide(III) Ions in Aqueous Medium. *Inorganic Chemistry* **2018,** *57* (17), 10984-10992.

46. Sather, A. C.; Berryman, O. B.; Rebek, J., Selective Recognition and Extraction of the Uranyl Ion. *Journal of the American Chemical Society* **2010,** *132* (39), 13572-13574.

47. Reeder, R. J.; Nugent, M.; Tait, C. D.; Morris, D. E.; Heald, S. M.; Beck, K. M.; Hess, W. P.; Lanzirotti, A., Coprecipitation of Uranium(VI) with Calcite: XAFS, micro-XAS, and luminescence characterization. *Geochimica et Cosmochimica Acta* **2001,** *65* (20), 3491-3503.

48. Wang, J.; Zhuang, S., Extraction and adsorption of U(VI) from aqueous solution using affinity ligand-based technologies: an overview. *Reviews in Environmental Science and Bio/Technology* **2019,** *18* (3), 437-452.

49. Hu, P.; Qian, L.; He, Y.; Wang, H.; Wu, W., Solvent extraction of uranium(VI) and thorium(IV) by N,N′-di-p-tolylpyridine-2,6-dicarboxamide from nitric acid solution. *Journal of Radioanalytical and Nuclear Chemistry* **2013,** *297* (1), 133-137.

50. Rao, T. P.; Metilda, P.; Gladis, J. M., Preconcentration techniques for uranium(VI) and thorium(IV) prior to analytical determination—an overview. *Talanta* **2006,** *68* (4), 1047-1064.

51. Hawkins, C. A.; Bustillos, C. G.; Copping, R.; Scott, B. L.; May, I.; Nilsson, M., Challenging conventional f-element separation chemistry – reversing uranyl(vi)/lanthanide(iii) solvent extraction selectivity. *Chemical Communications* **2014,** *50* (63), 8670-8673.

52. Kannappan, R.; Tanase, S.; Tooke, D. M.; Spek, A. L.; Mutikainen, I.; Turpeinen, U.; Reedijk, J., Separation of actinides and lanthanides: crystal and molecular structures of N,N′-bis(3,5-di-t-butylsalicylidene)-4,5-dimethyl-1,2-phenylenediamine and its uranium complex. *Polyhedron* **2004,** *23* (14), 2285-2291.

53. Pathak, P. N.; Veeraraghavan, R.; Prabhu, D. R.; Mahajan, G. R.; Manchanda, V. K., Separation Studies of Uranium and Thorium Using Di-2-Ethylhexyl Isobutyramide (D2EHIBA). *Separation Science and Technology* **1999,** *34* (13), 2601-2614.

54. Kannan, S.; Deb, S. B.; Gamare, J. S.; Drew, M. G. B., Coordination and separation studies of the uranyl ion with iso-butyramide based ligands: Synthesis and structures of [UO2(NO3)2(iC3H7CON{iC4H9}2)2] and [UO2(C6H5COCHCOC6H5)2(iC3H7CON{iC3H7}2)]. *Polyhedron* **2008,** *27* (12), 2557-2562.

55. Demir, S.; Brune, N. K.; Van Humbeck, J. F.; Mason, J. A.; Plakhova, T. V.; Wang, S.; Tian, G.; Minasian, S. G.; Tyliszczak, T.; Yaita, T.; Kobayashi, T.; Kalmykov, S. N.; Shiwaku, H.; Shuh, D. K.; Long, J. R., Extraction of Lanthanide and Actinide Ions from Aqueous Mixtures Using a Carboxylic Acid-Functionalized Porous Aromatic Framework. *ACS Central Science* **2016,** *2* (4), 253-265.

56. Keener, M.; Hunt, C.; Carroll, T. G.; Kampel, V.; Dobrovetsky, R.; Hayton, T. W.; Ménard, G., Redox-switchable carboranes for uranium capture and release. *Nature* **2020**.

57. Bingham, P. A.; Hand, R. J.; Stennett, M. C.; Hyatt, N. C.; Harrison, M. T., The Use of Surrogates in Waste Immobilization Studies: A Case Study of Plutonium. *MRS Proceedings* **2008,** *1107*, 421.

58. Deblonde, G. J. P.; Ricano, A.; Abergel, R. J., Ultra-selective ligand-driven separation of strategic actinides. *Nature Communications* **2019,** *10* (1), 2438.

59. Krauskopf, K. B., Thorium and rare-earth metals as analogs for actinide elements. *Chemical Geology* **1986,** *55* (3), 323-335.

60. De Roo, G.; Parsons, J. E., A methodology for calculating the levelized cost of electricity in nuclear power systems with fuel recycling. *Energy Economics* **2011,** *33* (5), 826-839.

61. Law, J. D.; Herbst, R. S.; Peterman, D. R.; Tillotson, R. D.; Todd, T. A., Development of a Cobalt Dicarbollide/Polyethylene Glycol Solvent Extraction Process for Separation of Cesium and Strontium to Support Advanced Aqueous Reprocessing. *Nuclear Technology* **2004,** *147* (2), 284-290.

62. Andrew, T. B.; Charles, L. B.; Durgesh, V. W.; Gary, A. B.; Michael, K. T.; Justin, R. W., Structure and spectroscopy of uranyl and thorium complexes with substituted phosphine oxide ligands. *Radiochimica Acta* **2015,** *103* (1), 49-56.

63. Kudryavtsev, I. Y.; Baulina, T.; Pasechnik, M.; Aisin, R.; Matveev, S.; Petrovskii, P.; Nifant'ev, E., Synthesis and coordination properties of new preorganized ligand on the triphenylphosphine oxide platform. *Russian Chemical Bulletin* **2013,** *62* (4), 1086-1090.

64. Levason, W.; Newman, E. H.; Webster, M., Tetrakis(triphenylphosphine oxide) complexes of the lanthanide nitrates; synthesis, characterisation and crystal structures of [La(Ph3PO)4(NO3)3]·Me2CO and [Lu(Ph3PO)4(NO3)2]NO3. *Polyhedron* **2000,** *19* (28), 2697-2705.

65. Quilès, F.; Nguyen-Trung, C.; Carteret, C.; Humbert, B., Hydrolysis of Uranyl(VI) in Acidic and Basic Aqueous Solutions Using a Noncomplexing Organic Base: A Multivariate Spectroscopic and Statistical Study. *Inorg. Chem.* **2011,** *50* (7), 2811-2823.

66. Pant, D. D.; Khandelwal, D. P., The absorption and fluorescence spectra of uranyl nitrate solutions at room temperature. *P. Indian Acad. Sci. A* **1959,** *50* (5), 323-335.

67. Sadowski, P.; Majdan, M., Spectroscopic investigation of lanthanide nitrates. *Monatshefte für Chemie / Chemical Monthly* **1995,** *126* (8), 863-870.

68. Brown, M. A.; Paulenova, A.; Gelis, A. V., Aqueous Complexation of Thorium(IV), Uranium(IV), Neptunium(IV), Plutonium(III/IV), and Cerium(III/IV) with DTPA. *Inorganic Chemistry* **2012,** *51* (14), 7741-7748.

69. Teixidor, F.; Núñez, R.; Viñas, C.; Sillanpää, R.; Kivekäs, R., Contribution of the nido-[7,8-C2B9H10]- Anion to the Chemical Stability, Basicity, and 31P NMR Chemical Shift in nido-o-Carboranylmonophosphines. *Inorganic Chemistry* **2001,** *40* (11), 2587-2594.

70. Fox, M. A.; Nervi, C.; Crivello, A.; Low, P. J., Carborane radical anions: spectroscopic and electronic properties of a carborane radical anion with a 2n + 3 skeletal electron count. *Chemical Communications* **2007,** (23), 2372-2374.

71. Zhang, J.; Fu, X.; Lin, Z.; Xie, Z., Supercarborane Radical Anions with 2n + 3 Electron Counts: A Combined Experimental and Theoretical Study. *Inorganic Chemistry* **2015,** *54* (4), 1965-1973.

72. Mercer, G. D.; Lang, J.; Reed, R.; Scholer, F. R., Electrolytic reduction of B-oxy derivatives of 2,3-dicarba-closo-undecaborane(11). *Inorganic Chemistry* **1975,** *14* (4), 761-763.

73. Fu, X.; Chan, H.-S.; Xie, Z., Synthesis and Crystal Structure of a 13-Vertex Carborane Radical Anion with 2n + 3 Framework Electrons. *Journal of the American Chemical Society* **2007,** *129* (29), 8964-8965.

74. Fox, M. A.; Nervi, C.; Crivello, A.; Batsanov, A. S.; Howard, J. A. K.; Wade, K.; Low, P. J., Structural, spectroscopic, electrochemical and computational studies of C,C′-diaryl-ortho-carboranes, 1-(4-XC6H4)-2-Ph-1,2-C2B10H10 (X = H, F, OMe, NMe2, NH2, OH and O−). *Journal of Solid State Electrochemistry* **2009,** *13* (10), 1483-1495.

75. Tricas, H.; Colon, M.; Ellis, D.; Macgregor, S. A.; McKay, D.; Rosair, G. M.; Welch, A. J.; Glukhov, I. V.; Rossi, F.; Laschi, F.; Zanello, P., Spectroscopic, structural, computational and

(spectro)electrochemical studies of icosahedral carboranes bearing fluorinated aryl groups. *Dalton Transactions* **2011,** *40* (16), 4200-4211.

76. Wee, K.-R.; Han, W.-S.; Cho, D. W.; Kwon, S.; Pac, C.; Kang, S. O., Carborane Photochemistry Triggered by Aryl Substitution: Carborane-Based Dyads with Phenyl Carbazoles. *Angewandte Chemie International Edition* **2012,** *51* (11), 2677-2680.

77. Weiss, R.; Grimes, R. N., Nuclear magnetic resonance relaxation in complex spin systems. Proton and boron-11 spin-lattice relaxation studies of carboranes and metallocarboranes. *J. Am. Chem. Soc.* **1977,** *99* (4), 1036-1042.

78. Abney, C. W.; Mayes, R. T.; Saito, T.; Dai, S., Materials for the Recovery of Uranium from Seawater. *Chemical Reviews* **2017,** *117* (23), 13935-14013.

79. Chen, L.; Bai, Z.; Zhu, L.; Zhang, L.; Cai, Y.; Li, Y.; Liu, W.; Wang, Y.; Chen, L.; Diwu, J.; Wang, J.; Chai, Z.; Wang, S., Ultrafast and Efficient Extraction of Uranium from Seawater Using an Amidoxime Appended Metal–Organic Framework. *ACS Applied Materials & Interfaces* **2017,** *9* (38), 32446-32451.

80. Piechowicz, M.; Abney, C. W.; Thacker, N. C.; Gilhula, J. C.; Wang, Y.; Veroneau, S. S.; Hu, A.; Lin, W., Successful Coupling of a Bis-Amidoxime Uranophile with a Hydrophilic Backbone for Selective Uranium Sequestration. *ACS Applied Materials & Interfaces* **2017,** *9* (33), 27894-27904.

81. Cong-Zhi, W.; Qun-Yan, W.; Jian-Hui, L.; Zhi-Fang, C.; Guo-Zhong, W.; Wei-Qun, S., Complexation of vanadium with amidoxime and carboxyl groups: uncovering the competitive role of vanadium in uranium extraction from seawater. *Radiochimica Acta* **2017,** *105* (7), 541-553.

82. Ladshaw, A. P.; Das, S.; Liao, W. P.; Yiacoumi, S.; Janke, C. J.; Mayes, R. T.; Dai, S.; Tsouris, C., Experiments and Modeling of Uranium Uptake by Amidoxime-Based Adsorbent in the Presence of Other Ions in Simulated Seawater. *Industrial & Engineering Chemistry Research* **2016,** *55* (15), 4241-4248.

83. Pan, H.-B.; Kuo, L.-J.; Wai, C. M.; Miyamoto, N.; Joshi, R.; Wood, J. R.; Strivens, J. E.; Janke, C. J.; Oyola, Y.; Das, S.; Mayes, R. T.; Gill, G. A., Elution of Uranium and Transition Metals from

Amidoxime-Based Polymer Adsorbents for Sequestering Uranium from Seawater. *Industrial & Engineering Chemistry Research* **2016,** *55* (15), 4313-4320.

84. Tokunaga, T. K.; Kim, Y.; Wan, J.; Yang, L., Aqueous Uranium(VI) Concentrations Controlled by Calcium Uranyl Vanadate Precipitates. *Environmental Science & Technology* **2012,** *46* (14), 7471-7477.

85. Endrizzi, F.; Rao, L., Chemical Speciation of Uranium(VI) in Marine Environments: Complexation of Calcium and Magnesium Ions with [(UO2)(CO3)3]4− and the Effect on the Extraction of Uranium from Seawater. *Chemistry – A European Journal* **2014,** *20* (44), 14499-14506.

86. Endrizzi, F.; Leggett, C. J.; Rao, L., Scientific Basis for Efficient Extraction of Uranium from Seawater. I: Understanding the Chemical Speciation of Uranium under Seawater Conditions. *Industrial & Engineering Chemistry Research* **2016,** *55* (15), 4249-4256.

87. Nipruk, O. V.; Chernorukov, N. G.; Volochai, A. A.; Arova, M. I., Study of the state of uranyl orthovanadate (UO2)3(VO4)2·4H2O in aqueous solutions. *Russian Journal of General Chemistry* **2013,** *83* (4), 636-641.

88. Sanding, A.; Bruno, J., The solubility of (UO2)3(PO4)2 · 4H2O(s) and the formation of U(VI) phosphate complexes: Their influence in uranium speciation in natural waters. *Geochimica et Cosmochimica Acta* **1992,** *56* (12), 4135-4145.

89. Fanizza, M. F.; Yoon, H.; Zhang, C.; Oostrom, M.; Wietsma, T. W.; Hess, N. J.; Bowden, M. E.; Strathmann, T. J.; Finneran, K. T.; Werth, C. J., Pore-scale evaluation of uranyl phosphate precipitation in a model groundwater system. *Water Resources Research* **2013,** *49* (2), 874-890.

90. Lobeck, H. L.; Balboni, E.; Parker, C. J.; Kohlgruber, T. A.; Xu, M.; Boukdad, S.; Ridder, H. M.; Traustason, H.; Isner, J. K.; Dzik, E. A.; Burns, P. C., Dissolution of poorly soluble uranyl phosphate phases in the Metaautunite Subgroup under uranyl peroxide cage cluster forming conditions. *American Mineralogist* **2020,** *105* (2), 182-193.

91. Arteaga-Müller, R.; Tsurugi, H.; Saito, T.; Yanagawa, M.; Oda, S.; Mashima, K., New Tantalum Ligand-Free Catalyst System for Highly Selective Trimerization of Ethylene Affording 1-

Hexene: New Evidence of a Metallacycle Mechanism. *Journal of the American Chemical Society* **2009,** *131* (15), 5370-5371.

92. Tsurugi, H.; Saito, T.; Tanahashi, H.; Arnold, J.; Mashima, K., Carbon Radical Generation by d0 Tantalum Complexes with α-Diimine Ligands through Ligand-Centered Redox Processes. *Journal of the American Chemical Society* **2011,** *133* (46), 18673-18683.

93. Tsurugi, H.; Tanahashi, H.; Nishiyama, H.; Fegler, W.; Saito, T.; Sauer, A.; Okuda, J.; Mashima, K., Salt-Free Reducing Reagent of Bis(trimethylsilyl)cyclohexadiene Mediates Multielectron Reduction of Chloride Complexes of W(VI) and W(IV). *Journal of the American Chemical Society* **2013,** *135* (16), 5986-5989.

94. Chu, J.; Carroll, T. G.; Wu, G.; Telser, J.; Dobrovetsky, R.; Ménard, G., Probing Hydrogen Atom Transfer at a Phosphorus(V) Oxide Bond Using a "Bulky Hydrogen Atom" Surrogate: Analogies to PCET. *Journal of the American Chemical Society* **2018,** *140* (45), 15375-15383.

95. Arnold, P. L.; Patel, D.; Wilson, C.; Love, J. B., Reduction and selective oxo group silylation of the uranyl dication. *Nature* **2008,** *451* (7176), 315-317.

96. Arnold, P. L.; Love, J. B.; Patel, D., Pentavalent uranyl complexes. *Coordination Chemistry Reviews* **2009,** *253* (15), 1973-1978.

97. Love, J. B., A macrocyclic approach to transition metal and uranyl Pacman complexes. *Chemical Communications* **2009,** (22), 3154-3165.

98. Yahia, A.; Arnold, P. L.; Love, J. B.; Maron, L., The Effect of the Equatorial Environment on Oxo-Group Silylation of the Uranyl Dication: A Computational Study. *Chemistry – A European Journal* **2010,** *16* (16), 4881-4888.

99. Pedrick, E. A.; Wu, G.; Hayton, T. W., Reductive Silylation of the Uranyl Ion with Ph3SiOTf. *Inorganic Chemistry* **2014,** *53* (23), 12237-12239.

100. Jones, G. M.; Arnold, P. L.; Love, J. B., Oxo–Group-14-Element Bond Formation in Binuclear Uranium(V) Pacman Complexes. *Chemistry – A European Journal* **2013,** *19* (31), 10287-10294.

101. Arnold, P. L.; Pécharman, A.-F.; Hollis, E.; Yahia, A.; Maron, L.; Parsons, S.; Love, J. B., Uranyl oxo activation and functionalization by metal cation coordination. *Nature Chemistry* **2010,** *2* (12), 1056-1061.

102. Seaman, L. A.; Pedrick, E. A.; Wu, G.; Hayton, T. W., Promoting oxo functionalization in the uranyl ion by ligation to ketimides. *Journal of Organometallic Chemistry* **2018,** *857*, 34-37.

103. Assefa, M. K.; Wu, G.; Hayton, T. W., Uranyl Oxo Silylation Promoted by Silsesquioxane Coordination. *Journal of the American Chemical Society* **2020,** *142* (19), 8738-8747.

104. Pedrick, E. A.; Wu, G.; Hayton, T. W., Oxo Ligand Substitution in a Cationic Uranyl Complex: Synergistic Interaction of an Electrophile and a Reductant. *Inorganic Chemistry* **2015,** *54* (14), 7038-7044.

105. Fortier, S.; Wu, G.; Hayton, T. W., Synthesis and Characterization of Three Homoleptic Alkoxides of Uranium: [Li(THF)]2[UIV(OtBu)6], [Li(Et2O)][UV(OtBu)6], and UVI(OtBu)6. *Inorganic Chemistry* **2008,** *47* (11), 4752-4761.

106. Myers, W. L. *A literature review on the chemical and physical properties of uranyl fluoride (UO sub 2 F sub 2)*; United States, 1990-08-01, 1990.

107. Lau, K. H.; Brittain, R. D.; Hildenbrand, D. L., Complex sublimation/decomposition of uranyl fluoride: thermodynamics of gaseous uranyl fluoride (UO2F2) and uranium oxide fluoride (UOF4). *The Journal of Physical Chemistry* **1985,** *89* (20), 4369-4373.

108. Kirkegaard, M. C.; Ambrogio, M. W.; Miskowiec, A.; Shields, A. E.; Niedziela, J. L.; Spano, T. L.; Anderson, B. B., Characterizing the degradation of [(UO2F2)(H2O)]7 4H2O under humid conditions. *Journal of Nuclear Materials* **2020,** *529*, 151889.

109. Kirkegaard, M. C.; Spano, T. L.; Ambrogio, M. W.; Niedziela, J. L.; Miskowiec, A.; Shields, A. E.; Anderson, B. B., Formation of a uranyl hydroxide hydrate via hydration of [(UO2F2)(H2O)]7·4H2O. *Dalton Transactions* **2019,** *48* (36), 13685-13698.

110. Kahlert, J.; Stammler, H.-G.; Neumann, B.; Harder, R. A.; Weber, L.; Fox, M. A., Crystal Structures of the Carborane Dianions [1,4-(PhCB10H10C)2C6H4]2− and [1,4-

(PhCB10H10C)2C6F4]2− and the Stabilizing Role of the para-Phenylene Unit on 2 n+3 Skeletal Electron Clusters. *Angewandte Chemie International Edition* **2014,** *53* (14), 3702-3705.

111. Kaim, W.; Hosmane, N. S.; Záliš, S.; Maguire, J. A.; Lipscomb, W. N., Boron Atoms as Spin Carriers in Two- and Three-Dimensional Systems. *Angewandte Chemie International Edition* **2009,** *48* (28), 5082-5091.

112. Morris, J. H.; Gysling, H. J.; Reed, D., Electrochemistry of boron compounds. *Chemical Reviews* **1985,** *85* (1), 51-76.

113. King, B. T.; Noll, B. C.; McKinley, A. J.; Michl, J., Dodecamethylcarba-closo-dodecaboranyl (CB11Me12•), a Stable Free Radical. *Journal of the American Chemical Society* **1996,** *118* (44), 10902-10903.

114. Hosmane, N. S.; Zhang, H.; Maguire, J. A.; Wang, Y.; Demissie, T.; Colacot, T. J.; Ezhova, M. B.; Lu, K.-J.; Zhu, D.; Gray, T. G.; Helfert, S. C.; Hosmane, S. N.; Collins, J. D.; Baumann, F.; Kaim, W.; Lipscomb, W. N., Chemistry of C-Trimethylsilyl-Substituted Heterocarboranes. 28. Selective Alkylation and Reactivity of "Carbons Adjacent" and "Carbons Apart" Tetracarba-nido-dodecaborane(12) Derivatives toward Group 1 and Group 2 Metals. Synthetic, Spectroscopic, and Structural Investigations on Lithium-, Sodium-, Potassium-, Cesium-, and Magnesium-Complexed C4B8 Carboranes. *Organometallics* **2000,** *19* (4), 497-508.

115. Zakharkin, L. I., Some recent advances in the chemistry of dicarba-closo-dodecaboranes. *Pure and Applied Chemistry* **1972,** *29* (4), 513-526.

116. Hosoi, K.; Inagi, S.; Kubo, T.; Fuchigami, T., o-Carborane as an electron-transfer mediator in electrocatalytic reduction. *Chemical Communications* **2011,** *47* (30), 8632-8634.

117. Weber, L.; Kahlert, J.; Brockhinke, R.; Böhling, L.; Halama, J.; Brockhinke, A.; Stammler, H.-G.; Neumann, B.; Nervi, C.; Harder, R. A.; Fox, M. A., C,C′-Bis(benzodiazaborolyl)dicarba-closo-dodecaboranes: Synthesis, structures, photophysics and electrochemistry. *Dalton Transactions* **2013,** *42* (30), 10982-10996.

118. Jin, G. F.; Hwang, J.-H.; Lee, J.-D.; Wee, K.-R.; Suh, I.-H.; Kang, S. O., A three-dimensional π-electron acceptor, tri-phenyl-o-carborane, bearing a rigid conformation with end-on phenyl units. *Chemical Communications* **2013,** *49* (82), 9398-9400.

119. Wee, K.-R.; Cho, Y.-J.; Song, J. K.; Kang, S. O., Multiple Photoluminescence from 1,2-Dinaphthyl-ortho-Carborane. *Angewandte Chemie International Edition* **2013,** *52* (37), 9682-9685.

120. Niphakis, M. J.; Georg, G. I., Synthesis of Tylocrebrine and Related Phenanthroindolizidines by VOF3-Mediated Oxidative Aryl-Alkene Coupling. *Organic Letters* **2011,** *13* (2), 196-199.

121. Kupchan, S. M.; Dhingra, O. P.; Kim, C.-K., Efficient intramolecular monophenol oxidative coupling. *The Journal of Organic Chemistry* **1978,** *43* (21), 4076-4081.

122. Reynolds, J. G.; Zalkin, A.; Templeton, D. H., Structure of uranyl nitrate-bis(tetrahydrofuran). *Inorg. Chem.* **1977,** *16* (12), 3357-3359.

123. Evans, W. J.; Giarikos, D. G.; Workman, P. S.; Ziller, J. W., Utility of Anhydrous Neodymium Nitrate as a Precursor to Extended Organoneodymium Nitrate Networks. *Inorganic Chemistry* **2004,** *43* (18), 5754-5760.

124. Lalancette, J. M.; Rollin, G.; Dumas, P., Metals Intercalated in Graphite. I. Reduction and Oxidation. *Can. J. Chem.* **1972,** *50* (18), 3058-3062.

125. Liu, Y.; Ren, W.-M.; Liu, C.; Fu, S.; Wang, M.; He, K.-K.; Li, R.-R.; Zhang, R.; Lu, X.-B., Mechanistic Understanding of Dinuclear Cobalt(III) Complex Mediated Highly Enantioselective Copolymerization of meso-Epoxides with CO2. *Macromolecules* **2014,** *47* (22), 7775-7788.

126. Sheldrick, G. M., *Acta Crystallographica Section A* **2015,** *A71*, 3-8.

127. Sheldrick, G. M., *Acta Crystallographica Section C* **2015,** *C71*, 3-8.

128. Dolomanov, O. V. B., L. J.; RGildea, R. J.; Howard, J. A. K.; Puschmann, H. J. , *Appl. Cryst.* **2009,** *42*, 339-341.

129. Chlistunoff, J.; Ziegler, K. J.; Lasdon, L.; Johnston, K. P., Nitric/Nitrous Acid Equilibria in Supercritical Water. *The Journal of Physical Chemistry A* **1999,** *103* (11), 1678-1688.

See you around UCSB!